THE UNIVERSITY OF CHICAGO

ELECTRODYNAMIC PROPERTIES, STRUCTURE, AND NON-EQUILIBRIUM DYNAMICS OF OPTICAL MATTER SYSTEMS

A DISSERTATION SUBMITTED TO
THE FACULTY OF THE DIVISION OF THE PHYSICAL SCIENCES
IN CANDIDACY FOR THE DEGREE OF
DOCTOR OF PHILOSOPHY

DEPARTMENT OF CHEMISTRY

BY
CURTIS WILLIAM PETERSON

CHICAGO, ILLINOIS
DECEMBER 2020

Contents

List of Figures

List of Tables

Acknowledgements

I would like to thank my advisor, Norbert Scherer. Your drive to push scientific boundaries and explore new fields, coupled with your commitment to doing work with integrity, has been a source of inspiration. I have grown intellectually more under your tutelage than at any other point in my life because of the freedom you have given my to develop my own ideas, and the important occasions where you recognized that I needed to focus on something specific. I would like to thank Suri Vaikuntanathan for useful conversations and for introducing me to some important work related to my own. I would also like to thank Stuart Rice. Your timely insights have made my work stronger. The words ’let me ask a stupid question’ evoke dread, curiosity, and excitement when you speak them.

I would like to thank all current and former members of the Scherer group. I would specifically like to thank Yuval Yifat, Delphine Coursault, and Nishant Sule, and Pat Figliozzi for creating an inviting group culture, several collaborations, and a lot of advice. I would like to thank Emmanuel Valenton for collaborating on experiments as well. I would like to thank Shiqi Chen for lending his mathematical expertise to improve my work. I would like to thank John Parker and Chatipat Lorpaiboon for performing simulations used in my work.

The work presented in this dissertation is the culmination of nearly a decade of education that started at a community college. I would not be in the position to write this dissertation if it were not for countless dedicated educators that turned my enthusiasm for the physical sciences into a passion. I would like to thank Haile Haile for teaching me to look for satisfying instead of satisfactory answers to problems. Your courses changed the trajectory of my

education. I would like to thank Lijin Shu for convincing me that graduate school was a realistic option. I would like to thank Martin Greven for mentoring me in undergraduate research.

I would like to thank my parents, Larry Peterson and Karen Peterson, for the patience they showed with as a young child that didn't always follow the rules or do what I was supposed to do. I would also like to thank them for setting a good example and showing me how a responsible person should behave.

Finally, I would like to thank Elizabeth Fei. Making it through graduate school would not have been possible without your constant love and support. Having you as a partner in life makes me aspire to be the best possible version of myself.

Abstract

Optical matter assemblies, specifically nanoparticles that interact and are electrodynamically bound into ordered structures, represent a new type of material that has novel structural and dynamic properties that are of fundamental and practical interest. Polarizable (and/or plasmonic) nano-particles exhibit strong interactions in optical fields (e.g., in optical traps) that result in emergent structures and non-equilibrium phenomena such as non-reciprocal forces and negative torques. Although these effects have been predicted and have begun to be demonstrated experimentally, our understanding of these phenomena is still limited.

In this dissertation I will discuss findings concerning the properties of optical matter systems. I will show that the long-range and periodic interactions between particles in optical matter systems that are the result of the coherent light scattered by the particles in the system have important electrodynamic and structural consequences. Symmetry also plays an important role in the dynamics of optical matter systems, and I will show that broken symmetry of several different types results in non-conservative dynamics. I will also show that rearrangements in optical matter systems are similar to reactions in chemical systems.

Chapter 1

Introduction

Over the last century, the fields of chemistry and material science have expanded to include abstractions away from atoms, molecules, and ions as the elementary building blocks of materials. Assemblies of microparticles or nanoparticles, biological molecules, and polymers form functional materials with novel mechanical, electrical, and photonic properties [1, 2, 3, 4, 5, 6, 7, 8]. Furthermore, when self-assembly occurs in systems where a constant, external source of energy is available new static and dynamic structures become accessible [9, 10, 11, 12]. Optical matter assemblies, specifically nanoparticles that interact and are electrodynamically bound into ordered structures, represent a new type of material that has novel structural and dynamic properties that are of fundamental and practical interest [13, 14, 15, 16, 17]. Polarizable (and/or plasmonic) nano-particles exhibit strong interactions in optical fields (e.g., in optical traps) that result in emergent structures and non-equilibrium phenomena such as non-reciprocal forces [18, 19] and negative torques [20, 21]. Although these effects have been predicted and have begun to be demonstrated experimentally, understanding of these phenomena is still limited.

The structure of optical matter is a result of the optical binding force [13, 14]. All optical matter systems considered in this dissertation are two-dimensional and the relevant particle correspond to a plane transverse to the direction of propagation of trapping laser. On a pairwise level, the optical binding force is the result of one particle in a strong optical field interacting with the light scattered by another [15]. The optical binding force between two particles that are separated by a small fraction of the incident wavelength is attractive if the particles are separated along the polarization direction and repulsive if the particles are separated perpendicular to the polarization direction [15, 17]. At larger separations, the phase of the light scattered by each particle plays a role in the structure of an optical matter cluster. Particles tend to prefer separations near integer multiples of the incident wavelength where the polarization of one particle is in phase with the incident light, creating a region of high intensity due to constructive interference [17]. For circular polarization, the optical binding force is cylindrically symmetric (isotropic) and structures tend to have hexagonal symmetry. A 2D optical matter cluster formed in a wide Gaussian beam is shown in Figure 1.1a. An optical binding potential can be constructed by calculating the work required to separate a pair of particles from some initial separation to a final separation R. An optical binding potential between two 150nm diameter silver nanoparticles calculated from a generalized mie theory simulation is shown in Figure 1.1b.

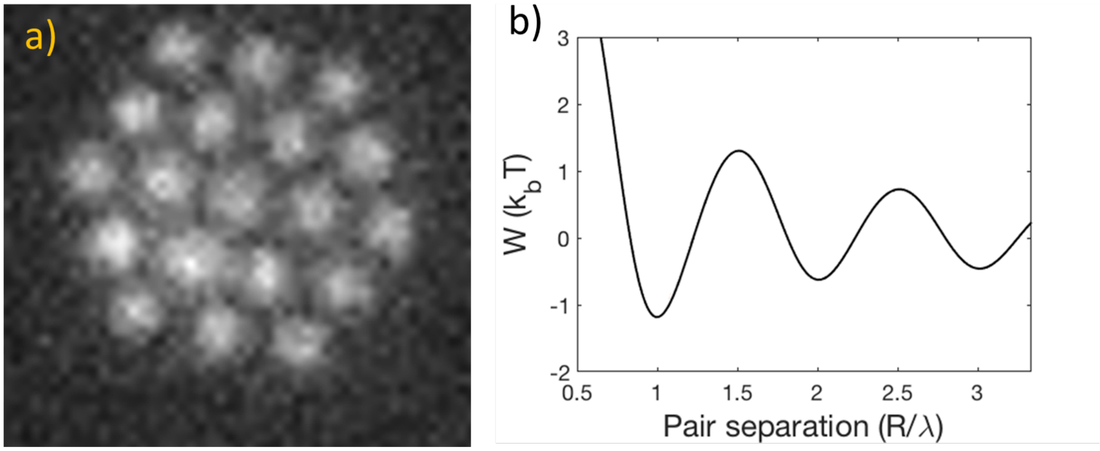

Figure 1.1: Optical matter cluster and optical binding potential. **(b)** 2D optical matter cluster formed in a wide Gaussian beam. **(b)** Optical binding potential constructed by calculating the work required in a generalized Mie theory simulation to separate two 150nm diameter silver nanoparticles from an initial separation to a variable final separation.

A constant flux of energy and momentum is required to maintain an optical matter system. Consider a single $150nm$ diameter silver nanoparticle in an optical trap. Its scattering cross section is roughly $\sigma_{sc} = 5 * 10^{-2} \mu m^2$. If the trapping beam is focused down to a spot with an area of $25\mu m^2$, then roughly 0.2% of the beam will be scattered by the particle. For a typical laser power $50mW$ the particle will scatter approximately $0.1mW$. This means that in $1ms$, the energy of the light scattered by the particle is on the order of $2 * 10^{13} kT$. While most of the light scattered by particles in an optical trap scatters isotropically, any imbalance in the system that causes even a small fraction of the incident light to scatter asymmetrically has the potential to drive the system far from equilibrium. An emerging body of work demonstrates that broken symmetry in optical matter systems result in imbalances in scattering that are accompanied by nonequilibrium phenomena [15, 21, 18, 22, 23].

1.0.1 Outlook

The work presented in this dissertation is focused on discovering and understanding the basic properties of optical matter systems. It is my hope that future researchers will be able to build on these basic properties to achieve new scientific and practical goals. All of the work presented in this dissertation is focused on optical matter with wavelength-scale separations. However, near-field interactions in optical matter systems have significantly stronger electrodynamic coupling than wavelength-separated particles.

In Chapter 5 it is shown that electrodynamic coupling is responsible for many-body (3 or more) nonreciprocal forces in asymmetric clusters of identical spherical particles. Therefore, I expect that non-equilibrium behavior is significantly more pronounced in optical matter systems when near-field pairs are present. However, studying optical matter systems with near-field pair present poses a significant challenge because the size of the point-spread function in our imaging system approaches relevant particle separations [20].

The experiments presented in this dissertation are done with relatively simple and static optical traps (*e.g.* ring traps). However, it is possible to construct more intricate optical traps by using a spatial light modulator to shape the phase profile of the optical beam [24, 25, 26]. I believe that future work will show that a wide range of structures can be built by tuning the shape, phase, intensity, and polarization profiles of optical traps. Furthermore, it has been shown that time-varying interactions between particles lead to self-assembly of structures that do not exist for static interactions [9].

The ejection of a newly formed physically bound dimer from an optical matter cluster is shown in Chapter 5. I find this example particularly interesting because the trapping laser transports single particles to a region of increased particle concentration, and nonreciprocal forces transport the dimer away from that region once a dimer is formed. In other words, single particles are brought to a 'reaction area' via optical forces, and once a dimer is formed, they are taken away from the 'reaction area'. I believe that this phenomenon could be expanded upon to create other schemes where the nonequilibrium dynamics that are inherent to optical matter systems induces useful context-dependent behavior that can be exploited to perform useful tasks.

1.0.2 Structure of dissertation

In Chapter 3 the electrodynamics of optical matter systems is explored. I establish the respective roles of interference and coupling in the coherent light scattered by OM arrays. Experiments and simulations together demonstrate that the spatial profile and directionality of coherent light scattered by optical matter arrays in the far-field is primarily due to interference, while electrodynamic coupling has a quantitative wavelength-dependent effect on the total amount of light scattered by the arrays. Furthermore, it is found that optical matter arrays exist in a regime where electrodynamic coupling is significantly enhanced by constructive interference; both the number of particles in the array as well as the particle size have a significant effect on the strength of the coupling. The work in this section shows that electrodynamic coupling in OM systems is significant due to constructive interference and that OM arrays are an avenue for studying collective electrodynamic excitations in the limit where interaction and coupling are described on an element-by-element basis.

In Chapter 4 it is shown that the long-range periodic nature of the optical binding interaction leads to unique structural features of optical matter arrays. I find that the long-range and periodic characteristics of the optical binding interaction result in several distinct structural features of optical matter clusters. It is also show that the periodic nature of the optical binding interaction favors structures with more inter-particle separations near integer multiples of the pairwise optical binding distance. Furthermore, I find significant changes in nearest neighbor distance compared to the two-particle optical binding distance and deviations from hexagonal symmetry. I construct a pairwise optical binding potential by calculating the work done separating two particles in plane-wave illumination, and find that summing the optical binding potential over particle pairs characterizes the stability of the system. I derive an analytical expression for the distortion energy associated with the symmetric stretching of small optical matter clusters and show that it correctly predicts the most stable lattice constant. Finally, it is shown that as the size of OM clusters grow, the lattice constant continues to increase as it approaches a value around 10% larger than the pairwise optical binding distance.

In Chapter 5, the correspondence between broken symmetry and non-equilibrium phenomena in optical matter systems is explored. Inter-particle forces in optical matter systems do not obey Newton's third law because conservation of momentum is only valid when the entire system, including the particles, the surrounding medium, and the incident and scattered light, are considered as a whole. Therefore, broken symmetry in an optical matter system can manifest broken symmetry in the scattering of the trapping laser that is balanced by net forces on the optical matter system.

The first considers spherical particles of unequal sizes[19]. It was previously shown theoretically that electrodynamic interactions between dissimilar optically trapped particles experience a force in a direction that is transverse to the light propagation direction, despite the absence of an external driving force. The direct measurement of so-called nonreciprocal forces in electrodynamically interacting heterodimers that are confined to pseudo one-dimensional geometries [27] in the absence of an external driving force. I show using equations in the point-dipole approximation that the difference in the phase of the polarizability of the two particles in the heterodimer is responsible for the non-reciprocal force. Experiments with particles of unequal sizes to two-dimensional optical traps are also presented, where the non-reciprocal forces result in the ejection of large particles from a cluster of smaller particles.

The second case considered is breaking the symmetry of the optical matter system by inducing a transverse phase gradient [28]. I establish that the net driving force on homodimers is modulated by a separation-dependent interference effect for small phase gradients. By contrast, large phase gradients break the symmetry of the interaction between particles and profoundly change the electrodynamic inter-particle energy landscape. The findings presented in this section are particularly important for understanding multi-particle dynamics during the self-assembly and rearrangement of optical matter.

To conclude Chapter 5, I utilize point-dipole equations to discuss other ways to break symmetry in optical matter systems. I show that anisotropic particles experience a configuration-dependent net force and derive an equation for the net force that is a generalization of the equation describing non-reciprocal forces on a heterodimer of spherical particles. I also show that for optical matter clusters consisting of three or more particles, electrodynamic coupling can break the symmetry and result in a net force on the cluster in the absence of an external driving force. I present recent experiments where electrodynamic coupling-induced torque is observed.

In chapter 6 structural rearrangements in optical matter systems are discussed. Barrier crossing trajectories directly measured in an optical matter experiment using optical microscopy to observe position and orientation changes of pairs of Ag nanoparticles, *i.e.* passing events, in an optical ring trap are analyzed. A two-step mechanism similar to a bimolecular exchange reaction or the Michaelis-Menten scheme is revealed by analysis that combines detailed knowledge of each trajectory, a statistically significant number of repetitions of the passing events, and the driving force-dependence of the process. It is found one particle allowing the other to pass. This simple experiment can readily be extended to study more complex barrier crossing processes bythat while the total event rate increases with driving force, this increase is only due to increased rate of encounters. There is no drive force-dependence on the rate of barrier crossing because the key motion for the process involves a random (thermal) radial fluctuation of replacing the spherical metal nanoparticles with anisotropic ones or by creating more intricate optical trapping potentials. It is also demonstrated how the concept of a reaction in optical matter systems can be generalized by analyzing the transition between two structural isomers of a six-particle optical matter cluster. Chapter 5 is concluded by demonstrating that the internal degrees of freedom in an optical matter system break detailed balance.

Chapter 2

Methods

2.1 Experimental methods

2.1.1 Optical trapping set-up

The optical trapping set-up used in the experiments detailed in this dissertation is based on the output beam from a titanium-sapphire (Ti:Sapphire) laser (Spectra-Physics 3900s) operating at $800nm$, pumped by a Spectra-Physics Millenia Vs 5 W laser. The output beam of the laser is directed through a Faraday isolator and then spatially filtered using a 4f system in conjunction with a diamond pinhole.

After the pinhole, the collimated Gaussian beam enters the section of the optical trapping set-up is shown in Figure 2.1. The beam is first directed through a beam stabilization system (Optics in Motion LLC) consisting of two beam splitters (BS), two quadrant photodiodes (QPD), and two fast-steering mirrors (FSM). If the position or angle of the beam deviates, the reflected spot on the QPD's moves off center, and feedback from the QPD's cause the FSM's to compensate. This configuration is necessary because the laser source sits on a separate table from the rest of the optical trapping set-up and the tables tend to drift with respect to one another slightly. After the beam stabilization system, the power of the beam is adjusted using a half wave-plate ($\lambda/2$) and polarizing beam splitter (PBS).

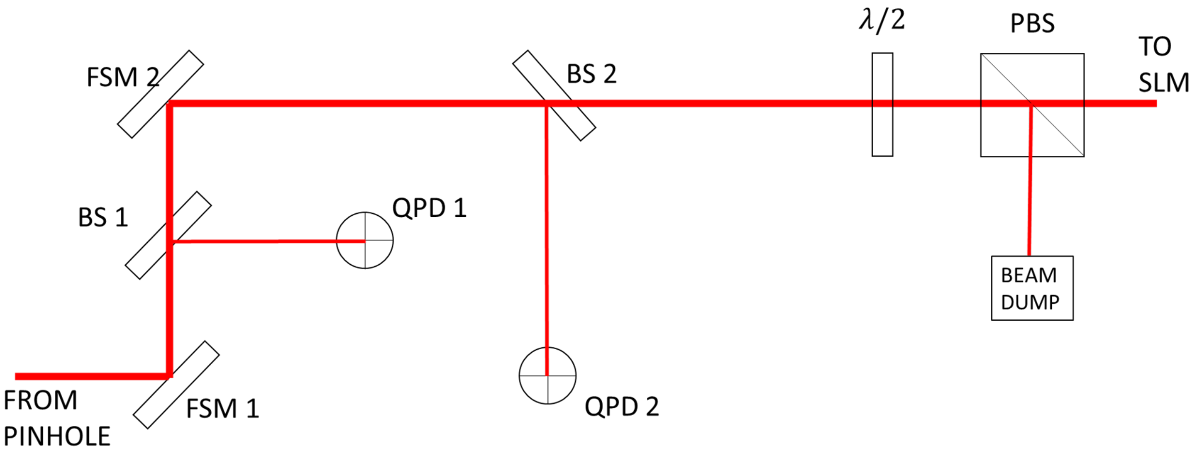

Figure 2.1: Experimental set-up from laser to SLM. FSM - fast steering mirror; BS - beam splitter; QPD - quadrant photodiode; $\lambda/2$ - half waveplate; PBS; polarizing beam splitter.

The second section of the optical trapping setup is shown in Figure 2.2. The phase and intensity profile of the optical trap can be controlled by modulating the phase of the beam using a spatial light modulator (SLM; BNS/Meadowlark HSPDM512-785nm). An example phase mask, which will form a ring trap with an azimuthal phase gradient when focused by the microscope objective (Nikon 60x Plan APO IR water immersion objective, NA=1.27), is shown in Figure 2.2 inset i. Immediately after reflecting from the SLM at a small angle, the collimated Gaussian beam maintains its intensity profile and takes on a phase profile dictated by the computer-controlled phase mask on the SLM. The back aperture of the microscope objective is situated at the opposite end of a 4f system from the SLM. The 4f system has two purposes. The first is to relay the phase information from the SLM to the back aperture of the microscope objective. This ensures that the spatial properties of the focused beam, *i.e.* the optical trap, is related to the phase mask by a Fourier relationship. The second is to resize the beam so that it fills the back aperture of the microscope objective. More filling of the back aperture of the objective translates to increased control over the fine details of the optical trap at the focus of the objective in the liquid sample cell that contains the nanoparticles in solution.

After the lens marked L2 the beam enters the microscope body. It is then reflected toward

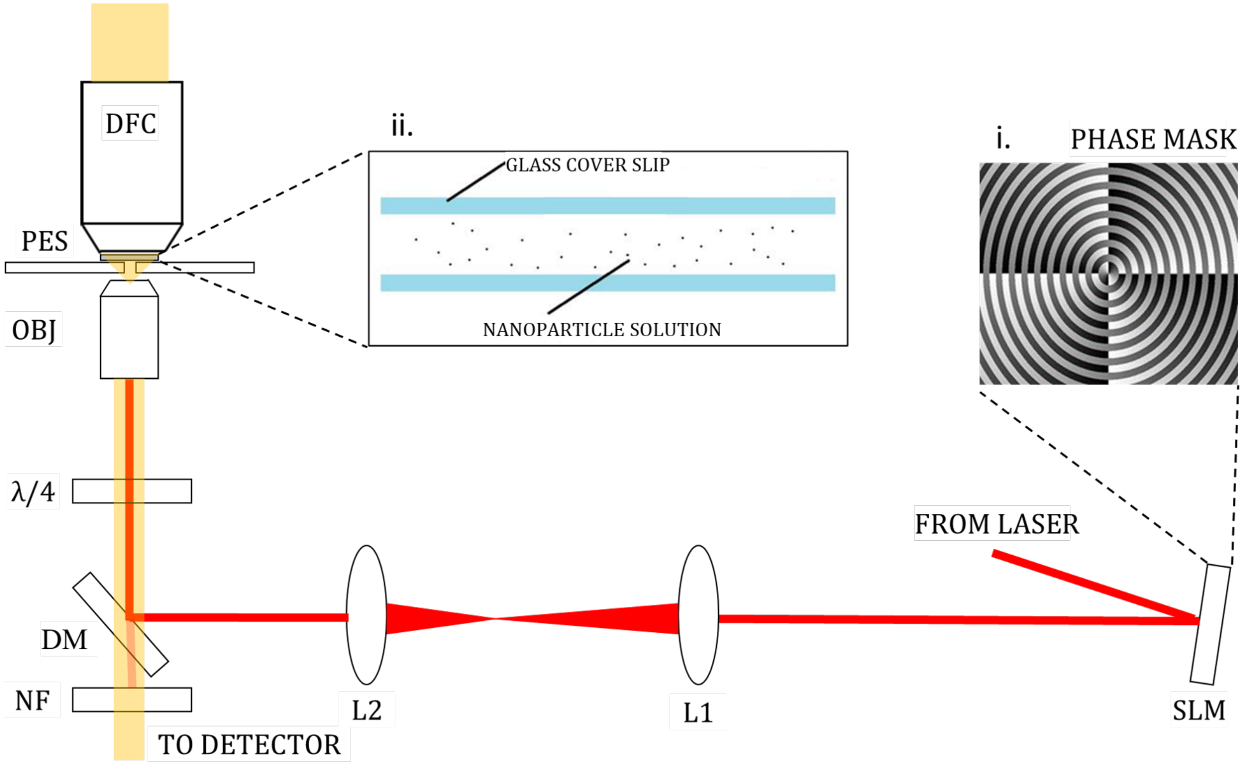

Figure 2.2: Experimental set-up after SLM. PBS - polarizing beam splitter; SLM - spatial light modulator; L - lens; DM - dichroic mirror; $\lambda/4$ - quarter waveplate; OBJ - objective; PES - piezoelectric translation stage; DFC - dark field condenser.

the objective by a dichroic mirror (DM). A quarter waveplate ($\lambda/4$) below the objective is used to change the polarization of the light from linear to circular if needed. The beam then enters the microscope objective and is focused to form the optical trap. The particles in the optical trap are imaged using halogen lamp illumination that is directed through a darkfield condenser (DFC). A schematic of the nanoparticle sample is shown in Figure 2.2 inset ii. It consists of a dilute nanoparticle solution sandwiched between two glass cover-slips. The optical trap is focused near the top cover-slip where radiation pressure acting on the particles is balanced by electrostatic repulsion between the cover-slip and the charged ligands on the particles. A piezoelectric stage (PES) is used to translate the sample in three dimensions.

The remaining scattered and reflected laser light is filtered out using a notch filter (NF) placed below the DM and the darkfield image is relayed to the detector. An sCMOS (Andor NEO) array detector is typically used. The experiments are recorded using the Andor SOLIS software. Under normal experimental conditions an exposure time of $\approx 1ms$ is used and videos of 1000-10000 frames are recorded at a framerate of $\approx 200Hz$. The entire detector does not have to be recorded at once; rather a 200x200 pixel region of interest is usually appropriate for an optical matter experiment. Decreasing the size of the region of interest allows for faster frame rates and decreases the size of the output files. Since the data is streamed to the detector's cache memorythis allows for accumulating more useful data videos in rapid succession.

2.1.2 Aligning and correcting the optical trapping beam

Many of the results in this dissertation depend on precise alignment of the trapping beam and elimination of optical aberrations. The rough alignment of the optical trapping beam can be done by removing the notch filter before the detector, decreasing the laser power, setting the exposure time to its minimum value, and viewing the reflection of the beam from the surface of the top cover-slip. If the beam is correctly aligned, its reflection should not move (shift) when the objective is moved up and down. The alignment of the beam can be

Mode Index	Mode Name	Effect
Z_0^0	piston	None
Z_1^{-1}	tilt	particles go to one side of ring
Z_2^{-2}	oblique astigmatism	particles form two lobes on opposite sides of ring
Z_2^0	defocus	particles become less tightly confined to ring
Z_3^{-3}	vertical trefoil	ring becomes slightly triangular

Table 2.1: Zernike modes and their effects on particles in a ring trap.

fine tuned by filling a ring-trap with particles. The trap will fill evenly only when the beam is very precisely aligned.

Optical aberrations can be corrected by adding Zernike polynomials to the phase profile of the SLM [29]. A ring trap is also convenient for fine-tuning the beam because each Zernike mode has a specific effect on the shape and filling of the trap. Table 2.1 lists few relevant Zernike modes and their effect on how particles fill a ring trap. Tilt, oblique astigmatism, and vertical trefoil have corresponding counterparts tip, vertical astigmatism, and oblique trefoil that differ only in orientation.

2.1.3 Creating wide Gaussian optical traps

A wide-diameter Gaussian optical trap can be created by focusing the beam onto the back aperture of the microscope objective reducing the numerical aperture and if small enough somewhat collimating the beam propagating through the sample. This is achieved by removing the lens labeled L1. The disadvantage of this method is that the phase-pattern on the SLM is not correctly transferred to the focus of the objective. Only simple phase masks are used in this configuration and Zernike polynomials are adjusted heuristically to achieve the most stable optical matter clusters.

2.1.4 Coherent imaging

The trapping laser light scattered from optical matter clusters can be imaged by replacing the dichroic mirror below the microscope objective with a 50:50 beam-splitter. The notch filter below the dichroic mirror is also replaced with a filter with smaller optical density ($OD = 5$). Dark-field illumination (for tracking particle positions) and scattered laser light are simultaneously imaged by attaching a two-channel imaging system (Optical Insights, DualView) between the microscope port and detector. The Dual View splits the image into two spatially separated images according to wavelength using a detachable dichroic beamsplitter with a cutoff wavelength of $560nm$. The light source for the darkfield imaging is switched to a $470nm$ LED (Thorlabs M470L3). A video in which a single particle fluctuated in a Gaussian trap for > 1000 frames was used to define the coodinate shift between the darkfield and backscattered laser images.

2.1.5 Sample preparation

The basic elements of the sample used in an optical matter experiment consists of a dilute nanoparticle solution sandwiched between two glass cover-slips, as depicted in Figure 2.2 inset ii. A thin spacer with a hole in the center is used to create the gap between the cover-slips where the nanoparticle solution resides. It usually takes around $20\mu L$ of nanoparticle solution to fill the sample. An adhesive spacer results in the most robust samples, but a thin silicone sheet has been used in some cases.

The cover-slips are treated according to one of two procedures. The first is to wet with methanol and dry using Nitrogen gas. This procedure ensures that the cover-slips are clean. A more involved preparation involves plasma etching the cover-slips for approximately 5 minutes with ozone. Plasma cleaning induces a negative charge on the cover-slip that enhances electrostatic repulsion between the particles and the cover-slip and helps prevent particle sticking. The cover-slip should be thoroughly cleaned and dried over-night before plasma cleaning.

The most commonly used nanoparticles are 150nm diameter spherical silver nanoparticles with PVP ligands. Typical dilutions of stock nanoparticle solutions range from 1:100 to 1:1000, depending on the initial concentration and type of experiment. The dilution of the solution is important for two reasons. First, the optical trap can fill to quickly or too slowly to get good data for a particular experiment if the dilution is inappropriate. Second, diluting the nanoparticle solution decreases the ionic strength of the solution and increases the electrostatic screening length. This prevents particles from aggregating together in optical traps, and also strengthens the repulsion between the top cover-slip and the particles to help prevent the particles from sticking.

2.2 Data analysis methods

2.2.1 Particle tracking

Particle tracking is broken down into two steps: localization and linking. Localization is the detection of particles in a particular frame, while linking is the formation of trajectories from the detected positions in a sequence of frames. Particle tracking is done using the Mosaic plugin in ImageJ [30], which uses the widely-known particle localization and linking methods developed by Crocker and Grier [31]. The relevant input parameters in the Mosaic plugin are the size of the particles, the threshold brightness for a detected particle (which can be either absolute or relative to the brightest pixel), the number of frames to allow a particle to 'disappear' before ending the trajectory, and the maximum amount a particle in a particular trajectory is allowed to move from frame to frame. The relevant output of Mosaic is a data table containing the frame number, trajectory number, coordinates, and brightness of each particle detected in each frame. The data table can subsequently be imported into Matlab or other data analysis software (see Appendix B for example).

2.2.2 Lattice fitting

I developed a lattice fitting algorithm that fits a set of particle positions to the best-fit hexagonal lattice. The best-fit hexagonal lattice is used for aligning images for averaging, cluster detection, and analysis of the correlated deviations of the particles from the lattice sites. The algorithm is based on minimizing the sum of squared distances from the particle positions to the nearest lattice sites. A range of evenly spaced lattice constants (d_n) and lattice angles (θ_m) are used to generate several test lattices. The test lattices are in turn centered on each particle position (x_i, y_i) and the nearest lattice site to each particle is identified for each test lattice. For each test lattice the sum of squared deviations ($\Delta^2 = \sum_i \delta_i^2$) between the particle positions and the corresponding nearest lattice sites is calculated. The set of parameters (d, θ, x_c, y_c) that correspond to the best-fit lattice is

$$(d, \theta, x_c, y_c) = \underset{(d,\theta,x_i,y_i)}{\arg\min} \sum_i \delta_i^2. \tag{2.1}$$

Once the lattice assignment is obtained, the lattice parameters can be refined analytically to obtain optimized lattice parameters denoted ($d^*, \theta^*, x_c^*, y_c^*$) [32]. Let

$$\begin{aligned} z_1 &= \begin{bmatrix} x_i + iy_i \\ \vdots \end{bmatrix} \\ z_2 &= \begin{bmatrix} x_i^l + iy_i^l \\ \vdots \end{bmatrix} \end{aligned} \tag{2.2}$$

where (x_i^l, y_i^l) are the coordinates of the lattice site assigned to the ith particle. The optimal translation r^* of the lattice matches the centers of mass of the particle positions with the assigned lattice sites

$$r^* = (re(\langle z_2 - z_1 \rangle), im(\langle z_2 - z_1 \rangle)) \tag{2.3}$$

where the angle brackets denote taking the mean value. After letting $Z = (z_1 - \langle z_1 \rangle) \cdot (z_2 - \langle z_2 \rangle)$ optimal parameter values θ^* and d^* are

$$\begin{aligned} \theta^* &= \theta - arctan(\frac{Im(Z)}{Re(Z)}) \\ d^* &= d \cdot \frac{|Z|}{\|z_1 - \langle z_1 \rangle\|^2}. \end{aligned} \tag{2.4}$$

Figure2.3a shows an experimental image of a hexagonal 7-particle optical matter cluster with the corresponding best-fit lattice superimposed. The agreement between the particle positions and the best-fit lattice is good. To quantitatively evaluate the effectiveness of the lattice fitting procedure, I generated 10000 sets of particle coordinates based on a perfectly ordered hexagonal cluster with identical and independently distributed (i.i.d.) Gaussian deviations from each lattice site. The distribution of the total squared deviations before lattice fitting should follow $\sum_i^{14} N(0, \sigma^2)^2 = \sigma^2 \chi^2(14)$ (χ^2 with 14 degrees of freedom), and if 4 degrees of freedom are fully subtracted, we should have $\frac{\Delta^2}{\sigma^2} = \chi^2(10)$. Figure 2.3b shows a comparison of the distribution of scaled fitting error $\frac{\Delta^2}{\sigma^2}$ to the $\chi^2(10)$ distribution. The two distributions are in excellent agreement and we can conclude that the optimal lattice parameters $(d^*, \theta^*, x_c^*, y_c^*)$ fully eliminate 4 degrees of freedom (2 translational, 1 rotational, and 1 scale) from the particle positions.

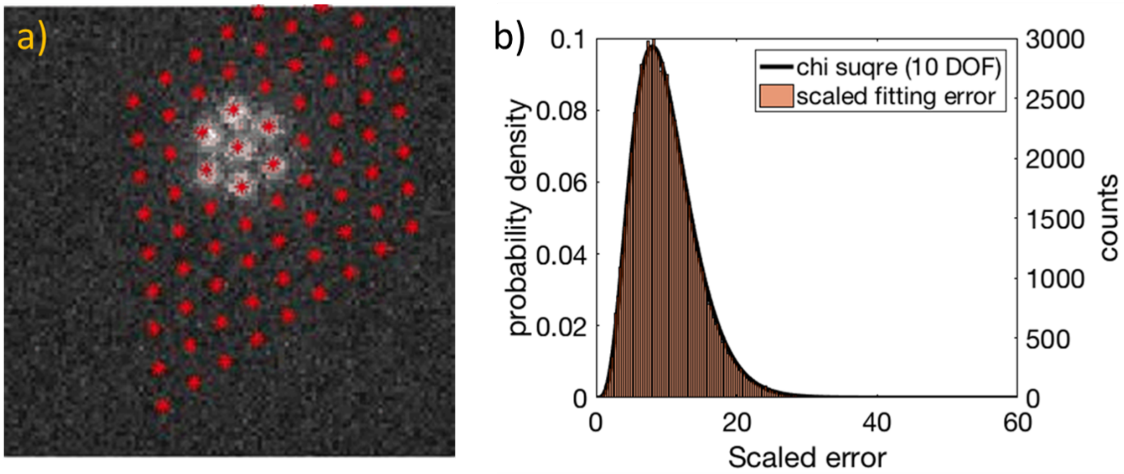

Figure 2.3: Fit lattice example and evaluation of fitting error. **(a)** Best-fit lattice superimposed on an experimental image. **(b)** Comparison between the distribution of scaled fitting error $\frac{\Delta^2}{\sigma^2}$ (brown bars) and the $\chi^2(10)$ distribution (black curve).

Once the occupied lattice sites are defined, it is possible to detect certain cluster shapes by counting the number of neighbors for each lattice site and then counting the number of sites with a particular number of neighbors. For example, the hexagonal 7-particle cluster shown in Figure 2.3a has 1 lattice site with 6 neighbors and 6 lattice sites with 3 neighbors. The number of nearest neighbors is not sufficient to differentiate between every possible cluster lying on a hexagonal lattice, but it is a sufficient to differentiate between several relevant clusters such as the six-particle triangle, chevron, and parallelogram clusters discussed in Chapter 4.

For specific cluster types the best-fit lattice can be used as a reference structure to translate and orient the particle coordinates relative to the underlying lattice. Figure 2.4 shows the translated and oriented set of particle positions for frames when a specific cluster was detected. The positions were translated so that the best-fit lattice site corresponding to position A is at the origin and rotated so that the best-fit lattice site corresponding to position B is on the y axis. This procedure is used to align images for averaging and to visualize the deviations of particle positions from lattice sites.

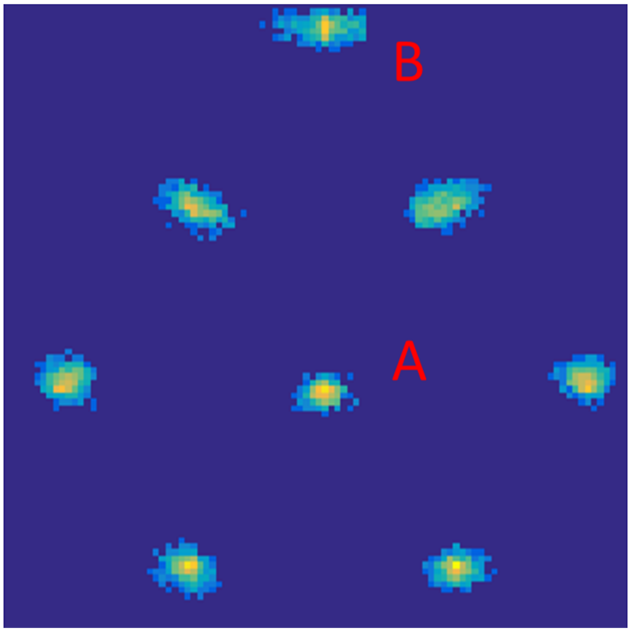

Figure 2.4: Translated and oriented set of particle positions for frames when a specific cluster was detected. The positions were translated so that the best-fit lattice site corresponding to position A is at the origin and rotated so that the best-fit lattice site corresponding to position B is on the y axis. The image is a visualization of particle fluctuations about lattice sites.

2.3 Theoretical methods

Our group has developed fast and accurate methods for simulating optical matter. However, approximate but tractable equations in the Rayleigh limit (not accounting for higher-order multipole modes) offer significant insight into the nature of several of the phenomena observed in optical matter systems. The force in the x_i direction acting on an oscillating dipole $\overline{\boldsymbol{p}}$ illuminated by an arbitrary source can be expressed as [15, 33]

$$\langle F_{x_i} \rangle = \frac{1}{2} Re \left[\overline{\boldsymbol{p}}^* \frac{\partial \overline{\boldsymbol{E}}}{\partial x_i} \right] \tag{2.5}$$

where $\overline{\boldsymbol{E}}$ is the electric field at the position of the dipole. The polarization can be expressed generally in terms of a polarizability tensor as $\overline{\boldsymbol{p}} = \overline{\overline{\boldsymbol{\alpha}}}\overline{\boldsymbol{E}}$. The elements of the polarizability matrix corresponding to the long ($\alpha_{\parallel}$) and short ($\alpha_{\perp}$) axes of an prolate spheroidal particle is [34]

$$\begin{aligned} \alpha_{\parallel(\perp)} = \alpha_{\parallel(\perp)}^{uncorrected} H = V\epsilon_m\epsilon_0 \frac{\epsilon_p - \epsilon_m}{\epsilon_m + L_{\parallel(\perp)}(\epsilon_p - \epsilon_m)} H \\ H = \left[1 - \frac{ik\alpha_{\parallel(\perp)}^{uncorrected}}{6\pi\epsilon_0\epsilon_m}\right]^{-1} \end{aligned} \tag{2.6}$$

where V is the volume of the particle, ϵ_m is the permittivity of the surrounding medium, ϵ_p is the permittivity of the particle, ϵ_p is the vacuum permittivity, H is a correction that accounts for radiative damping [35], and L are depolarization factors given by

$$\begin{aligned} L_{\parallel} = \frac{1-e^2}{e^2}\big(-1 + \frac{1}{2e} ln \frac{1+e}{1-e}\big) \\ L_{\perp} = \frac{1}{2}(1 - L_{\parallel}) \end{aligned} \tag{2.7}$$

where e is the eccentricity of the spheroidal particle. For the special case of a spherical particle, $L_{\parallel} = L_{\perp} = \frac{1}{3}$ and $\alpha_{\parallel} = \alpha_{\perp}$ [34].

For an arbitrary collection of particles at positions $\boldsymbol{r}_n$ the electric field at a position $\boldsymbol{r}$ is

$$\overline{\boldsymbol{E}}(\boldsymbol{r}) = \overline{\boldsymbol{E}}_0 + \sum_n \overline{\overline{\boldsymbol{G}}}(\boldsymbol{r}, \boldsymbol{r}_n)\overline{\overline{\boldsymbol{\alpha}}}_n \overline{\boldsymbol{E}}(\boldsymbol{r} = \boldsymbol{r}_n) \tag{2.8}$$

where is the incndent electric field $\overline{\overline{\boldsymbol{G}}}(\boldsymbol{r}, \boldsymbol{r}_n)$ is the dyadic Green's tensor that propagates the field due to an oscillating dipole at position $\boldsymbol{r}_n$ to the position $\boldsymbol{r}$. The elements of the dyadic Green's tensor (the x_i component of the electric field due to the x_j component of the polarization) are given by [15]

$$\mathbf{G}_{x_i x_j} = \frac{e^{ikR}}{4\pi\epsilon_0\epsilon_m R^3}\left[(3 - 3ikR - k^2R^2)\frac{x_i x_j}{R^2} + (k^2R^2 + ikR - 1)\delta_{ij}\right] \tag{2.9}$$

where R is the distance $|\boldsymbol{r} - \boldsymbol{r}_n|$.

Equations 2.5-2.9 provide the general framework that I use to derive analytical expressions that help understand various phenomena in optical matter systems. Depending on the situation, different approximations can be made to allow these equations to provide clear insights into specific physical situations.

The first simplification that is possible is isotropic polarizabilities. The polarizability of a spherical particle can be represented as a scalar instead of a tensor, which limits the number of terms that appear. The second simplification is to choose a convenient geometry. If two particles lie along a principal axis, Equation 2.9 becomes significantly more simple. Finally, to fully solve Equation 2.8, a self-consistent solution needs to be found. However, the field at each particle can be approximated by allowing only up to a certain order of multiple scattering. This approximation also allows physical phenomena to be attributed to specific orders of scattering.

I also use Equations 2.5-2.9 for analytical electrodynamic force calculations. I manually solved for the relevant partial derivatives of the dyadic Green's tensor and input the results in Matlab. The Matlab code is printed in Appendix B.

Chapter 3

Electrodynamics in optical matter systems

3.1 Electromagnetic interference and coupling in nanoparticle-based optical matter systems

3.1.1 Introduction

Particles in optical traps interact with one-another electrodynamically through optical binding forces. As a result the particles tend to self-organize into ordered optical matter (OM) arrays with preferred inter-particle separations near integer multiples of the incident laser wavelength[13, 14, 36]. The optical binding forces arise from the interaction between the polarization of each particle with the incident and scattered light[15]. OM arrays are open, nonequilibrium systems because the coherent light source that mediates the optical binding forces also establishes a constant flux of electromagnetic energy through the system. Conversion or redirection of the momentum from the incident laser light makes phenomena such as non-reciprocal[18, 19] forces and negative optical torque[37, 38, 20, 21] possible. A full description of an OM array requires knowing the detailed properties of both the incident and scattered light in addition to the positions, sizes, shapes, and compositions of each of the particles. While there has been steady progress toward understanding how tailoring the phase and intensity profiles of the incident fields can affect the dynamics and structure of OM arrays[27, 39, 40, 41, 28], the characteristics of coherent light scattered by OM arrays is an area of current research[42, 43]. In particular, although both interference and electrodynamic coupling (*i.e.* the polarization induced in one particle by the light scattered from neighboring particles) have been shown to have distinct effects on the dynamics of OM arrays, their respective influence on the coherent light scattered by OM arrays and interdependency has received less attention.

Electrodynamic coupling can be categorized into two regimes[44, 45]. In near-field coupling the interaction between particles with separations much smaller than the wavelength of light is treated as a quasi-static interaction[46, 47]. In far-field coupling the in-plane dipolar scattering from large 1D and 2D arrays of particles dramatically effects each particle's polarization; the interaction between particles is frequently treated with a self-consistent approach that invokes the periodicity of the array[48, 49, 50, 51]. A commonality between both types of coupling is modification of the polarization of a particle in the array or structure due to light scattered by other nearby particles. The crossover from near-field to far-field coupling is usually defined in terms of the particle diameter and the wavelength of incident light. Inter-particle separations in OM arrays, typically close to the wavelength of light, are near this crossover distance. However, the approaches typically used in the near- and far-field coupling regimes are not suitable for describing coupling in small OM arrays. A quasi-static approach is inappropriate because retardation is significant over the wavelength-scale distances characteristic of OM arrays, and the finite size of the arrays precludes a self-consistent approach.

In this paper we show that optical matter arrays exist in an intermediate regime where interference both determines the spatial profile of the light scattered by the array, and also enhances electrodynamic coupling between the array's constituent members. We show that the images obtained with coherent backscattered light (termed coherent imaging) from OM arrays contrast strongly with those obtained with incoherent light. Diffraction and fringe patterns visible in the coherent images characterize the electric field intensity surrounding the OM arrays. More striking is the replacement of particle-centric images obtained with incoherent light illumination with images where the intensity is shifted between particles when visualized with coherent light. We investigate the directional scattering of coherent light over polar angles by performing generalized Mie theory (GMT) calculations of ordered OM arrays with 1-7 particles. In contrast to the largely dipolar scattering of a single particle [52], the light scattered from ordered OM arrays develops a lobed structure with maxima in specific sideways, forward, and backward directions. This scattering can also be described in terms of collective modes[23].

We find that the total scattering of the OM arrays at the trapping laser wavelength grows super-extensively when nanoparticles are added to the cluster. We show that the super-extensive growth of the scattering is the result of electrodynamic coupling. We quantify the strength of electrydynamic coupling in OM arrays at the trapping laser wavelength by calculating the ratio of the total electric field intensity at a vacant site in the array to the incident intensity, and find that the contribution from neighboring particles becomes significant even for small (1-6 neighboring particles) OM arrays. Our spectroscopic investigation of coherently illuminated OM arrays extends our investigation to multiple wavelengths and establishes that a collective resonance develops at the expense of the single-particle Mie resonance scattering from individual particles. We discuss our results in the context of the point-dipole approximation and show that electrodynamic coupling in OM arrays is strengthened by constructive interference. We suggest that OM arrays are analogous to an avenue for studying surface lattice resonances (SLRs) but in the small array limit where interaction and coupling is described on an element-by-element basis.

3.1.2 Experimental setup

Our experiments were conducted with a single-beam optical tweezers in an inverted microscope as described previously[17]. A schematic of the experimental set-up is shown in Figure 3.1. A dilute solution of PVP-coated 150nm Ag nanoparticles was placed inside a fluid filled sample chamber made from an adhesive spacer sandwiched between two glass cover-slips. A cw Ti-sapphire laser focused at the back aperture of a 60x microscope objective (Nikon SAPO 60x water; $NA = 1.27$) created a collimated beam that pushes and traps a small number of particles close to the top glass surface of the sample chamber Electrostatic repulsion between the surface ligands on the nanoparticles and the charges on the glass cover-slip balances the radiation pressure, resulting in a 2D trapping condition. The focus of the optical trapping beam was adjusted with a spatial light modulator (SLM; Meadowlark) to create an inward directed phase gradient at the trapping plane that increased the confinement of the nanoparticles. The trapping laser was circularly polarized in all experiments and calculations.

To image the coherent back-scattered light, we employed a 2-channel configuration where one channel accepted $475nm$ incoherent LED darkfield illumination, and the other channel filtered out the LED light and accepted the backscattered laser light but with significant attenuation ($OD = 5$). The two channels form spatially separated images on the same CMOS detector (Andor Neo). The simultaneous measurements are necessary because the particle positions are not obvious from the images of backscattered coherent light as can be seen in Figure 3.1b-g. No additional field stops or aperature stops were introduced to the optical path.

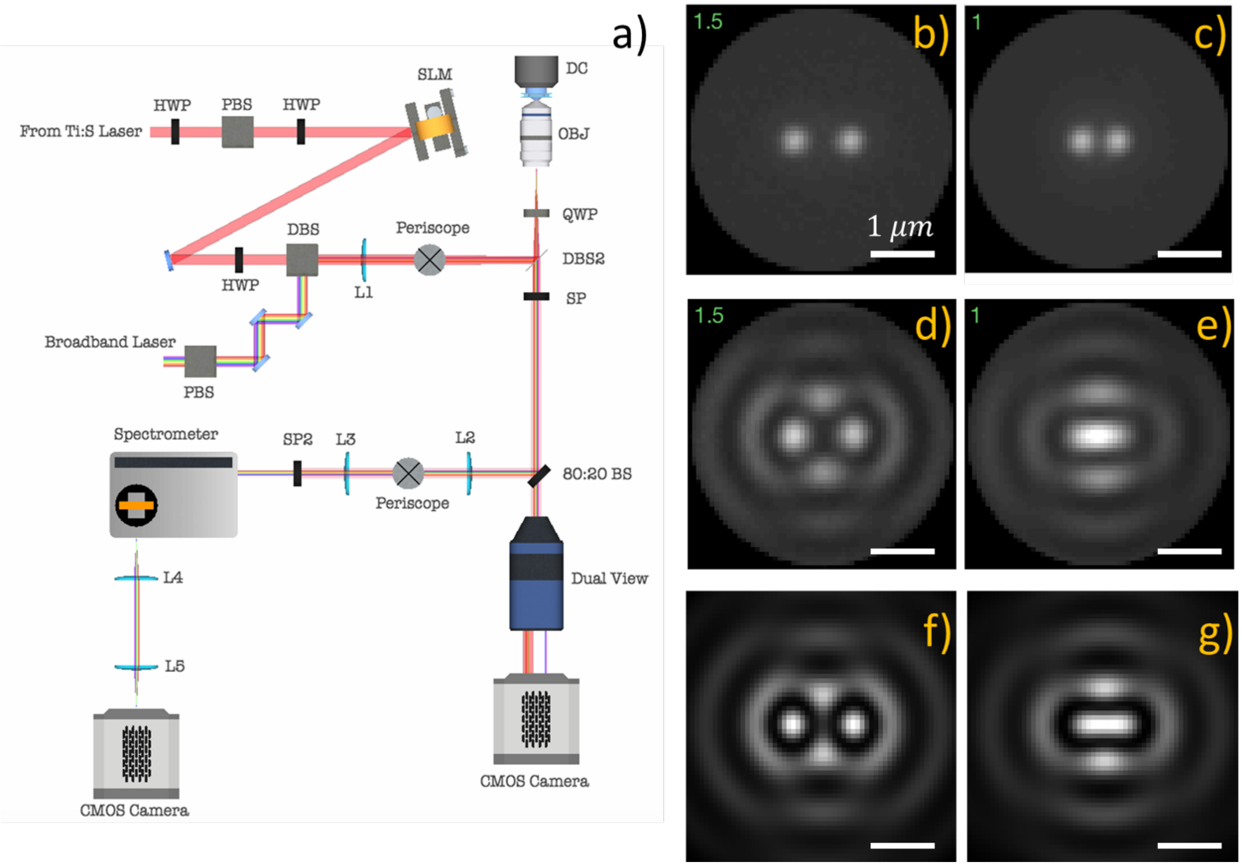

Figure 3.1: **(a)** Optical trapping setup with simultaneous video microscopy and backscattered spectral measurements. HWP - half wave plate; QWP - quarter wave plate; SLM - spatial light modulator; DBS - dichroic beam splitter; PBS - polarizing beam splitter; SP - short-pass filter. **(b-c)** Incoherent (darkfield; NA = 1.27) images of a NP dimer at separations of 1.5λ (b) and λ (c). **(d-e)** Coherent (backscattered; NA = 1.27) images of NP dimer at separations of 1.5λ (d) and λ (e). **(f-g)** Simulated coherent (backscattered; NA = 1.00) images of NP dimer at separations of 1.5λ (f) and λ (g). See videos 2 and 3 for a sequence of images for different inter-particle separations obtained with incoherent and coherent light.

3.1.3 Coherent imaging of OM arrays

The optically trapped particles in our experiments rotate, translate, and dynamically reconfigure in the water solution due to Brownian motion[39, 17]. Therefore, raw darkfield microscopy videos typically show particles with fluctuating configurations where the probability of each specific configuration depends on the inter-particle forces. Particle separations with integer multiples of the trapping wavelength in the solvent medium $\lambda = \lambda_{laser}/n$, where n is the index of refraction, are favored due to optical binding[13, 14, 15, 17]. The individual images containing two randomly fluctuating particles in the optical trap are processed by the following protocol: the particle pair is tracked using Mosaic (ImageJ) and centered with respect to its "center of mass", rotated with respect to the orientation of the pair, and averaged in bins conditioned on inter-particle separation to dramatically improve the signal-to-noise ratio of the images. (see SI for further details; see video 1 for the raw data and videos 2, 3 for averaged and aligned videos measured with incoherent and coherent light, respectively).

Figures 3.1b,c show averaged dark-field images measured with incoherent light where the pair of particles is separated by λ and 1.5λ, respectively. The images show that the incoherent light scattered from each of the particles is manifested as well-defined circular spots regardless of inter-particle distance to separations of 300nm. Averaged images measured with coherent light are shown for the same separations in Figures 3.1d,e. The images for particles separated by $r = 1.5\lambda$ show two distinct spots and a pattern of fringes around the dimer with bright spots on the perpendicular bisector between the particles. The image for $r = \lambda$ shows a single elongated spot that is reminiscent of σ-bonding orbitals in diatomic molecules[53]. The fringe pattern also changes at $r = \lambda$ compared to $r = 1.5\lambda$ with the first ring of fringes becoming ellipsoidal. We performed GMT calculations to generate simulated images for the particle configurations shown in Figure 3.1b-e ($\lambda = 800nm$). The simulated images closely match each of our experimental results measured with coherent light scattered from the OM arrays when the simulated numerical aperture (NA) is set to 1.00. We believe the Fresnel reflection losses at high NA inside the objective reduces the effective NA of the experimental image.

Figure 3.1 demonstrates that the image of a pair of nanoparticles illuminated by coherent light depends on the distance between them. We also recorded images of small 2D OM arrays illuminated by spatially coherent light. Figure 3.2a-c shows aligned and averaged coherent images for three different arrays; the associated averaged incoherent darkfield illumination images are shown in the insets. A real-space lattice fitting procedure was employed to detect ordered arrays and define the rotation and translation required for the averaging of each raw experimental image. The OM array in Figure 3.2a is a 6-particle triangular configuration, as shown by the incoherent darkfield image in the inset. In the coherent image the positions of the corner particles are bright, while the positions of the three interior particles are dimmer by comparison. Moving away from the array, bright fringes are visible with maximum intensity located outward from the three central particles in the triangle. The array in Figure 3.2b is a different six-particle arrangement (termed a chevron) with a concave edge as shown in the inset. Its coherent image contains a smooth bright fringe following the arc of positions of the outer particles with the center particle appearing dark. There are exterior fringes projected outward from the bisectors of each of the 5 exterior edges of the array, and a bright fringe located between the two interior edges. Figure 3.2c shows the coherent image for the 7-particle hexagonal array obtained by adding a particle to the array in Figure 3.2b. The coherent image is annular with a dark center that resembles a benzene π-orbital[53]. There are fringes located outward from the bisector of each edge of the hexagon. The arrays in Figure 3.2 a, b, and c have 3-fold, 2-fold, and 6-fold rotational symmetry, respectively, which matches the symmetry of each array. Figures 3.2d-f show simulated coherent backscattering images ($\lambda = 800nm$; $NA = 1.00$) for each of the experimentally measured arrays in Figure 3.2a-c. The agreement between the measured and simulated images is very good.

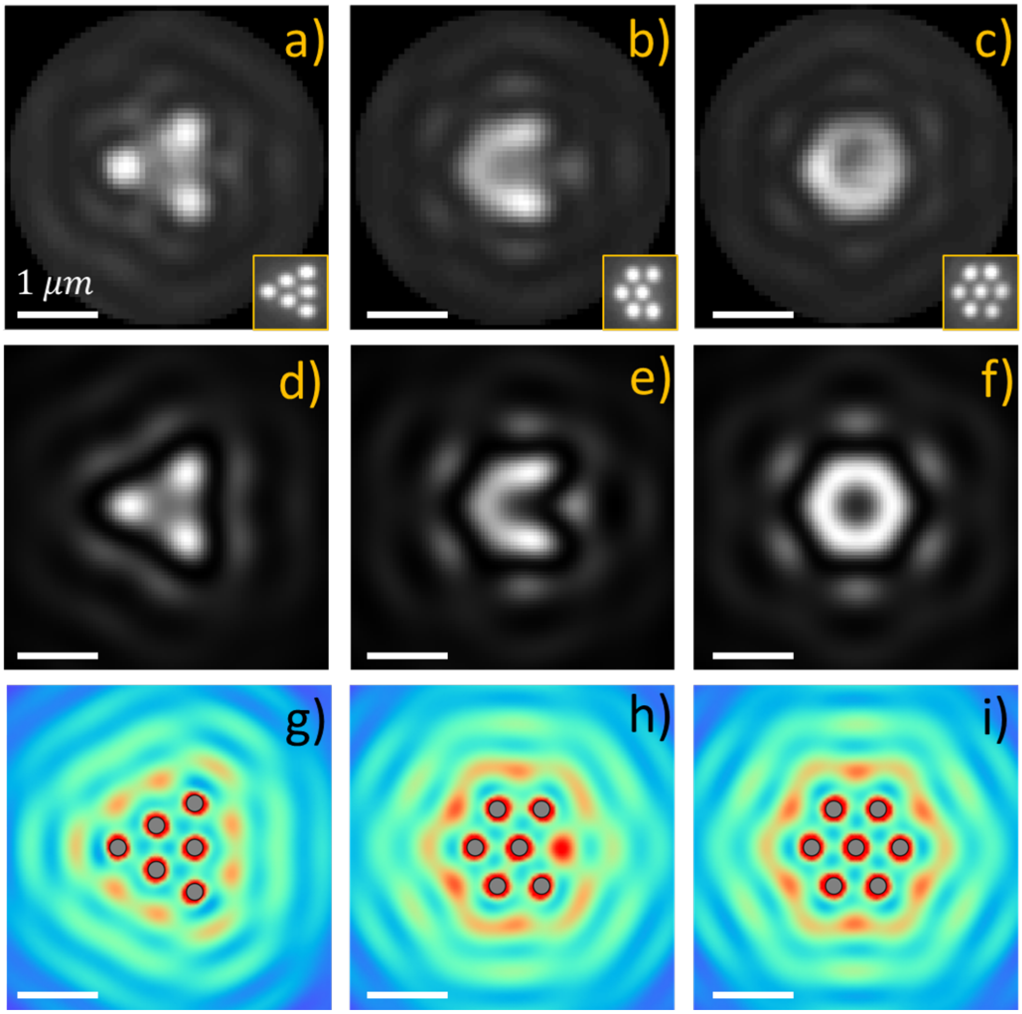

Figure 3.2: Coherently imaged OM arrays and comparison to the simulated electric field intensity. **(a-c)** Experimental coherent backscattered images of OM arrays with 6 (a-b) and 7 (c) particles. The insets show the corresponding averaged incoherent (darkfield) images. **(d-f)** Simulated coherent backscattered images each of the three OM arrays as panels a, b, and c, respectively. **(g-i)** Simulated electric field intensity (color: red-blue) within and around each of the OM arrays for comparison with the results of coherent imaging. The nanoparticle are gray filled circles.

Figures 3.2g-i show the simulated electric field intensity within and around each of the three arrays for comparison with the experimental and simulated coherent backscattering images. Figure 3.2g exhibits two local intensity maxima outside each edge of the triangle that are in a similar location to bright fringes in the simulated coherent image. In the experimental image, the two bright fringes merge into a single fringe. In Figure 3.2h-i the intensity maxima just outside the array are also coincident with fringes in the coherent images. The correspondence between the coherent images in Figures 3.2a-f and the simulated near-field electric field intensity in Comparison of the coherent images in Figures 3.2a-c (experimental) and d-f (simulated) and the electric field distributions in Figures 3.2g-i is clearly different inside the OM array, but improves moving outward.

The relationship between the electric field intensity distribution and the coherent images of OM arrays is due to far-field interference[54]. For plane-wave illumination with incident electric field E_0 the electric field intensity the at a point (ρ, ϕ) in the transverse plane is given by[52]

$$I(\rho, \phi) = E_0^2 + 2E_0|\tilde{A}|\frac{\cos(k\rho + \varphi_s)}{k\rho} \tag{3.1}$$

where $\tilde{A}$ is a complex constant related to the nanoparticle's polarizability and φ_s is a phase shift factor. Meanwhile, the field in the image plane scattered by a point dipole $\boldsymbol{\mu}_i$ located at the origin (in the paraxial limit) is[52]

$$\boldsymbol{E}(\rho, \phi) = \tilde{B}\frac{J_1[k\rho\sin(\theta_{\mathrm{obj}})]}{k\rho}\boldsymbol{\mu} \tag{3.2}$$

where $\tilde{B}$ is a complex constant and J_1 is a Bessel function and θ_{obj} is the collection angle of the microscope objective. Replacing the Bessel function by its asymptotic form and including the electric field reflected off the water-glass interface E_r, the intensity is

$$I(\rho, \phi) \propto E_r^2 + 2E_r|\tilde{B}||\boldsymbol{\mu}|\frac{\cos(k\rho\sin(\theta_{\mathrm{obj}}) + \pi/4)}{(k\rho)^{3/2}} \tag{3.3}$$

Comparing Equation (3.3) to Equation (3.1) shows that for a perfect objective ($sin(\theta_{obj}) = 1$; $N.A. = 1.33$) the coherent images and the electric field intensity for a single particle have identical features up to a constant phase shift, although the image intensity modulation falls off faster as $\rho^{3/2}$. Equations 3.1-3.3 apply to single particles. The difference between the coherent images and the near-field intensity in the interior of the cluster are due to the reduced NA of our experimental coherent images.

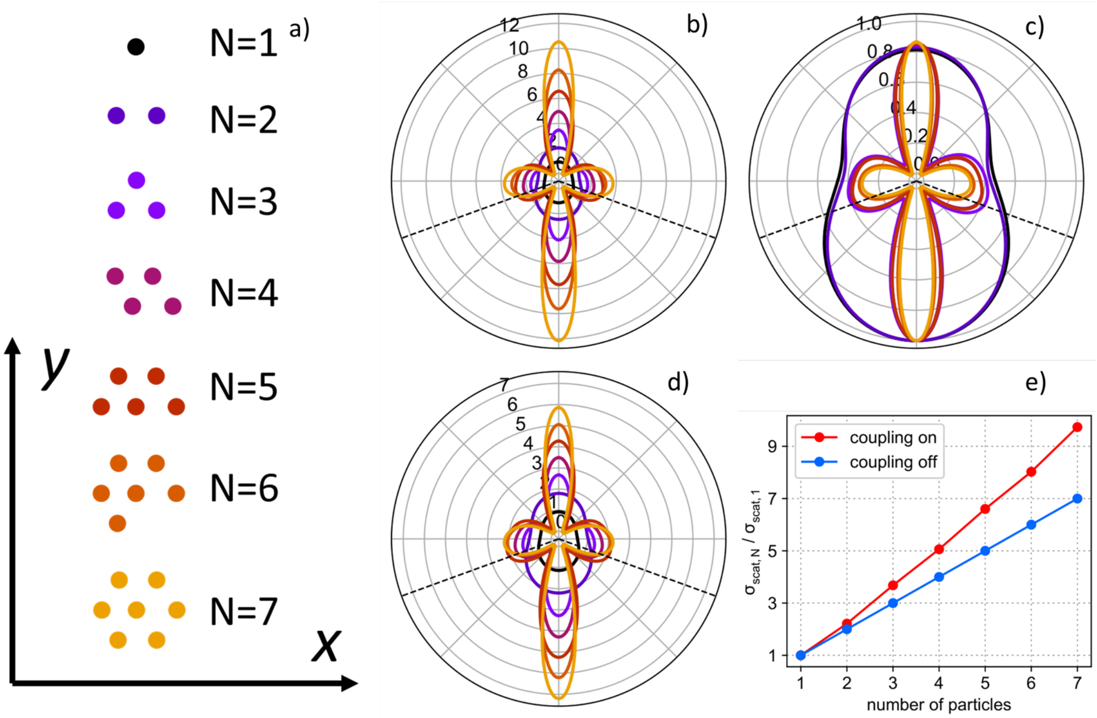

Figure 3.3: Projections of the far-field angular scattering ($\lambda = 800nm; 600nm$ in water) onto the yz plane from NP arrays with 1-7 particles and effect of coupling on magnitude of total scattering. (a) OM arrays (lattice spacing $= 600nm$) and color coding for (b-d). The incident field propagates along the z direction (upward on the page). (b) Angular scattering normalized by the number of particles in the array. (c) Angular scattering normalized to unity. (d) The same as (b), but with interpaticle coupling disabled. (e) Total scattering normalized by single particle scattering with coupling enabled (red) and disabled (blue). Comparing (b) to (d) shows that coupling increases the strength of the far-field scattering. On the other hand, coupling does not significantly change the shape of the angular fields.

3.1.4 Separating interference from coupling in OM arrays

Figures 3.1 and video 3 demonstrate that the separation between particles has a dramatic effect on the images of coherent light scattered by a pair of particles, and Figure 3.2 demonstrates that the size and shape of the OM array does as well. However, the relative importance of interference and coupling needs to be established. We have carried out GMT calculations at a wavelength of $800nm$ ($600nm$ in water) for ordered OM arrays with a lattice spacing of $600nm$ with 1-7 particles to facilitate a quantitative comparison between the light scattered by OM arrays with different numbers of particles. The simulated OM arrays have the structures and orientations shown in Figure 3.3a. Projections of the scattered intensity onto the y-z plane are shown in Figure 3.3b-c when normalized to one (b), and by number of particles (c). A single particle scatters in all directions, although there is a greater scattering intensity in the forward and backward ($\pm z$; up/down) directions than in the sideways (y; left/right) directions. The pattern is reminiscent of a dipole emitter, but is altered due to the high order (*e.g.* quadrupole) modes of the GMT description of a single 150nm diameter Ag NP, and by the broken symmetry between forward and backward scattering. As more particles are added to the OM array, the scattering intensity develops a strong lobe-structure with maxima in the forward ($+z$) and backward ($-z$)directions, and smaller maxima in the sideways ($\pm y$) directions. The change going from 2 to 3 particles is particularly striking and notable because this is the first cluster where a particle is added offset from the x axis.

Figures 3.3b-c show that the directional scattering from an OM array is altered significantly compared to a single particle. We modified the calculations in Figure 3.3b-c by disabling coupling between the particles so that the polarization induced in each particle is only due to the incident field. The results are shown in Figure 3.3d-e. The shape of the angular scattering profile is nearly identical, but the magnitude is twofold greater than when coupling is allowed. Specifically, the total scattering cross section (at a wavelength matching the lattice spacing) of an OM array with N particles σ_N is directly proportional to N as $\sigma_N = N\sigma_1$ with coupling disabled, while σ_N grows super-extensively (*i.e.* faster than N) with coupling enabled.

We also repeated our calculations of coherent images with coupling disabled to determine if the images are affected by coupling. We find that the resulting images are nearly identical to the results shown in Figures 3.1-3.2 with coupling enabled (see SI).

The results in Figures 3.1 through 3.3 demonstrate that the imaging and directionality of light scattered by OM arrays are primarily influenced by interference, and that electrodynamic coupling changes the magnitude but not the spatial characteristics of the scattered coherent light. There are two (limiting) cases where electrodynamic coupling between nanoparticles is particularly important. When inter-particle separations are small compared to the wavelength of light, retardation can be neglected and the interaction between particles can be treated as electrostatic; *i.e.* as between the surface charges of the two particles in a pair or dimer[46, 47]. On the other hand, large field enhancements can occur in extended, regularly spaced arrays of particles at wavelengths near the array spacing due to constructive interference[50].

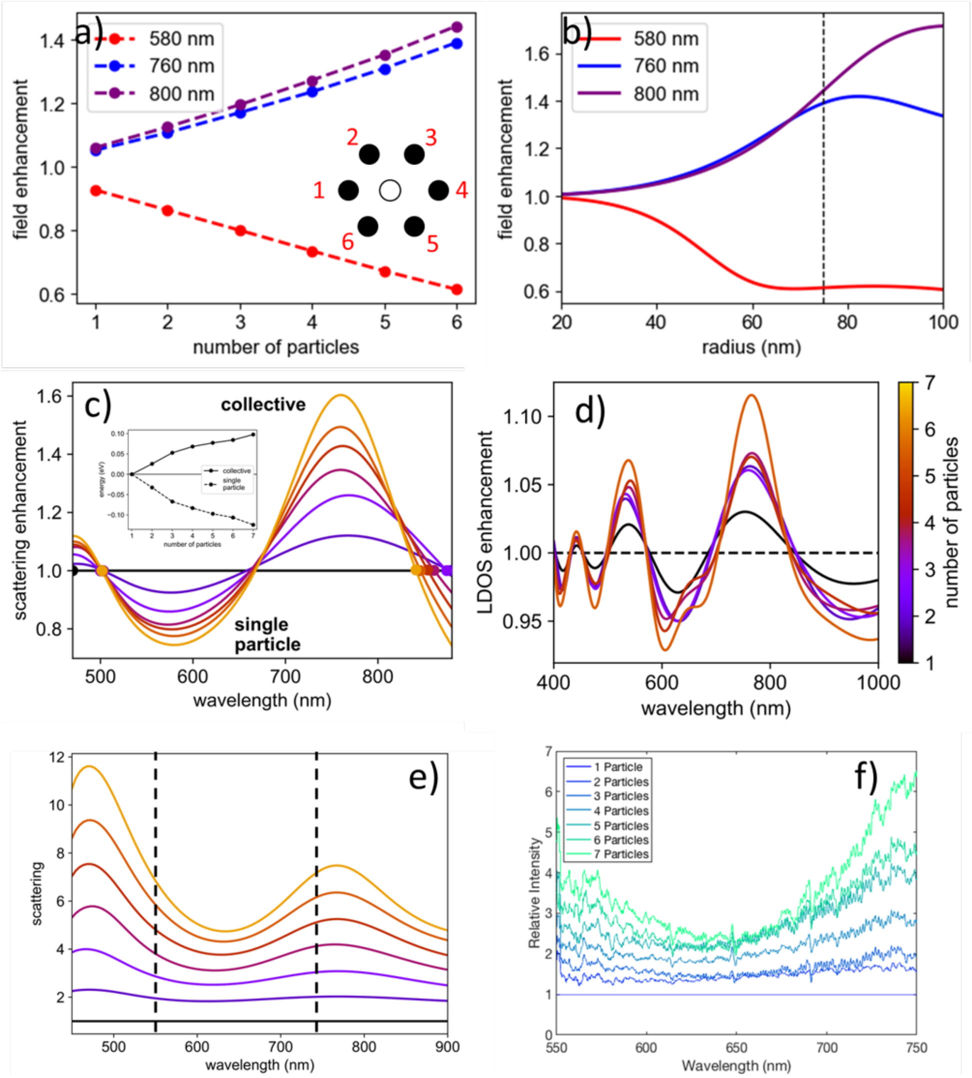

Figure 3.4: Electrodynamic coupling and emergence of a collective scattering mode in OM arrays. **(a)** Electric field enhancement at the vacant location of the center particle in a hexagonal OM array for varying number of particles at wavelengths of 800nm (violet), 760nm (blue), and 580nm (red). **(b)** Six-particle results from panel (a) repeated for varying particle-size (radius) at wavelengths of 800nm (violet), 760nm (blue), and 580nm (red). **(c)** Simulated scattering enhancement as a function of wavelength in OM arrays versus number of particles. The inset shows the integral of the energy ranges corresponding to the single-particle Mie resonance and the collective mode induced by electrodynamic coupling. **(d)** Local density of (electromagnetic) states enhancement in OM arrays for 1-7 particles **(e)** Simulated wavelength-dependent total scattering of the NP arrays normalized by particle number. **(f)** Experimental back-scattering spectra of NP arrays normalized by a 1NP spectra measured with spatially coherent light. Note the spectral range of the experiment corresponds to that between the dashed vertical lines in (e).

3.1.5 Spectral dependence on coupling

We have shown that electrodynamic coupling between particles leads to increased scattering of coherent light at the trapping laser wavelength ($800nm$; $600nm$ in water) in OM arrays, and now turn our attention to the origin of the coupling. We carried out GMT calculations to study the effects of the number of particles, size of particles, and excitation wavelength on the coherent light scattered by OM arrays. Figure 3.4a shows the ratio of the total field to the incident field at the (empty) location of the center particle in a hexagonal 7-particle OM array for wavelengths of $800nm$ (violet), $760nm$ (blue), and $580nm$ (red). For $\lambda = 800nm$ and $\lambda = 760nm$ the enhancement is small (≈ 7 percent) with a single particle nearby. However, every particle added to the array contributes to a growing enhancement so that the scattered field is nearly half the magnitude of the incident field for 6 nearby particles, and the growth from 1-6 is nonlinear. Conversely, at $\lambda = 580nm$ the total field at the location of the center particle diminisheds monotonically with particle number compared to the incident field. Figure 3.4b shows the six-particle simulation repeated with variable particle radius ranging from $20nm$ to $100nm$ for the same wavelengths as Figure 3.4a. The dependence of the field enhancement at each wavelength is nonlinear, and the magnitude of the field enhancement approaches 1 as the size of the particles decrease and increases with increasing particle size for $\lambda = 800nm$ and $\lambda = 760nm$ (with a peak near $80nm$) while it decreases with increasing particle size for $\lambda = 580nm$. This result follows from changes in the scattering cross sections as the volume decreases $\propto r^3$ and the dipolar resonance red-shifts with increasing size. Figures 3.4a-b show that significant electrodynamic coupling occurs even in small arrays (2-7 particles) due to the combined scattering from several neighbors for particles larger than $50nm$ in radius.

So far we have focused on the scattering of coherent light at a few wavelengths by OM arrays. We will now discuss the scattering of a spatially coherent broadband light source by OM arrays. Figure 3.4c shows the scattering enhancement (compared to N-fold multiplication of the single-particle scattering) as a function of wavelength for OM arrays with

1-7 particles. Consistent with the results in Figure 3.3e, the scattering grows super-extensively at wavelengths near the trapping wavelength. The dependence of this scattering enhancement on electrodynamic coupling suggests that it is collective in nature. Figure 3.4c also shows that the scattering near the single-particle Mie resonance decreases as the number of nanoparticle constituents in the OM array increases. The inset in Figure 3.4c shows the integral of the scattering enhancement for the collective and single-particle resonances. As the number of particles is increased, the integral of the collective mode enhancement steadily increases while the integral of the single-particle mode diminishes. Figure 3.4c shows that as more particles are added to the OM array the scattering of coherent light becomes increasingly influenced by the collective resonance coinciding with the diminishment of the Mie resonances of the individual particles in the array.

The local density of (electromagnetic) states (LDOS) at a certain location within or near an OM array controls the emission rate of a dipole emitter placed at that location[55, 56]. In the limit of large arrays of plasmonic particles the local density of states enhancement for specific in-plane wave vectors occurs together with large field enhancements[51]. Small ordered OM arrays are in the opposite limit, but the significant field enhancement shown in Figures 3.4a-b suggest that some degree of LDOS enhancement is expected. Figure 3.4d shows the measured local density of states enhancement (LDOS) in an OM array for 1-7 nanoparticles. As more particles are added to the OM array, LDOS enhancement becomes increasingly prominent near the trapping laser wavelength.

To experimentally determine the wavelength-dependent scattering enhancement in OM arrays, we measured backscattered spectra from a coherent broadband source. These results can be used to establish the effects of electrodynamic coupling in OM arrays. A backscattering geometry was chosen for excitation and detection so that the direction of propagation is normal to the plane of the array because an in-plane component of the incident wave vector changes the phase relationship between the particles in the array[50]. Surface lattice resonances (SLR's) that arise in extended arrays result in sharp resonances at wavelengths near the lattice spacing[48, 49, 50, 51]. Although we anticipate a similar enhancement at wavelengths near the wavelength of the trapping laser because it defines characteristic optical binding distance, the trapping laser wavelength needs to be filtered out because it is much more intense than the coherent broadband source. To meet these technical constraints we employed a pulsed supercontinuum fiber laser (Fianium WL400-4-PP), operating at maximum intensity with a 5.00 MHz pulse repetition rate, coupled to a computer-controlled variable interference filter (Fianium SuperChrome) set to its maximum bandwidth. As shown in Figure 3.1a, the broadband beam was directed to travel collinear with the trapping laser into the optical trap, and the back-scattered light was sent through a 50:50 beam splitter and notch filter (Semrock StopLine NF03-785E-25) to remove the backscattered light from the trapping laser intensity. 20% of the light was directed towards a CMOS array detector for imaging (Andor DC-152Q-COO-F1) and the remaining 80% of light was directed towards a spectrograph (Andor Shamrock SR-193i-B1-SIL). A pair of relay lenses (Thorlabs AC508-100-B-ML) with focal length f=100mm were then used to bring the resulting spectrum from the spectrograph to a second CMOS array detector (Andor NEO-5-5-CL3). The imaging and spectral CMOS detectors were synchronized so that the spectral measurement would be taken at the same frame rate and duration as the imaging. Once an OM array had formed both detectors were started and 1000 images and spectra were acquired at 160 fps. The spectra were classified by specific numbers of nanoparticles, and as arising from ordered *vs.* disordered arrays based on the fitting error (*i.e.* deviations of the particle positions from the lattice) resulting from real-space lattice fitting of the OM arrays in each frame.

Figure 3.4e shows simulated backscattered spectra for an OM array consisting of 1-7 particles normalized by the single particle spectrum. As particles are added to the array, peaks in scattering enhancement emerge near $500nm$ and $800nm$. The experimentally measurable range of wavelengths is indicated by the black vertical dashed lines in Figure 3.4e. Figure 3.4f shows the experimentally measured backscattered coherent spectra normalized by the single-particle scattering spectrum. The experimental and simulated spectra of the OM arrays are in good agreement.

3.1.6 Discussion and Conclusions

We have shown that coupling and interference have distinct effects on the scattering of coherent light by OM arrays. Figures 3.1 and 3.2 show that the images of the backscattering of the coherent trapping laser from an OM array are dramatically different from the images of the particles illuminated by an incoherent source. Furthermore, the coherent images of the OM array have common features with the near-field intensity because both are controlled by similar phase-dependent relationships. Figure 3.3 shows that coupling has a minimal effect on the qualitative spatial characteristics of coherent light scattered by OM arrays. However, coupling leads to an enhancement of the total scattering at the trapping laser wavelength. Figure 3.4 demonstrates that while coupling enhances scattering at wavelengths near the trapping laser wavelength, total scattering is not enhanced at all wavelengths.

However, our results also suggest that there is an important relationship between interference and coupling that can be understood using a simplified model. Consider a two-dimensional cluster of particles with isotropic polarizability α arranged in the transverse plane of an electromagnetic plane-wave with wavelength λ_0 . The polarization of particle i is proportional to the total electric field at the location of particle i as $\mathbf{p}_i = \alpha \mathbf{E}_{r=r_i}$ with

$$\begin{aligned} \mathbf{E}_{r=r_i} &= \mathbf{E}_0 + \alpha \sum_{j\neq i} \mathbf{G}(r_i, r_j)\mathbf{E}_{r=r_j} \\ &\approx \mathbf{E}_0 \left[1 + \alpha \sum_{j\neq i} \mathbf{G}(r_i, r_j) + \alpha^2 \sum_{j\neq i} \sum_{l\neq j} \mathbf{G}(r_i, r_j)\mathbf{G}(r_j, r_l) + ... \right] \end{aligned} \tag{3.4}$$

where $\mathbf{E}_0$ is the incident electric field and $\mathbf{G}(r_i, r_j)$ is the tensor that propagates the scattered field at position r_j resulting from a dipole at position r_i

$$\mathbf{G}_{lm} = \frac{e^{ikR}}{4\pi\epsilon_0\epsilon_m R^3} \left[(3 - 3ikR - k^2R^2)\frac{R_l R_m}{R^2} + (k^2R^2 + ikR - 1)\delta_{lm} \right] \tag{3.5}$$

where l and m are polarization directions, $R = |r_i - r_j|$ is the distance between the two particles, and k is the wave-vector of the incident light. At single-wavelength distances $kR = 2\pi$, so that the far-field terms in the propagator with $\frac{1}{R}$ dependence give the largest contribution, although all terms are significant. According to equations 3.4 and 3.5, the polarization of a particle in an OM array will have the largest contribution from light scattered by neighboring particles when all of the scattered contributions are in-phase, *i.e.* when they are interfering constructively.

Figure 3.4a shows that each particle added to the OM array increases electric field strength at the central particle near the trapping laser wavelength. In the context of equation 3.4, an increasing portion of the polarization of the central particle is induced by scattered light from neighboring particles as particles are added to the OM array. The scattered light from each of the added particles is in phase at the location of the center particle because they are all the same distance from the center particle and the circularly polarized excitation is isotropic in the polar symmetry of the array. The relative phase between the incident and scattered light, however, depends on the lattice spacing in comparison to the wavelength of the excitation. For the trapping laser, the laser wavelength and lattice spacing are nearly equal and the scattered light interferes constructively with the incident light. For other wavelengths the interference can be destructive. At $560nm$ the interference is destructive and the field at the location central particle is diminished.

The total strength of the coupling also depends on the size (and polarizability) of the particles. Figure 3.4b shows that while the $150nm$ diameter particles used in our experiments and most calculations are shown lead to significant coupling in OM arrays, particles with diameters under $100nm$ lead to much smaller coupling. Therefore, the geometry, inter-particle separations, and choice of particles in OM arrays contribute to the significant electrodynamic coupling that we report here. Equation 3.4 is an approximate solution for the scattered field at the location of a particle in an OM array expanded in orders of scattering. Each scattering order is weaker by a factor of αG. Based on the results in Figure 3.4a, we can approximate that the terms in αG are of the magnitude ≈ 0.05 As an OM array grows, an increasing number of terms contribute to higher-order scattering, giving rise to the nonlinear enhancement shown in Figure 3.4a.

In this work we focused on the electrodynamic properties of small OM arrays. In the limit of large regular arrays of nanoparticles one finds a sharp peak in their scattering spectra with a central wavelength near the lattice spacing. This is known as a surface lattice resonance (SLR)[48, 49, 50, 51]. The enhanced scattering associated with the SLR can be derived analytically as a consequence of strong electrodynamic coupling by employing a self-consistent solution in the limit of a large lattice[50].

Electrodynamic coupling in OM arrays is in a distinct regime compared to other typical examples of coupling. Near-field electrodynamic coupling between pairs of particles is usually significant for inter-particles separations much smaller than the wavelength of light. On the other hand, constructive interference can lead to significant coupling in very large (extended) arrays of particles. Electrodynamic coupling in OM arrays is near the crossover between the two limits. While the magnitude of the field scattered from a single particle is small, the combined contributions from several nearby particles, interfering constructively, leads to significant field enhancement and coupling. Therefore, OM arrays are an avenue for studying SLRs in the opposite, small array limit where interaction and coupling is described on an element-by-element basis. These field enhancements and coupling could also be exploited for applications in nonlinear optics, where the phenomena have an E^{2n} dependence, with n indicating the order of nonlinearity[57, 58].

Chapter 4

Structure of optical matter systems

4.1 Structural Properties of Clusters Formed by the Long-Range Periodic Optical Binding Interaction

4.1.1 Introduction

The stability and morphology of small clusters of particles are dictated by the nature of their interactions. For pair interactions that are dominated by excluded volume and very short-range attraction the energy of the cluster is directly proportional to the number of points of contact between the particles, leading to a small number of structures with nearly the same binding energy[59, 60, 61]. For pair interactions with multiple length scales (*e.g.* a short-range attractive and long-range repulsive component), a rich variety of density dependent phases and water-like anomalies have been observed[62, 63, 64].

Optical binding is a long-range periodic electrodynamic interaction between nano or micro-scale particles that is generated by a coherent light source[13, 15]. It was recently suggested that clusters of nanoparticles formed by optical binding (optical matter clusters) have enhanced stability of extended periodic structures due to the periodic nature of the optical biding forces[39]. However, phenomena reported in other systems with long-range pair potentials, including non-hexagonal packing and water-like anomalies, have not been reported in optical matter systems.

In this paper we show that the long-range and periodic nature of the optical binding forces result in several distinct structural features in optical matter clusters. We analyze a large volume of experimental and simulated data of 2-dimensional optical matter structures to deduce the structural properties and relative probabilities of the most stable structures. We determine that the most stable structures of these clusters are the same as the ground state structures of two-dimensional clusters with short-range attractive interactions[59, 60, 61]; the binding energies of the latter structures are degenerate. However, the relative stability of each optical matter structure as a function of laser power shows that the long-range optical binding interactions lifts the energy degeneracy between the structures. Furthermore, we measure significant increases in nearest neighbor distance compared to the two-particle optical binding distance[15, 17]; the latter is λ/n whereλ is the trapping laser wavelength and n is the index of refraction of the medium. We also find that the fully relaxed optical matter arrays obtained in simulations with no thermal fluctuations are distorted relative to a reference hexagonal lattice, including the existence of a five fold symmetric cluster that does not lie on a hexagonal lattice.

We construct a pairwise optical binding potential by calculating the work done separating two particles in plane-wave illumination, and find that summing the optical binding potential over particle pairs characterizes the stabilities of the clusters. The success of this simplified approach transcends the presence of non-conservative forces[65] and many-body electrodynamic coupling (see chapter 3). We derive an analytical expression for the distortion energy associated with the symmetric stretching of small optical matter clusters and show that it correctly predicts the lattice constant of the most stable structures. Finally, as the size of OM clusters grow, the nearest neighbor separation continues to increase as it approaches a value around 10% larger than the pairwise optical binding distance.

4.1.2 Long-range periodic potentials

We performed Langevin dynamics (LD) simulations for six-particle clusters with two different analytical pair potentials and similar confining forces of the optical trap that allow contrasting the structures formed with short-range single-well and long-range periodic potentials. Figures 4.1a and b show Lennard-Jones (LJ) and optical binding (OB) potentials, respectively. The LJ potential is defined so that the minimum matches the first minimum in the optical binding potential and the depth matches the distance from the first minimum to the first local maximum in the optical binding potential. The pairwise distances for two typical six-particle clusters, the chevron (red) and the triangle (blue) are marked by circles with the size of the circle denoting the number of occurrences distances that have a particular value. Figures 4.1 a-b suggest that we should expect that the chevron is slightly more stable for the LJ potential[66] because it has more pairwise distances with shorter values, while the triangle is more stable for the OB potential because it has more pairwise distances at the second optical binding distance.

To measure the stability of different arrangements we developed a cluster detection algorithm based on the commonly observed hexagonal symmetry of the clusters when the trapping laser is circularly polarized[67]. First, the hexagonal lattice that minimizes the distance from each measured particle position to the nearest lattice site is found. This minimization is carried out over four degrees of freedom: two translational, one rotational, and one scale parameter. Next, each particle is assigned to a lattice site if it is within a cutoff distance of that site. Once the occupation of each lattice site is known, the number of neighboring occupied lattice sites are counted and the set of numbers of neighbors at each occupied site is used to distinguish between common six-particle structures (*e.g.* trangle, chevron, parallelogram). Figure 4.1c shows the detected probabilities for the three lowest energy six-particle clusters. The triangle and parallelogram cluster (blue and magenta, respectively) are relatively rare in the LJ potential, while the chevron cluster type makes up the majority of the detected cluster types. The combined probability of all three cluster types (black) is close to 1 for the chosen temperature and potential well depth in our simulations, meaning that other cluster types are rare. For the optical binding potential, the parallelogram is no longer detected, the triangle increases in probability, and the chevron decreases in probability, and other cluster types are similarly rare.

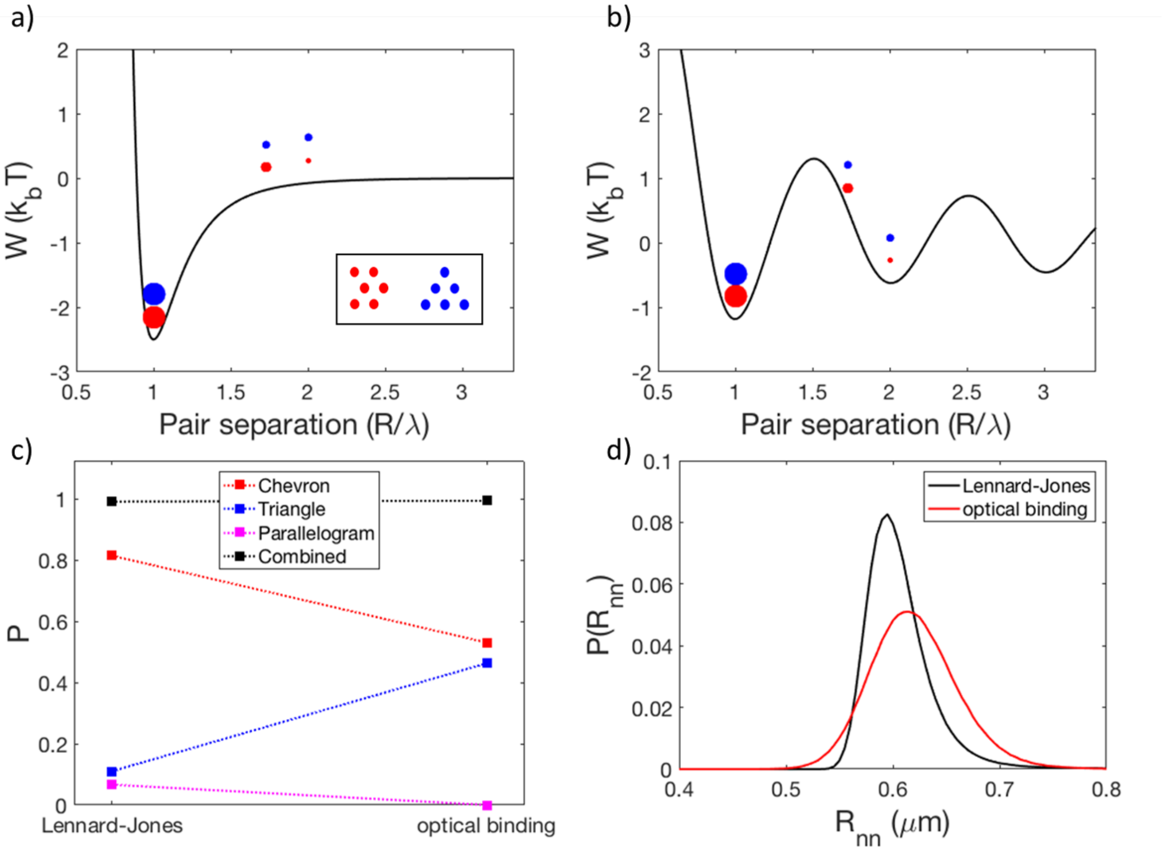

Figure 4.1: Comparison between LD simulations with the Lennard-Jones and optical binding potentials. **(a)** Lennard-Jones potential. Inter-particle separations for triangle and chevron configurations are marked with red and blue circles, respectively. **(b)** Lennard Jones potential. **(c)** Detected cluster-type probability for the chevron (red), triangle (blue), parallelogram (magenta), and combined (black) in LD simulations with the Lennard-Jones and optical binding potentials. **(d)** Probability distributions of nearest neighbor distances in LD simulations with the Lennard-Jones (black) and optical binding (red) potentials.

Figure 4.1d shows probability distributions of the nearest-neighbor distances in the LJ and OB potential simulations. Both probability distributions reflect their underlying potential. The distribution for the LJ potential is more narrow and skewed toward longer distances while the distribution for the OB potential is wider and more symmetric. For the LJ potential (black) the maximum probability for nearest neighbor distance coincides with the location of the minimum energy. However, for the OB potential the maximum probability is shifted to a larger distances than the first local minimum in the OB potential.

4.1.3 Experimental observation of six-particle OM clusters

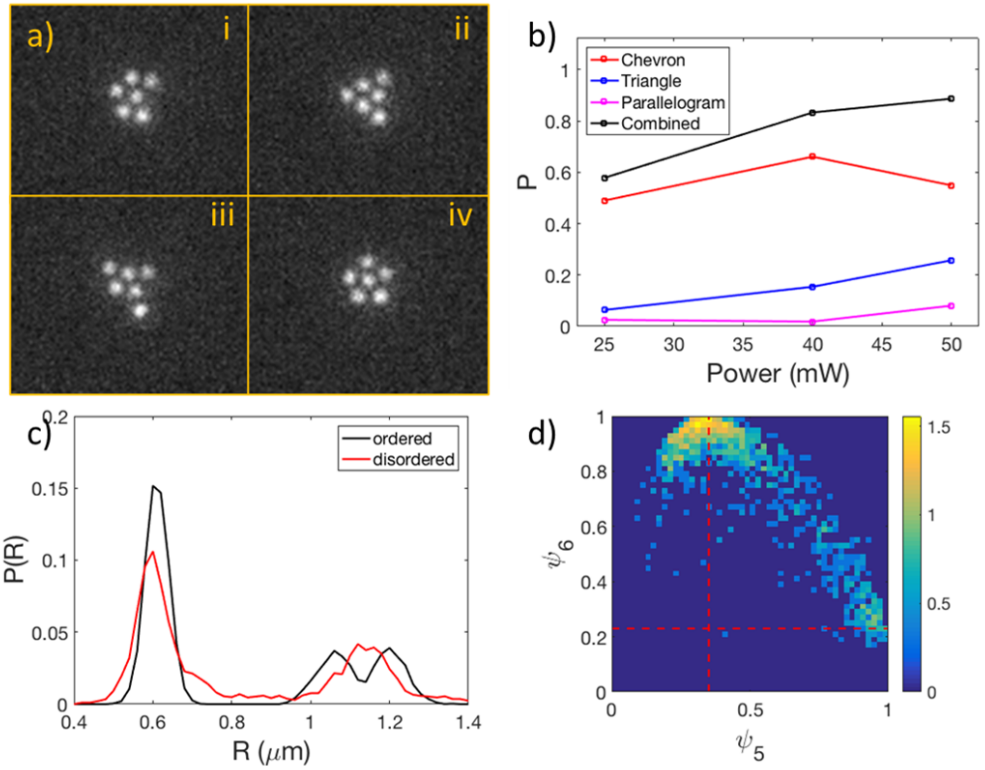

Figure 4.2: Analysis of experimentally observed optical matter clusters. **(a)** Experimental still-frames. i. chevron cluster ii. triangle cluster iii. excited state iv. five-fold symmetric cluster **(b)** Detected cluster-type probability for the chevron (red), triangle (blue), parallelogram (magenta), and combined (black) in experiments at different trapping laser powers. **(c)** Distribution of inter-particle separations conditioned on whether the cluster is ordered (black) or disordered (red). **(d)** Distribution of angular order parameters ψ_5 vs ψ_6.

Since our experiments are performed in solution at room temperature, and typical energy barriers to rearrangements of clusters are usually on the order of a few $k_B T$, clusters in our optical binding experiments frequently rearrange over the time-scale of a typical experiment and it is feasible to sample a large number of configurations. Figure 4.2a shows snap shots of typical six-particle structures seen in an optical binding experiment. Panel i and ii show the chevron and triangle arrangements, while panel iii shows a less compact higher energy arrangement and panel iv shows a five-fold symmetric arrangement.

The relative probability of a certain cluster type in thermal equilibrium compared to another depends on the free energy difference between those two configurations according to

$$\frac{P_A}{P_B} = e^{\frac{\Delta F}{k_B T}} = e^{\frac{\Delta U - T\Delta S}{k_B T}} \tag{4.1}$$

where P_A and P_B are the probabilities of states A and B, ΔU is the potential energy difference between states A and B, T is the temperature of the system, ΔS is the entropy difference between states A and B, and k_B is the Boltzmann constant. The optical binding force is directly proportional the intensity of the incident light, and therefore the potential energy difference ΔU between two non-degenerate configurations can be tuned in optical matter clusters. Therefore, we expect that the dependence of cluster type probability on laser power characterizes the free energy relationships between the sates measured.

Figure 4.2b shows the detected probability of the six-particle clusters that are most common as a function of laser power. The combined probability is plotted in black. The total probability increases with power. If the three states detected are the lowest energy states, the combined probability should approach 1 as the laser power increases. The probability of the triangle cluster similarly increases with increasing power. However, while the probability of the chevron cluster increases from $25mW$ to $40mW$, it decreases from $40mW$ to $50mW$. The parallelogram only occurs with significant probability at $50mW$. As power increases, the ratio of probabilities of detecting the triangle compared to the chevron, $\frac{P_{tri}}{P_{chev)}}$, also increases. This suggests that the triangle cluster is lower in energy than the chevron, while the chevron is favored by entropy.

Figure 4.2c shows a comparison of the nearest neighbor distances in six particle 2D optical matter clusters conditioned on lattice fitting error. The most probable nearest neighbor distance for small lattice fitting error (black) is slightly smaller than the most probable nearest neighbor distance for large lattice fitting error (red). This is related to the increased nearest neighbor distance for clusters formed with the optical binding potential compared to the LJ potential, as shown in Figure 4.1d.

To measure the prevalence of five-fold symmetric clusters compared to clusters with hexagonal symmetry we developed two angular order parameters, ψ_5 and ψ_6. The five-fold symmetric cluster is detected as a chevron by the cluster-type detection algorithm (with large fitting error). For each frame where the chevron is detected we calculated the angle between each pair of adjacent exterior particles with the vertex at the center of mass of the cluster for $\psi 5$ and the central lattice site for ψ_6. The definitions of ψ_5 and ψ_6 are

$$\begin{aligned} \psi_5 &= \frac{1}{5}\sum_i Re[e^{2\pi\theta_i * 5}] \\ \psi_6 &= \frac{1}{5}\sum_i Re[e^{2\pi\theta_i * 6}] \end{aligned} \tag{4.2}$$

where θ_i are the angles between adjacent exterior particles. The values for ψ_5 and ψ_6 for is 1 the ideal five-fold symmetric and chevron clusters, respectively.

Figure 4.2d the distribution of ψ_6 versus ψ_5 for an experiment performed at 50 mW. The values of ψ_5 for the ideal chevron cluster and ψ_6 for the ideal five-fold symmetric cluster are marked with red dashed lines. Concentrations of probability corresponding to both the chevron and the five-fold symmetric cluster are visible. Figure 4.2d shows that both the chevron and the five-fold symmetric cluster are stable states, although the five-fold symmetric cluster is significantly more rare.

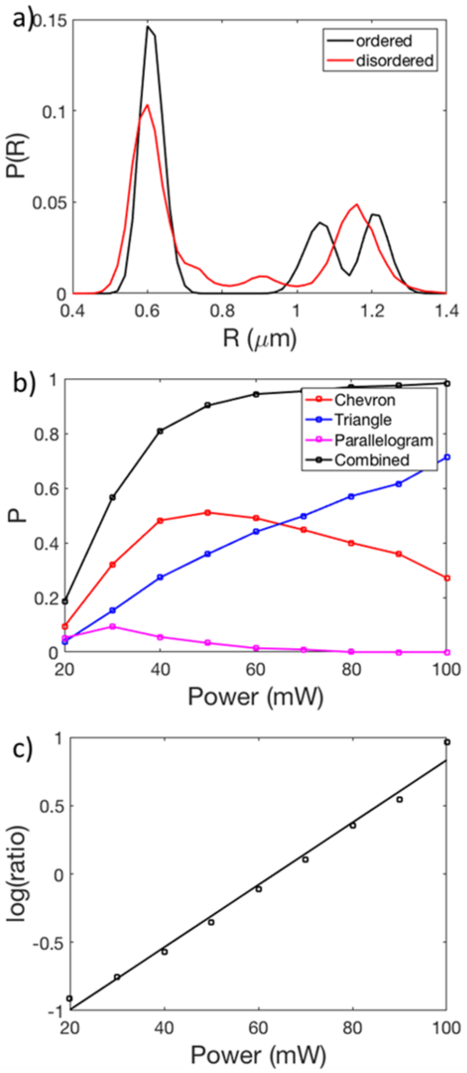

Figure 4.3: Analysis of simulated optical matter clusters. **(a)** Distribution of inter-particle separations conditioned on whether the cluster is ordered (black) or disordered (red). **(b)** Detected cluster-type probability for the chevron (red), triangle (blue), parallelogram (magenta), and combined (black) in simulations at different trapping laser powers. **(c)** Ratio of probability of the triangle cluster over the chevron cluster plotted vs power on a semi-logarithmic scale.

Simulated observation of six-particle OM clusters

We performed coupled electrodynamics and Langevin mechanics simulations to compare with our experimental findings in a controlled environment. Figure 4.3a shows shows a comparison of the nearest neighbor distances in 2D six particle clusters conditioned on lattice fitting error. As is the case for our experimental results shown in Figure 4.2c, the most probable nearest neighbor distance for small lattice fitting error (black) is slightly smaller than the most probable nearest neighbor distance for large lattice fitting error (red).

Figure 4.3b shows a plot of detected cluster probability vs power. The magenta curve corresponds to the parallelogram, the blue curve corresponds to the triangle, the red curve is the chevron, and the black curve corresponds to the sum of all three cluster types. The parallelogram is only detected at low powers. The probability of detecting the triangle increases monotonically with power. The probability of detecting the chevron increases at low power and then decreases at high power. These results (other than the parallelogram) are consistent with our experiments. Figure 4.3c shows the ratio of the probability of detecting the triangle and the probability of detecting the chevron as a function of power on a semi-logarithmic scale. The plot falls on a straight line, indicating that the ratio of probabilities has an exponential dependence in accordance with equation 4.1.

OM clusters are non-equilibrium systems because some of the optical forces involved in their formation are non-conservative. Therefore, a particular configuration of an OM cluster does not technically have an associated energy. However, the relative importance of conservative and non-conservative forces has not been established, and several studies treating OM clusters as equilibrium systems have shown reasonable results. We developed a distortion energy parameter to evaluate how consistent our results are with a simplified picture that only depends on pairwise potential energy. First we calculate the work done separating a pair of optically bound particles from a starting distance r_0 to another distance r. For six particles, this work curve is used to map each of the 15 pairwise distances r_{ij} to a particular energy W_{ij}. We define distortion energy as

$$W = \sum_{ij} W(r_{ij}) - W_{ref} \tag{4.3}$$

where W_{ref} is a the total energy of a reference structure. We chose the ideal chevron with a lattice constant equal to the wavelength of the trapping laser as our reference structure. Since all optical binding forces are proportional to the intensity of the trapping laser, our the work curve only needs to be calculated at a single power and can be scaled with trapping laser power.

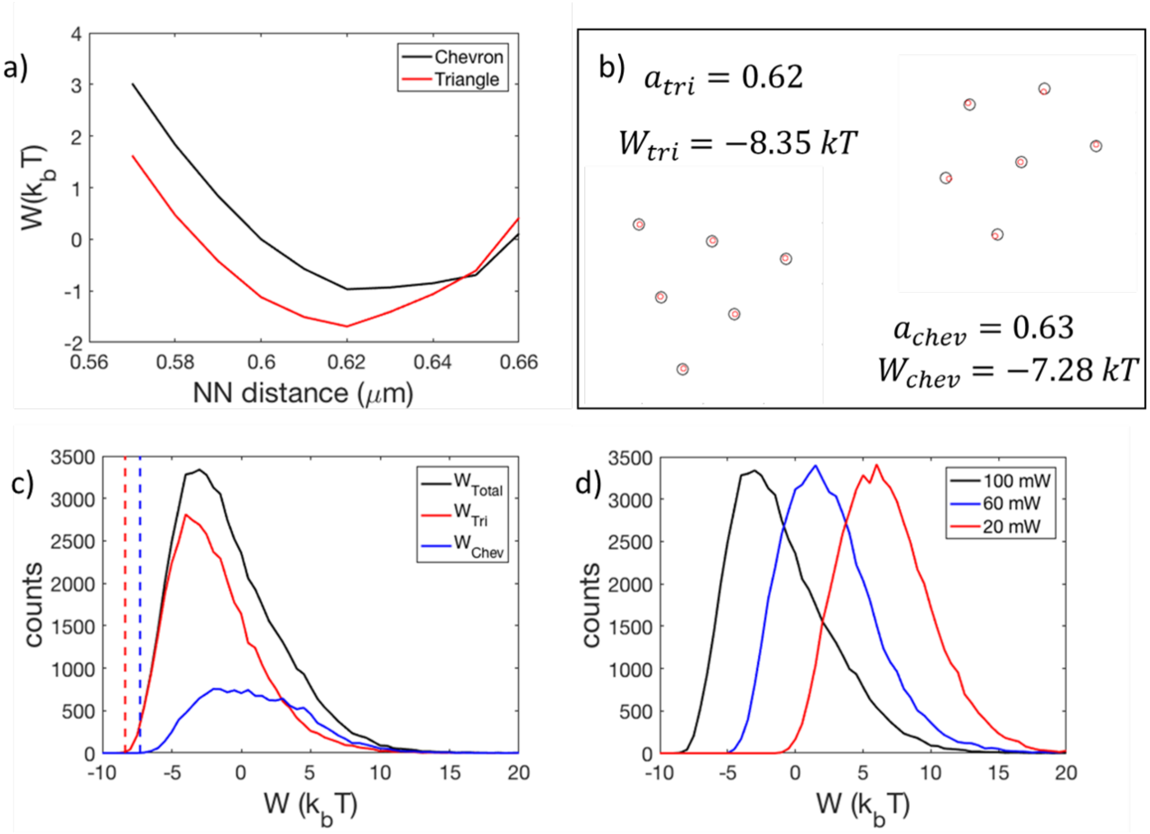

Figure 4.4: Distortion energy in optical matter clusters. **(a)** Distortion energy for symmetric stretching of chevron (black) and triangle (red) OM clusters **(b)** Fully relaxed triangle and chevron OM clusters **(c)** Distortion energy distribution of six-particle simulation performed at $100mW$ for the chevron (blue)and triangle (red) clusters. The total is plotted in black. **(d)** Distortion energy distributions at three different trapping laser powers.

Figure 4.4a shows a plot of W vs lattice constant for perfect chevron (black) and triangle (red) clusters. Both curves show that dilation of the lattice constant is energetically favorable, and that lattice constants of around $620nm$ minimize energy. We performed simulations with no thermal fluctuations to find the local energy minima for the triangle and chevron clusters. The results are shown in Figure 4.4b with particle positions marked in red and best-fit lattice sites marked as black circles. The lattice constant of the fully relaxed chevron is $630nm$ and the lattice constant of the fully relaxed triangle is $620nm$. Figure 4.4b also shows that the fully relaxed chevron and triangle clusters are slightly distorted compared to a perfect hexagonal lattice.

Figure 4.4c shows the distribution of distortion energy for a simulation conducted at $100mW$. The black curve represents the distortion energy regardless of cluster type. The distribution of the total distortion energy has a sharp rise followed by a slower decay. The peak of the distribution is at slightly negative distortion energy, indicating that on average the cluster finds low-energy configurations compared to the perfect chevron with a lattice constant equal to the optical binding distance. The red (triangle) and blue (chevron) curves represent the distribution of distortion energy conditioned on cluster type. The triangle configuration is on average lower in energy compared to the chevron configuration, and the increase in the curve at low energy is significantly more steep. Figure 4.4d shows histograms of the total energy for simulations performed at $20mW$, $60mW$, and $100mW$. As power increases the average distortion energy decreases and the distributions become more skewed.

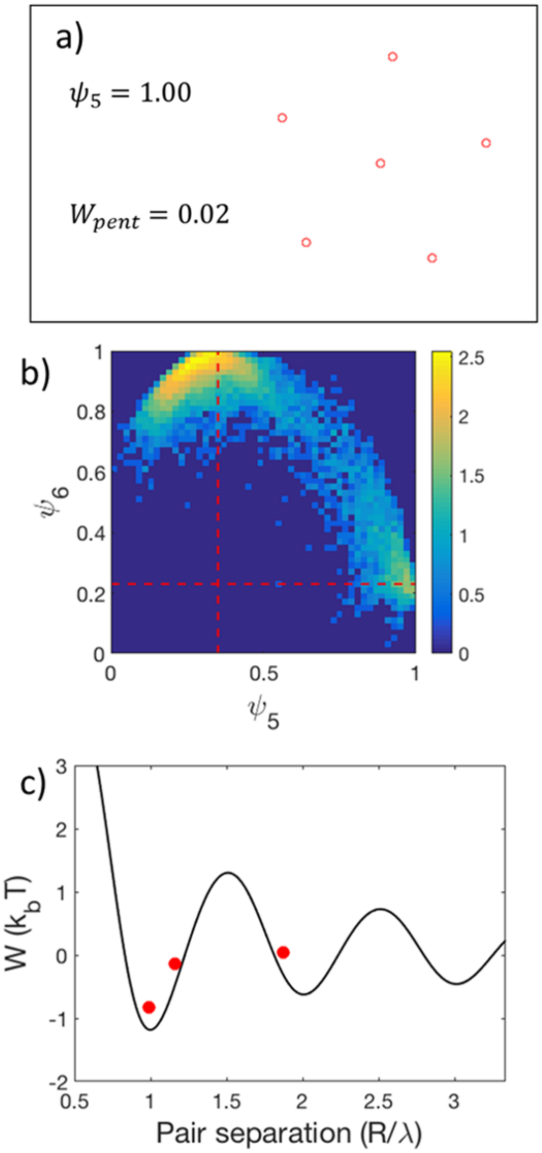

Figure 4.5: Analysis of five-fold symmetric clusters in simulated data **(a)** Distortion energy for symmetric stretching of chevron (black) and triangle (red) OM clusters **(b)** Distribution of angular order parameters ψ_5 vs ψ_6. **(c)** Schematic showing the distances in the five-fold symmetric cluster and the optical binding potential for comparison.

We have shown that the most common stable configurations of 2D OM clusters have deviations from hexagonal symmetry. Figure 4.2d shows that a five-fold symmetric cluster is also stable. Figure 4.5a shows the fully relaxed five-fold symmetric cluster. The measured value of the angular order parameter $\psi_5 = 1$ confirms that this configuration is five-fold symmetric. The distortion energy measured for this configuration is very close to 0, meaning that it is higher in energy than the fully relaxed triangle and chevron configurations, but still energetically accessible according to the distributions shown in Figure 4.4c-d. Figure 4.5b shows the distribution of ψ_5 vs ψ_6 for a simulation at $100mW$. Similar to the experimental result in Figure 4.2b, there are concentrations of points near $\psi_5 = 1$ and $\psi_6 = 1$.

Figure 4.5c marks each of the three inter-particle separations present in the five-fold symmetric cluster with red dots. Each separation has 5 instances in the cluster. The shortest distance is from the center particle to each of the five outer particles. This distance is slightly smaller than the optical binding distance. The second distance is the spacing between each of the particles around the perimeter of the cluster. It is slightly larger than the optical binding distance. The third distance is the distance across the cluster. This is slightly shorter than the second optical binding distance.

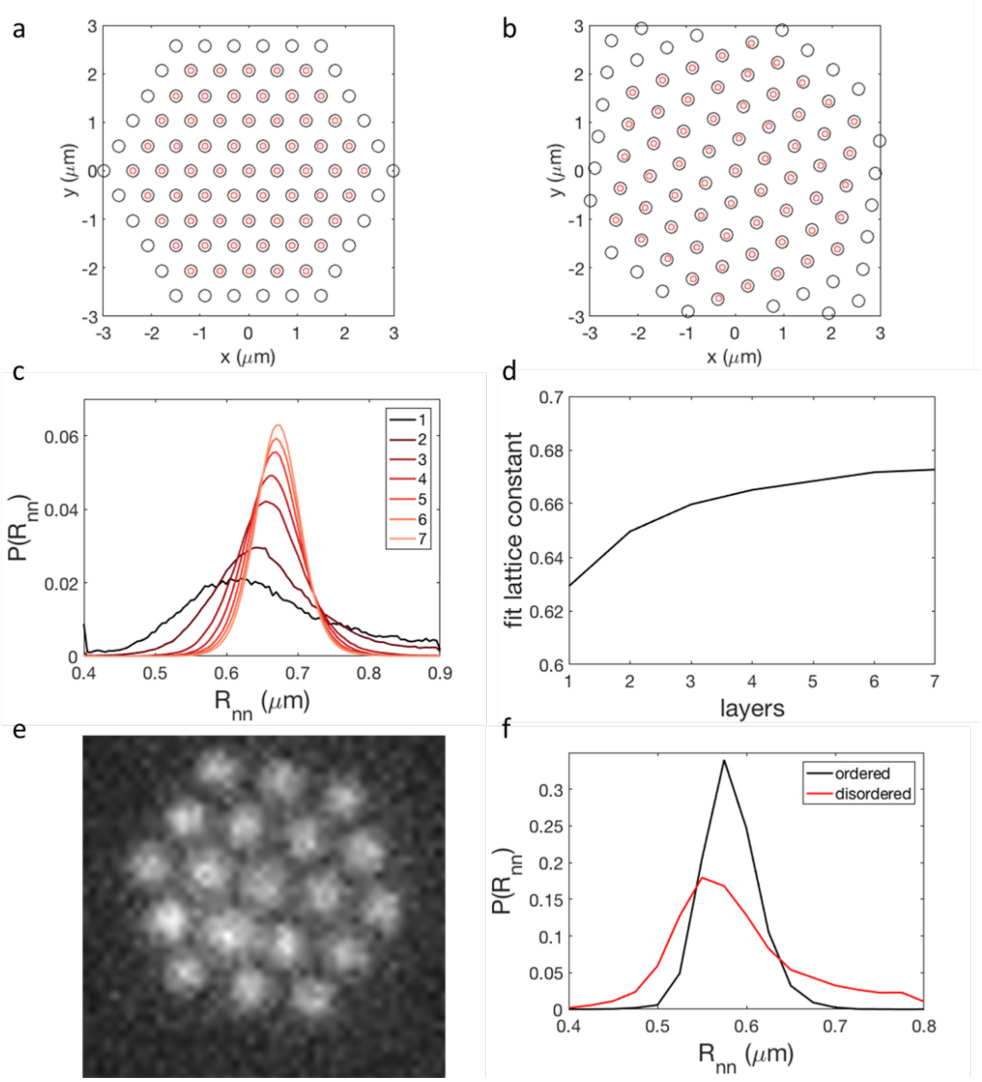

Figure 4.6: Analysis of large OM clusters **(a)** Fully relaxed 61-particle cluster with the Lennard-Jones potential. **(b)** Fully relaxed 61-particle cluster with GMT interactions. **(c)** Distributions of nearest neighbor distances for simulated hexagonal OM clusters with 1-7 layers from GMT-LD simulations **(d)** Fit lattice constants of fully relaxed OM clusters with 1-7 layers **(e)** Experimentally observed 21-particle cluster **(f)** Distribution of inter-particle separations conditioned on whether the cluster is ordered (black) or disordered (red).

We performed simulations and experiments to show how the long-range periodic optical binding interaction manifests in larger clusters. Figure 4.6a and b show fully relaxed 61-particle clusters formed in simulations without thermal fluctuations for LJ and GMT interactions, respectively. Both clusters relax to similar hexagonal configurations. However, in conjunction with the results for smaller clusters, the relaxed optical matter cluster has a dilated lattice constant and significantly larger deviations from the lattice sites than the LJ cluster.

Figure 4.6c shows the distribution of nearest neighbor distances obtained from GMT-LD simulations of hexagonal clusters performed at $300K$ with 1-7 layers of particles. For the smallest cluster (7 particles), the nearest neighbor distance is around $630nm$, similar to the six particle case. As layers are added to the cluster, two trends are apparent. First, the width of the nearest neighbor distance distribution becomes more narrow. Second, the peak of the nearest neighbor distribution increases and appears to asymptotically approach approximately $680nm$. Figure 4.6d shows a plot of best-fit lattice constant versus number of layers for non-thermal simulations. Similar to the simulation results at $300K$, the best-fit lattice constant increases and appears to asymptotically approach $680nm$. This is a significant shift from the optical binding distance.

Figure 4.6e shows a still frame of an experimentally observed a 20-particle OM cluster. The cluster continuously transitions between ordered configurations on a hexagonal lattice and disordered configurations. Figure 4.6f shows histograms of the nearest neighbor separation conditioned on whether the cluster has small (black) or large (red) fitting error with respect to the best fit hexagonal lattice. Similar to the 6-particle results shown in Figures 4.2-Figure 4.3, the nearest neighbor distance is shifted toward longer distances when the cluster is closer to an underlying hexagonal lattice.

4.1.4 Discussion

Our results highlight several key features of small OM clusters. While the most common configurations resemble the ground states of clusters formed with short-range attractive interactions, the long-range periodic nature of the optical binding potential breaks the degeneracy between clusters with an equal number of nearest neighbor 'bonds' and energetically favors clusters with an increased number of occurrences of distances near the second pairwise optical binding site. The resulting power-dependence of cluster-type probability reveals the underlying competition between entropy and energy with respect to the stability of a particular configuration.

At high trapping laser power the probabilities of the chevron and triangle configurations account for almost all experimental clusters observed, so it is reasonable to assume that they are energetically favorable compared to other configurations. However, Figure 4.2c suggests that for both the chevron and triangle configurations stretching of the nearest neighbor distance is energetically favorable. Explicitly, the rate of change of potential energy achieved by stretching or compressing the configuration is

$$\frac{\partial U}{\partial a} = \sum_i n_{r=r_i} \frac{r_{i0}}{a_0} \frac{\partial U^{pair}}{\partial r_i}\Big|_{r=r_i} \tag{4.4}$$

where a is the lattice constant of the cluster, r_i are the unique inter-particle distances with $n_{r=r_i}$ copies in the cluster, and $U^{pair}(r_i)$ is the pairwise optical binding potential. Equation 4.4 facilitates a qualitative understanding of the stretching of the nearest-neighbor distance shown experimentally in Figure 4.1e and in simulation in Figure 4.2a. The slope of the pairwise optical binding potential at $r = \lambda$ and $r = 2\lambda$ is zero, and negative at $r = \sqrt{3}\lambda$. Therefore, a small stretching of the lattice constant is clearly energetically favorable for both the triangle and chevron structures.

The quantitative dependence of the potential energy difference ΔU associated with stretching the lattice constant by an amount Δa starting from a_0 can be obtained by approximating the pairwise optical binding potential at the first and second optical binding sites as harmonic with spring constants κ_1 and κ_2 and at $\sqrt{3}\lambda$ as linear with slope m. Integrating equation 4.4 yields

$$\Delta U(\Delta a) = (9\kappa_1 + 8\kappa_2)\frac{\Delta a^2}{2} + 4\sqrt{3}m\Delta a \tag{4.5}$$

for the chevron and

$$\Delta U(\Delta a) = (9\kappa_1 + 12\kappa_2)\frac{\Delta a^2}{2} + 3\sqrt{3}m\Delta a \tag{4.6}$$

for the triangle. Equations 4.5 and 4.6 can be minimized to approximate the distance where energy is minimized. Local fits of the optical binding potential at $100mW$ yield $\kappa_1 = 100\frac{kT}{\mu m^2}$, $\kappa_2 = 45\frac{kT}{\mu m^2}$, and $m = -10\frac{kT}{\mu m}$, giving $\Delta a_{min} = .018\mu m$ for the triangle and $\Delta a_{min} = .027\mu m$ for the chevron.

The energetically favorable dialation of OM clusters does not fully account for the lowest energy structures. Electrodynamics simulations performed in the absence of thermal fluctuations (*i.e.* $T = 0K$) reveal that distortions compared to a hexagonal lattice are energetically favorable. The amount of distortions present in the relaxed structures depends on the shape of the cluster. The deviations of the triangle ground state structure from the underlying hexagonal lattice are extremely small. The chevron features larger deviations than the triangle, but they are still small compared to typical thermal fluctuations at room temperature.

However, the stable five-fold symmetric cluster does not even lie on an underlying hexagonal lattice. The five-fold symmetric six-particle cluster is stabilized by the long-range periodic nature of the optical binding potential, and the inter-particle separations of that cluster are consistent with Equation 4.4.

4.1.5 Conclusion

In this chapter we demonstrated the features of small clusters formed by the long-range periodic optical binding potential. We found that compared to small clusters formed with the single-well Lennard Jones potential, the probability of the most common structures for OM clusters is power dependent and suggests that the dominant factor is competition between energy and entropy. We found that the lattice constant in OM clusters dilates when the cluster becomes more ordered, reminiscent of a water-like anomaly, and we created a simplified model that elucidates the origins of this dilation for small clusters. We constructed a distortion energy parameter that shows that while OM clusters are non-equilibrium systems where electrodynamic coupling and many-body interactions cannot be discounted, the prevalence of structures of the system is well-described by treating the interactions as conservative and pairwise. We showed that a five-fold symmetric cluster is stable and fairly common in the plethora of structures formed. The details of both the first and second optical binding wells contribute to the stability of the five-fold symmetric structure. Finally, we showed that as OM clusters grow in size, the fully relaxed clusters have small distortions from a hexagonal lattice who's lattice constant approaches a value more than 10% larger than the pairwise optical binding distance. Our work shows that many steady-state features of OM clusters can be effectively explained by treating the interactions as pairwise and conservative, *i.e.* with an optical binding potential. However, this perspective does not explain the observed non-equilibrium phenomena and dynamics that have been previously reported such as nonreciprocal forces [18, 19] and negative optical torque [38, 20, 21, 23].

Our findings are relevant to a number of other fields. There are both well-studied and emerging systems with long-range interactions or interactions with competing length scales, and the connection between the exact details of the potential and important phenomena such as phase transitions are the subjects of past and current work[62, 63]. The advantage of OM clusters compared to many other systems with multi-scale potentials is that the exact coordinates of the system can be directly observed in experiments and transitions between states are common enough to sample in a typical experiment while still being slow enough to follow in detail. The presence of phenomena reminiscent of water-like anomalies and the stability of five-fold symmetric clusters opens the possibility of directly observing phase transitions with high spatial and time resolution.

Chapter 5

Broken symmetry in optical matter systems

5.1 Nonreciprocal forces in optical matter heterostructures

The following section is reproduced in part with permission from: Yifat, Yuval, Delphine Coursault, Curtis W. Peterson, John Parker, Ying Bao, Stephen K. Gray, Stuart A. Rice, and Norbert F. Scherer. Reactive optical matter: light-induced motility in electrodynamically asymmetric nanoscale scatterers. *Light: Science & Applications 7, no. 1 (2018): 1-7.*

From Newton's third law, which is known as the principle of *actio et reactio*, we expect the forces between interacting particles to be equal and opposite for closed systems. Otherwise, "nonreciprocal" forces can arise [68]. This has been shown theoretically in the interaction between dissimilar optically trapped particles that are mediated by an external field [18]. As a result, despite the incident external field not having a transverse component of momentum, the particle pair experiences a force in a direction that is transverse to the light propagation direction [18, 69].

In this section, we directly measure the net nonreciprocal forces in electrodynamically interacting asymmetric nanoparticle dimers and nanoparticle structures that are illuminated by plane waves and confined to pseudo one-dimensional geometries. We show via electrodynamic theory and simulations that interparticle interactions cause asymmetric scattering from heterodimers. Therefore, the putative nonreciprocal forces are actually a consequence of momentum conservation. Our study demonstrates that asymmetric scatterers exhibit directed motion stemming from the breakdown of mirror symmetry in the electrodynamic interactions that are induced by the incident light.

The development of light-driven nanomotors, which are devices that convert light energy into autonomous motion, has attracted tremendous interest [70]. Various optical methods can produce rotational motion [71] or, using primarily photoreactive materials, translational motion [72]. A promising direction toward creating such nanomotors has arisen from recent theoretical work that predicted that dissimilar particles that are illuminated by an electromagnetic plane wave will experience a "nonreciprocal" net force [18, 69]. This self-induced motion occurs in the absence of an applied external driving force in the transverse plane. Rather, the transverse motion of an electrodynamically bound particle pair arises in reaction to its asymmetric scattering; *i.e.* the dimer acts as an asymmetrical object. Electrodynamics simulations demonstrated that these nonreciprocal forces vary with interparticle separation [18, 69]. However, there has not been a direct and straightforward experimental demonstration of this phenomenon.

In this letter, we experimentally demonstrate this optical self-motility phenomenon with optically bound dimers of dissimilar-size metallic nanoparticles (NPs), thereby rectifying the deficiency. Our experimental findings are quantitatively supported by electrodynamic simulations. In addition, we demonstrate optical self-motility beyond particle pairs by generating and measuring the translational motion of asymmetrical nanoparticle assemblies.

Our experiments were performed using a standard optical trapping setup with a Ti:Sapphire laser operating at $\lambda = 800nm$ [73, 20]. We used a tightly focused circularly polarized spatially phase-modulated beam of light to form an optical ring trap [73, 74]. A schematic diagram of the system is shown in Figure 5.1a. We trapped a mixture of 150-nm- and 200-nm-diameter Ag NPs and measured their motion via dark-field microscopy at a high frame rate (290fps). The particle positions were tracked [75, 76, 22] and their precisely determined positions were used to calculate the angular position, namely, θ_i of particles $i = 1, 2$ on the ring. The central angle of the pair, which is denoted as θ_c, was defined as the mean angular position of the particles (Figure 5.1b). The particle radii were differentiated by their scattering intensity (and image size) on the array detector (see SI). We observed directed motion of each electrodynamically interacting pair of dissimilar particles, which is termed a heterodimer, toward the larger particle (Figure 5.1c and Supplementary videos S2 and S3). By contrast, when two particles of the same size come into close proximity, thereby creating a homodimer, they do not exhibit directed motion. These observations are in agreement with forces that we calculated using Generalized Mie Theory (GMT, see SI), which are shown in Figure 5.1d. For a stable optically bound pair [13, 15, 39] (i.e., particles that are separated by $\approx \lambda/n_b$ in water, where n_b is the refractive index) where $\boldsymbol{F}_2 - \boldsymbol{F}_1 = 0$ the transverse force on the pair satisfies $\boldsymbol{F}_{net} = \boldsymbol{F}_2 + \boldsymbol{F}_1 = 0$ only when the two particles have identical radii [18, 69]. The homodimer results can be interpreted as stemming from the conservation of linear momentum due to mirror symmetry between the particles. This symmetry is broken for the heterodimer. While this interpretation would suffice for linearly polarized light, our use of circularly polarized light introduces an equal and opposite (i.e., anti-parallel) force on each nanoparticle that

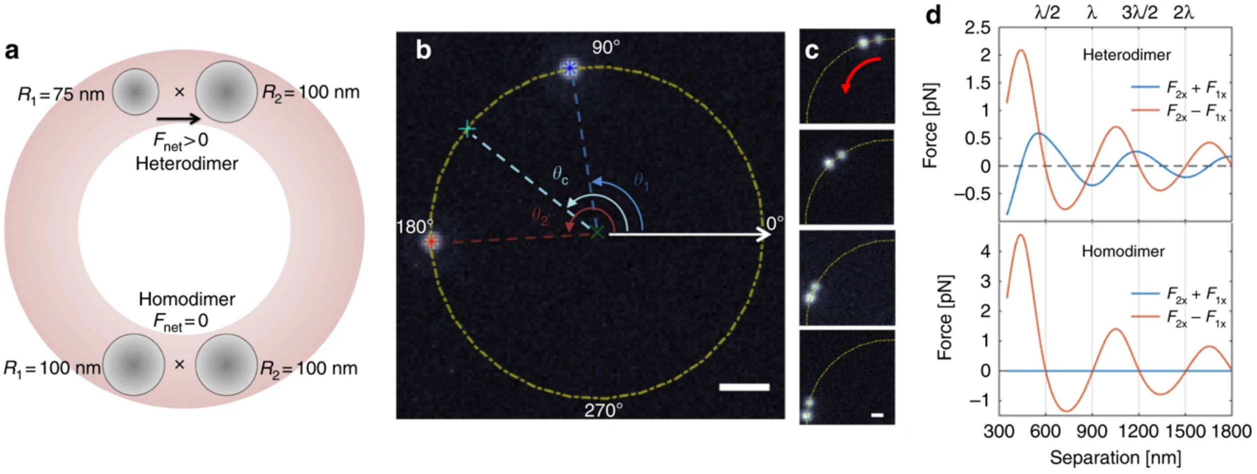

Figure 5.1: (a) A schematic diagram of the experiment: Two dissimilar particles in a ring trap (top) experience a net force, namely, $F_{net} \neq 0$ thereby resulting in observable motion. Two identical particles experience $F_{net} = 0$ (bottom). (b) An experimental image and the coordinate system. The trap location is indicated by a dot-dashed yellow circle. The particle locations in the trap are θ_1 and θ_2. Their mean angular position is θ_c. The scale bar is $1\mu m$. (c) Image sequence of a directed motion event of a heterodimer. When $150nm$ and $200nm$ diameter Ag NPs are at optical binding distance, we observe directed motion toward the larger particle. The time difference between the frames is $75ms$ and the scale bar is $500nm$. (d)The sum and difference of the forces on both particles (calculated using GMT) as a function of the separation for a heterodimer (top) and a homodimer (bottom). The particle sizes and orientation are are identical to those in panel (a).

is directed perpendicular to the interparticle separation. These anti-parallel forces create a torque on the dimer and cause it to rotate as a rigid body. However, full or free rotation was not observed in our experiment because the ring trap is constricted in its radial direction. The resulting optical gradient force counteracts particle displacements away from the maximal intensity. Manifestations of this torque and its effect will be investigated in future work.

Figure5.2a shows representative time trajectories of θ_c for the homodimer and heterodimers whose images are shown in the insets. The motion of the pair is directed toward the larger particle and, therefore, can move clockwise or counterclockwise around the ring, depending on the heterodimer orientation. The motion of the heterodimer cannot arise solely from asymmetric hydrodynamic interactions. Hydrodynamic interaction between particles cannot shift the center of the distribution of the Brownian displacements of each of the particles in the heterodimer away from zero displacement without a source of transverse momentum.

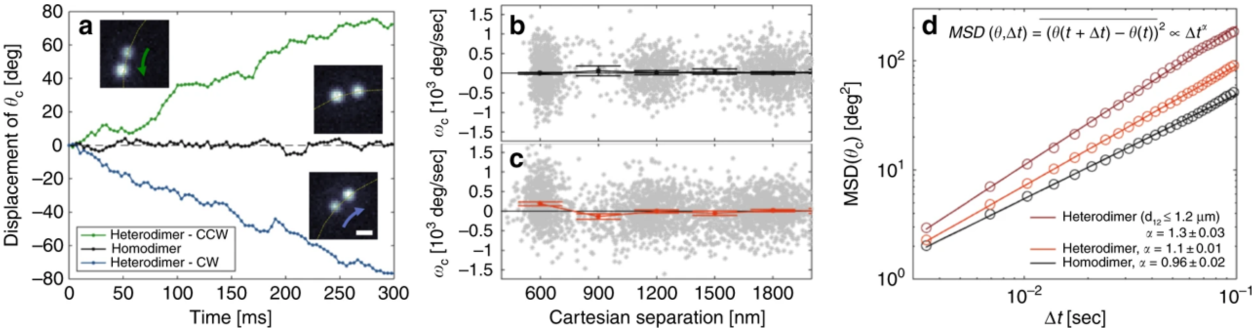

Figure 5.2: (a) Example trajectories for a homodimer (black) and a heterodimer (color) that are moving in counterclockwise (green) and clockwise (blue) directions. Distribution of instantaneous angular velocities (gray dots) and the mean angular velocities of the homodimers. (b-c) Distribution of instantaneous angular velocities (gray dots) and the mean angular velocities of the (b) homodimers and heterodimers (c) as a function of interparticle separation. The bin size is $300nm$. The mean angular velocity value was calculated by fitting a Gaussian function to the instantaneous velocity distribution. The error bars are the 3σ confidence intervals for fitted means of the distribution. Positive velocity is defined as motion of the heterodimer toward the larger NP. (d) The calculated mean square displacement (MSD) values for the homodimer data that are shown in (b) (black), the heterodimer data that are shown in (c) (orange), and the subset of the heterodimer data where the interparticle separation was $\leq 1.2\mu m$. The exponents were obtained from a linear fit of the MSDs shown; individual trajectories are shown in the Supporting Information. The error bars are 3σ confidence intervals.

We repeated the experiment many times with various nanoparticles and, hence, homodimers and heterodimers (see the Methods section and SI for full details) and combined the results. Figures 5.2b and c show the angular velocity distributions and the mean angular velocities of the dimer center, which is denoted ω_c, as a function of the interparticle separation for the full homodimer and a heterodimer data sets. The instantaneous angular velocity, which is denoted $\omega_{c,n}$, is defined as the difference in the central angle of the pair in the sequential frames $n, n+1$ ($i.e.$ $\omega_{c,n} = \frac{\theta_{n+1}-\theta_n}{\Delta t}$, where n is the frame number and Δt is the time step). In an overdamped system, $\omega_c \propto F_{net}$. To combine data with different heterodimer orientations, we define positive velocity as the vector from the smaller particle toward the larger particle. Heterodimers exhibit a positive mean angular velocity when the particles are at optical binding separation $600 \pm 150nm$ and a negative mean angular velocity when the separation is $\frac{3}{2}\frac{\lambda}{n_b}$ ($i.e.$ $900 \pm 150nm$). By contrast, the mean angular velocity for a homodimer is zero for all separations. These observations are in accordance with our prediction from GMT electrodynamics calculations (see Figure 5.1d). Both the change in the sign of the mean velocity of particle pairs at optical binding and at $\frac{3}{2}\frac{\lambda}{n_b}$ separations and the motion of the pair toward the larger, thermally hotter particle, demonstrate that the driven motion is a result of the electromagnetic field and not heating-induced self-thermophoresis [77] (see SI for details).

Figure 5.2d shows the (average) mean square displacement (MSD) of θ_c for the homo and heterodimer trajectories. The exponent, α, of $MSD(\Delta t) = D\Delta t^{\alpha}$ (with diffusion coefficient D and lag time Δt) for the homodimer is $\alpha = 0.96 \pm 0.02$, as expected for a diffusing Brownian particle [78]. For heterodimers, we observe $\alpha > 1$, which indicates driven motion [79], and an even greater value, namely, $\alpha = 1.3 \pm 0.03$, when we only consider trajectories for which the particle separation is less than $1.2\mu m$; that is, two optical binding separations. This value was chosen to allow longer trajectories for analysis (see SI for more details about the number of experiments and the trajectories that were analyzed).

Our findings are related to recent publications that report the calculation and measurement of the dynamics resulting from an asymmetry in the linear or angular momentum of the light that is scattered by optically trapped objects [80, 41] in a tractor beam configuration. We extended previous theoretical work, which considered particles in a linearly polarized beam [18], to circular polarization to explain the self-motility of electromagnetically interacting dimers (see SI for a detailed discussion). We also simulated the dynamics of Ag NP dimers using GMT [81, 82]. Each dimer, which consisted of two spherical Ag NPs with radii R_1 and R_2 that were separated by a distance d along the x-axis, was placed in a water medium ($n_b = 1.33$) with an incident right-handed-circularly (RHC) polarized plane wave (of $800nm$ vacuum wavelength). Forces were calculated by integrating the Maxwell stress tensor over a closed surface surrounding the particles. This calculation enforces conservation of linear momentum. Simulations were performed in which R_2 was varied for three values of R_1 at a separation of $d = 600nm$ (Figure 5.3a). When $R_1 = R_2$, $\boldsymbol{F}_{net,x} = 0$ vanishes, as expected for the homodimer. When $R_1 < R_2$, $\boldsymbol{F}_{net,x} > 0$ causing the heterodimer to move in the +x-direction. If $R_1 > R_2$ the net force is reversed and the heterodimer moves in the –x-direction. In both cases the motion is in the direction from the small particle to the larger one.

Additional simulations were performed for fixed nanoparticle radii with varying separation from $d = \lambda/2n_b$ to $d = 3\lambda/n_b$. Figure 5.3b shows the net force on the heterodimers as a function of d:$\boldsymbol{F}_{net,x} > 0$ at separations near $600nm$ and $1200nm$, *i.e.*, at stable optical binding configurations; and $\boldsymbol{F}_{net,x} < 0$ for particle separations near $900nm$ and $1500nm$, where the heterodimer is also in an unstable configuration. Increasing the size of the larger nanoparticle increases $\boldsymbol{F}_{net,x}$, but does not otherwise change the functional form of the force curves.

For our total system (particle and fields) to conserve linear momentum, the total momentum that is carried by the electromagnetic field that is scattered from the particle pair must be equal and opposite to the induced momentum of the dimer. Figure 5.3c–f shows a separation-dependent imbalance of angular scattering due to dipolar interference, *i.e.*, more light is scattered in one direction than in the other. For $d = \lambda/n_b$ and $d = 2\lambda/n_b$ (stable optical binding configurations), more light is scattered in the –x-direction and the net force

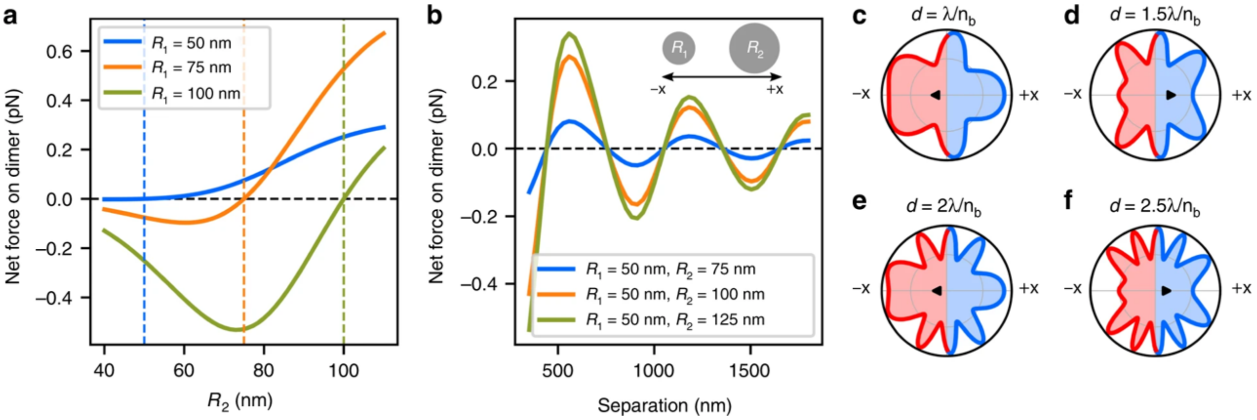

Figure 5.3: (a)The net force on the dimer, $\boldsymbol{F}_{net,x}$, as a function of the radius of particle 2 with three different radius values for particle 1: $50nm$, $75nm$, and $100nm$. The dashed lines indicate the cases of the three homodimers, where $\boldsymbol{F}_{net,x}$ vanishes. (b) $\boldsymbol{F}_{net,x}$ vs. separation for three heterodimers. (c-f) Angular scattering intensity in the xy-plane from the $R_1 = 75nm$ and $R_1 = 100nm$ heterodimer for various dimer separations d. The black triangle indicates the center of mass ("CM") of the angular distribution. We define the positive x-direction to be pointing from the smaller particle to the larger particle. Stable optical binding configurations ($d = \lambda, 2\lambda$) scatter more in the negative x-direction, whereas unstable configurations $d = 1.5\lambda, 2.5\lambda$) scatter more in the positive x-direction

that acts on the dimer is in the +x-direction. Similarly, for $d = 3\lambda/2n_b$ and $d = 5\lambda/2n_b$ (unstable configurations; see Figure 5.1d), more light is scattered in the +x direction, which corresponds to a net force in the $-x$-direction. This asymmetry in the far-field angular scattering creates a force on the dimer, thereby setting it in motion. The simulation results also confirm the switching of sign of the force observed in our experiments (Figure 5.2b) for various particle separations. Note that asymmetric scattering has been reported for plasmonic Yagi–Uda nanoantennas that were fabricated on a fixed substrate [83, 84].

An expression for the net optical force on a dimer (of spherical isotropic particles A and B) in a plane transverse to the propagation of plane-wave illumination be obtained in the point dipole approximation. The component of the electric field in the i direction at particles A and B (at only the first order of scattering) [15] is

$$E_A^i = E_0^i + G_{ij}^{AB} E_0^j \alpha^B; \quad E_B^i = E_0^i + G_{ij}^{BA} E_0^j \alpha^A \tag{5.1}$$

where E_0^i is the incident electric field, α^A or α^B is the polarizability of particle A or B, and

G_{ij}^{AB} are the elements of the dyadic Green's function for the vector between particles A and B. If we assume that the particles lie on the x axis, only the diagonal elements of G_{ij}^{AB} are non-zero. For a circularly polarized plane wave propagating in the z direction this leads to a net force in the x direction F_x^{net} on the dimer

$$\begin{aligned} F_{net,x} = \frac{E_0^2}{2}\mathrm{Re}\Bigg[&(\alpha^{A*}\alpha^{B} - \alpha^{A}\alpha^{B*})\frac{\partial}{\partial x}(G_{xx} + G_{yy}) + \\ &(\alpha^{A*}|\alpha^{B}|^2 - |\alpha^{A}|^2\alpha^{B*})\left(\frac{\partial G_{xx}}{\partial x}G_{xx}^{*} + \frac{\partial G_{yy}}{\partial x}G_{yy}^{*}\right)\Bigg]. \end{aligned} \tag{5.2}$$

This equation extends the treatment derived in [18] from particles trapped in a linearly polarized plane wave to a plane wave with circular polarization. Equation 5.2 equals zero when $\alpha^A = \alpha^B$, in accordance with the experimental and simulation results presented in the main text.

Equation 5.2 also vanishes if the two polarizabilities are proportional by a factor of a real number (e.g. $\alpha^A = C\alpha^B$ where C is a real number). The first term in Equation 5.2 can be rewritten to directly depend on the phase difference $\Delta\phi$ between the two polarizabilities α_A and α_B. The first term can be rewritten as

$$F_{net,x} = \frac{E_0^2}{2}\mathrm{Re}\left[2i * (\alpha^{A'}\alpha^{B''} - \alpha^{A''}\alpha^{B'}) * \frac{\partial}{\partial x}(G_{xx} + G_{yy})\right]. \tag{5.3}$$

where $\alpha^{'}$ and $\alpha^{''}$ are the real and imaginary parts of α, respectively. Letting $\phi_A = |\alpha_A| * tan^{-1}\frac{Im(\alpha_A)}{Re(\alpha_A)}$ and $\phi_B = |\alpha_B| * tan^{-1}\frac{Im(\alpha_B)}{Re(\alpha_B)}$ and $f(R) = Re\big[i * \frac{\partial}{\partial x}(G_{xx} + G_{yy})\big]$ gives

$$F_{net,x} = E_0^2 * f(R)|\alpha_A||\alpha_B|\big(cos(\phi_A)sin(\phi_B) - sin(\phi_A)cos(\phi_B)\big) = E_0^2 * f(R)|\alpha_A||\alpha_B|sin(\Delta\phi). \tag{5.4}$$

The dependence of the net nonreciprocal force on the phase difference between the two polarizabilities allows us to better understand the nature of the phenomenon. Figure 5.4a

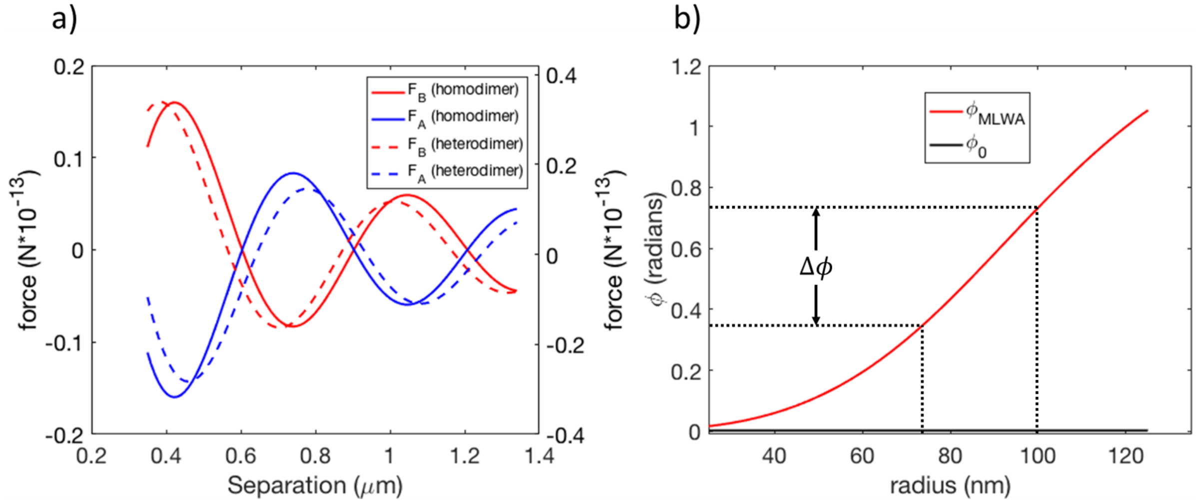

Figure 5.4: (a) Forces on particles A (blue) and B (red) in a homodimer (solid; left axis) and heterodimer (dashed; right axis). The phase difference between the polarizabilities α_A and α_B in the case of a heterodimer results in a phase shift of the force curves for each particle. (b) Phase of the polarizability of a spherical silver nanoparticle at 800nm with variable radius calculated with (black) and without (red) the MLWA correction.

shows the forces on two particles A (blue) and B (red) in a homodimer (solid; left axis) where $r_A = r_B = 75nm$ and heterodimer (dashed; right axis) where $r_A = 100nm$ and $r_B = 75nm$. For the heterodimer, the force curves are shifted in opposite directions by $\approx 40nm$, corresponding to a phase difference of $\frac{40nm}{600nm} * 2\pi = 0.42$ radians. The point at $600nm$ where the two curves corresponding to the homo-dimer cross is the first optical binding site. They cross at a value of zero, reflecting the absence of a net force on the homodimer. The two force curves still cross near $600nm$ for the heterodimer, but the point where they cross is no longer at zero. This corresponds to the dynamic bound state with a non-zero net force observed in the experiment.

Figure 5.4b shows the phase of the polarizability calculated using 2.6 with and without the MLWA approximation [35]. For silver nanoparticles at $800nm$, the phase of the polarizability is very small regardless of particle size before the MLWA approximation is applied. However, the MLWA approximation applies a significant size-dependent phase shift to the polarizability. The imaginary contribution to the polarizability due to radiative damping outweights the contribution due to the bulk dielectric properties of silver by several orders of magnitude.

The phases of a $75nm$ and $100nm$ radius nanoparticle are marked on the plot. The phase difference $\Delta\phi$ is consistent with the 0.42 radians calculated from the $\approx 40nm$ shift of the force curves.

So far, we have confined our study of nonreciprocal forces to pseudo-1D configurations. We now turn our attention to two-dimensional clusters containing different types of particles. Figure 5.5a-b show two possible configurations of a cluster containing 6 particles with $r = 75nm$ and one particle with $r = 100nm$. In Figure 5.5a the small particles are placed symmetrically around the large particle and the pairwise non-reciprocal forces (directed toward the large particle) cancel. Figure 5.5b shows a cluster with the small particles arranged asymmetrically around the large particle. In this case, the pairwise nonreciprocal forces do not cancel, and the total force on the large particle is directed toward a gap in the smaller particles. In this scenario, the sum of non-reciprocal forces will tend to push the large particle out of the cluster.

In experiments with particles of mixed sizes, large particles are typically observed outside of clusters made up of smaller particles. Figure 5.5c shows a still-frame from an experiment with a mixture of $150nm$ and $200nm$ particles. In this experiment, a large particle is observed orbiting around a cluster of smaller particles. The orbital motion is due to spin-to-orbital angular momentum conversion induced by the symmetry of the optical matter cluster [23]. Figure 5.5d shows a plot of all particle positions observed in the experiment, with the large particle marked as red and the small particles marked as black. Clearly, the red particle is excluded from the cluster of smaller particles. This suggests that in two dimensions, non-reciprocal forces result in the self-sorting of particles based on the phase of their polarizability.

Experimentally, it is difficult to observe the ejection of a large particle in mixed-size optical matter experiments because once the large particle is on the outside of the cluster, it has to work against the nonreciprocal forces to re-enter. However, we have found that bound dimers of particles, which can form due to the compressive optical forces within the cluster, are also

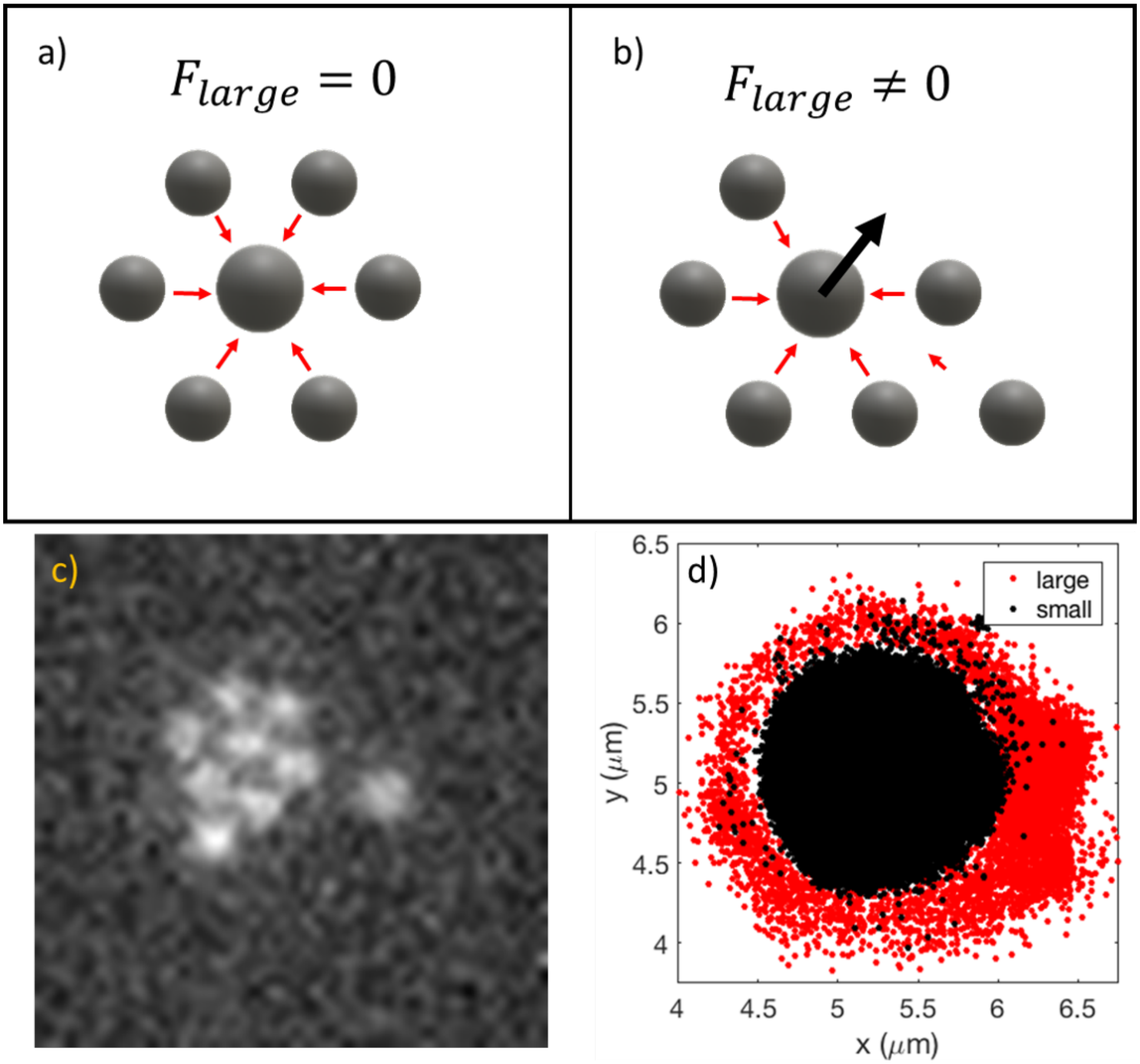

Figure 5.5: Nonreciprocal forces in 2D heterostructures. (a) Diagram of the pairwise nonreciprocal forces in a symmetric 2D optical matter heterostructure. The sum of the forces is 0. (b) Diagram of the pairwise nonreciprocal forces in a asymmetric 2D optical matter heterostructure. The sum of the forces points toward a gap in the structure. (c) Experimental image of a 2D optical matter heterostructure. A large particle is excluded from a cluster of smaller particles. (d) Scatter plot of the detected locations of the large (red) and small (black) particles in the experiment shown in panel (c).

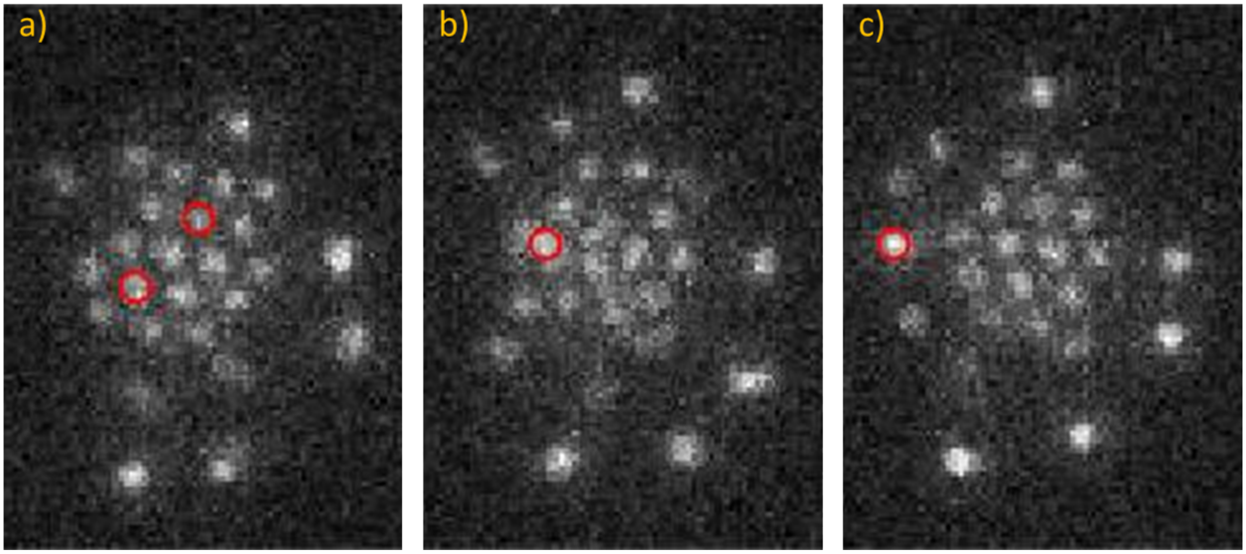

Figure 5.6: Formation and escape of a dimer from a 2D optical matter cluster (a) Experimental image of a 2D optical matter structure with several large objects on its periphery. Red circles mark two particles that come together to form a dimer. (b) Experimental image of a 2D optical matter structure at the moment where a dimer begins to form. The dimer is marked by a red circle. (c) Experimental image of a 2D optical matter structure after a dimer has been ejected. The dimer that recently formed is marked by a red circle.

ejected from optical matter clusters. Figure 5.6a-c shows a sequence of images demonstrating the formation and ejection of a dimer from a 2D optical matter cluster. Figure 5.6a shows a 2D optical matter cluster with bright particles on the periphery. Two particles in the cluster that fuse to become a bound dimer are marked by red circles. In Figure 5.6b the the two particles come in close proximity due to thermal fluctuations. The two particles form a dimer and are ejected from the cluster. The dimer is marked by a red circle in Figure 5.6c. The number of particles counted before and after the event shown in Figure 5.6a-c reflect a net loss of one particle, consistent with the formation of a bound dimer.

We also performed optical matter experiments with a mixture of 150nm gold and silver nanoparticles. The experiments were recorded on a color camera so that we could differentiate between gold and silver particles. A still-frame from the experiment is shown in Figure 5.7a. The phase of the polarizability for gold and silver nanoparticles with variable size is plotted in Figure 5.7b. The phase difference is much smaller, and consequentially the magnitude of

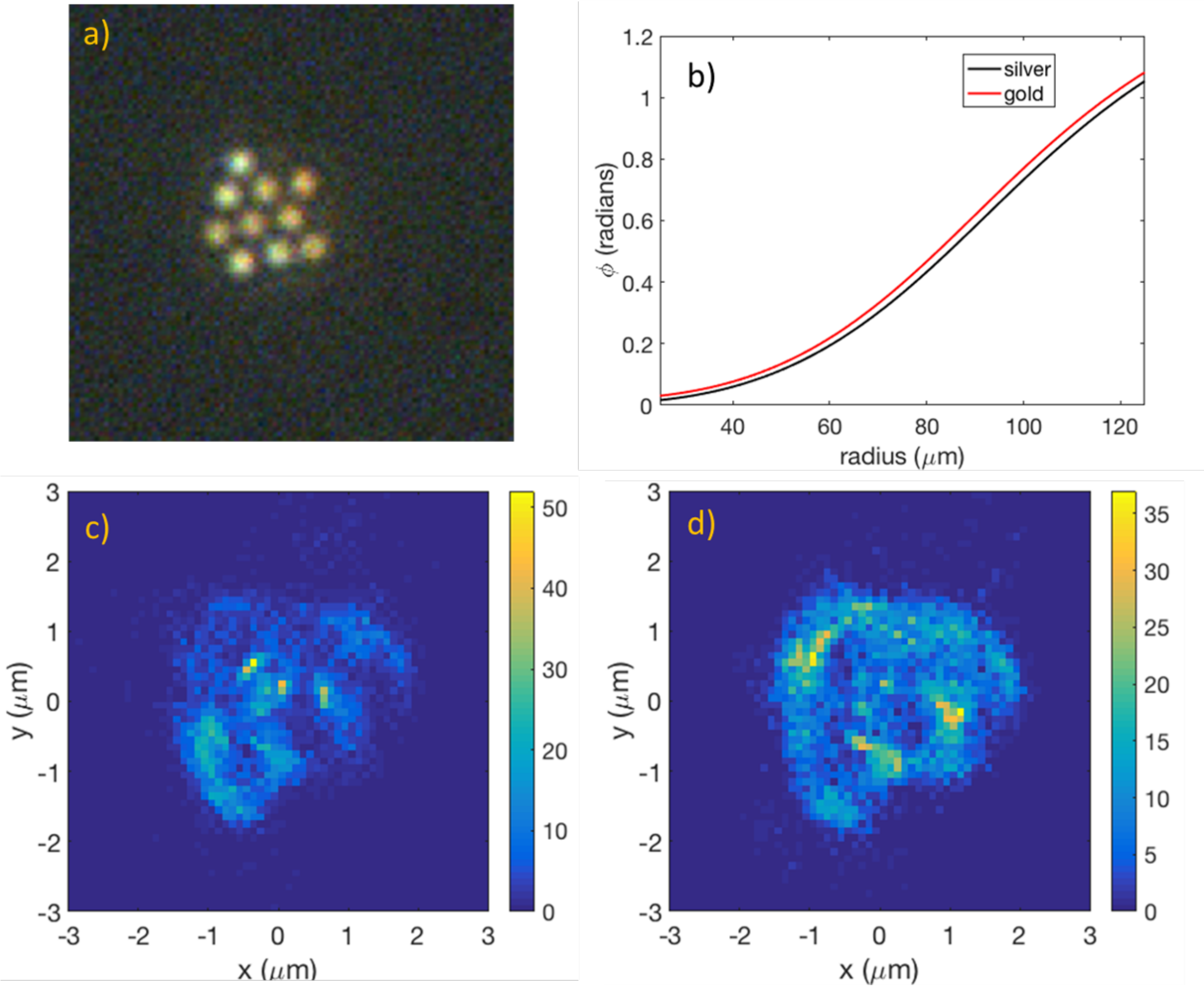

Figure 5.7: 2D mixed gold-silver optical matter array. (a) Experimental image of a mixed gold-silver optical matter array. (b) Phase of the polarizability of spherical silver (black) and gold (red) nanoparticles with $800nm$ illumination for varying radius. (c) Distribution of positions for particles detected as gold. (d) Distribution of positions for particles detected as silver.

non-reciprocal forces are expected to be much smaller. Figures 5.7c-d show the distributions of particles detected as gold (c) and silver (d) (see Appendix A for detection method). There is no clear bias for either of the particles to be excluded from the cluster.

In this section, we have experimentally demonstrated driven motion of both Ag NP heterodimers and intrinsically asymmetric scatterers in optical ring traps, namely, 1-D plane wave fields. Our electrodynamic simulations indicate that the net force on a dimer is accompanied by a net asymmetric scattering in the opposite direction. Therefore, we attribute the driven (reactive) motion of asymmetric optical matter systems to the conservation of linear momentum. Fundamentally, this self-motility follows from Noether's theorem and the conservation of total momentum of particles and fields for systems with broken mirror symmetry [85]. Analytical equations in the point-dipole approximation showed that the non-reciprocal forces arise from the phase difference in the polarizability of dissimilar particles in a hetero-dimer. The phase difference in the polarizability of the particles results in a shift in the force curves of the two particles. The magnitude of the shift in the force curves is consistent with the phase difference induced by radiative damping and described by the MLWA approximation [35].

Generating directed motion at the nanoscale is challenging [86] due to the overdamped nature of dynamics at low Reynolds number and the Brownian forces that are antithetical to orientational control of nanoscale objects. Optical trapping offers a variety of solutions to these challenges since it enables precise control over the positions and orientations of trapped particles. Although systematic driving forces can be applied via the use of phase gradients, apparent nonreciprocal forces, such as those that are explored above, create self-motile particles that do not require specific chemical environments or chemical fuels [87] or complex structures [88]. Therefore, optically controlled asymmetric nanoparticle assemblies, such as those that are reported here, can be used as active colloids [87] and fully controllable "nanoswimmers" for research in soft condensed matter and biophysics. In two dimensions, nonreciprocal forces tend to separate particles in optical matter clusters based on size. Recent work has demonstrated the sorting of particles in optical matter systems using time-varying fields [89, 90]. Our results, by contrast, show that it is possible to achieve passive sorting in simple steady-state optical beams. The results shown in Figure 5.6 demonstrate that nonreciprocal forces can even be used to create a passive optical matter 'factory', where light is used to gather single particles, and once the particles fuse to form a dimer, the same light induces nonreciprocal forces that push the dimer to the periphery of the cluster.

5.2 Controlling the dynamics and optical binding of nanoparticle homodimers with transverse phase gradients

The following section is reproduced with permission from: Peterson, Curtis W., John Parker, Stuart A. Rice, and Norbert F. Scherer. Controlling the dynamics and optical binding of nanoparticle homodimers with transverse phase gradients. *Nano letters 19, no. 2 (2019): 897-903.* ©American Chemical Society

5.2.1 Introduction

Particles in optical traps [91, 92] interact with one another *via* scattered electromagnetic fields, and assemble into stable structures known as Optical Matter [13, 14] (OM). OM is commonly compared to conventional chemically bonded materials because OM tends to adopt periodic lattice structures [36, 16, 17, 40]. Since OM assemblies are maintained by a constant flux of energy through the system, broken symmetry in the constituents of OM assemblies can result in nonequilibrium driven dynamics [82, 93, 68, 94, 18, 69, 95, 96, 19]. Nonequilibrium dynamics in OM assemblies can also arise from the intrinsic momentum of light [97, 98, 99, 20, 100, 71] or transverse phase gradients [101, 102, 103, 40, 73, 104]. However, the emergent forces and stable configurations arising from *interacting particles* in a phase gradient have not been explained. Relevant recent work involving multiple particles in tractor beam experiments has shown that unexpected changes to the sign and magnitude of optical forces emerge when the trapped particles are close enough to interact *via* the trapping light [41], but there has not been a detailed theoretical description of this effect.

In this letter we explore the pairwise interactions between 150nm Ag nanoparticles in transverse phase gradients. We demonstrate experimentally and theoretically that the effects of phase gradients are manifested in different ways depending on their strength. For small phase gradients the net force on a pair of identical particles exhibits a separation-dependent periodic modulation compared to isolated particles. By contrast, large phase gradients break the symmetry of the interaction between particles. As a result, the location, strength, and number of stable optical binding locations of a pair of electrodynamically interacting nanoparticles depends on the strength of the incident gradient.

5.2.2 Forces from phase differences

The electromagnetic interaction between particles with separations on the wavelength scale is greatly influenced by the phases of the incident field and the field scattered from other nearby particles [15]. A schematic of two particles, A and B, separated by a distance R in the

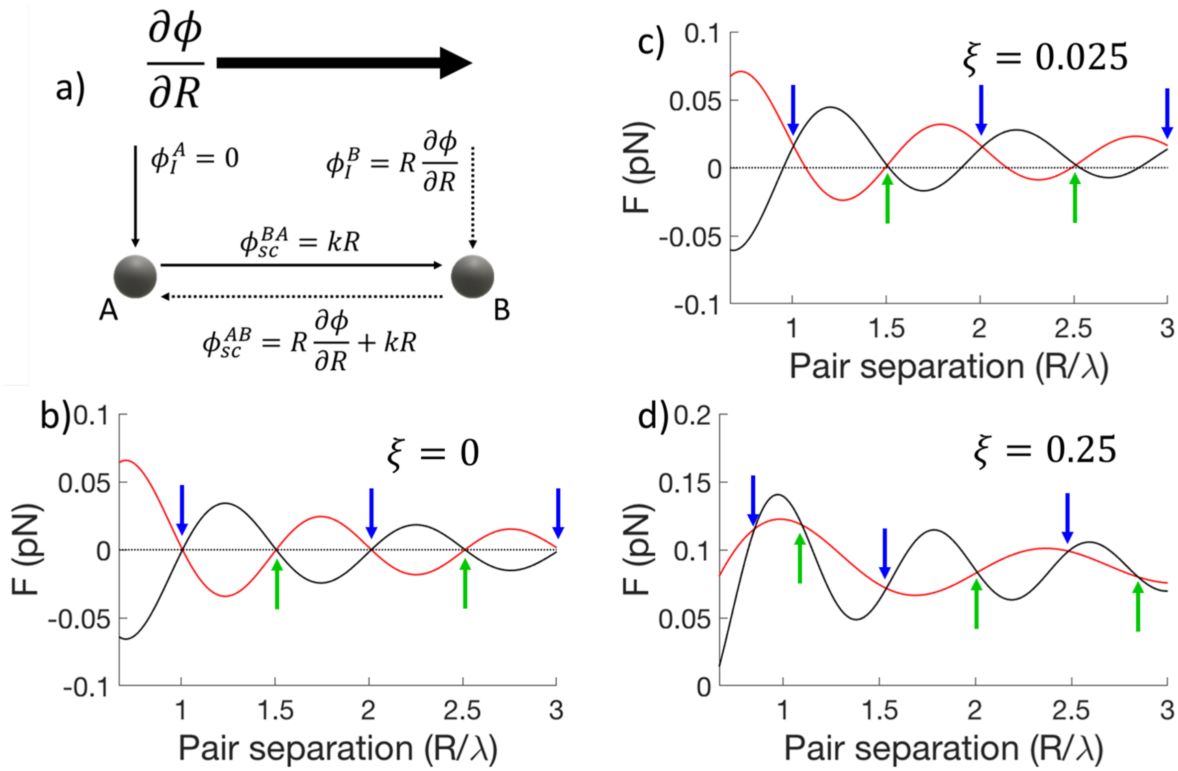

Figure 5.8: Electrodynamically interacting particles in a linear phase gradient. (a) Schematic of two electrodynamically interacting particles A and B in a transverse phase gradient, $\frac{\partial \phi}{\partial R}$. (b-d) Electrodynamic forces on particles A (black) and B (red) along the inter-particle axis for $\frac{\partial \phi}{\partial R} = 0$, $\frac{\partial \phi}{\partial R} = 0.025k$, and $\frac{\partial \phi}{\partial R} = 0.25k$, where $\xi k = \frac{\partial \phi}{\partial R}$ and $k = 2\pi/\lambda$ is the magnitude of the wavevector of the incident electromagnetic field. Blue arrows point to optical binding locations (minima in the inter-particle energy landscape) and green arrows point to unstable equilibrium separations (maxima in the inter-particle energy landscape). Note that the position of the arrows changes significantly for (d) compared to (b) and (c).

presence of a linearly varying phase gradient $\frac{\partial\phi}{\partial R}$ is shown in Figure 5.8a. Setting the phase of the incident field at particle A (ϕ_I^A) to zero, $\phi_I^B = R\frac{\partial\phi}{\partial R}$. The phase of the field scattered from A to B and from B to A is $\phi_{sc}^{BA} = kR$ and $\phi_{sc}^{AB} = kR + R\frac{\partial\phi}{\partial R}$, respectively. Then the phase difference between the incident and scattered fields at particles A and B is

$$\begin{aligned} \Delta\phi_A &= \phi_{sc}^{AB} - \phi_I^A = R\Big[k + \frac{\partial\phi}{\partial R}\Big]; \\ \Delta\phi_B &= \phi_{sc}^{BA} - \phi_I^B = R\Big[k - \frac{\partial\phi}{\partial R}\Big]. \end{aligned} \tag{5.5}$$

Equation 5.5 suggests two different regimes of interaction between particles A and B in the presence of a phase gradient: an "interference regime" for small phase gradients where $\Delta\phi_A \approx \Delta\phi_B \approx kR$, and an "asymmetric regime" for large phase gradients where $\Delta\phi_A \neq \Delta\phi_B$. Due to the form of Equation 5.5, it is convenient to introduce a dimensionless parameter that describes the strength of the phase gradient $\xi = \frac{\partial\phi}{\partial R}/k$, where $k = \frac{2\pi}{\lambda}$ is the magnitude of the wavevector and λ is the wavelength of the incident field of the trapping laser. See the Supporting Information for further discussion.

Following the analysis of Dholakia *et al.* [15], the total force on Particle A along the R direction in the point-dipole approximation (see the Supporting Information) is

$$F_R^A = \frac{1}{2} Re\left[\Big(\alpha_0^* \overline{\mathbf{E}}_0^{A*} + (\alpha_0^*)^2 \overline{\mathbf{E}}_0^{B*} \overline{\overline{\mathbf{G}}}^{AB*}\Big) \frac{\partial \overline{\mathbf{E}}_0^{A}}{\partial R} + |\alpha_0|^2 \overline{\mathbf{E}}_0^{A*} \frac{\partial \overline{\overline{\mathbf{G}}}^{AB}}{\partial R} \overline{\mathbf{E}}_0^{B}\right] \tag{5.6}$$

where α_0 is the polarizability of the identical isotropic particles, $*$ denotes complex conjugate, $\overline{\mathbf{E}}_0^{A}$ and $\overline{\mathbf{E}}_0^{B}$ are the incident electric field (vectors) at particle A and B, and $\overline{\overline{\mathbf{G}}}^{AB}$ is the dyadic Green's function that propagates the scattered field from particle B to particle A. The force on particle B can be obtained from Equation 5.6 by exchanging the labels A and B.

Figures 5.8b-d show the calculated values of the force in the R direction (*i.e.* along the inter-particle axis) on particles A (red) and B (black) for phase gradients of $\xi = 0$, $\xi = 0.025$, and $\xi = 0.25$. See the Supporting Information for forces calculated for several other values of ξ. Figure 5.8b for $\xi = 0$ shows that the net force $F_{net} = F_A + F_B$ is zero for all separations, which occur at integer multiples of λ. With $\xi = 0.025$ (Figure 5.8c) F_{net} is generally non-zero, but the optical binding locations are not appreciably changed. However, for $\xi = 0.25$ the difference between $\Delta\phi_A$ and $\Delta\phi_B$ is significant and the optical binding locations are shifted away from $R = m\lambda$, where $m = 1, 2, 3, ...$ is an integer.

5.2.3 Small phase gradient regime

As an experimental realization of the simple scheme depicted in Figure 5.8a we trapped PVP-coated 150nm spherical Ag nanoparticles (NPs) with a cw Ti:Sapphire laser in water ($\lambda = 800nm$ in vacuum; $600nm$ in water). The trapping laser beam was modified by a spatial light modulator SLM and was focused by a 60x objective to form an optical ring trap as previously described [73, 105] (see the Supporting Information). The power of the laser entering the microscope objective was $100mW$, from which we estimated a local electric field strength of $10^6 V/m$ in the ring trap. An azimuthal phase gradient [102] that depends on the topological charge of the beam, l, can be added to the ring. The effective strength of the phase gradient, ξ, can be increased by decreasing the size of the ring. Therefore, different combinations of the integer number of phase wrappings l and the ring radius r allow for a large number of different phase gradients to study. An image from a video of the experiment is shown in Figure 5.9a. The ring trap that the particles are confined to is indicated as a green dashed circle. The actual ring trap is not observed due to optical filtering. Inter-particle separations are calculated as Cartesian separation so that they are relevant to Equations 5.5 and 5.6. However, particle velocities are calculated in cylindrical coordinates (r, θ), $v = \frac{r\Delta\theta}{\Delta t}$, to account for the curved path that the particles follow.

The net force on an electrodynamically interacting homo-dimer, $F_{net} = F_A + F_B$, determines the dynamics of the particle pair. Following from Stokes' law [66] and the overdamped conditions of the experiment, the average velocity of the center of mass of the homo-dimer,

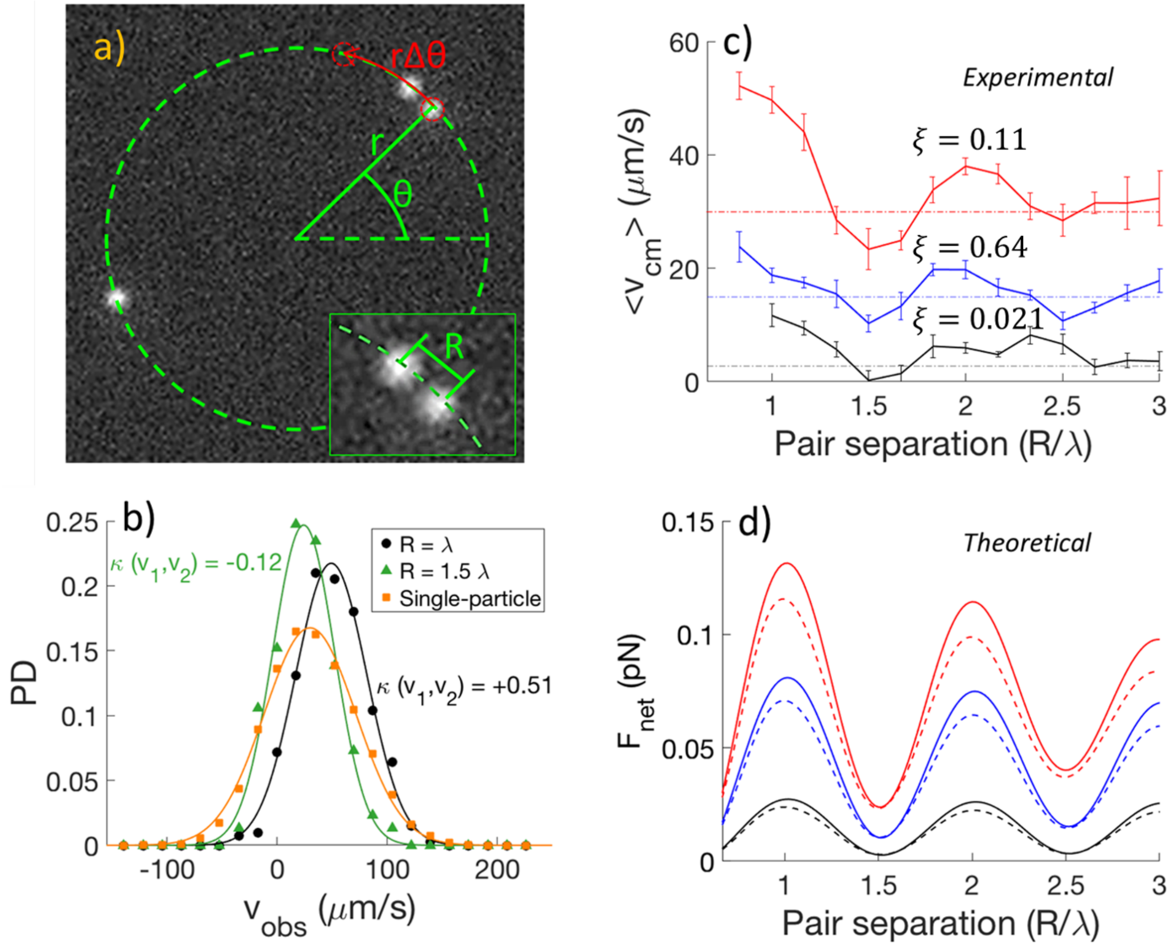

Figure 5.9: Experimental image and separation dependence of the driving force for small phase gradients. (a) A darkfield microscopy image of three 150nm Ag NPs (white spots) in a ring trap (green dashed circle). Also shown are the cylindrical coordinates employed in the analysis. Separations are measured as Cartesian distance as shown in the inset. (b) Conditional PDFs of v_{cm} for $R_0 = \lambda$ (black) and $R_0 = 1.5\lambda$ (green) with $\xi = 0.11$. The velocity correlation $\kappa(v_1, v_2)$ at each separation is shown next to the corresponding curve. The PDF of single-particle velocities for particles separated by $> 3\mu m$ from their nearest neighbor is shown in orange. (c) Plots of $\langle v_{cm} \rangle$ as a function of R for $\xi = 0.021$ (black), $\xi = 0.064$ (blue), and $\xi = 0.11$ (red). The horizontal dashed lines are the average single-particle velocities as in panel (b). (d) Calculated values of the net force on a homo-dimer *via* Equation 5.6 (solid) and GMT (dashed) in the $\vec{R}$ direction for phase gradients of $\xi = 0.021$ (black), $\xi = 0.064$ (blue), and $\xi = 0.11$ (red).

$\langle v_{cm} \rangle$, in the absence of interactions is the same as the velocity of an isolated particle , v_{iso}, under the same optical conditions. Hydrodynamic interactions require a relatively small correction to the velocity that decays monotonically with R for our experimental conditions (see the Supporting Information). [106] The predicted separation between the particles and the coverglass surface (i.e., the upper boundary of the sample cell) is approximately one particle radius[73], and the resulting modification of the Stokes' drag force is expected to be less than a factor of two.[107]

Figure 5.8c, for small phase gradients, suggests that a drifting electrodynamically bound pair will exhibit an enhanced net force when the separation is $R = \lambda$; that is, $F_{net} > 2F_{A,iso}$. When the separation is $R = 1.5\lambda$ the pair will be unbound and exhibit diminished net force; that is, $F_{net} < 2F_{A,iso}$. Since the separation between particles in a homo-dimer fluctuates due to Brownian forces, we determine the separation dependence of v_{cm} from conditional probability distribution functions (PDFs) $P(v_{cm}|R_0, \delta) = P(v_{cm}|R \in [R_0 - \delta, R_0 + \delta])$, *i.e.* the probability distribution of v_{cm} given that R is within a certain range $\pm\delta$ of a particular value R_0. Figure 5.9b shows the conditional PDFs of v_{cm} for $R_0 = \lambda$ and $R_0 = 1.5\lambda$ with $\delta = 0.125\mu m$ and $\xi = 0.11$ (as determined by the radius r of the ring trap and the topological charge l). Note that δ is much larger than the error in particle localization. The PDFs have a Gaussian shape where the mean value $\langle v_{cm} \rangle$ depends on the deterministic driving force. The width of the distribution depends both on the diffusion coefficient of the individual particles and the degree to which their motion is correlated. Gaussian fits to each PDF yield $\langle v_{cm} \rangle = 49\mu m/s$ for $R_0 = \lambda$ (black) and $\langle v_{cm} \rangle = 24\mu m/s$ (green) for $R_0 = 1.5\lambda$, matching the behavior predicted for small phase gradients, *i.e.* Figure 5.8c. The correlation of v_1 and v_2, $\kappa(v_1, v_2)$, shows that the homo-dimers move as bound pairs when $R_0 = \lambda$, while their motion is uncorrelated when $R_0 = 1.5\lambda$. The correlated motion at $R_0 = \lambda$ is a consequence of optical binding and is the reason the Gaussian distribution for $R_0 = \lambda$ is wider than the one for $R_0 = 1.5\lambda$. Optical binding distances in small phase gradients has been discussed at length in Figliozzi *et al.*[73] (see the Supporting Information). Figure 5.9b also shows the single-particle velocities v_{iso} for $\xi = 0.11$ (orange). The single-particle velocity distribution is wider compared to v_{cm} because it represents a single random variable as opposed to an average of two.

Figure 5.9c shows plots of $\langle v_{cm} \rangle$ as a function of R_0 for different strengths of the phase gradient: $\xi = 0.021$ (black), $\xi = 0.064$ (blue), and $\xi = 0.11$ (red). The velocity is measured at each separation by fitting the conditional PDF with a Gaussian function; the mean of the fit is the plotted value and the error bars are the 95% confidence interval of the mean. The horizontal dashed lines are the average *single-particle* velocities for each phase gradient. The single-particle driving force increases linearly with phase gradient [73, 102]. Figure 5.9c shows that the driving forces for all three phase gradients are enhanced ($F_{net} > 2F_{A,iso}$) near $R_0 = \lambda$, and diminished ($F_{net} < 2F_{A,iso}$) near $R_0 = 1.5\lambda$ in agreement with Figure 5.9b. A periodic behavior is more apparent for larger phase gradients; a second peak in $\langle v_{cm} \rangle$ is visible near $R_0 = 2\lambda$ and a second minimum is visible near $R_0 = 2.5\lambda$ for $\xi = 0.064$ and $\xi = 0.11$.

We evaluated Equation 5.6 for phase gradients matching our experimental values to explain the separation dependence of the driving force. Figure 5.9d shows calculated values of the net force on a homo-dimer along the inter-particle axis for phase gradients of $\xi = 0.021$ (black), $\xi = 0.064$ (blue), and $\xi = 0.11$ (red). The most apparent feature in these curves is the periodic modulation of the net force with maximum and minimum values at integer and half integer multiples of λ, respectively. It is also apparent that the strength of the modulation increases with the magnitude of the phase gradient.

We also performed more rigorous generalized Mie theory (GMT) calculations (see the Supporting Information for details). In addition to accounting for the finite size of particles and infinite orders of scattering, our GMT simulations accurately model the experimental ring-trap geometry and account for possible deviations from Eq 5.5 for large phase gradients. The net forces from our GMT simulations are shown as dashed curves in Figure 5.9d. The GMT results agree with our theoretical point-dipole calculations, validating the model in Figure 5.8 and Equations 5.5 and 5.6. In water at $20C$, Stokes' law predicts that a spherical

$150nm$ particle will be pushed at $35\mu m/s$ by a constant $0.05pN$ force. $35\mu m/s$ is closest to the single particle velocity for $\xi = 0.11$ in Figure 5.9c, and we can see from Figure 5.9d that a constant force of $0.05pN$ is reasonable for this phase gradient. This agreement, within better than an order of magnitude, shows that our theoretical parameters (*e.g.* $E_0 = 10^6 V/m$) are in reasonable agreement with experiment. Therefore, Figures 5.9 c and d can be compared directly using the conversion factor $0.1pN = 70\mu m/s$.

The results shown in Figure 5.9 can be understood as interference effects that are a consequence of the symmetric part of Equation 5.5; *i.e.*, $\Delta\phi_A = \Delta\phi_B \approx kR$. In the limit of no phase gradient this phase difference gives rise to optical binding through the second term of Equation 5.6 [15]. For small phase gradients, optical binding still occurs at separations where $kR = 2\pi m$, but there is now a separation-dependent net force on the homo-dimer. The result is a driven bound pair where the motion of the two particles is correlated. The first term in Equation 5.6 can be interpreted as a periodic modification of the single-particle driving force. The $\alpha_0 \overline{\mathbf{E}}_0^*$ part of the first term of equation 5.6 corresponds to the "single-particle" driving force, while the $(\alpha_0^*)^2 \overline{\mathbf{E}}_0^* \overline{\overline{\mathbf{G}}}^*$ part of the first term corresponds to a separation-dependent modification of the driving force in the presence of another particle. When $kR = 2\pi m$ the two contributions are in-phase and constructive interference enhances the driving force. Conversely, when $kR = \pi(2m+1)$ destructive interference diminishes the driving force. Since the modified driving force is proportional to $\frac{\partial\phi}{\partial R}$, larger phase gradients will give rise to larger modulation of the total force, as shown in Figure 5.9c and d.

5.2.4 Large phase gradient regime

For large phase gradients, *i.e.* where the phase gradient becomes comparable to the magnitude of the wavevector of the trapping light, k, we expect that the symmetry of the interaction between particles is broken, as described by Equation 5.5. We performed experiments in this regime. The black curves in Figure 5.10a-c are experimentally measured PDFs of inter-particle separations with $\xi = 0.23$ (a), $\xi = 0.29$ (b), and $\xi = 0.34$ (c). The maxima of probability

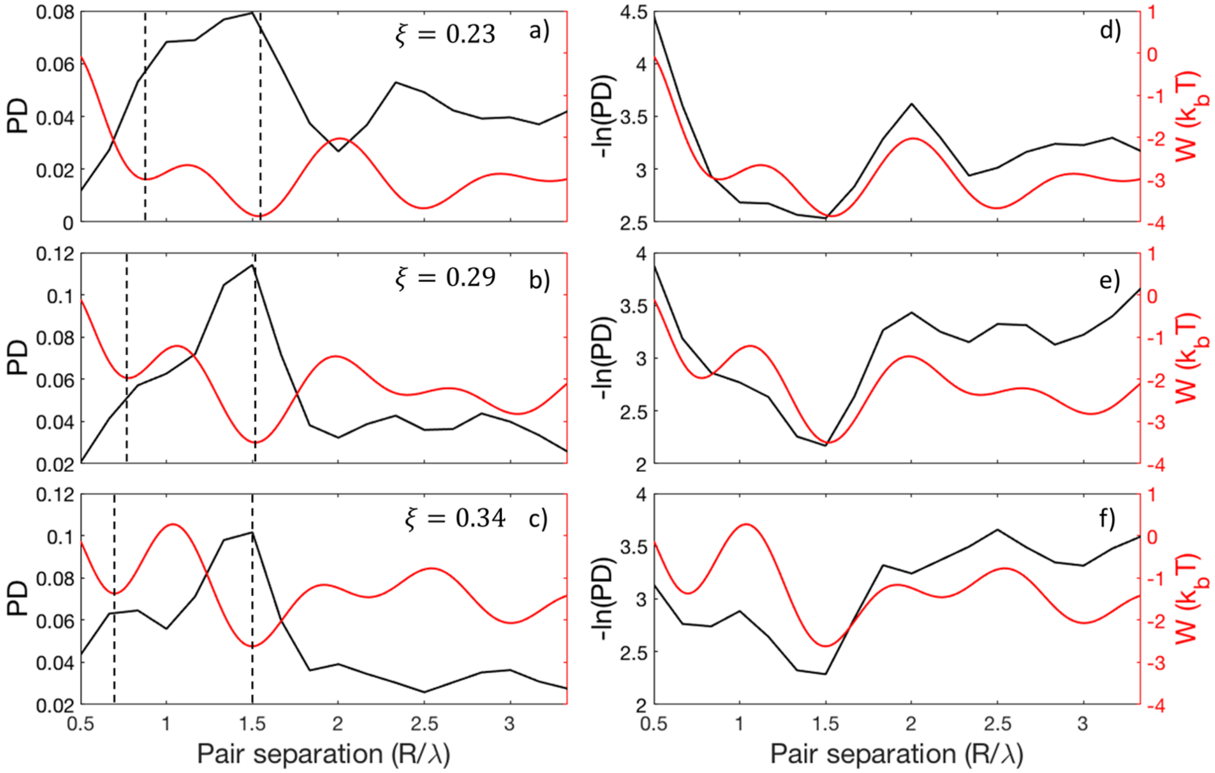

Figure 5.10: Phase gradient dependence of optical binding for large phase gradients. (a)-(c) Measured inter-particle separation PDFs (black curves, left axis) for $\xi = 0.23$, $\xi = 0.29$, and $\xi = 0.34$. The electrodynamic interaction potential is also plotted in units of k_BT (red curves, right axis). The vertical dashed lines mark the first two minima in the electrodynamic interaction potential. (d)-(f) Measured inter-particle separation PDFs from (a)-(c) replotted as $-ln(PD)$ (black curves, left axis) to allow direct comparison to the corresponding electrodynamic interaction potentials (red curves, right axis).

density are significantly shifted from the traditional locations of optical binding (*i.e.* optical binding at $R = m\lambda$).

To compare the experimentally measured PDFs to theoretical predictions made from Equation 5.6 we define the electrodynamic interaction potential, W, as the work needed to separate two particles along the inter-particle axis from some minimum separation R_1 to another particular separation R_2 (see the Supporting Information for discussion.)

$$W(R_2, R_2) = -\int_{R_1}^{R_2} (F_R^B - F_R^A)\, dR'. \tag{5.7}$$

Although optical forces are generally non-conservative [65, 108], W is a meaningful energy coordinate along a 1-dimensional path. Stable optical binding locations correspond to energy minima and unstable equilibrium separations correspond to energy maxima.

The red curves in Figure 5.10a-c show plots of W as a function of separation starting from $R_1 = 300nm$ for $\xi = 0.23$, $\xi = 0.29$, and $\xi = 0.34$. W is plotted in units of k_bT where k_b is Boltzmann's constant and $T = 298K$ to emphasize that optical binding is comparable with thermal energy under our experimental conditions. The vertical black dashed lines in Figure 5.10a-c are located at the first two energy minima for each corresponding energy curve. There are peaks in the experimental PDFs near the minima in energy (W), indicating optical binding. A more direct comparison between the experimental PDFs of inter-particle separation and W is possible through the relation $G(x)/k_bT = -ln(P(x))$ where $G(x)$ is a potential of mean force and $P(x)$ is the PDF of the coordinate x observed at temperature T. Figures 5.10d-f show the experimental PDFs from Figures 5.10a-c replotted as $-ln(PDF)$. There is good agreement between our theoretical predictions and experimental measurements, although there are some deviations. There are two important factors that affect the correspondence between our theoretical prediction for W and our experimentally measured PDFs. First, the experiment is carried out at room temperature, while our analytical electrodynamics calculations do not account for thermal motion of the particles. Second, the relationship between a potential of mean force and a corresponding probability distribution function is only valid for equilibrium systems, while our experiments are non-equilibrium. Therefore, we represent the results as $-ln(PDF)$ as opposed to calling it a PMF.

Figure 5.11 further demonstrates the dependence of the energy landscape W on the phase gradient. Figure 5.11a shows the experimental inter-particle separation PDF for $\xi = 0.34$ (black). The distribution is well fit with a sum of two Gaussian functions (red) up to $1.2\mu m$. The experimentally measured optical binding distances are defined as the mean values of each of the two Gaussian terms in the fit, while the theoretical optical binding locations (dashed lines) are the positions of the mimima in the energy curves shown in Figures 3a-c. Figure 5.11b shows a direct comparison between the experimental and theoretical optical

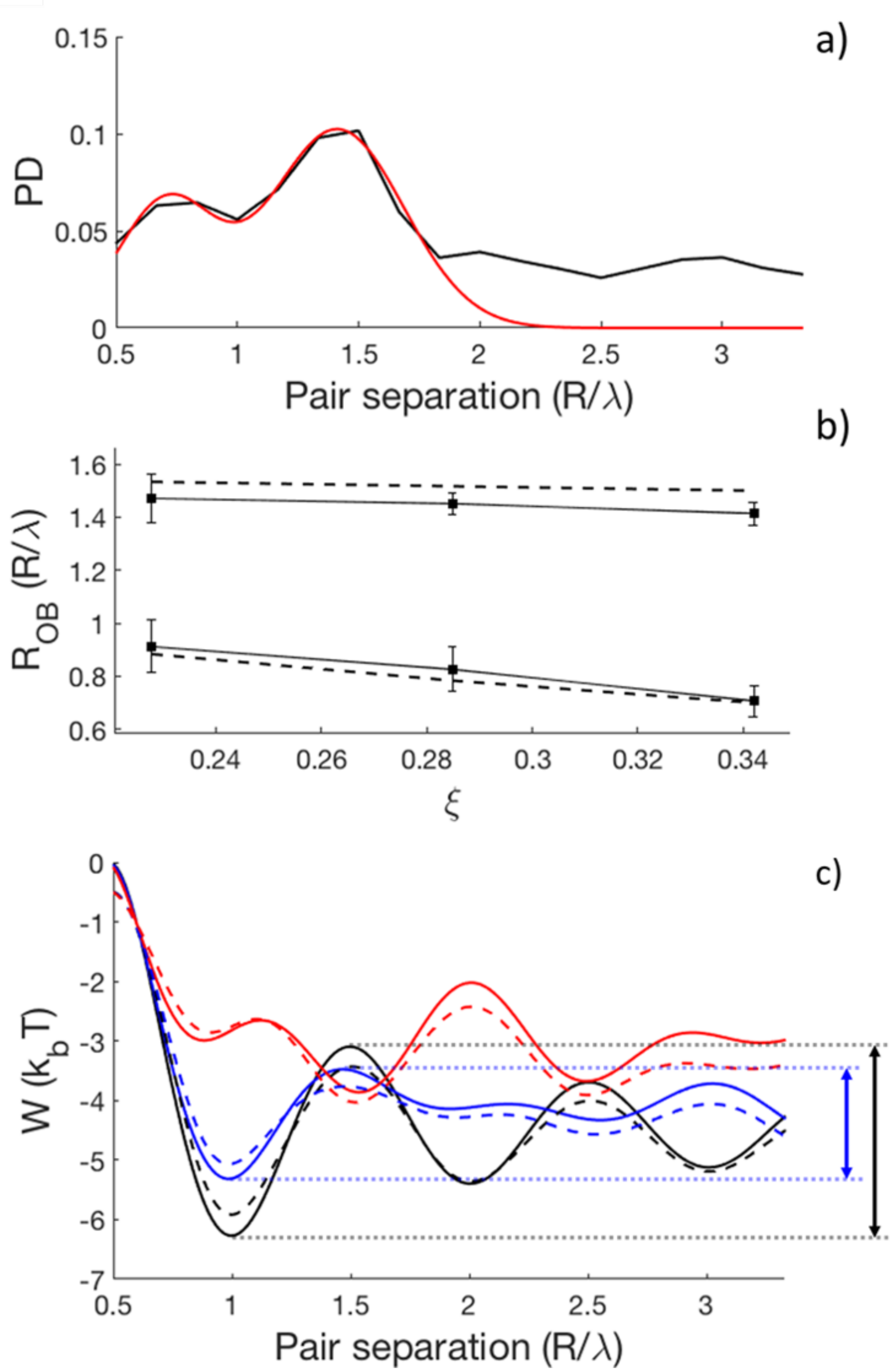

Figure 5.11: Quantitative comparison of theoretical and experimental optical binding locations. (a) Fit of experimental inter-particle separation PDF (black) for $\xi = 0.34$ with a sum of two Gaussian functions (red) up to $R = 2.0\lambda$. (b) Comparison of theoretical (dashed lines) and experimental (black squares connected by solid lines) optical binding locations.(c) Analytical (solid) and GMT (dashed) electrodynamic interaction potentials for $\xi = 0$ (black), $\xi = 0.11$ (blue), and $\xi = 0.23$ (red). The GMT curves were shifted down by 0.5 k_bT for clarity. The energy required to escape the first optical binding location (toward larger separation) for $\xi = 0$ and $\xi = 0.11$ is shown by the black and blue double-headed arrows, respectively.

binding locations, where the error bars are the 95% confidence intervals for the mean values of the fitted Gaussians (R_{OB}) (black squares connected by solid lines). The agreement between theory and experiment is very good, although the peaks the optical binding locations near 1.5λ are slightly shifted toward smaller separations than theory for all three measured phase gradients.

Figure 5.11c shows a comparison of $W(R)$ calculated with Equation 5.6 (solid lines) and our GMT simulations (dashed lines) for no ($\xi = 0$; black), moderate ($\xi = 0.11$; blue), and large ($\xi = 0.23$; red) phase gradients. The energy required to escape the first optical binding locations (toward larger separation) for $\xi = 0$ and $\xi = 0.11$ is shown as the black and blue double-headed arrows, respectively. In the limit of no phase gradient the energy minima are at integer multiples of λ, as expected. For the intermediate value of $\xi = 0.11$ the first optical binding location is at $R = \lambda$, but the work curve becomes increasingly irregular with increasing separation. The red curve corresponds to $\xi = 0.23$ and is identical to the red curve in Figure 5.10a. The location of optical binding and the magnitudes of features in the energy curve are very different from the limit of no phase gradient due to the highly asymmetric interactions predicted from Equation 5.5. In particular, the first two optical binding locations occur at $R \approx 0.8\lambda$ and $R \approx 1.5\lambda$, where the latter is in fact an unstable equilibrium separation for small phase gradients. The more rigorous GMT simulations show excellent qualitative agreement with the theoretical model, but the barrier heights are generally slightly smaller.

The results shown in Figures 5.10 and 5.11 demonstrate the symmetry-breaking effects of strong phase gradients. Whereas optical binding locations are relatively unchanged for small phase gradients, the energy landscape that embodies optical binding is dramatically changed by large phase gradients. In the context of Equation 5.5, the separation dependences of the phase difference at particles A and B diverge from one another. As ξ becomes a significant fraction of 1 the effects of this splitting becomes dramatic, as shown in Figure 5.8d. As a result, the typical periodic length-scale associated with optical binding (for no phase gradient as in Figure 5.8b) is no longer relevant. While the net force on a homodimer in the large phase-gradient regime is still modulated with distance, the distance-dependence is no longer periodic and the magnitude of the modulation is proportionally smaller due to the splitting in Equation 5.5 (see Supporting Information for example).

Our study has fundamental and practical significance in the field of optical manipulation and self-assembly [109, 96, 17]. In this letter, we addressed a fundamental question concerning the formation of optical matter arrays: How is optical manipulation of multiple particles different from optical manipulation of a single particle? Transverse phase gradients are a tunable parameter in optical trapping experiments that allow specifically tailoring the optical forces on a (trapped) particle. We have shown that these forces are dramatically altered by the presence of another nearby particle. For small phase gradients, the net force is modulated by a separation-dependent interference effect. When the phase gradient becomes strong enough, the symmetry of the interaction between nanoparticles is broken and the distances at which stable optical binding occurs change. Our findings show that tuning the phase of the incident light allows accessing a broader range of stable structures, thereby enhancing the versatility of optical binding as a means for self-assembly.

5.3 Other types of broken symmetry

In this section we will discuss two additional conditions in which symmetry is broken in optical matter systems, and show that in both cases the broken symmetry results in a net force. The first condition is for identical but anisotropic particles. Recent computational work [95] has shown that pairs of nanowires in optical traps experience a configuration-dependent net force. We will show that in the point-dipole approximation this net force is a direct consequence of anisotropic polarizability. The second condition is where the polarization of the incident light can break the symmetry between identical particles in an optical matter cluster. This effect has been observed in the literature [82], but a mechanism was not proposed. We will show that the net force arises due to electrodynamic coupling between the particles in the cluster.

5.3.1 Anisotropic particles

Anisotropic particles are represented by a polarizability tensor $\overline{\overline{\boldsymbol{\alpha}}}$ in the point-dipole approximation [34]. For an ellipsoidal particle aligned along one of the principal axes $\overline{\overline{\boldsymbol{\alpha}}}$ has three diagonal elements, $\alpha_{x_i x_i}$, and the off-diagonal elements, $\alpha_{x_i x_j}$, are zero. When the particle is rotated in the (x, y) plane by an angle θ, the new polarizability tensor is given by

$$\overline{\overline{\boldsymbol{\alpha}}}_\theta = \overline{\overline{\boldsymbol{Q}}}(\theta)\overline{\overline{\boldsymbol{\alpha}}}_0\overline{\overline{\boldsymbol{Q}}}(\theta)^T \tag{5.8}$$

where $\overline{\overline{\boldsymbol{Q}}}(\theta)$ is the rotation matrix corresponding to an angle θ. In this section We will only consider rotations in the (x, y) plane. If the particle is rotated by an arbitrary angle, the off-diagonal elements $\alpha_{x_i x_j}$ are no longer zero. Starting from Equation 2.8 and allowing one order of scattering, the electric field at the location of two ellipsoidal particles labeled A and B is

$$\begin{aligned} \overline{\boldsymbol{E}}(\boldsymbol{r}_A) &= \overline{\boldsymbol{E}}_I(\boldsymbol{r}_A) + \overline{\overline{\boldsymbol{G}}}(\boldsymbol{r}_A, \boldsymbol{r}_B)\overline{\overline{\boldsymbol{\alpha}}}_B\overline{\boldsymbol{E}}_I(\boldsymbol{r}_B) \\ \overline{\boldsymbol{E}}(\boldsymbol{r}_B) &= \overline{\boldsymbol{E}}_I(\boldsymbol{r}_B) + \overline{\overline{\boldsymbol{G}}}(\boldsymbol{r}_B, \boldsymbol{r}_A)\overline{\overline{\boldsymbol{\alpha}}}_A\overline{\boldsymbol{E}}_I(\boldsymbol{r}_A) \end{aligned} \tag{5.9}$$

where $\overline{\boldsymbol{E}}_I$ is the incident electric field. Inserting the expression for the field at $\boldsymbol{r}_A$ into equation 2.5 gives the following expression for the time-averaged electrodynamic force on particle A in the x_i direction:

$$\begin{aligned} \langle F^A_{x_i} \rangle = \frac{1}{2} Re \Bigg[& \overline{\overline{\boldsymbol{\alpha}}}^*_A \overline{\boldsymbol{E}}_I(\boldsymbol{r}_A)^* \frac{\partial \overline{\boldsymbol{E}}_I(\boldsymbol{r}_A)}{\partial x_i} + \\ & \overline{\overline{\boldsymbol{\alpha}}}^*_A \overline{\overline{\boldsymbol{G}}}^* (\boldsymbol{r}_A, \boldsymbol{r}_B) \overline{\overline{\boldsymbol{\alpha}}}^*_B \overline{\boldsymbol{E}}^*_I(\boldsymbol{r}_B) \frac{\partial \overline{\boldsymbol{E}}_I(\boldsymbol{r}_A)}{\partial x_i} + \\ & \overline{\overline{\boldsymbol{\alpha}}}^*_A \overline{\boldsymbol{E}}^*_I(\boldsymbol{r}_A) \frac{\partial \overline{\overline{\boldsymbol{G}}}(\boldsymbol{r}_A, \boldsymbol{r}_B)}{\partial x_i} \overline{\overline{\boldsymbol{\alpha}}}_B \overline{\boldsymbol{E}}_I(\boldsymbol{r}_B) \Bigg]. \end{aligned} \tag{5.10}$$

If we assume that the pair of particles lies in the (x, y) plane, and that the incident electric field is a plane-wave propagating in the z direction, the first two terms in Equation 5.10 become zero for forces in the x and y directions. The force on particle B is given by exchanging the labels A and B. If we further assume that the incident light is polarized along the x direction Equation 5.10 simplifies to (written element-wise)

$$\langle F^A_{x_i} \rangle = \frac{E_I^2}{2} \sum_{x_l=x,y,z} \sum_{x_m=x,y,z} Re\left[\alpha^{A*}_{x,x_l} \frac{\partial G_{x_l,x_m}(\boldsymbol{r}_A, \boldsymbol{r}_B)}{\partial x_i} \alpha^B_{x_m,x} \right]. \tag{5.11}$$

Equation 5.11 shows that new forces arise for anisotropic particles. If the polarizabilities $\overline{\overline{\boldsymbol{\alpha}}}^A$ and $\overline{\overline{\boldsymbol{\alpha}}}^B$ only have diagonal elements, only the term corresponding to $\alpha^A_{x,x}$ and $\alpha^B_{x,x}$ survives. Assume that the pair of particles is oriented along the y axis. In this configuration, $\frac{\partial G_{x,x}(\boldsymbol{r}_A, \boldsymbol{r}_B)}{\partial y} = 0$ and subsequently $\langle F^A_y \rangle = 0$. However, if $\overline{\overline{\boldsymbol{\alpha}}}^A$ and $\overline{\overline{\boldsymbol{\alpha}}}^B$ have off-diagonal elements, then other elements in the dyadic Green's tensor become relevant and a force in the y direction is possible.

The net force in the x_i direction, obtained by inverting the labels A and B, and adding the results to Equation 5.11. Using the fact that, due to symmetry,

$$\overline{\overline{\boldsymbol{G}}}(\boldsymbol{r}_A, \boldsymbol{r}_B) = \overline{\overline{\boldsymbol{G}}}(\boldsymbol{r}_B, \boldsymbol{r}_A) \tag{5.12}$$

and

$$\frac{\partial \overline{\overline{\boldsymbol{G}}}(\boldsymbol{r}_A, \boldsymbol{r}_B)}{\partial x_i} = -\frac{\partial \overline{\overline{\boldsymbol{G}}}(\boldsymbol{r}_A, \boldsymbol{r}_B)}{\partial x_i}. \tag{5.13}$$

The net force on a pair of anisotropic particles is

$$\begin{aligned}
\langle F^A_{x_i} \rangle + \langle F^B_{x_i} \rangle = \frac{E_I^2}{2} \sum_{x_l=x,y,z} \sum_{x_m=x,y,z} Re\Bigg[& \alpha^{A*}_{x,x_l} \frac{\partial G_{x_l,x_m}(\boldsymbol{r}_A, \boldsymbol{r}_B)}{\partial x_i} \alpha^B_{x_m,x} - \\
& \alpha^{B*}_{x,x_l} \frac{\partial G_{x_l,x_m}(\boldsymbol{r}_A, \boldsymbol{r}_B)}{\partial x_i} \alpha^A_{x_m,x} \Bigg] \\
= \frac{E_I^2}{2} \sum_{x_l=x,y,z} \sum_{x_m=x,y,z} Im\left[\frac{\partial G_{x_l,x_m}(\boldsymbol{r}_A, \boldsymbol{r}_B)}{\partial x_i} \right] * (\alpha^{A'}_{x,x_l} \alpha^{B''}_{x,x_l} - \alpha^{A''}_{x,x_l} \alpha^{B'}_{x,x_l}).
\end{aligned} \tag{5.14}$$

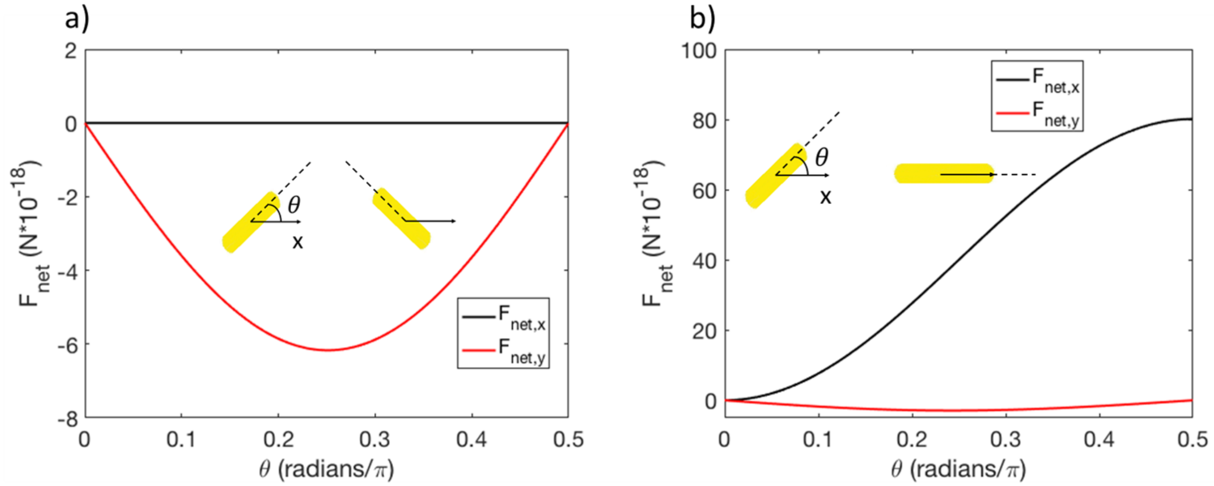

Figure 5.12: Orientation-dependent net forces on dimers of gold nanorods. (a) Net force in the x (black) and y (red) directions for a pair of rods rotated by angles θ and $-\theta$ to form a symmetric pair. (b) Net force in the x (black) and y (red) directions for a pair of rods where only one rod is rotated by an angle θ.

Equation 5.14 is a generalization of Equation 5.2 to include anisotropic polarizabilities. Non-reciprocal forces can arise either in a heterodimer ($i.e.$ $\overline{\overline{\boldsymbol{\alpha}}}_0^A \neq \overline{\overline{\boldsymbol{\alpha}}}_0^B$) or in a homodimer, where the anisotropic particles have different orientations ($i.e.$ $\overline{\overline{\boldsymbol{\alpha}}}_0^A = \overline{\overline{\boldsymbol{\alpha}}}_0^B$ but $\overline{\overline{\boldsymbol{\alpha}}}_\theta^A \neq \overline{\overline{\boldsymbol{\alpha}}}_\theta^B$).

Figure 5.12 shows the net force on a dimer of nanorods (gold; 100nm x 50nm) that are separated by 600nm for variable relative orientations and polarization in the y direction. In Figure 5.12a the rods are rotated by angles of θ and $-\theta$ so that the pair remains symmetric. The net force in the x (black) and y (red) directions are plotted. The net force in the x direction is zero regardless of the orientation of the rods. The net force in the y direction is zero when the rods are aligned with the x and y axes. When $0 < \theta < \pi/2$ there is a net force in the $-y$ direction. In Figure 5.12b one rod is rotated by an angle of θ and the other is stationary. As θ increases, the net force in the x direction increases toward a maximum at $\theta = \pi/2$, while a smaller net force in the $-y$ direction decreases for $0 < \theta < \pi/4$ and then increases back toward zero for $\pi/4 < \theta < \pi/2$.

5.3.2 Coupling-induced symmetry breaking

Nonreciprocal forces can also be the result of symmetry breaking that is induced by electrodynamic coupling depending on the symmetry of the cluster and incident field. Consider a cluster of 3 identical spherical particles labeled A, B, and C, each with polarizability α, situated arbitrarily in the transverse plane of plane-wave illumination. Allowing for one order of scattering, the polarization and electric field gradient at the location of particle A is

$$\begin{aligned} \bar{\boldsymbol{p}}_A &= \alpha(1 + \alpha\overline{\overline{\boldsymbol{G}}}(\boldsymbol{r}_A,\boldsymbol{r}_B) + \alpha\overline{\overline{\boldsymbol{G}}}(\boldsymbol{r}_A,\boldsymbol{r}_C) \\ \frac{\partial\overline{\boldsymbol{E}}}{\partial x_i} &= \alpha\left(\frac{\partial\overline{\overline{\boldsymbol{G}}}(\boldsymbol{r}_A,\boldsymbol{r}_B)}{\partial x_i} + \frac{\partial\overline{\overline{\boldsymbol{G}}}(\boldsymbol{r}_A,\boldsymbol{r}_C)}{\partial x_i}\right)\overline{\boldsymbol{E}}. \end{aligned} \tag{5.15}$$

Inserting Equations 5.15 into Equation 2.5 and summing over all particles yields the net force on the trimer

$$\begin{aligned} \langle F^A_{x_i}\rangle + \langle F^A_{x_i}\rangle + \langle F^A_{x_i}\rangle = \frac{|\alpha|^2}{2} Re\Bigg[\overline{\boldsymbol{E}}^*\Bigg(&\frac{\partial\overline{\overline{\boldsymbol{G}}}(\boldsymbol{r}_A,\boldsymbol{r}_B)}{\partial x_i} + \frac{\partial\overline{\overline{\boldsymbol{G}}}(\boldsymbol{r}_A,\boldsymbol{r}_C)}{\partial x_i} + \\ \frac{\partial\overline{\overline{\boldsymbol{G}}}(\boldsymbol{r}_B,\boldsymbol{r}_A)}{\partial x_i} + \frac{\partial\overline{\overline{\boldsymbol{G}}}(\boldsymbol{r}_B,\boldsymbol{r}_C)}{\partial x_i} + &\frac{\partial\overline{\overline{\boldsymbol{G}}}(\boldsymbol{r}_C,\boldsymbol{r}_B)}{\partial x_i} + \frac{\partial\overline{\overline{\boldsymbol{G}}}(\boldsymbol{r}_C,\boldsymbol{r}_A)}{\partial x_i}\Bigg)\overline{\boldsymbol{E}}\Bigg] + \\ \frac{|\alpha|^2}{2} Re\Bigg[\alpha^*\overline{\boldsymbol{E}}^*\Bigg[\overline{\overline{\boldsymbol{G}}}^*(\boldsymbol{r}_A,\boldsymbol{r}_B)\Bigg(&\frac{\partial\overline{\overline{\boldsymbol{G}}}(\boldsymbol{r}_A,\boldsymbol{r}_C)}{\partial x_i} + \frac{\partial\overline{\overline{\boldsymbol{G}}}(\boldsymbol{r}_B,\boldsymbol{r}_C)}{\partial x_i}\Bigg) + \\ \overline{\overline{\boldsymbol{G}}}^*(\boldsymbol{r}_B,\boldsymbol{r}_C)\Bigg(&\frac{\partial\overline{\overline{\boldsymbol{G}}}(\boldsymbol{r}_B,\boldsymbol{r}_A)}{\partial x_i} + \frac{\partial\overline{\overline{\boldsymbol{G}}}(\boldsymbol{r}_C,\boldsymbol{r}_A)}{\partial x_i}\Bigg) + \\ \overline{\overline{\boldsymbol{G}}}^*(\boldsymbol{r}_C,\boldsymbol{r}_A)\Bigg(&\frac{\partial\overline{\overline{\boldsymbol{G}}}(\boldsymbol{r}_A,\boldsymbol{r}_B)}{\partial x_i} + \frac{\partial\overline{\overline{\boldsymbol{G}}}(\boldsymbol{r}_C,\boldsymbol{r}_B)}{\partial x_i}\Bigg)\Bigg]\overline{\boldsymbol{E}}\Bigg]. \end{aligned} \tag{5.16}$$

The terms in Equation 5.16 that are proportional to $|\alpha|^2$ are two-body terms resulting from the component of the polarization due to the incident field and the field gradient due to the scattered field. The terms that are proportional to $|\alpha|^2\alpha^*$ are three-body terms resulting from the polarization due to the light scattered by a neighboring particle, and the field gradient due to the light scattered from a different neighboring particle. While the two-body

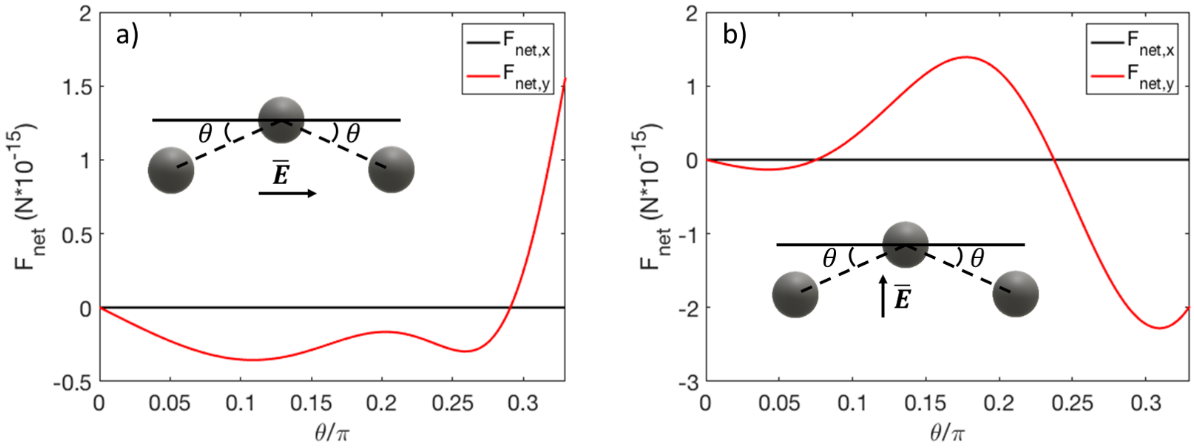

Figure 5.13: Angle-dependent net forces on trimers of silver nanoparticles. (a) Net force in the x and y directions on a trimer with the angle θ from the central particle to the two outer varying from 0 to $\pi/3$ with polarization along the x direction. (b)Net force in the x and y directions on a trimer with the angle θ from the central particle to the two outer varying from 0 to $\pi/3$ with polarization along the y direction.

terms cancel due to the symmetry of the dyadic Green's function (Equations 5.12-5.13), the three-body terms do not generally cancel. In other words, electrodynamic coupling can induce nonreciprocal forces between identical spherical particles in optical matter systems.

Figure 5.13 shows calculations of the net force on a cluster of three identical spherical particles in the point dipole approximation for x (a) and y (b) polarized incident light. The trimer starts in a linear configuration along the x axis, and is bent by a variable angle θ until it forms an equilateral triangle (at $\theta = \pi/3$). The net force in the x direction is zero for both polarizations and all angles. The net force in the y direction is 0 when $\theta = 0$, which is a consequence of the fact that $\boldsymbol{r}_A - \boldsymbol{r}_B = \boldsymbol{r}_B - \boldsymbol{r}_C$ for this configuration. As θ increases the net force in both the x and y directions is generally non-zero.

In this section we have seen that nonreciprocal forces can occur in optical matter clusters of identical particles if their polarizabilities are orientation-dependent, or as a three-body force induced by electrodynamic coupling. The multitude of ways that broken symmetry results in nonreciprocal forces and other strange phenomena in optical matter systems reflects the inherently non-equilibrium nature of optical matter systems. The work in this section approaches the problem of broken symmetry in a simplified context. However, in a real system the consequences of the types of nonreciprocal forces demonstrated here are only starting to be explored.

Chapter 6

Rearrangement dynamics in optical matter systems

6.1 Direct visualization of barrier crossing dynamics in a driven optical matter system

The following section is reproduced with permission from: Figliozzi, Patrick, Curtis W. Peterson, Stuart A. Rice, and Norbert F. Scherer. Direct visualization of barrier crossing dynamics in a driven optical matter system. *ACS nano 12, no. 6 (2018): 5168-5175.*

6.1.1 Introduction

Chemical and physical processes are commonly represented in terms of ensemble averages that provide a link between microscopic and macroscopic dynamics. While the microscopic details of a process may vary from one realization to another, one can obtain an ensemble averaged macroscopic description of the process in the form of a kinetic rate law[66, 110]. These statistical interpretations of a process do not provide detailed descriptions of individual particle motion and various deviations from an averaged macroscopic mechanism. The development of new techniques that allow chemical and physical processes to be studied on an individual event or molecule basis, together with growing realization of the ubiquity and variety of important processes that are determined by single-molecule motion, have brought "single-molecule" measurements to the forefront of the physical sciences[111, 112, 113, 114, 115, 116, 117, 118]. The many repetitions of identical experiments that characterize single particle (*e.g.* molecule) measurements replace ensemble averages with probability distributions and families of trajectories that can be used to link the single-molecule and macroscopic properties of a process and separate the common and the fluctuating contributions to the particle dynamics[119, 120].

Microscopic visualization of particles in an optical trap and the consequences of their manipulation with external fields has had a large impact in single molecule biophysics[121, 122]. Whereas most such studies use a typically micron-scale visualized particle (or AFM cantilever)[123] to report on or manipulate the molecule(s) it is attached to, nano- and meso-scale particles can be systems of investigation in and of themselves[17, 40, 114, 124, 20, 71]. Both classes of experiments, *i.e.*, reporting on cognate molecules or the particle systems themselves, can be readily repeated under uniform conditions, allowing kinetic data to be extracted. The high level of spatial and temporal detail combined with the potential to obtain a statistically significant number of repetitions in optical trapping experiments makes them an ideal system in which to study the link between the microscopic and macroscopic dynamics and kinetic behavior of a system.

In the present paper, we study the physical passing of particles in an optical ring trap and do so for different driving forces. The positions and motion of single Ag nanoparticles are measured by (darkfield) digital microscopy; precise tracking of each particle from frame to frame allows their dynamics to be studied with nanoscale detail. The large number of Ag nanoparticle trajectories measured allows obtaining a detailed kinetic description of the process. Our studies involve plasmonic nanoparticles that are confined to quasi-one-dimensional optical ring traps and subjected to a controlled driving force. These particles feel a variety of forces that can all be leveraged to change the energy landscapes and driving forces. The dynamics of particle passing, *i.e.* a sign change in the orientation of a particle pair, are influenced by the combined effect of the electrodynamic forces confining the particles to the ring trap[15], the random thermal forces expressed as Brownian motion of the particles[78], and the electrodynamic driving force that propels the particles around the ring[102].

The present experiment involving the visualization of a driven optical matter system is designed to mimic the steps of a bimolecular reaction[125]. The highly detailed experimental data allowed us to recognize and validate a two-step mechanism analogous to an exchange reaction or the Michaelis-Menten scheme for the particle passing process involving formation of an encounter complex surrmounting an energy barrier, and progressing through a transition state. The first step is found to depend on the driving force in the ring, while the second step involves a thermally activated process without a driving force dependence. We created a stochastic microscopic model that reproduces statistical distributions measured using input data from a large number of independent trajectories in order to describe the second step. The advantage offered by our system is that it allows full and explicit characterization of particle dynamics vs. the dynamics that are presumed to take place on molecular size and timescales[126].

6.1.2 Ag nanoparticle trapping and passing

Ag nanoparticles were trapped and driven in a transverse plane over a glass coverslip using an optical ring trap as described previously by Figliozzi *et al.*[73]. Briefly, an 800 nm laser was reflected from a spatial light modulator (SLM) acquiring a suitable phase-encoded profile *i.e.* Bessel function and an azimuthal phase gradient to create an optical ring trap when focused by a microscope objective (Olympus 60x water). The power of the optical beam after the SLM and before the back aperture of the objective was 40 mW. A strong scattering force caused the 150 nm diameter Ag nanoparticles to be held close to the glass surface balanced by electrostatic repulsion of the charged particles from the charged glass surface. An azimuthal phase gradient in the optical ring trap caused the nanoparticles to be driven[102] around the trap along a quasi-one-dimensional path. (Figure 6.1a). The driving force in the optical ring trap was controlled by the topological charge l (the number of 2π phase wrappings in one complete circuit around the ring) of the ring trap, which was varied from $l = 1$ to $l = 5$ in the present experiment.

Figure 6.1a shows an image (raw data) of two Ag NPs in the trap. The arrow indicates their direction of directed motion. The laser power was lower in the present experiments compared to optimal trapping conditions in our previous study[73] to reduce the strength of the radial confinement of the Ag NPs. As a result, particles in the trap travel around the ring at a slower rate and have a wider radial distribution due to the diminished transverse intensity gradient force. They can undergo Brownian fluctuations in the radial direction and can pass each other due to radial position fluctuations, as shown in the inset to Figure 6.1a. The trajectories of the Ag nanoparticles in the optical ring trap are naturally described in a polar coordinate system, r and θ, as shown in Figure 6.1a. The polar coordinates for each experiment were calculated by using a least squares routine to fit a circle of radius r_0 to the positions of all Ag NPs accumulated over a single experiment for a given value of l[127].

We define a passing event using a relative coordinate system, $\Delta r = r_2 - r_1$ and $\Delta\theta = \theta_2 - \theta_1$ where the subscripts 1 and 2 refer to the particles that are initially leading and trailing,

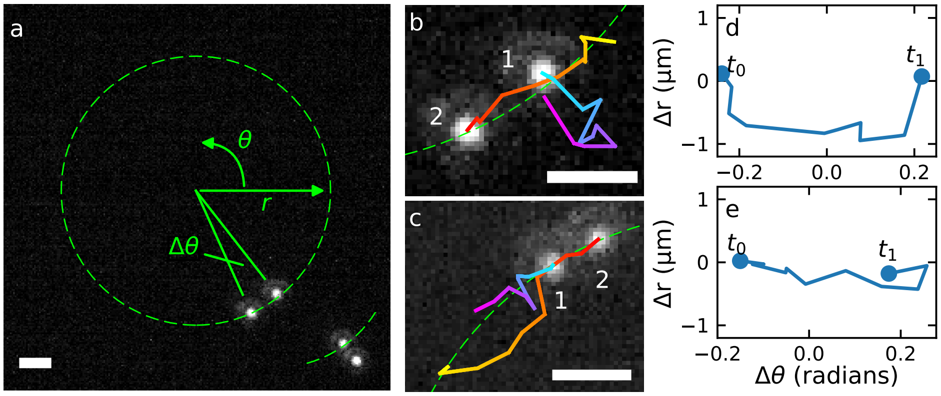

Figure 6.1: A pair of Ag nanoparticles in an optical ring trap and representative passing events that can occur. (a) Two Ag nanoparticles in a ring trap (dashed circle) with radius $r_0 = 4.5\mu m$. The inset shows part of an image recorded at a slightly later time where one of the particles has fluctuated off the ring. The coordinates r and θ are also shown in a. The driving force is in the counter-clockwise direction. (b,c) Two examples of passing events (each at $L = 5$ and $\approx 0.1s$ in duration) with the changing color on the particle path representing time propagation. In (b) the leading particle fluctuates away from the radius r_0 of the ring trap, while in (c) the trailing particle fluctuates from the ring trap and simultaneously passes the leading particle. (d,e) Trajectories of the passing events shown in (b) and (c), respectively, in terms of relative coordinates $\Delta\theta$ and Δr.

respectively. A passing event occurs when there is a sign change in $\Delta\theta$. In general, a particle pair takes a random path through the two dimensional coordinate space $(\Delta r, \Delta\theta)$ during such an event. Figure 6.1b shows the trajectories of both particles in a pair during a passing event. The chronological evolution of each particle's motion is encoded in color (red to yellow and magenta to blue for the trailing and leading particles, respectively). In this example the leading particle (in the direction of the applied driving force) fluctuates radially away from the mean radius r_0 of the ring trap while the trailing particle remains near r_0 and passes the lead particles driven by the applied optical force. A second passing event, along with individual particle motions, is shown in Figure 6.1c. Note that in this example the trailing particle passes around the leading particle.

The trajectories of the passing events shown in Figures 6.1b,c are shown in terms of $(\Delta r, \Delta\theta)$ in Figures 6.1d and e, respectively. The trajectories of passing events always start with $\Delta\theta < 0$ and progress to $\Delta\theta > 0$ because the relative coordinate system is designed with the leading particle at the origin. The beginning and endpoints of the trajectory in $(\Delta r, \Delta\theta)$ are indicated in Figure 6.1d and e by the time points t_0 and t_1, respectively.

If each passing event is defined as a particular trajectory through the two-dimensional coordinate space $(\Delta r, \Delta\theta)$, the dynamics of the process will depend on the probability $P(\Delta r, \Delta\theta)$ of finding the system at a specific point in this space. Figure 6.2a shows this probability distribution for data aggregated over all experiments. We see that it is most likely to find Δr near zero for $\Delta\theta > 0.1 rad$, which corresponds to a chord length of 600 nm. This distance is associated with the expected separation for the electrodynamic interaction known as *optical binding* at $\sqrt{\Delta r^2 + (r\Delta\theta)^2} \approx \lambda_{incident}/n$,[13, 15, 16] where n is the index of refraction of the medium ($n = 1.33$ in water). However, it becomes extremely unlikely to find Δr near zero for smaller values of $\Delta\theta$ due to electrostatic and electrodynamic repulsion between the charged Ag NPs[128]. Moreover, the particles never overlap in the images (videos) meaning they do not pass over each other in the axial direction of laser propagation. Therefore, for $\Delta\theta$ to be near zero at least one of the particles must be displaced off the ring (away from r_0), and the passing process is 2-dimensional.

Figure 6.2b shows a subset of the total probability density function (PDF) $P_{passing}(\Delta r, \Delta\theta)$ obtained by selecting only trajectories from a 30 frame window centered on each passing event. Applying this condition does not change the qualitative features of the PDF. The mean paths of the passing events (aggregated over all experiments, which were separated depending on whether Δr is positive or negative at $\Delta\theta = 0$, are shown in red. These mean paths emphasize that the Ag NP passing process involves changes in both Δr and $\Delta\theta$. Figure 6.2c shows a scatter plot of the points $(\Delta r, \Delta\theta)$ within a 30 frame window with the passing event at the center with the mean path through $(\Delta r, \Delta\theta)$ separated according to low (blue), medium (orange), and high (green) driving forces. The driving force appears to have, at most, a small effect on the mean path the system takes through $(\Delta r, \Delta\theta)$ during a passing event.

6.1.3 Mechanism for passing

We have discussed the nanoparticle passing process in terms of quantities averaged over many trajectories. Because we have access to individual trajectories, however, it is possible to deduce a mechanism or mechanisms by which the passing occurs. Since Δr must deviate from 0 for a passing event to occur, it is important to determine the typical radial fluctuations of both particles involved in the event. Figure 6.3a show two likely mechanisms for the passing. In scheme I, the leading particle momentarily jumps away from the mean radius r_0 of the trap and the trailing particle then passes it. Conversely, in scheme II, the trailing particle jumps away from the mean radius r_0 of the trap while simultaneously passing the leading particle. In both of these schemes, only one particle fluctuates radially away from r_0. The trajectories shown in Figure 6.1 b and c respectively reflect schemes I and II.

Figure 6.3b shows a conditional separation of the PDFs of particle pair deviations from the ring trap at the time of passing combining events measured for all values of l. The PDFs are separated into two groups corresponding to the particle in the pair that is closer to r_0 and the particle that is further from r_0 at the time of the passing event. The particle closer to r_0 is approximately Gaussian distributed in Δr, while the particle further from the trap has no probability density at r_0. This result indicates that in the majority of passing events only one particle fluctuates radially while the other remains confined to the mean radius, r_0, of the ring. Figure 6.3c shows a different conditional separation of the particle radial deviation PDFs into two groups corresponding to the particles in the pair that are initially leading and trailing. This alternative condition results in slightly different PDFs compared to those shown in Figure 6.3a, implying that either the leading or trailing particle can be the one to fluctuate radially away from r_0, as depicted in schemes I and II in Figure 6.3a.

To estimate the prevalence of each schemes shown in Figure 6.1a, we re-mixed the PDFs in Figure 6.3b in different proportions according to the relationship

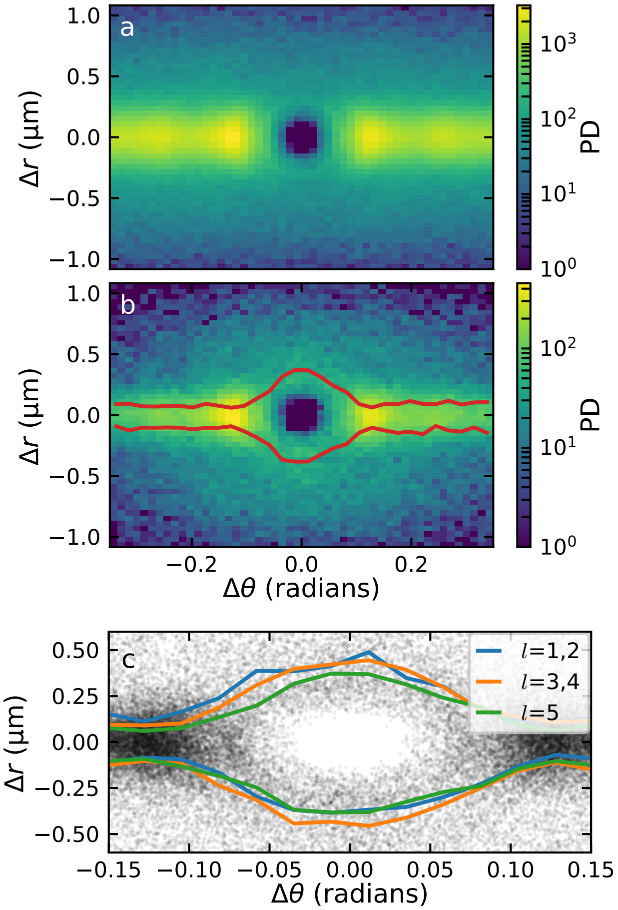

Figure 6.2: Probability density in relative coordinates $(\Delta\theta, \Delta r)$ and most probable paths for passing. (a) Total probability density over all experiments for all driving forces. (b) Conditional probability density in 30 frame windows centered on each passing event, over all experiments for all driving forces. (c) Scatter plot of points obtained from the same condition used in (b), with colored lines depicting the mean path of particles through $(\Delta\theta, \Delta r)$. Note that $\Delta\theta = 0.13rad = 600nm$ chord length so the regions of high point density correspond to optical binding.

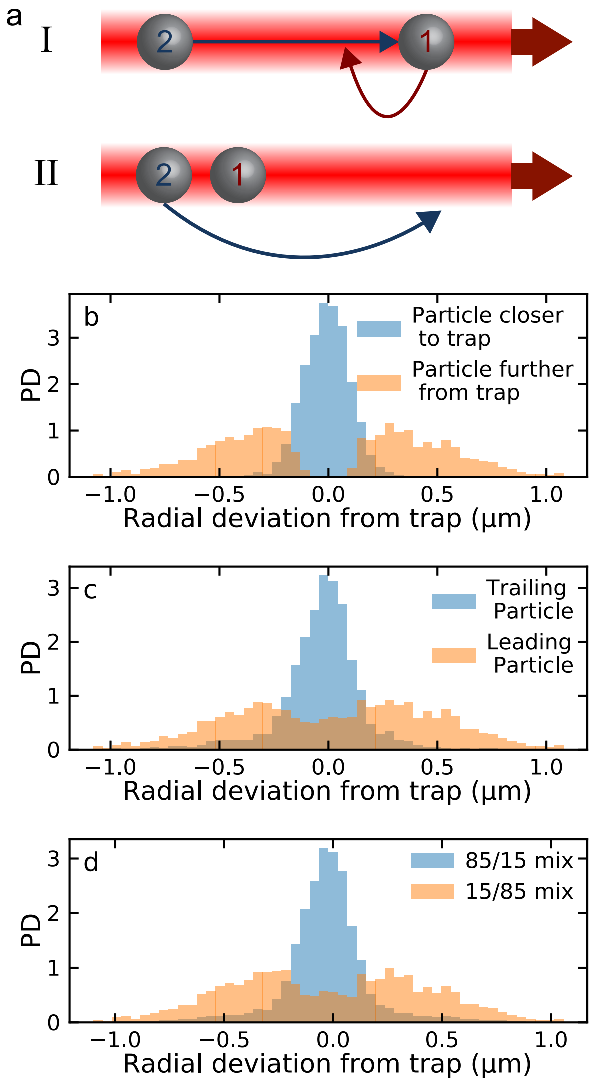

Figure 6.3: Two possible passing schemes and their related probability distributions. (a) Two possible schemes by which passing events take place. Scheme I is related to Figure 6.1b where the leading particle fluctuates away from the ring trap while the trailing particle moves past it. Scheme II is related to Figure 6.1c where the trailing particle fluctuates away from the trap and passes the leading particle. (b) PDFs of particle pair deviations from the ring trap during passing events for all values of l for the particle closer to (blue) and further from (orange) r_0 at the time of passing. (c) PDFs of particle pair deviations from the ring trap during passing events for all values of l for the particle trailing (blue) and leading (orange) just before the event. (d) Remixing of the PDFs in (b) *via* Equation 6.1 with $C_{11} = C_{22} = 0.85$ and $C_{12} = C_{21} = 0.15$.

$$\begin{aligned} P_1' &= C_{11}P_1 + C_{12}P_2 \\ P_2' &= C_{21}P_1 + C_{22}P_2 \end{aligned} \tag{6.1}$$

where P_1 and P_2 are the PDFs of the particles closer to and further from r_0 in Figure 6.3b, respectively, while P_1' and P_2' are the PDFs for the trailing and leading particles. The C_{ij} are the coefficients that determine the proportion of the mixing. Mechanistically, the diagonal elements in C_{ij} correspond to scheme I, while the off-diagonal elements correspond to scheme II. Figure 6.3d shows the histograms obtained when $C_{11} = C_{22} = 0.85$ and $C_{12} = C_{21} = 0.15$, which gives the best match between Figure 6.3c and d. Therefore, the passing events occur 85% of the time *via* scheme I and 15% of the time *via* scheme II .

6.1.4 Electrodynamic interactions and potentials of mean force

We now turn to the question of how passing events depend on the electrodynamic interactions between particles, and the electrodynamic potential created by the ring trap. One important type of electrodynamic interaction between trapped particles is optical binding [15, 13], which results from the incident electric field interfering with the scattered electric field from each particle. In our experiments the polarization state of the trapping beam is horizontal in the laboratory frame aligned along the 0 to π coordinate of the ring shown in Figure 6.1a. The optical binding interaction is strongest between nanoparticles oriented perpendicular to the polarization.

We simulated the optical binding potential in the optical ring trap by starting from the pair-wise electrodynamic potential[17] obtained from finite difference time domain (FDTD) simulations and extending these results around a circle of the same radius as the experimental ring trap and weighting it by the measured probability of finding a particle at each θ position on the ring (this probability is modulated by varying speed in different sections of the ring for linear polarization[73]). Figure 6.4a shows this estimated optical binding potential for a pair of Ag NPs around the ring trap. The optical binding interaction is most likely to stabilize a particle position away from the ring near $\pi/2$ and $3\pi/2$, and the interaction is symmetric about these points.

The actual tightness or looseness of single Ag NP confinement created by the optical ring trap in the radial direction is visualized in Figure 6.4b, which shows all single particle trajectories in an experiment ($l = 5$). It is apparent that deviations from r_0 are much more common near $2\pi/3$ and $5\pi/3$ compared to $\pi/3$ and $4\pi/3$. The reason for diminished confinement in these regions is a slight astigmatism introduced to the phase function on the SLM used to create the optical trap[129, 29]. Therefore, recording the θ locations of all the passing events allows ascertaining whether passing behaves as a concerted rotation of the optically bound particle pair or as spontaneous radial fluctuations in the regions of reduced confinement.

The distribution of passing events with respect to θ shown in Figure 6.4c indicates that passing events have maximum probability density near $2\pi/3$ and $5\pi/3$ and minimum probability density near $\pi/3$ and $4\pi/3$. This distribution is clearly dominated by the reduced radial confinement effect depicted in Figure 6.4b compared to the electrodynamic binding of Figure 6.4a. Another experiment performed with clockwise (reversed) rotation ($l = -5$) shows a very similar θ-dependent probability of passing to that shown in Figure 6.4c. This rules out any possible memory-dependent effects on the location of passing. Therefore, somewhat surprisingly given the obvious presence of optical binding in Figure 6.2c, the single particle dynamics are much more important than interactions between particles with regard to the passing mechanism.

The θ-dependent probability of passing reflects a barrier to the passing process whose height depends on the angular position of the particles in the ring. We can construct a potential of mean force (PMF) in the $\Delta\theta$ coordinate in the vicinity of a particular value of θ, denoted as θ_0 by considering the conditional probability distribution $P(\Delta\theta|\theta \in [\theta_0 - \delta, \theta_0 + \delta])$; *i.e.*, the probability distribution of the angular separation $\Delta\theta$ given that the θ position of a particle pair is within some range $\pm\delta$ of θ_0, the point of interest on the ring. Figure 6.4d shows the conditional PMF with θ_0 at the centers of the red (high passing probability) and purple (low passing probability) regions in Figure 6.4c. The increased rate of passing near $2\pi/3$ and $5\pi/3$ compared to $\pi/3$ and $4\pi/3$ corresponds to a barrier that is about 1.5 k_BT lower in the regions of high passing probability compared to the low probability regions. Since this free energy landscape more closely resembles Figure 6.4b compared to Figure 6.4a it is consistent with the second step in the mechanism for passing depending primarily on the single-particle potential of the optical trap rather than on interactions between particles.

It is possible that at high enough laser intensity, a different mechanism that depends on electrodynamic interaction between particles could become dominant. The single-particle trapping potential will become steeper in the radial direction at higher laser intensity, thus reducing the probability of large enough fluctuations from r_0 to allow passing events to happen. Conversely, optical interaction between particles will be stronger. However, exploring such a crossover is beyond the scope of this paper.

6.1.5 Analogy to bimolecular mechanism

Since the particles are being driven around the ring trap, elucidation of the mechanism for particle passing requires considering the effect of the electrodynamic driving force. Figure 6.5a shows the rate of events (per second) for driving forces increasing from $l = 1$ to $l = 5$. Since the data are collected from many experiments that have different numbers of particles n (*i.e.* $n = 2 - 6$ particles in the ring at the same time), the rates are normalized by the combinatorial number of possible particle pairs in a given experiment

$$\binom{n}{2} = \frac{n!}{2!(n-2)!} \tag{6.2}$$

where n is the number of particles in a given experiment. Figure 6.5a shows that the total event rate increases with with driving force. An increase in reaction rate with increasing driving force is predicted by both Arrhenius (or transition state) theory [130] and Kramers

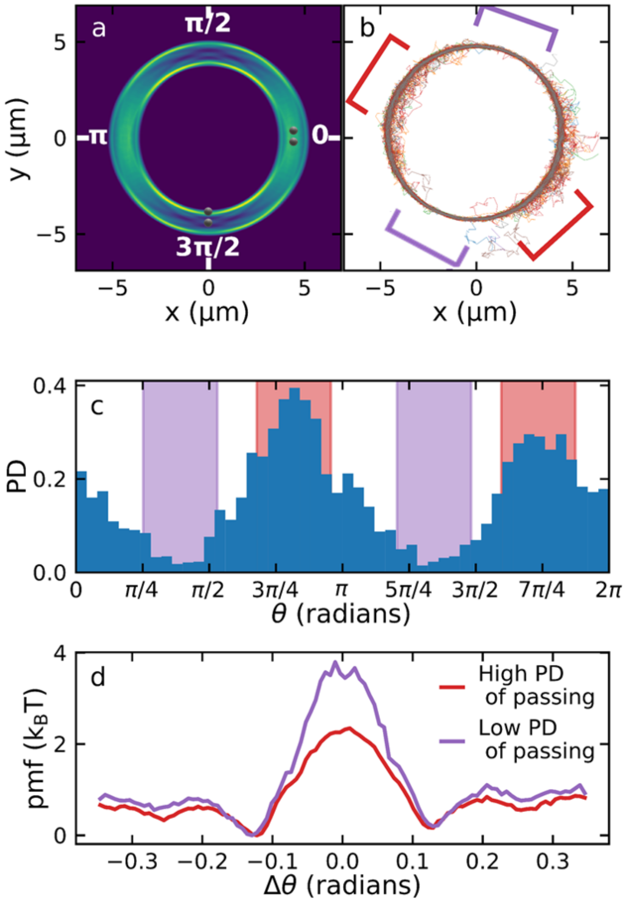

Figure 6.4: Factors that can affect the passing event location and barrier height changes for the passing process. (a) Simulated optical binding potential obtained by extending the pair-wise electrodynamic potential for a particle with fixed optical polarization to the pair on a circle of the same radius as the experimental ring trap, and weighting it by the probability of finding a particle at each θ position on the ring. These θ-dependent electrodynamically preferred orientations of Ag nanoparticle pairs are shown schematically. (b) Superposition of single Ag NP trajectories for a representative experiment. Radial fluctuations away from r_0 are much more likely at $2\pi/3$ and $5\pi/3$ compared to $\pi/3$ and $4\pi/3$. The red and purple shading denotes regions of high and low passing event probability, respectively. (c) Probability density of passing events vs. angular position on the ring trap. (d) Potential of mean force (pmf) in coordinate $\Delta\theta$ in areas of high (red) and low (purple) probability of passing event occurrence.

theory[131]. However, since these theoretical descriptions were formulated for simple reaction mechanisms with single steps, it is necessary to establish a reaction mechanism to understand the increase in the "reaction" rate in our experiments.

To do this, we introduce a two step process analogous to a bimolecular exchange reaction or the Michaelis-Menten scheme

$$A + B \rightleftharpoons AB \rightleftharpoons AB^{\ddagger} \rightarrow B + A \tag{6.3}$$

where $A + B$ are the two separated particles in their original (spatial) order, AB is the particle pair once they are within a certain distance (*i.e.* an optically bound pair that is analogous to an encounter complex), $AB^{\ddagger}$ is the structure at the transition state, and $B + A$ is the separated particle pair after the passing event with exchange of orientational order. In this mechanism, the total rate depends both on the formation of a particle pair (encounter complex), and an activated process to progress from the encounter complex to the reordered pair (product). The rate of the first step, forming the complex, should depend on the total number of particles, and we have accounted for it being proportional to the number of possible particle pairs by using equation 6.2. In general, each particle is driven around the ring at slightly different speeds because of the slight polydispersity of our nanoparticle sample ($d = 148nm \pm 5nm$). The differential speed of each particle contributes to the total rate of the first step. The particle-sizing measurements are detailed in the Supporting Information of Sule *et al.*[20]

Although it is likely that the first step of the mechanism equation 6.3 is drive force-dependent, it is not immediately obvious if the second step also has a driving force dependence. To address this, we consider the kinetics of the second step more closely. Figures 6.5b-d shows the distance traveled by a particle pair (within a certain threshold distance) from formation to completion of the passing event, and Figures 6.5e-g show the corresponding distribution of event times from pair formation to completion. The event time distributions show that once the particle pair is formed the process follows an exponential rate law that is not affected by driving force.

Figures 6.5e-g show exponential fits of experimentally measured lifetime distributions, which indicates the second step is a first order kinetic process described by

$$\frac{dP(AB)}{dt} \propto e^{-kt} \tag{6.4}$$

where k is the characteristic rate constant of the process and $P(AB)$ is the survival probability of the encounter complex. It is important to note that the distribution of Δt_i does not appreciably change with drive force, and consequently Δt_i were sampled from the same distribution obtained by averaging over results for all driving forces. To test the hypothesis that once the encounter complex is formed the kinetics of the process no longer depend on driving force, we created a simple stochastic model for travel distance

$$d_i(v(l), D, \Delta t_i) = N(v(l)\Delta t_i, 2D\Delta t_i) = v(l)\Delta t_i + \sqrt{2D\Delta t_i}N(0,1) \tag{6.5}$$

where d_i is the distance traveled in a particular realization of the process, v is the driving force-dependent drift speed of a particle in the ring trap measured from experimental data, D is the diffusion constant of a particle in the ring trap, $N(0,1)$ is a random variable with a normal distribution with zero mean and variance of 1, and Δt_i is the lifetime of the encounter complex, which is an exponentially distributed random variable. We ran 10000 realizations of this process. The resulting PDFs, shown as red curves in Figures 6.5b-d, closely match our experimental data, validating our simple stochastic model.

While the total rate of the passing event process increases with driving force, our simulations show that once the encounter complex, AB, is formed the driving force-dependence disappears. This implies that the driving force-dependence is contained completely in the first step in equation 6.3. In the language of chemical reactions, increasing the driving force has an effect analogous to increasing the frequency of encounters between reactants (*e.g.* enzyme and substrate) without affecting the energetics of the ensuing reaction. This is in contrast to theories commonly employed to predict the effect of a driving force on the rate of

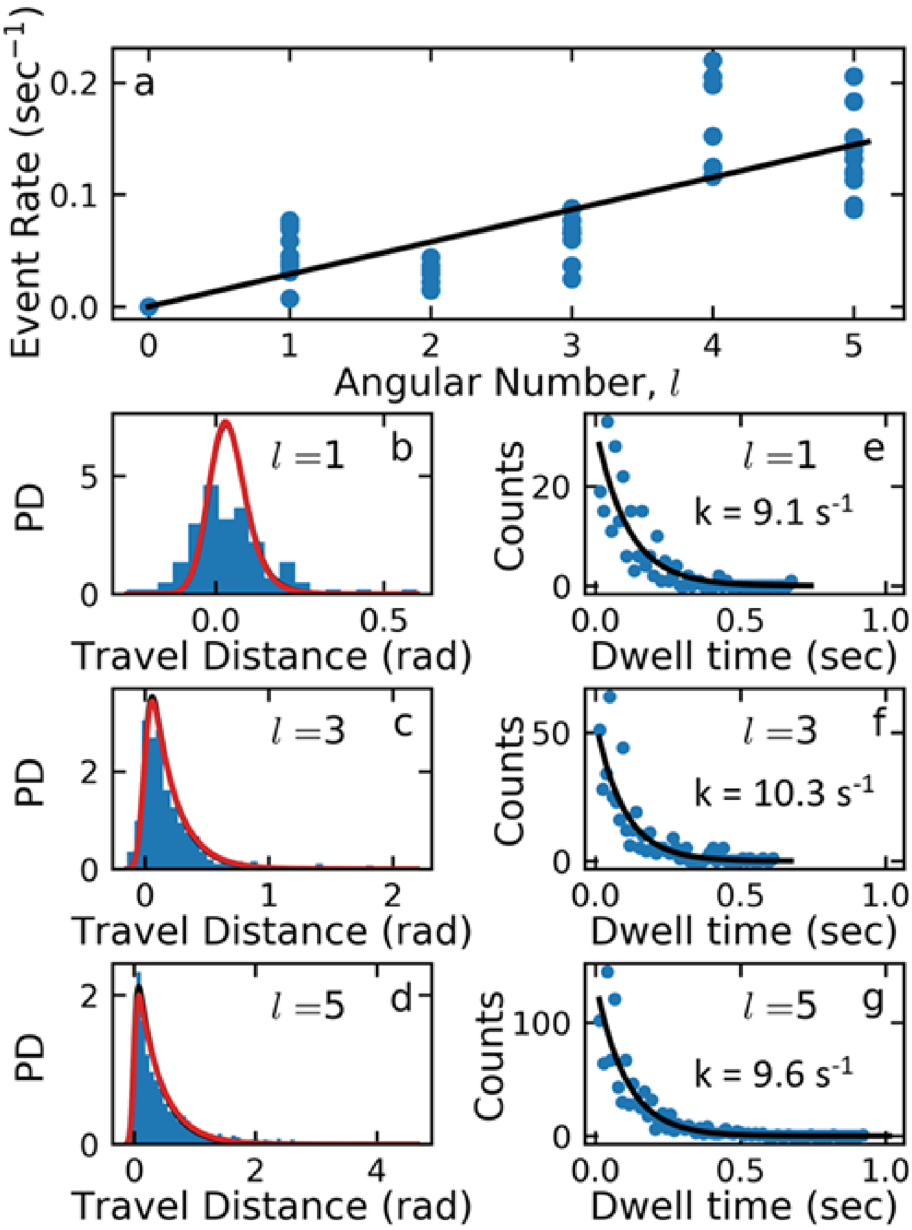

Figure 6.5: Kinetics of passing events and relation to a two-step stochastic mechanism. (a) Rate of passing events vs. driving force. (b-d) Distance traveled by a particle pair from formation to completion of the passing event. The solid red curves are theoretical histograms simulated *via* equation 6.5. (e-g) Distributions of event times from start to finish corresponding to the events in (b-d). Fitted rate constants are given in each panel.

a reaction, where the driving force induces a tilt in the free energy surface that lowers the effective barrier of activation of the reaction[130, 131].

The mechanism of our Ag NP passing event process has now fully taken shape. In the first step two particles must approach each other to form an encounter complex. This encounter complex is at an optical binding separation of a particle pair. In fact, the dense collection of points in Figure 6.2c at $\Delta\theta = -0.12 rad$ reflects this initial complex. The rate of formation of the encounter complex depends both on the number of particles (through equation 6.2) and the drive force at as seen in Figure 6.5a. Once the optically bound encounter complex is formed, completion of the subsequent activated process obeys an exponential rate law. We conclude from Figure 6.3 that typically only one particle fluctuates radially away from the ring trap, and most (85%) of the time the front particle is the one which undergoes this fluctuation. From the propensity for only a single particle to fluctuate radially away from r_0 and the kinetic data in Figure 6.5, it is apparent that the rate of the first order kinetic process is simply due to thermal forces pushing one of the particles out of the trap, as suggested in the schemes of Figure 6.3.

6.1.6 Barrier Crossing and Recrossing

High time and spatial resolution in optical trapping experiments allows for determination of detailed trajectories through a barrier region, as seen in Figure 6.6 a and b. While most passing event trajectories resemble those shown in Figure 6.1 and Figure 6.6a,b, that is, single barrier crossing events, we also observe barrier recrossing. Figure 6.6c,d shows a passing event that involves multiple crossings before the process is complete. A number of trajectories exhibit such barrier re-crossing, implying that a more accurate analysis of this electrodynamically driven nanoparticle system should include a correction to transition state theory.

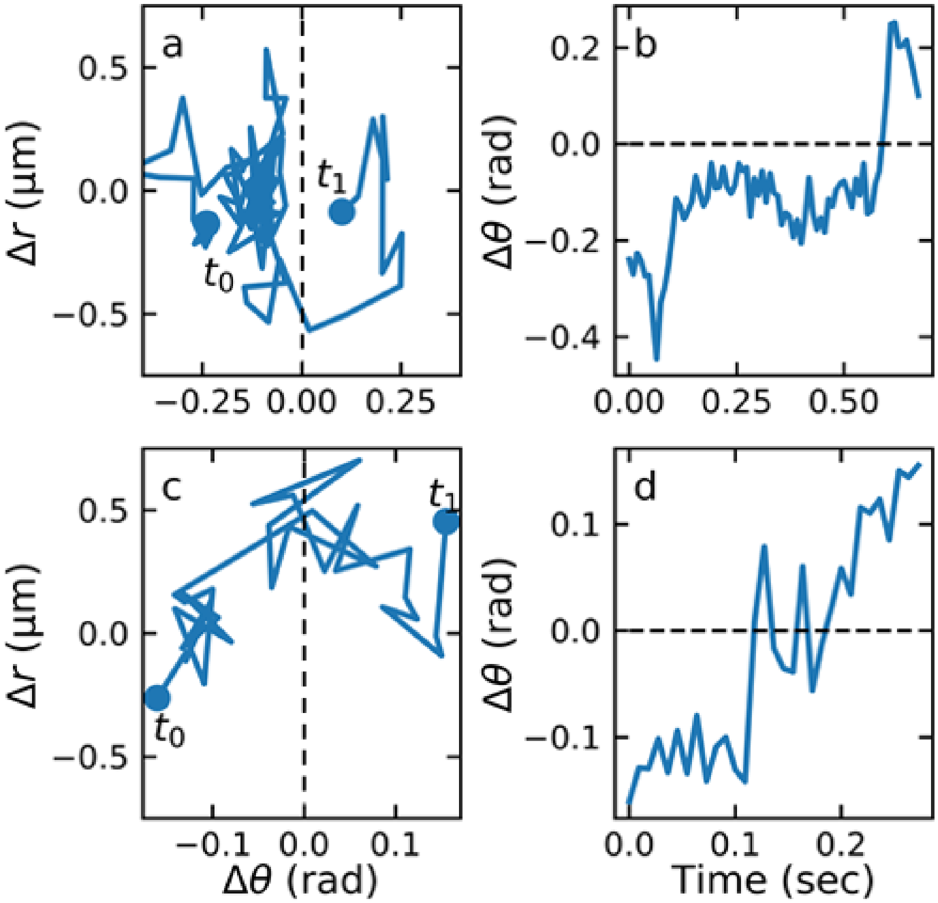

Figure 6.6: Barrier recrossing from detailed trajectory information available in optical trapping experiments. (a,c) Two trajectories that show significant waiting times in coordinates ($\Delta\theta$,Δr). (b,d) Trajectories from (a,c) in coordinates (t,$\Delta\theta$). Barrier recrossing about $\Delta\theta = 0$ is evident in (d).

6.1.7 Conclusion

Transition paths in thermally activated processes such as protein and DNA folding have only recently been related[118], but the reaction coordinate was inferred from the position of beads connected to the molecule of interest using a handle (*e.g.* ds-DNA). The response of both of these extraneous portions of the the experimental system are convoluted with the molecular signal of interest, complicating the experimental analysis[132]. In experiments where the system of interest is directly observed, dynamics and the reaction coordinate are also directly determined, eliminating these complications. Optical trapping experiments have the potential to explore questions regarding non-equilibrium transport at a single-particle level due to their ability to shape both conservative and non-conservative force fields.

We studied individual passing events of pairs of Ag nanoparticles in an optical ring trap with a controlled adjustable driving force. Our detailed and precisely localized trajectory data measured over many realizations of this process along with stochastic model simulations allowed identification of a detailed mechanism casting this problem in close analogy with bimolecular exchange reactions in solution. The passing event process is also analogous to a Michaelis-Menten scheme with an intermediate complex followed by barrier crossing as described by equation 6.3 but where the rate of reaction (passing events) increases with driving force. Our detailed trajectories reveal a two-step mechanism where the driving force increases the rate of the first step, while the second step is independent of driving force. Surprisingly, the second step is thermally activated barrier crossing of the encounter complex formed in the first step. The exponentially distributed survival probability of the encounter complex implies that the second step is a first order kinetic process, *i.e.* there is a constant probability density at any given time that the reaction will progress to completion, so the two-step characteristic of the passing process is crucial to the explanation of this type of driving force-dependence. Furthermore, the decay rate of this survival probability does not depend on the azimuthally directed driving force, which suggests that the reaction coordinate for this step lies significantly in the radial (Δr) direction that is orthogonal to the

θ and $\Delta\theta$ aspect of passing. Finally, the level of detail available in nanoparticle visualization experiments allowed direct observation of barrier recrossing. However, we do not treat this phenomenon in detail in this paper.

The present paper is the initial report of this approach to study barrier crossing phenomena. Many variations and interesting situations are envisioned for future studies. Optical traps can be shaped with high precision to design conservative and nonconservative forces, and strong inter-particle forces related to optical binding can be utilized to study the effects of interaction in these potentials. Therefore, experiments can be designed to extend our approach to other chemical and physical processes by tailoring specific forces and interactions to reflect the behavior in an analogous system or to examine idealized theoretical scenarios.

6.1.8 Methods

Experimental The experiments were preformed with 150nm diameter Ag nanoparticles (NanoXact Silver KJW1882 0.02 mg/ml) held and driven in an optical ring vortex as previously described[39, 73]. The 800 nm beam from a Ti-Sapphire laser is phase modulated with a spatial light modulator (SLM; Hamamatsu X10468-02) to produce the optical ring vortex [27, 39]. The experiments used ∼45 mW beam power going into the back aperture of the microscope objective. Citrate capped 150 nm Ag nanoparticles (NanoComposix) are diluted 200x in Nanopure water and placed into a sample chamber as described previously[73]. The scattering force of the laser applied to the nanoparticles pushes them very close to the glass-water interface of the top coverslip of the fluid well. The nanoparticles are held in one plane perpendicular to the optical axis due to a balance of the scattering force and the electrostatic repulsion the particles have with the electrically charged glass surface [73]. The Ag nanoparticles are trapped and driven around the optical ring with a drive force determined by the number of azimuthal phase wrappings, l, applied in the phase modulation pattern on the SLM. The motion of the Ag nanoparticles is visualized *via* darkfield microscopy and captured with a sCMOS camera (Andor Neo) at 110 frames per second. A variety of different experiments were performed at different l's with each one consisting of 45 s–90 s (5000 to 10,000 frames) of video. In order to resolve distinct particle shapes without blurring or distortion a camera exposure of 2×10^{-3} s to 6×10^{-4} s was used when capturing video.

Particle Tracking Particle trajectories were extracted from the video data using the Python particle tracking software package TrackPy [127]. A cluster tracking algorithm in TrackPy is used to accurately track the nanoparticles even when two or more nanoparticles become part of a cluster [133]. The optimal parameters for each experiment were determined by hand and were set so that the number of particles identified in each frame is consistent with the number of particles in the experiment. Frames where the focus drifted were removed from particle tracking as the particle tracking algorithm would find false positives in the de-focused image of the particles. However, this method of particle localization uses the center-of-mass method which can lead to significant errors especially when particles come in close proximity, and the SPIFF algorithm was used to alleviate these errors[76, 22]. A refinement algorithm was used that improves the accuracy of the positions of the particles by performing a non-linear least-squares (NLLS) fit of a Gaussian function to each distribution of pixel intensities for each nanoparticle. This allows extracting the particle positions with much greater accuracy especially in the case of overlapping features.

6.2 Collective coordinates in optical matter systems

We saw in Section 6.1 that the process of one particle passing another in a driven ring trap is analogous to a two-step chemical reaction. In this section we will show how the concept of a reaction coordinate can be generalized to include structural transformations in optical matter systems. Figure6.7 shows a common structural transformation for a 2D optical matter cluster, namely the transition from the triangle configuration (a) through a transition state (b) and to the chevron configuration (c).

To determine whether the transition shown in Figure 6.7 typically follows a well-defined

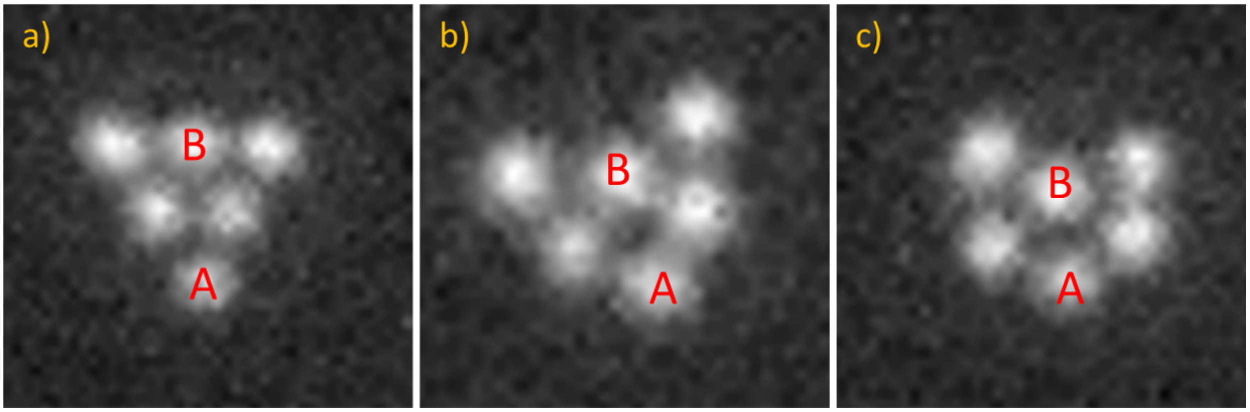

Figure 6.7: Structural transition from the triangle cluster to the chevron cluster (a) Triangle cluster. The distance between the particles labelled A and B serves as a reaction coordinate. (b) Possible transition state between triangle and chevron clusters. (c) Chevron cluster.

path, we used the lattice fitting algorithm described in Section 2.2.2 to eliminate the translational and rotational degrees of freedom from simulated and experimental trajectories containing the transition. The first step is to detect the cluster types as described in Section 2.2.2. Once the cluster types are detected, the set of all positions where the triangle and chevron are detected have to be positioned and oriented so that they reflect changes in the internal degrees of freedom, and not the translational or rotational degrees of freedom. The translation freedom is eliminated by subtracting the center of mass of each frame or timestep from all of the positions. The rotational freedom is eliminated by measuring the angle between specific sites of the best-fit lattice in each frame, and rotating the particle coordinates about their center of mass to compensate for the measured angle of the lattice. For more details, see full analysis code in Appendix B.

Figure 6.8 shows the distributions of translated and rotated particle coordinates conditioned on the distance between the two particles marked A and B in Figure 6.7 for a 55000 frame simulation (a-c) and a 1000 frame experiment (d-f). Figure 6.8 a and d show the particle positions of the triangle configuration. The tightness of the spots verifies that the rotation and translation of the particle coordinates worked properly. Figure 6.8 b and e show the distribution of particle positions when the distance between the particles marked A and B is near halfway between its value for the triangle and chevron configurations. The

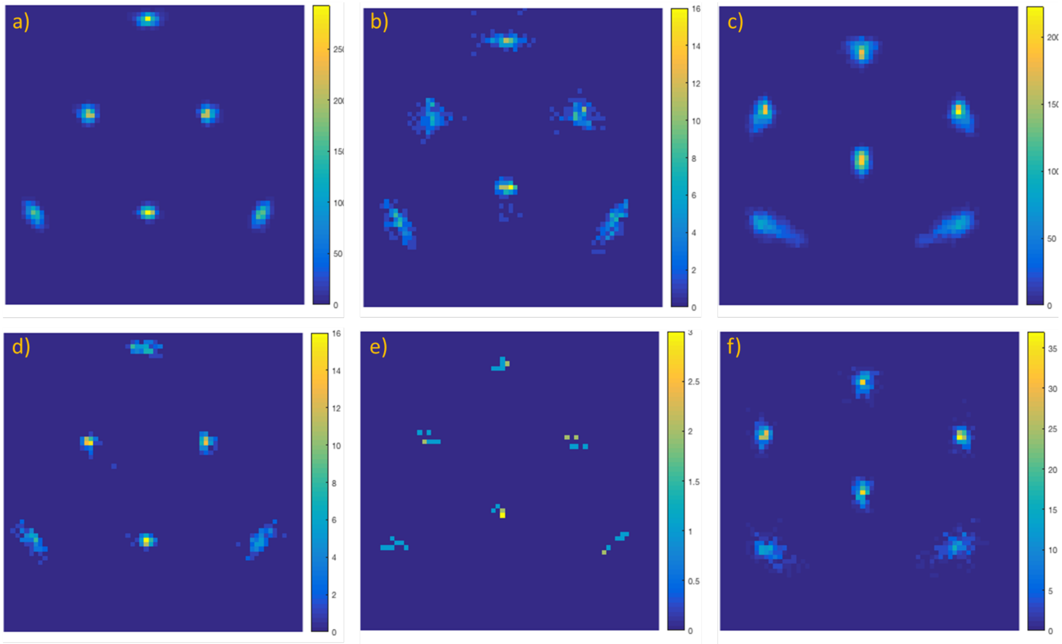

Figure 6.8: Translated and rotated particle positions for (a) the triangle, (b) the transition state, and (c) the chevron clusters.

number of total counts is significantly lower in this region, consistent with the notion that the distributions reflect a transition state. The positions of the particles are spread out compared to the triangle configuration. Figure 6.8 c and f show the distribution of particle positions for the chevron configuration. The blurring of the bottom two spots corresponds to the detection of the five-fold symmetric cluster discussed in section 4.1.

Figure 6.8 suggests that the deviations of the particles from the corresponding lattice sites are correlated. If the deviations are i.i.d. Gaussian the sum of squared deviations ($\Delta^2 = \sum_i \delta_i^2$) is expected to follow the $\chi^2(2N-4)$ distribution. Figure 6.9a shows the cumulative distribution functions of $\frac{\Delta^2}{\sigma^2}$ for 6-particle GMT-LD simulations conducted at a range of laser powers conditioned on the triangle being detected. The CDF of $\chi^2(8)$ is plotted in black. The inset a plot of the CDF of $\frac{\Delta^2}{\sigma^2}$ (red diamonds) and the CDF of $\chi^2(8)$ for comparison. For the simulation with $20mW$ (blue) the scaled error CDF is in excellent agreement with the $\chi^2(8)$ distribution. As laser power increases the tails of the scaled error CDF's extend toward larger and larger values. Figure 6.9b shows the cumulative distribution

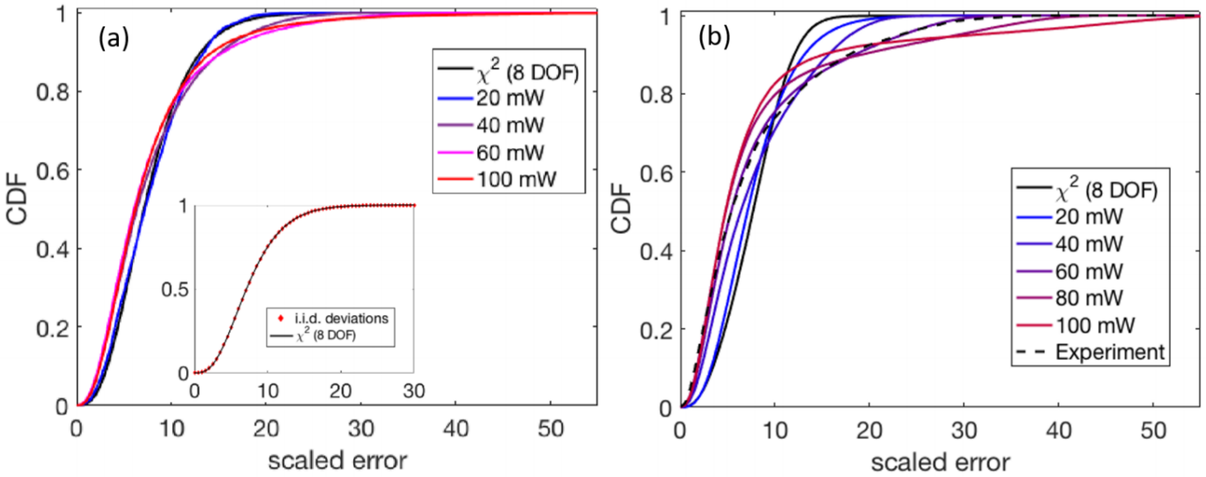

Figure 6.9: Squared deviations of particle positions from best-fit lattice sites. (a) Squared deviations of particle positions from best-fit lattice sites in simulations at a range of laser powers (blue-red) and the $\chi^2(8)$ distribution when the triangle is detected. (inset) Comparison between squared particel deviations for i.i.d. Gaussian deviations from lattice sites and the $\chi^2(8)$ distribution. (b) Squared deviations of particle positions from best-fit lattice sites in simulations at a range of laser powers (blue-red), an experiment conducted at $60mW$ (black dashed), and the $\chi^2(8)$ distribution for all configurations.

functions of $\frac{\Delta^2}{\sigma^2}$ for 6-particle GMT-LD simulations conducted at a range of laser powers regardless of which cluster is detected. Compared to the results in Figure 6.9a, the deviations from the $\chi^2(8)$ CDF are larger. Simulations performed by Chatipat Lorpaiboon.

The results in Figure 6.8-6.9 suggest that optical matter systems fluctuate along collective coordinates, and that as the trapping laser power increases correlated motion becomes increasingly important. For equilibrium systems the movement along collective coordinates is expected to obey detailed balance[111, 134], *i.e.* the forward and backward flux between all regions in the phase space of the system is equal. However, optical matter systems are nonequilibrium systems. While transfer of linear and angular momentum from the incident field to optical matter systems has been shown to result in rotation and translation of the system[82, 73, 20, 21], the question whether detailed balance is broken with respect to the internal coordinates in an optical matter system remains.

We conducted GMT-LD simulations of an 8-particle optical matter cluster depicted in Figure 6.10a. This particular 8-particle cluster has significant distortions compared to the hexagonal lattice. For a cluster that lies on an underlying hexagonal lattice with lattice vector length a, the two edge-lengths of the cluster, depicted by red arrows, are $\sqrt{3}a$ and $2a$. Histograms of the 4 edge lengths taken from a GMT-LD simulation are shown in Figure 6.10b. The 4 distributions are nearly identical, and are centered at $1.2\mu m$. Therefore, this cluster deviates significantly from an underlying hexagonal lattice.

We can construct a simple phase space in terms of the edge-lengths of the cluster to test whether detailed balance is broken. First, we label each distance + or − depending on whether its value is larger or smaller than the mean value of $1.2\mu m$. If we consider the two distances depicted in Figure 6.11a, this defines a phase space that consists of 4 regions as depicted in Figure 6.10c. The the elements of the total flux matrix T_{ij} are the number of observed transitions from state i to j (*i.e.* $T_{ij} = \pi_j Pij$ where π_j is the probability of finding the system in state j and P_{ij} is the Markov transition matrix element from state j to state i). A scaled color visualization of the total flux matrix is shown in Figure 6.10d. The total flux matrix is slightly asymmetric, reflecting the possibility of broken detailed balance.

We compared the total flux matrix depicted in Figure 6.10d between simulations conducted at three different laser powers. Figure 6.11a-c shows the three total flux matrices and Figure 6.11d-f shows the values of the net flux, $T_{ij} - T_{ji}$. Across all three powers, the total flux matrices and the net flux remain nearly identical. The values of the net flux define a cycle through the constructed phase space. For the labels depicted in Figure 6.11c the net flux moves (in a cycle) from $1 \rightarrow 2 \rightarrow 4 \rightarrow 3 \rightarrow 1$. This type of cycle is only possible in a nonequilibrium system, and is thus a direct consequence of the optical binding interaction being mediated by an external energy source.

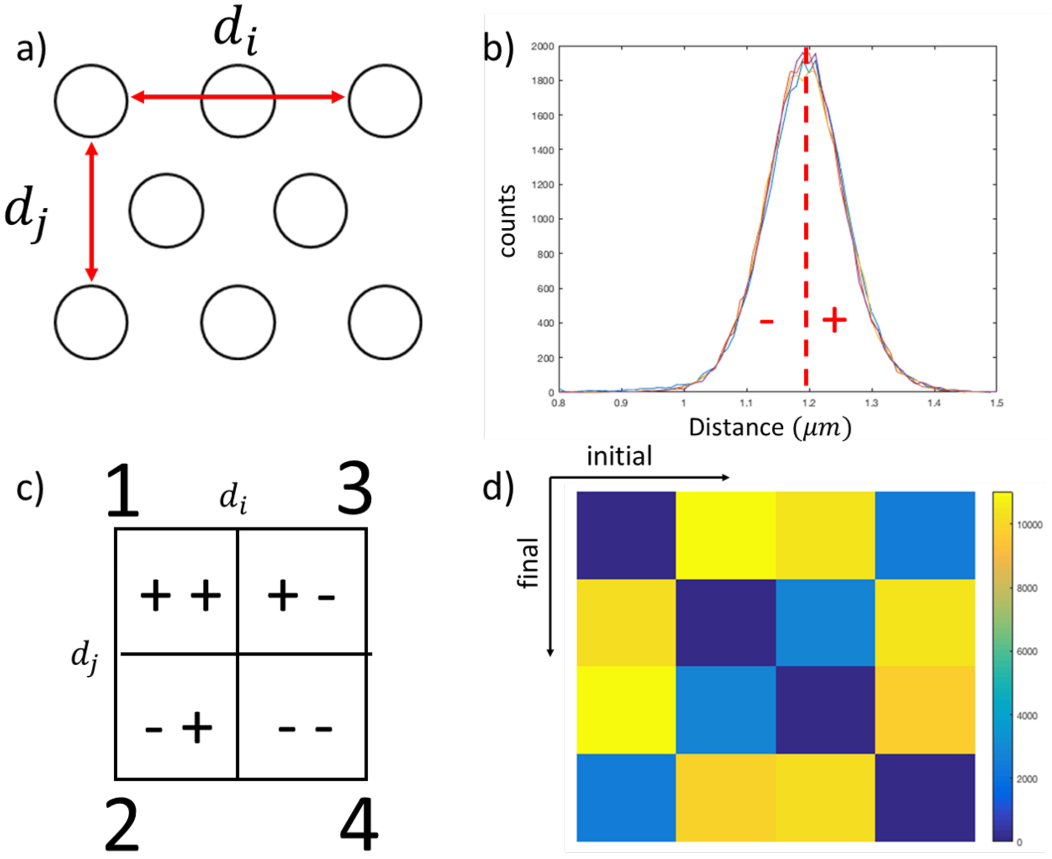

Figure 6.10: Measuring detailed balance in an 8-particle optical matter cluster (a) Corner-to-corner distances in an 8-particle optical matter cluster (red double arrows) (b) Distribution of corner-to-corner distances. When one of the distances is less than its mean value the variable is labeled - and when the distance is greater than its mean value the variable is labeled +. (c) 4 possible states for the 8-particle cluster shown in panel (a) based on two corner-to-corner separations: 1 (++), 2 (-+), 3 (+-), and 4 (–). (d) Scaled-color visualization of the total flux matrix for the 8-particle cluster shown in panel (a). The initial state is along the horizontal direction and the final state is along the vertical direction. Each count represents one observed transition.

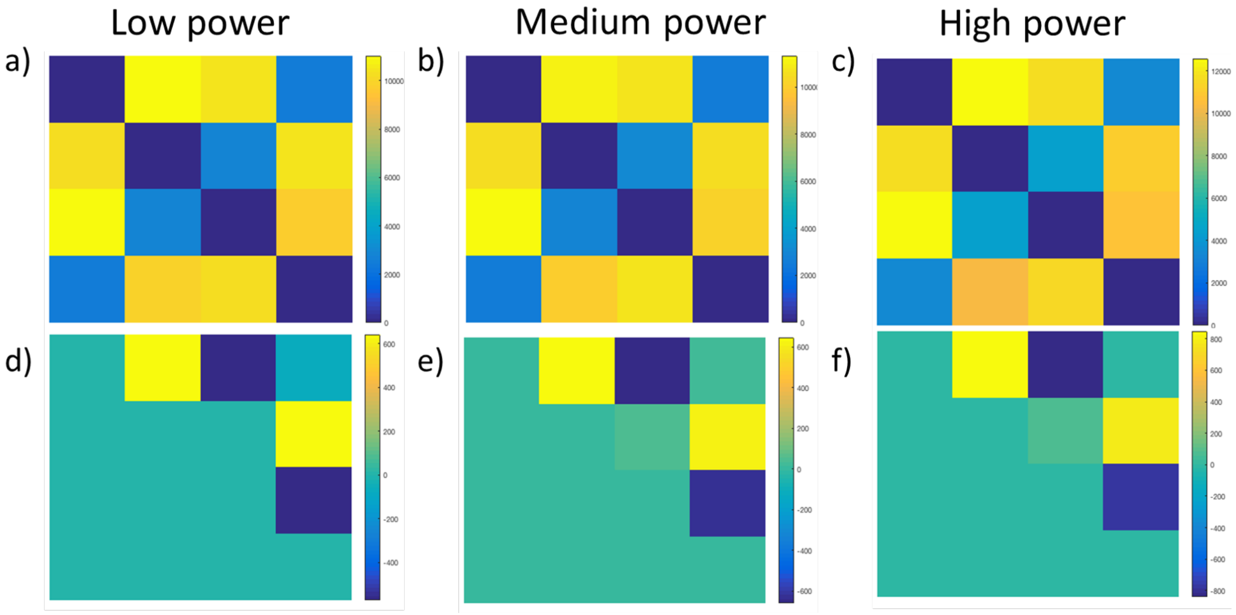

Figure 6.11: Broken detailed balance in an 8-particel optical matter cluster (a-c) Total flux matrices introduced in Figure 6.10d for GMT-LD simulations performed at low (a), medium (b), and high (c) power. Each count represents on observed transition. (d-f) Net flux ($T_{ij} - T_{ji}$) for the total flux matrices shown in (a-c).

Appendices

Appendix A

Detecting particle type by color

This section outlines the procedure for differentiation between gold and silver particles in a color .tif video file separated into three channels. The first step is to track the particle positions, as described in Section 2.2.1. The next step is to mask the three channels of each image so that every pixel value outside a radius $r = 3$ from a tracked particle position is set to zero. Examples of raw and masked images are shown in Figure A.1

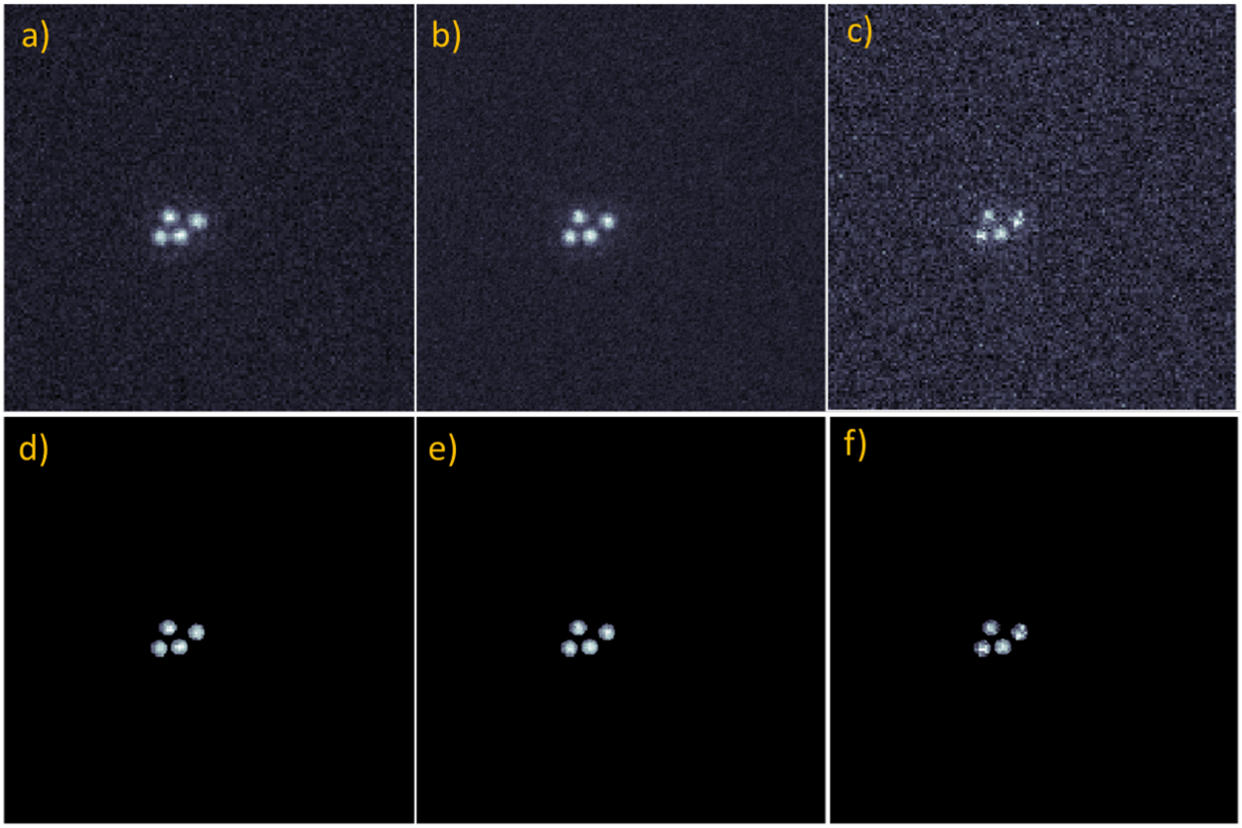

Figure A.1: Binary masking of color images based on particle positions. **(a-c)** Raw red (a), blue (b), and green (c) channels of a color experimental image. **(d-f)** Red (a), blue (b), and green (c) channels of a color experimental image that have been masked so that every pixel value outside a radius $r = 3$ from a tracked particle position is set to zero.

Once the image is masked, the average of the sum of unmasked pixels around each unmasked particle defines an RGB vector for that particle type

$$\chi^{R,G,B} = \frac{\sum_{pixels} I_{R,G,B}}{n_{particles} * \sum_{R,G,B} \sum_{pixels} I_{R,G,B}} \tag{A.1}$$

where $I_{R,G,B}$ is the red, green, or blue intensity of a pixel. Figure A.2 shows histograms of $\chi_{R,G,B}$ calculated over several frames for (a) gold particles and (b) silver particles. The locations of the distributions corresponding to each color have distinct locations for the silver and gold particles, and thus it is possible to differentiate between them. The average values of each channel of $\chi_{R,G,B}$, denoted $\tilde{\chi}_{R,G,B}$, will be used as reference values.

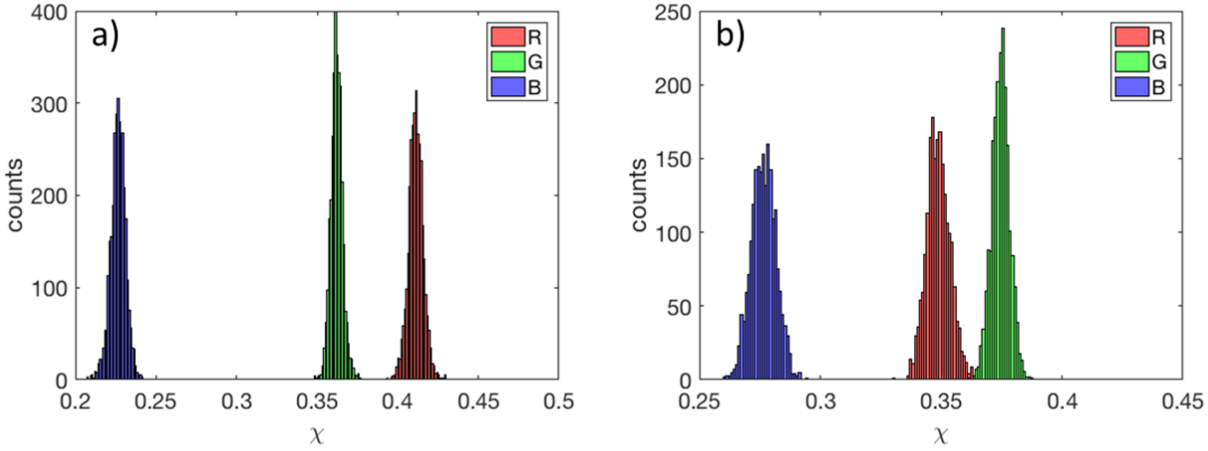

Figure A.2: Histograms of $\chi_{R,G,B}$ calculated over several frames for **(a)** gold particles and **(b)** silver particles.

In a video with an unknown particle type that has been masked the same way as the reference videos, let $Y^{R,G,B}$ be the summed intensity values of the pixels surrounding a specific particle location for the red, green, and blue channels. The projection of $Y^{R,G,B}$ onto $\chi_{R,\tilde{G},B}$

$$F = \frac{Y \cdot \tilde{\chi}_{R,G,B}}{|Y||\tilde{\chi}_{R,G,B}|}. \tag{A.2}$$

The reference $\tilde{\chi}_{R,G,B}$ that yields the maximum F is taken as the particle identity. Two examples from frames of a video containing a mixture of gold and silver particles is shown below in Figure A.2. Particles detected as gold in (a-b) are plotted as red dots in (c-d).

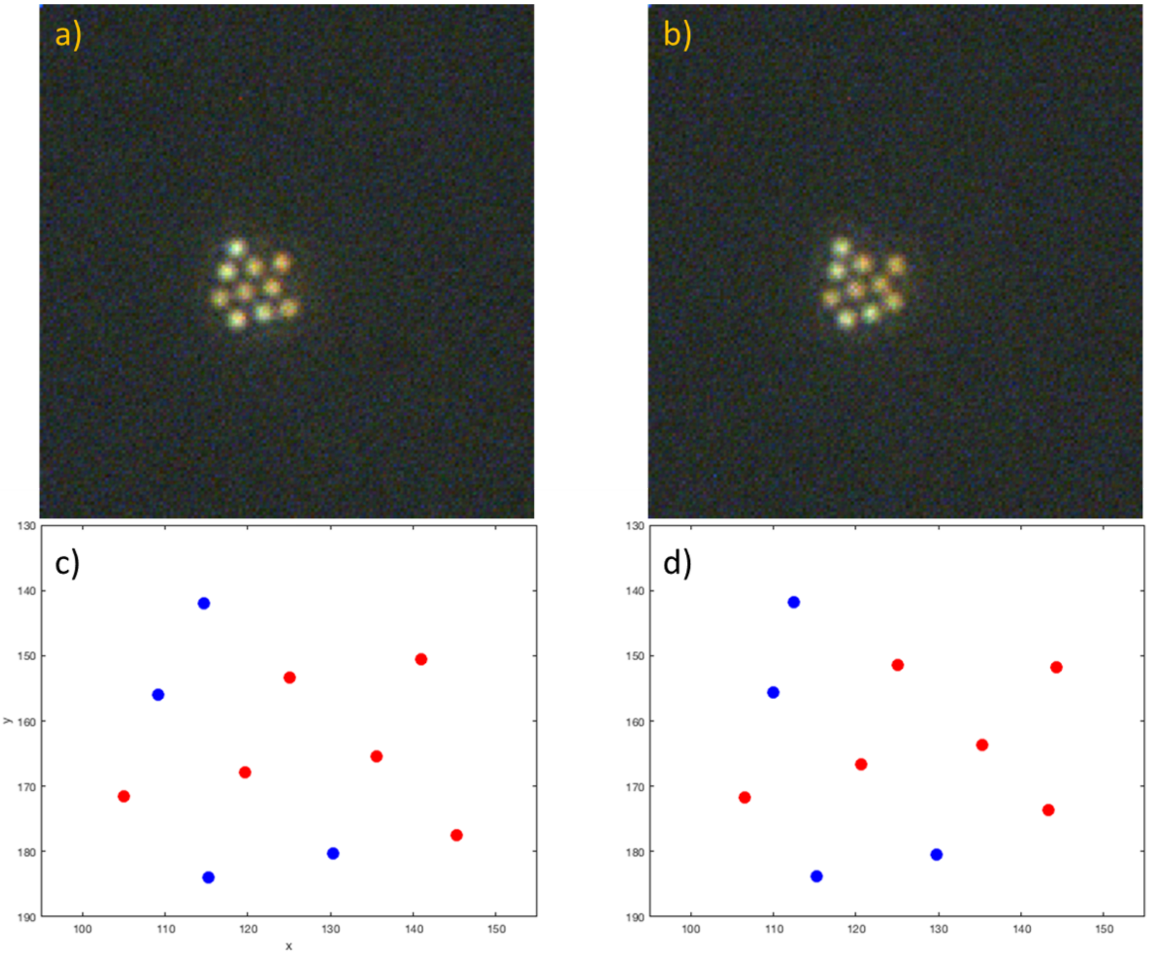

Figure A.3: Example of particle detection by color. Particles detected as gold in (a-b) are plotted as red dots in (c-d).

Appendix B

MATLAB code

B.1 Importing data

B.1.1 Function for importing tab-delineated .txt files from Mosaic

```
function [Trajectory,Frame,x,y,m0] = import_data(folder_path,
    ↪ file_name)
```

```
filename = strcat(folder_path,file_name,'.txt');
```

Initialize variables.

```
%filename = '/Users/Curtis/Documents/MATLAB/Laser_bleedthrough/
    ↪ Results_10122018_d.txt';
delimiter = '\t';
```

Read columns of data as strings:

For more information, see the TEXTSCAN documentation.

```
formatSpec = '%q%q%q%q%q%q%[^\n\r]';
```

Open the text file.

```
fileID = fopen(filename,'r');
```

Read columns of data according to format string.

This call is based on the structure of the file used to generate this code. If an error occurs for a different file, try regenerating the code from the Import Tool.

```
dataArray = textscan(fileID, formatSpec, 'Delimiter', delimiter,
   ↪ 'ReturnOnError', false);
```

Close the text file.

```
fclose(fileID);
```

Convert the contents of columns containing numeric strings to numbers.

Replace non-numeric strings with NaN.

```
raw = repmat({''},length(dataArray{1}),length(dataArray)-1);
for col=1:length(dataArray)-1
    raw(1:length(dataArray{col}),col) = dataArray{col};
end
numericData = NaN(size(dataArray{1},1),size(dataArray,2));

for col=[1,2,3,4,5,6,7]
    % Converts strings in the input cell array to numbers.
       ↪ Replaced non-numeric
    % strings with NaN.
```

```
rawData = dataArray{col};
for row=1:size(rawData, 1)
    % Create a regular expression to detect and remove non-
        ↪ numeric prefixes and
    % suffixes.
    regexstr = '(?<prefix>.*?)(?<numbers>([-]*(\d+[\,]*)
        ↪ +[\.]{0,1}\d*[eEdD]{0,1}[-+]*\d*[i]{0,1})|([-]*(\d
        ↪ +[\,]*)*[\.]{1,1}\d+[eEdD]{0,1}[-+]*\d*[i]{0,1}))(?<
        ↪ suffix>.*)';
    try
        result = regexp(rawData{row}, regexstr, 'names');
        numbers = result.numbers;

        % Detected commas in non-thousand locations.
        invalidThousandsSeparator = false;
        if any(numbers==',');
            thousandsRegExp = '^\d+?(\,\d{3})*\.{0,1}\d*$';
            if isempty(regexp(numbers, thousandsRegExp, 'once
                ↪ '));
                numbers = NaN;
                invalidThousandsSeparator = true;
            end
        end
        % Convert numeric strings to numbers.
        if ~invalidThousandsSeparator;
            numbers = textscan(strrep(numbers, ',', ''), '%f')
                ↪ ;
```

```
                numericData(row, col) = numbers{1};
                raw{row, col} = numbers{1};
            end
        catch me
        end
    end
end
```

Replace non-numeric cells with NaN

```
R = cellfun(@(x) ~isnumeric(x) && ~islogical(x),raw); % Find non-
   ↪ numeric cells
raw(R) = {NaN}; % Replace non-numeric cells
```

Allocate imported array to column variable names

```
Trajectory = cell2mat(raw(:, 2));
Frame = cell2mat(raw(:, 3));
x = cell2mat(raw(:, 4));
y = cell2mat(raw(:, 5));
m0 = cell2mat(raw(:,7));
```

Clear temporary variables

```
clearvars filename delimiter formatSpec fileID dataArray ans raw
   ↪ col numericData rawData row regexstr result numbers
   ↪ invalidThousandsSeparator thousandsRegExp me R;
clearvars VarName1

end
```

B.1.2 Script for formatting output of import_data function

```
clearvars Data x y

folder_path = '/Users/Curtis/Documents/MATLAB/
   ↪ long_range_interactions/Datasets/';
file_name = 'Results_8272020_4';
[Trajectory,Frame,x,y,m0] = import_data(folder_path,file_name);

Frame2 = Frame(2:end) + 1;
Trajectory2 = Trajectory(2:end);
xtemp = x(2:end);
ytemp = y(2:end);
m0temp = m0(2:end);

Data = [Frame2 Trajectory2 xtemp ytemp m0temp];
Data = sortrows(Data,1);

clearvars file_name folder_path Frame2 Trajectory2 xtemp ytemp
   ↪ temp temp2 m0temp Trajectory m0 Frame x y

x = zeros(50,max(Data(:,1)));
y = zeros(50,max(Data(:,1)));
x_linked = zeros(50,max(Data(:,1)));
y_linked = zeros(50,max(Data(:,1)));



for n = 1:max(Data(:,1))
```

```
    temptraj = nonzeros((Data(:,1) == (n)).*Data(:,2));
    tempx = nonzeros((Data(:,1) == (n)).*Data(:,3));
    tempy = nonzeros((Data(:,1) == (n)).*Data(:,4));
    temptraj2 = 1:1:length(tempx);
    x_linked(temptraj,n) = tempx;
    y_linked(temptraj,n) = tempy;
    x(temptraj2,n) = tempx;
    y(temptraj2,n) = tempy;

end

clearvars n

%temp = sortrows(Data,2);
%temp2 = temp(:,5);

clearvars temptraj temptraj2 tempx tempy
```

B.2 Lattice fitting and cluster detection

B.2.1 Function that takes (x, y) coordinates and returns best-fit hexagonal lattice

```
function [x_si,y_si,lattice_positions_centered,order_param,
   ↪ lattice_assignment,d_lattice,theta_lattice,cp] =
   ↪ lattice_assignment_algorithm_vectorized(x,y)

    %This function fits a lattice to tracked particle positions.
```

```
    ↪ The required
%inputs are x(particle) and y(particle).

np = length(nonzeros(x)); %Specify the number of particles
pixelsize = .072; %Conversion factor between pixels and
    ↪ microns
x_si = nonzeros(x)*pixelsize; %Particle positions in microns
y_si = nonzeros(y)*pixelsize;

lattice_size = 4; %Specify the size of the lattice (in terms
    ↪ of 2n+1 lattice vectors)
[temp1,temp2] = meshgrid(-lattice_size:lattice_size);
coeff_matrix(:,:,1) = temp2;
coeff_matrix(:,:,2) = temp1;

%clearvars temp1 temp2 dist

particle_list = 1:1:np; %Specify which particles to fit (
    ↪ default is 1:np)
```

Parameters

```
d_spacing = 0.0025; %Specify which lattice vector lengths to
    ↪ try
d_start = .540;
d_end = .630;

theta_spacing = .05; %Specify which lattice angles lengths to
```

```
    ↪ try
theta_start = pi/3 − pi/6; %Second lattice vector has defined
    ↪ offset
theta_end = pi/3 + pi/6;
```

This section of the code creates lattice vectors for ALL specified distances and angles.

```
\begin{lstlisting}
d_temp = d_start:d_spacing:d_end;
theta1_temp = theta_start:theta_spacing:theta_end;
theta2_temp = theta1_temp + pi/3;



for n1 = 1:length(d_temp)
    x1_temp(n1,:) = d_temp(n1)*cos(theta1_temp);
    y1_temp(n1,:) = d_temp(n1)*sin(theta1_temp);
    x2_temp(n1,:) = d_temp(n1)*cos(theta2_temp);
    y2_temp(n1,:) = d_temp(n1)*sin(theta2_temp);
end

num_params = length(d_temp)*length(theta1_temp);

x1_temp = reshape(x1_temp,1,1,1,num_params); %reshape the
    ↪ array of lattice vectors for vectorized multiplication
y1_temp = reshape(y1_temp,1,1,1,num_params);
x2_temp = reshape(x2_temp,1,1,1,num_params);
```

```
y2_temp = reshape(y2_temp,1,1,1,num_params);


lattice_vectors_temp(:,:,:,1) = x1_temp.*coeff_matrix(:,:,1) +
    ↪  x2_temp.*coeff_matrix(:,:,2);
lattice_vectors_temp(:,:,:,2) = y1_temp.*coeff_matrix(:,:,1) +
    ↪  y2_temp.*coeff_matrix(:,:,2);


%matrix_size = [size(coeff_matrix,1) size(coeff_matrix,2)
    ↪ length(d_temp)*length(theta1_temp) 2];
```

This section centers ALL lattices on ALL particles and calculates the sum the deviations from the lattice.

```
\begin{lstlisting}
x_reshaped = reshape(x_si,1,1,1,(length(particle_list))); %x
    ↪ and y need to be reshaped for vectorized multiplication
y_reshaped = reshape(y_si,1,1,1,(length(particle_list)));



for n2 = 1:length(particle_list) %This loop tries centering
    ↪ the test-lattices on each particle


    particle_list_temp = particle_list(particle_list ~=
        ↪ particle_list(n2));
    particle_list_temp = reshape(particle_list_temp,1,1,length
        ↪ (particle_list_temp));
    lattice_dist_temp_x = x_reshaped(particle_list_temp) - (
        ↪ x_si(particle_list(n2)) + lattice_vectors_temp
```

```
        ↪ (:,:,:,1));
      lattice_dist_temp_y = y_reshaped(particle_list_temp) - (
        ↪ y_si(particle_list(n2)) + lattice_vectors_temp
        ↪ (:,:,:,2));
      lattice_dist_temp = lattice_dist_temp_x.^2 +
        ↪ lattice_dist_temp_y.^2;

      [min_temp] = min(lattice_dist_temp,[],1);
      [min_temp] = min(min_temp,[],2);
      min_temp = sum(min_temp,4);

      min_temp = reshape(min_temp,size(lattice_vectors_temp,3)
        ↪ ,1);

      lattice_dist_sum_temp(:,n2) = min_temp; %This loop builds
        ↪ a (num_params)X(num_particles) array of the sum of
        ↪ suqred lattice distances
  end

  [order_param_temp,particle_index_temp] = min(
    ↪ lattice_dist_sum_temp,[],2); %These four lines finds the
    ↪  lattice parameters and central
  [order_param,param_index] = min(order_param_temp);
    ↪                              %particle that result in the
    ↪ smallest sum suqred distance
  central_particle = particle_index_temp(param_index);
  cp = [x_si(central_particle),y_si(central_particle)];
```

```
[d_ind,theta_ind] = ind2sub([length(d_temp) length(theta1_temp
    ↪ )],param_index); %These three lines unravel the param
theta_lattice = [theta1_temp(theta_ind); theta2_temp(theta_ind
    ↪ )];                %index to recover the best theta and d
d_lattice = d_temp(d_ind);
```

The best lattice is reconstructed

```
x1 = d_lattice*cos(theta_lattice(1)); %Reconstruct lattice
    ↪ vectors
y1 = d_lattice*sin(theta_lattice(1));
x2 = d_lattice*cos(theta_lattice(2));
y2 = d_lattice*sin(theta_lattice(2));



for n1 = 1:size(coeff_matrix,1)
    for n2 = 1:size(coeff_matrix,2)
        lattice_positions(n1,n2,1) = x1*coeff_matrix(n1,n2,1)
            ↪ + x2*coeff_matrix(n1,n2,2);
        lattice_positions(n1,n2,2) = y1*coeff_matrix(n1,n2,1)
            ↪ + y2*coeff_matrix(n1,n2,2);

        lattice_positions_centered(n1,n2,1) =
            ↪ lattice_positions(n1,n2,1) + x_si(
            ↪ central_particle);
        lattice_positions_centered(n1,n2,2) =
            ↪ lattice_positions(n1,n2,2) + y_si(
```

```
                ↪ central_particle);
        end
    end
```

Lattice assignment is recovered (each particle assigned to closest site; duplicates possible

```
    for n1 = 1:np

        x_dist_temp = (lattice_positions_centered(:,:,1) - x_si(n1
            ↪ )).^2;
        y_dist_temp = (lattice_positions_centered(:,:,2) - y_si(n1
            ↪ )).^2;
        sq_dist_temp = x_dist_temp + y_dist_temp;
        [mindist_temp1,ind1_temp] = min(sq_dist_temp,[],1);
        [~,ind2_temp] = min(mindist_temp1);
        lattice_assignment(n1,1) = ind1_temp(ind2_temp);
        lattice_assignment(n1,2) = ind2_temp;
    end

end
```

B.2.2 Function that returns translations, rotation, and scale for optimized lattice parameters

```
% Determine r
z1 = complex(r1(:,1),r1(:,2));
```

```
z2 = complex(r2(:,1),r2(:,2));
az1 = mean(z1);
az2 = mean(z2);
z = az2-az1;
r = [real(z) imag(z)];

%Determine other optimal parameters
z1 = z1-az1;
z2 = z2-az2;
a = norm(z1)^2;
err = norm(z2)^2;
zz1 = dot(z1,z2);
zz_1 = dot(z1,conj(z2));
b1 = abs(zz1);
b_1 = abs(zz_1);
err1 = -b1^2/a;
err_1 = -b_1^2/a;
if (err1<=err_1)
    mirr = 1;
    err = err+err1;
    sc = b1/a;
    theta = -angle(zz1);
else
    mirr = -1;
    err = err+err_1;
    sc = b_1/a;
    theta = -angle(zz_1);
```

```
end
err = err^0.5;
end
```

B.2.3 Function that defines the occupation of lattice sites based on a cutoff distance

```
function [number_neighbors,lattice_positions_cluster,hex_indicator
    ↪ ,occupied] = lattice_occupation(x_si,y_si,lattice_positions)

dist_tol = .25;

clearvars occupied_temp occupied
occupied = zeros(size(lattice_positions,1),size(lattice_positions
    ↪ ,2),size(lattice_positions,4));
lattice_positions_cluster(:,:,1,:) = occupied;
lattice_positions_cluster(:,:,2,:) = occupied;
for n1 = 1:size(lattice_positions,4)
    for n2 = 1:size(lattice_positions,1)
        for n3 = 1:size(lattice_positions,2)
            [dist_temp,indextemp] = min(sqrt((x_si(:,n1) -
                ↪ lattice_positions(n2,n3,1,n1)).^2) + ((y_si(:,n1
                ↪ ) - lattice_positions(n2,n3,2,n1)).^2));

            if dist_temp < dist_tol
                occupied(n2,n3,n1) = 1;
                lattice_positions_cluster(n2,n3,1,n1) = x_si(
                    ↪ indextemp,n1);
```

```
                lattice_positions_cluster(n2,n3,2,n1) = y_si(
                  ↪ indextemp,n1);
            end

        end
    end


end

clearvars number_neighbors

hex_index = [1 0; 1 -1; 0 1; 0 -1; -1 0; -1 1];
number_neighbors = occupied;

for n1 = 1:size(occupied,3)
    for n2 = 1:size(hex_index,1)
        neighbors_temp = circshift(occupied(:,:,n1),hex_index(n2
          ↪ ,1),1);
        neighbors_temp = circshift(neighbors_temp,hex_index(n2,2)
          ↪ ,2);
        number_neighbors(:,:,n1) = number_neighbors(:,:,n1) +
          ↪ neighbors_temp;
    end
end
```

```
hex_indicator = number_neighbors == 7;
hex_sites = hex_indicator;
for n1 = 1:size(hex_index,1)
    hex_sites_temp = circshift(hex_indicator,hex_index(n1,1),1);
    hex_sites_temp = circshift(hex_sites_temp,hex_index(n1,2),2);
    hex_sites = hex_sites + hex_sites_temp;

end

lattice_positions_cluster_tempx(:,:,:) = lattice_positions
    ↪ (:,:,1,:);
lattice_positions_cluster_tempy(:,:,:) = lattice_positions
    ↪ (:,:,2,:);

%lattice_positions_cluster_tempx = lattice_positions_cluster_tempx
    ↪ .*hex_sites;
%lattice_positions_cluster_tempy = lattice_positions_cluster_tempy
    ↪ .*hex_sites;
%lattice_positions_cluster(:,:,1,:) =
    ↪ lattice_positions_cluster_tempx;
%lattice_positions_cluster(:,:,2,:) =
    ↪ lattice_positions_cluster_tempy;

number_neighbors = (number_neighbors - 1).*occupied;
occupied = logical(occupied);
clearvars lattice_positions_hex_tempx lattice_positions_hex_tempy
```

B.2.4 Function that detects common 6-particle clusters

```
function [cluster_type] = cluster_detection_6p(number_neighbors)

clearvars neighbor_count cluster_type_temp cluster_type

cluster_1_ind = [0 3 0 3 0 0]';
cluster_2_ind = [0 2 3 0 1 0]';
cluster_3_ind = [0 2 2 2 0 0]';



cluster_type_temp = zeros(1,size(number_neighbors,3));
for n1 = 1:size(number_neighbors,3)

    for n2 = 1:6
        neighbor_count(n2,n1) = sum(sum(number_neighbors(:,:,n1)
          ↪ == n2));
    end

    if neighbor_count(:,n1) == cluster_1_ind
       cluster_type_temp(n1) = 1;

    elseif neighbor_count(:,n1) == cluster_2_ind
        cluster_type_temp(n1) = 2;

    elseif neighbor_count(:,n1) == cluster_3_ind
        cluster_type_temp(n1) = 3;
```

```
%       elseif neighbor_count(:,n1) == cluster_4_ind
%           cluster_type_temp(n1) = 4;
%
%       elseif neighbor_count(:,n1) == cluster_5_ind
%           cluster_type_temp(n1) = 5;
    end



end

cluster_type = cluster_type_temp;
```

B.2.5 Script that fits hexagonal lattice to (x, y) trajectories with a variable number of particles

```
%%This is the simplest lattice fitting algorithm; the brute-force
%%assignment is performed every frame. Input is to arrays x and y
   ↪ with
%%dimensions [num_particles num_frames].


min_frame = 1;
max_frame = 5000;



for n1 = min_frame:max_frame
    n1
```

```
np = length(nonzeros(x(:,n1)));
[x_si_temp,y_si_temp,lattice_positions_centered_temp,
   ↪ order_param_temp,lattice_assignment_temp,d_lattice_temp,
   ↪ theta_lattice_temp,cp_temp] =
   ↪ lattice_assignment_algorithm_vectorized(x(:,n1),y(:,n1))
   ↪ ;
x_si(1:length(x_si_temp),n1) = x_si_temp;
y_si(1:length(x_si_temp),n1) = y_si_temp;

%Analytical minimization minimizes the distances between two
   ↪ sets of
%points, r1 and r2.
for n2 = 1:np
     r1(n2,1,n1) = x_si(n2,n1);
     r1(n2,2,n1) = y_si(n2,n1);
     r2(n2,1,n1) = lattice_positions_centered_temp(
        ↪ lattice_assignment_temp(n2,1),
        ↪ lattice_assignment_temp(n2,2),1);
     r2(n2,2,n1) = lattice_positions_centered_temp(
        ↪ lattice_assignment_temp(n2,1),
        ↪ lattice_assignment_temp(n2,2),2);
end

[r,mirr,d_theta,sc,err] = latt_fit_refine(r1(:,:,n1),r2(:,:,n1
   ↪ )); %Analytical minimization function that gives
   ↪ translation,
error_refined(n1) = err.^2;
```

```
    ↪                                              %rotation, and
    ↪ scale factor for best fit
cp(n1,:) = cp_temp + r;
scale(n1) = sc;
d_lattice_refined(n1) = d_lattice_temp*scale(n1);
theta_lattice_refined(:,n1) = theta_lattice_temp + d_theta;
mirror(n1) = mirr;

lattice_positions_temp(:,:,1) =
    ↪ lattice_positions_centered_temp(:,:,1) - mean(r2(:,1,n1)
    ↪ );
lattice_positions_temp(:,:,2) =
    ↪ lattice_positions_centered_temp(:,:,2) - mean(r2(:,2,n1)
    ↪ );
lattice_positions_rot(:,:,1) = lattice_positions_temp(:,:,1)*
    ↪ cos(d_theta) - lattice_positions_temp(:,:,2)*sin(d_theta
    ↪ );
lattice_positions_rot(:,:,2) = lattice_positions_temp(:,:,1)*
    ↪ sin(d_theta) + lattice_positions_temp(:,:,2)*cos(d_theta
    ↪ );
lattice_positions_rot_scale = lattice_positions_rot*sc;
lattice_positions_centered_refined(:,:,1,n1) =
    ↪ lattice_positions_rot_scale(:,:,1) + mean(r2(:,1,n1));
lattice_positions_centered_refined(:,:,2,n1) =
    ↪ lattice_positions_rot_scale(:,:,2) + mean(r2(:,2,n1));

%[lattice_positions_centered_refined(:,:,1:2,n1)] =
```

```
    ↪ lattice_construction(d_lattice_refined(n1),
    ↪ theta_lattice_refined(:,n1),cp(n1,:));
end
```

B.2.6 Script that translates and rotates clusters detected as triangle

```
%This script rotates and translates the images associated with a
  ↪ 6-particle
%hexagonal cluster so that their position and orientation are the
  ↪ same, and
%averages those images togther

%Calling this function takes fit lattice positions and returns the
%following:
%-Number of hexagonal neighbors
%-The positions of occupied hexagonal lattice sites
%-An indicator of whether a hexagonal cluster exists in that frame
%-A binary matrix representing occupation of lattice sites

[number_neighbors,lattice_positions_cluster,hex_indicator,occupied
  ↪ ] = lattice_occupation(x_si,y_si,
  ↪ lattice_positions_centered_refined);

%Calling this function identifies the cluster type in a given
  ↪ frame and
%returns a cluster type variable

[cluster_type] = cluster_detection_6p(number_neighbors);
```

```
%A rotation matrix is created for every frame based on the fit
    ↪ lattice
%angle

%Find the frames where the specified cluster exists
index1 = find(cluster_type == 1);
index2 = find(cluster_type == 2);

num_frames = size(lattice_positions_centered_refined,4);

%Find that lattice sites that define the position and orientation
    ↪ of
%cluster type1 (triangle)
corner_index_temp = occupied*0;
intirior_index_temp = occupied*0;

corner_index_temp(:,:,index1) = (number_neighbors(:,:,index1) ==
    ↪ 2);
intirior_index_temp(:,:,index1) = (number_neighbors(:,:,index1) ==
    ↪  4);

corner_index_temp = logical(corner_index_temp);
intirior_index_temp = logical(intirior_index_temp);

tri_corners_lattice(:,:,1,index1) = reshape(
    ↪ lattice_positions_centered_refined(:,:,1,index1),[9 9 length
    ↪ (index1)]).*corner_index_temp(:,:,index1);
tri_corners_lattice(:,:,2,index1) = reshape(
```

```
    ↪ lattice_positions_centered_refined(:,:,2,index1),[9 9 length
    ↪ (index1)]).*corner_index_temp(:,:,index1);
tri_intirior_lattice(:,:,1,index1) = reshape(
    ↪ lattice_positions_centered_refined(:,:,1,index1),[9 9 length
    ↪ (index1)]).*intirior_index_temp(:,:,index1);
tri_intirior_lattice(:,:,2,index1) = reshape(
    ↪ lattice_positions_centered_refined(:,:,2,index1),[9 9 length
    ↪ (index1)]).*intirior_index_temp(:,:,index1);

tri_corners(:,:,1,index1) = reshape(lattice_positions_cluster
    ↪ (:,:,1,index1),[9 9 length(index1)]).*corner_index_temp(:,:,
    ↪ index1);
tri_corners(:,:,2,index1) = reshape(lattice_positions_cluster
    ↪ (:,:,2,index1),[9 9 length(index1)]).*corner_index_temp(:,:,
    ↪ index1);
tri_intirior(:,:,1,index1) = reshape(lattice_positions_cluster
    ↪ (:,:,1,index1),[9 9 length(index1)]).*intirior_index_temp
    ↪ (:,:,index1);
tri_intirior(:,:,2,index1) = reshape(lattice_positions_cluster
    ↪ (:,:,2,index1),[9 9 length(index1)]).*intirior_index_temp
    ↪ (:,:,index1);

distances_tri_positions = zeros(3,3,num_frames);
bisectors = zeros(4,num_frames);
min_bisector = zeros(1,num_frames);
ref_lattice_sites = zeros(2,2,num_frames);
```

```
for n1 = 1:length(index1)
    tri_corners_tempx = tri_corners(:,:,1,index1(n1));
    tri_corners_tempy = tri_corners(:,:,2,index1(n1));
    tri_intirior_tempx = tri_intirior(:,:,1,index1(n1));
    tri_intirior_tempy = tri_intirior(:,:,2,index1(n1));

    x1_temp = tri_corners_tempx(corner_index_temp(:,:,index1(n1)))
       ↪ ;
    x2_temp = tri_intirior_tempx(intirior_index_temp(:,:,index1(n1
       ↪ )));
    y1_temp = tri_corners_tempy(corner_index_temp(:,:,index1(n1)))
       ↪ ;
    y2_temp = tri_intirior_tempy(intirior_index_temp(:,:,index1(n1
       ↪ )));
    x1_temp_lattice = nonzeros(tri_corners_lattice(:,:,1,index1(n1
       ↪ )));
    x2_temp_lattice = nonzeros(tri_intirior_lattice(:,:,1,index1(
       ↪ n1)));
    y1_temp_lattice = nonzeros(tri_corners_lattice(:,:,2,index1(n1
       ↪ )));
    y2_temp_lattice = nonzeros(tri_intirior_lattice(:,:,2,index1(
       ↪ n1)));
    dist_tri_temp = distance_calculator_subsets(x1_temp,y1_temp,
       ↪ x2_temp,y2_temp);
    distances_tri_positions(:,:,index1(n1)) = dist_tri_temp;
    bisectors_temp = nonzeros((dist_tri_temp > 0.8).*dist_tri_temp
       ↪ );
```

```
    bisectors(1:length(bisectors_temp),index1(n1)) =
       ↪ bisectors_temp;
    min_bisector(index1(n1)) = min(nonzeros(bisectors(:,index1(n1)
       ↪ )));



    [index_temp1,index_temp2] = find(dist_tri_temp == min_bisector
       ↪ (index1(n1)));

    ref_lattice_sites(1,1,index1(n1)) = x1_temp_lattice(
       ↪ index_temp1(1));
    ref_lattice_sites(1,2,index1(n1)) = y1_temp_lattice(
       ↪ index_temp1(1));
    ref_lattice_sites(2,1,index1(n1)) = mean(x1_temp_lattice) +
       ↪ mean(x2_temp_lattice);
    ref_lattice_sites(2,2,index1(n1)) = mean(y1_temp_lattice) +
       ↪ mean(y2_temp_lattice);
end
outer_point(1,:) = reshape(ref_lattice_sites(1,1,:),[1 num_frames
   ↪ ]);
outer_point(2,:) = reshape(ref_lattice_sites(1,2,:),[1 num_frames
   ↪ ]);

for n1 = 1:num_frames
    central_point(1,n1) = mean(nonzeros(x_si(:,n1)));
    central_point(2,n1) = mean(nonzeros(y_si(:,n1)));
end
```

```
rotation_tempx = central_point(1,:) - outer_point(1,:);
rotation_tempy = central_point(2,:) - outer_point(2,:);

rotation_angle = -atan2(rotation_tempy,rotation_tempx);
rotation_matrix(1,1,:) = cos(rotation_angle);
rotation_matrix(1,2,:) = -sin(rotation_angle);
rotation_matrix(2,1,:) = sin(rotation_angle);
rotation_matrix(2,2,:) = cos(rotation_angle);
%The images are centered at the central point and rotated by the
   ↪ rotation
%angle in each frame
for n1 = 1:length(index1)

    x_cent(:,index1(n1)) = x_si(:,index1(n1)) - central_point(1,
       ↪ index1(n1));
    y_cent(:,index1(n1)) = y_si(:,index1(n1)) - central_point(2,
       ↪ index1(n1));

    x_cent(:,index1(n1)) = x_cent(:,index1(n1)).*(x_si(:,index1(n1
       ↪ )) ~= 0);
    y_cent(:,index1(n1)) = y_cent(:,index1(n1)).*(y_si(:,index1(n1
       ↪ )) ~= 0);

    x_cent_rot(:,index1(n1)) = x_cent(:,index1(n1))*
       ↪ rotation_matrix(1,1,index1(n1)) + y_cent(:,index1(n1))*
       ↪ rotation_matrix(1,2,index1(n1));
```

```
    y_cent_rot(:,index1(n1)) = x_cent(:,index1(n1))*
       ↪ rotation_matrix(2,1,index1(n1)) + y_cent(:,index1(n1))*
       ↪ rotation_matrix(2,2,index1(n1));

end

%The centered and rotated particle positions are collected and
   ↪ reshaped
number_particles = 6;
x_cent_hist_temp(:,index1) = x_cent_rot(1:number_particles,index1)
   ↪ ;
y_cent_hist_temp(:,index1) = y_cent_rot(1:number_particles,index1)
   ↪ ;

x_hist_tri = zeros(number_particles,num_frames);
y_hist_tri = zeros(number_particles,num_frames);

x_hist_tri(:,index1) = x_cent_hist_temp(:,index1);
y_hist_tri(:,index1) = y_cent_hist_temp(:,index1);

min_dist = 0.78;
binsize = 0.01;
spacing = 0.01;
max_dist = 1.05;
averaging_distances = max_dist:(-spacing):min_dist;
clearvars index_dist x_cent_hist y_cent_hist

vidObj = VideoWriter(strcat('transition_tri','.avi'));
```

```
open(vidObj);

%for n1 = 1:46
for n1 = 1:length(averaging_distances)
    index_dist_temp = find((min_bisector > (averaging_distances (
        ↪ n1)- binsize/2)).*(min_bisector < (averaging_distances(
        ↪ n1) + binsize/2)).*(min_bisector ~= 0));
    index_dist(n1,1:length(index_dist_temp)) = index_dist_temp;

    x_cent_dist_hist_temp = x_cent_hist_temp(:,nonzeros(index_dist
        ↪ (n1,:)));
    y_cent_dist_hist_temp = y_cent_hist_temp(:,nonzeros(index_dist
        ↪ (n1,:)));

    n_frames_temp = size(x_cent_dist_hist_temp,1)*size(
        ↪ x_cent_dist_hist_temp,2);

    x_cent_hist(1:n_frames_temp,n1) = reshape(
        ↪ x_cent_dist_hist_temp,[n_frames_temp 1]);
    y_cent_hist(1:n_frames_temp,n1) = reshape(
        ↪ y_cent_dist_hist_temp,[n_frames_temp 1]);
    imagesc(hist3([nonzeros(x_cent_hist(:,n1)) nonzeros(
        ↪ y_cent_hist(:,n1))],'Ctrs',{-2:0.025:2 -2:0.025:2}))
    axis([50 115 50 115])
    axis off
    axis square
    %colormap gray
```

```
    currFrame = getframe;
    writeVideo(vidObj,currFrame);

end

close(vidObj);

figure
imagesc(hist3([nonzeros(x_cent_hist) nonzeros(y_cent_hist)],'Ctrs',{-2:0.025:2 -2:0.025:2}))



%imagesc(log(hist3([x_cent_hist y_cent_hist],[100 100])),[0 7])



clearvars index_temp index_temp2 n1 x_cent_hist_temp y_cent_hist_temp central_point
```

B.3 Particle type detection by color

B.3.1 Function for masking images so only pixels near particles are non-zero

```
function mask = particle_mask(x,y,pixel_index)
    np = length(x);
    mask = pixel_index(:,:,1)*0;
```

```
    if np ~= 0
        for n1 = 1:np
            xdist_temp = pixel_index(:,:,1) - x(n1);
            ydist_temp = pixel_index(:,:,2) - y(n1);
            sq_dist_temp = xdist_temp.^2 + ydist_temp.^2;
            mask_temp(:,:,n1) = (sq_dist_temp < 36);
        end
        mask = ((mask + sum(mask_temp,3)) ~= 0);
    end


end
```

B.3.2 Function for calculating RGB values for particles in masked images

```
function rgb_per_particle = rgb_values(x,y,pixel_index,img_temp)
    np = length(x);
    c1_value_temp = 0;
    c2_value_temp = 0;
    c3_value_temp = 0;
    if np ~= 0
        for n1 = 1:np
            xdist_temp = pixel_index(:,:,1) - x(n1);
            ydist_temp = pixel_index(:,:,2) - y(n1);
            sq_dist_temp = xdist_temp.^2 + ydist_temp.^2;
            mask_temp = (sq_dist_temp < 36);
            c1_value_temp(n1) = sum(sum(mask_temp.*img_temp(:,:,1)
                ↪ ));
```

```
            c2_value_temp(n1) = sum(sum(mask_temp.*img_temp(:,:,2)
              ↪ ));
            c3_value_temp(n1) = sum(sum(mask_temp.*img_temp(:,:,3)
              ↪ ));
        end
    end
rgb_per_particle = [c1_value_temp; c2_value_temp; c3_value_temp]';
end
```

B.3.3 Script for detecting particle type by color in color .tif videos

```
min_frame = 1;
max_frame = 2000;

for n1 = min_frame:max_frame
    rgb_image(:,:,:,n1) = imread('Mov g.tif',n1);
end

pixel_index_temp1 = 1:1:size(rgb_image,2);
pixel_index_temp2 = 1:1:size(rgb_image,1);

[pixel_index_temp3,pixel_index_temp4] = meshgrid(pixel_index_temp1
  ↪ ,pixel_index_temp2);

pixel_index(:,:,1) = pixel_index_temp3;
pixel_index(:,:,2) = pixel_index_temp4;

clearvars pixel_index_temp1 pixel_index_temp2 pixel_index_temp3
```

```
    ↪ pixel_index_temp4

rgb_image_masked = rgb_image*0;

for n1 = min_frame:max_frame
    mask_temp = particle_mask(nonzeros(x(:,n1)),nonzeros(y(:,n1)),
        ↪ pixel_index);
    mask(:,:,n1) = uint8(mask_temp);

    rgb_image_masked(:,:,1,n1) = rgb_image(:,:,1,n1).*mask(:,:,n1)
        ↪ ;
    rgb_image_masked(:,:,2,n1) = rgb_image(:,:,2,n1).*mask(:,:,n1)
        ↪ ;
    rgb_image_masked(:,:,3,n1) = rgb_image(:,:,3,n1).*mask(:,:,n1)
        ↪ ;

end

for n1 = min_frame:max_frame
    np_temp = length(nonzeros(x(:,n1)));
    sum_intensity(n1,1) = sum(sum(rgb_image_masked(:,:,1,n1)));
    sum_intensity(n1,2) = sum(sum(rgb_image_masked(:,:,2,n1)));
    sum_intensity(n1,3) = sum(sum(rgb_image_masked(:,:,3,n1)));

    ave_intensity(n1,1) = sum(sum(rgb_image_masked(:,:,1,n1)))/
        ↪ np_temp;
    ave_intensity(n1,2) = sum(sum(rgb_image_masked(:,:,2,n1)))/
```

```
        ↪ np_temp;
    ave_intensity(n1,3) = sum(sum(rgb_image_masked(:,:,3,n1)))/
        ↪ np_temp;

    intensity_proportion(n1,1) = ave_intensity(n1,1)/sum(
        ↪ ave_intensity(n1,:));
    intensity_proportion(n1,2) = ave_intensity(n1,2)/sum(
        ↪ ave_intensity(n1,:));
    intensity_proportion(n1,3) = ave_intensity(n1,3)/sum(
        ↪ ave_intensity(n1,:));

end

intensity_proportion(isnan(intensity_proportion)) = 0;

ave_proportion(1) = mean(nonzeros(intensity_proportion(:,1)));
ave_proportion(2) = mean(nonzeros(intensity_proportion(:,2)));
ave_proportion(3) = mean(nonzeros(intensity_proportion(:,3)));

np = sum(x ~= 0);
rgb_per_particle = zeros([max(np),3,length(min_frame:max_frame)]);
proportion_per_particle = zeros([max(np),3,length(min_frame:
    ↪ max_frame)]);

particle_type = zeros([max(np),length(min_frame:max_frame)]);
x = x(1:max(np),:);
y = y(1:max(np),:);
```

```
b1 = load('ave_proportion_movf');
b1 = b1.ave_proportion;
b2 = load('ave_proportion_movh');
b2 = b2.ave_proportion;


for n1 = min_frame:max_frame

    rgb_values_temp = rgb_values(nonzeros(x(:,n1)),nonzeros(y(:,n1
       ↪ )),pixel_index,double(rgb_image(:,:,:,n1)));
    rgb_per_particle(1:size(rgb_values_temp,1),1:size(
       ↪ rgb_values_temp,2),n1) = rgb_values_temp;
    proportion_per_particle(1:size(rgb_values_temp,1),1:size(
       ↪ rgb_values_temp,2),n1) = rgb_values_temp./sum(
       ↪ rgb_values_temp,2);

    a = proportion_per_particle(:,:,n1);

    score1_temp = sum(a.*b1,2)./(sqrt(sum(a.^2,2))*sqrt(sum(b1.^2)
       ↪ ));
    score2_temp = sum(a.*b2,2)./(sqrt(sum(a.^2,2))*sqrt(sum(b2.^2)
       ↪ ));
    type1_temp = score1_temp >= score2_temp;
    type2_temp = score2_temp > score1_temp;
    particle_type_temp = 1*type1_temp + 2*type2_temp;
    particle_type(1:max(np),n1) = particle_type_temp;
```

```
end

type1_count = sum(particle_type == 1);
type2_count = sum(particle_type == 2);
```

Appendix C

Supplementary Information for Published Papers

The following section is reproduced in part with permission from: Yifat, Yuval, Delphine Coursault, Curtis W. Peterson, John Parker, Ying Bao, Stephen K. Gray, Stuart A. Rice, and Norbert F. Scherer. Reactive optical matter: light-induced motility in electrodynamically asymmetric nanoscale scatterers. *Light: Science & Applications 7, no. 1 (2018): 1-7.*

Supporting Information: Reactive optical matter: light-induced motility in electrodynamically asymmetric nanoscale scatterers

Yuval Yifat,[†,⊥] Delphine Coursault,[†,⊥] Curtis W. Peterson,[†,‡,⊥] John Parker,[†,¶,⊥]
Ying Bao,[†,§] Stephen K. Gray,[∥] Stuart A. Rice,[†,‡] and Norbert F. Scherer[*,†,‡]

†*James Franck Institute, The University of Chicago, 929 E. 57th Street, Chicago, Illinois 60637, USA*

‡*Department of Chemistry, The University of Chicago, 929 East 57th Street, Chicago, Illinois 60637, USA*

¶*Department of Physics, The University of Chicago, 929 East 57th Street, Chicago, Illinois 60637, USA*

§*Present address: Department of Chemistry, Western Washington University, 516 High Street, Bellingham, WA 98225, USA*

∥*Center for Nanoscale Materials, Argonne National Laboratory, 9700 South Cass Avenue, Argonne, Illinois 60439, USA*

⊥*These authors contributed equally*

E-mail: nfschere@uchicago.edu

Experimental setup

A diagram of the setup used to trap the 150nm and 200nm Ag nanoparticles is shown in Figure S1(a). The setup consisted of a continuous wave Ti:sapphire laser emitting linearly polarized light at a wavelength of 790 nm. The beam was collimated and reflected off a spatial light modulator (SLM; BNS/Meadowlark HSPDM512-785nm), which was used to shape the beam by imparting the phase necessary for a ring trap. The phase mask used in the experiment is shown in Figure S1(b). The beam was reflected from a dichroic mirror and into an inverted optical microscope (Nikon Ti), through a quarter wave plate, which is used to control its polarization (*i.e.* convert from linear to circular), and through a 60x IR corrected water immersion objective (Nikon 60x Plan APO IR water immersion objective, NA=1.27). The total optical power of the trapping laser measured before the dichroic mirror was 150 mW, giving a power density of $1.5\,\mathrm{MW\,cm^{-2}}$ at the focus.

Figure S1(c) is an image of the ring trap. In order to measure the beam dimensions we removed the near-IR filter before the sCMOS detector (Andor Neo; 6.5 μm pixel size) and imaged the reflection of the beam off the coverslip. The beam was focused slightly beneath the top coverslip. The ring was measured to have a radius of 3.4 μm and a 500 nm width (i.e. FWHM) of the annulus. In addition to the ring trap that was used in the experiments, there was a noticeable focused Gaussian beam in the center of the ring trap (i.e. a zero-order reflection from the SLM) that had no effect on the experimental results due to its large distance (R=3.4 µm) from the particle locations on the ring.

The beam was focused into a sample cell that was filled with a solution of 150 nm and 200 nm silver nanoparticles coated with polyvinylpyrrolidone (PVP). The stock solutions were diluted in 18 MΩ DI water at a ratio of 1:200. The particles were illuminated using a dark-field condenser, and the light they scattered was captured by the objective and imaged onto a sCMOS detector with a total magnification of 90x, giving an effective pixel size of 72 nm. The particle motion was captured in a 120x120 pixel region of interest on the detector with an exposure time of 1 ms at a frame rate of 289 frames per second.

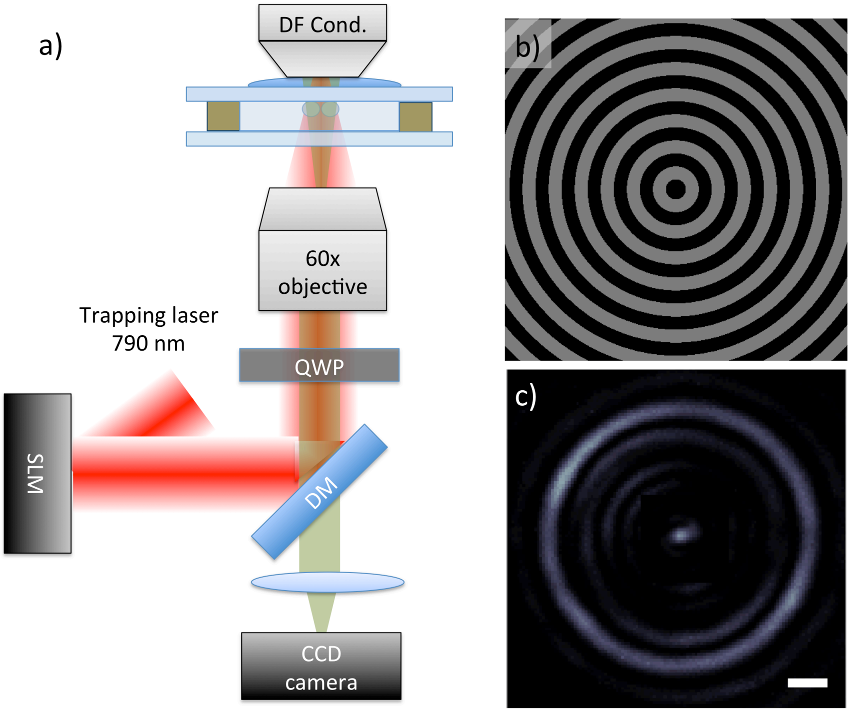

Figure S1: (a) Diagram of experimental trapping setup described in the text. SLM-Spatial Light Modulator, DF Cond. - Dark-field condenser, DM - Dichroic mirror. QWP Quarter wave plate. Trapping laser is reflected from the SLM which is used for beam shaping. Dark-field (high N.A.) illumination that scatters from the Ag nanoparticles is collected by the microscope objective, spectrally filtered and imaged to a sCMOS array detector. (b) The phase mask used to create the ring trap used in our experiments. The phase mask only uses two phase levels (black pixel level = 0 phase shift, gray pixel level = π phase shift). (c) Image of the ring trap on the sCMOS detector. The Gaussian spot in the center is the zero-order reflection of the trapping laser from the SLM. The spot did not affect our experiments due to the large diameter of the trap. Scale bar is 1μm.

Characteristics of Ag nanoparticles

The particles used for the trapping experiments described in the main text are an equal mixture of 150 nm diameter and 200 nm diameter PVP coated silver nanoparticles (NanoComposix; 150 nm diameter: NanoXact Silver KJW1882 0.02 mg ml^{-1}; 200 nm diameter: NanoXact Silver DAC1326 0.02 mg ml^{-1}). Each stock solution was diluted in DI water (at a ratio of 1:200) and equal volumes were combined.

The identification of the different sized particles was achieved by analyzing their relative brightness and size on the sCMOS detector. See Figure S2(a,c) for representative images of a 150 nm (Fig S2(a)) and a 200 nm (Fig S2(c)) Ag nanoparticle imaged with our optical setup. The visual difference between the two particle images was verified as being due to their physical size by a spectroscopic measurement. Individual particles were captured in a Gaussian trap and the light scattered from them was directed through the side port of the microscope, into a spectrometer (Andor Shamrock 193 imaging spectrograph; SR 193i-B1-SIL), and detected with an EM-CD array detector (Andor Newton).

Figure S2(b,d) shows the spectral measurement for the particles imaged in Figure S2(a,c) along with the expected scattering cross-section calculated from Mie theory[S1]. As can be seen in Figure S2(b), the spectral measurement from a trapped 150 nm diameter Ag nanoparticle is in agreement with the calculated Mie scattering spectrum. The abrupt decrease in signal at 750 nm is due to a near-IR filter placed after the dichroic mirror to block the reflected laser light. On the other hand, Figure S2(d) shows that the the spectral response of the 200 nm Ag nanoparticle is blue-shifted compared to the expected theoretical scattering for a 200 nm particle, and is in closer agreement with the spectrum calculated for a 175 nm Ag nanoparticle. Repeating this experiment for different particles showed a variance in the measured spectral response from the 200 nm particles, and a consistent spectral result from the 150 nm particles.

The plethora of spectra for 200 nm diameter Ag nanoparticles implies dispersion in size or shape or both. This size (shape) dispersion was confirmed by electron microscopy imaging of

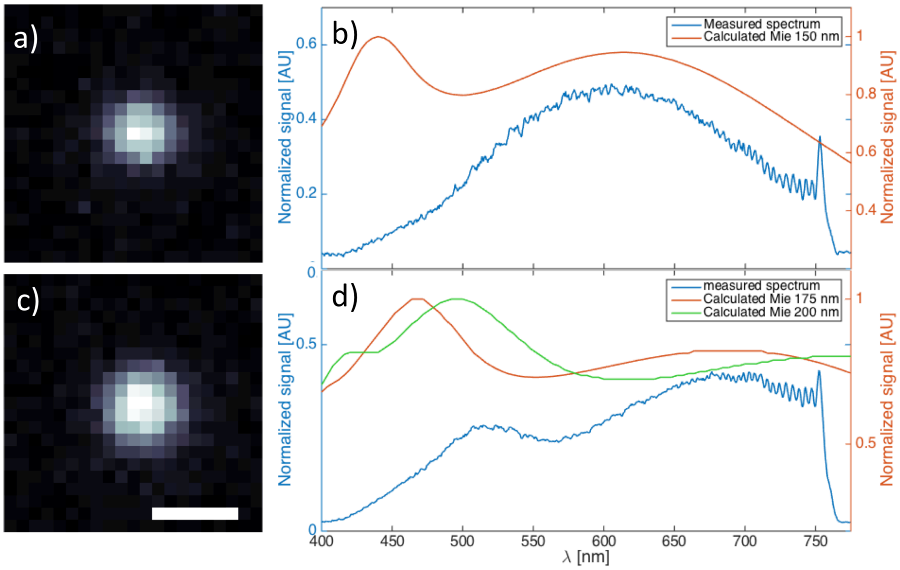

Figure S2: (a) Representative image of a 150 nm diameter Ag nanoparticle trapped in a Gaussian beam. (b) Measured scattering spectrum (blue) from the 150 nm diameter particle shown in panel (a) as well as the calculated theoretical Mie scattering for 150 nm diameter Ag nanoparticle suspended in water (red). Spectra were measured by directing the scattered light through the side port of the inverted optical microscope to a spectrometer. The abrupt drop in signal from 750 nm is due to a near-IR notch filter used to block scattered light from and reflections of the trapping beam reaching the detector. Conversely, light from 500 - 750 nm was used to image the nanoparticles by dark-field microscopy. (c) Representative image of a 200 nm diameter Ag nanoparticle trapped in a Gaussian beam. Intensity scales of images (a) and (c) are identical. Scale bar is 500 nm and applies to (a) and (c). (d) Measured scattering (blue) from the 200 nm diameter particle shown in panel (c) as well as calculated theoretical Mie scattering for 175 nm (red) and 200 nm (green) diameter Ag nanoparticles suspended in water.

the different sized nanoparticles. The particles were drop cast on a copper grid and imaged using a Transmission Electron Microscope (TEM; FEI Tecnai F30 300kV FEG) using a magnification of 145,000x (see Fig S3(a,c)). The 150 nm Ag particles are uniform in size and nearly spherical in shape (but with facets), whereas the 200 nm particles were noticeably less spherical and less uniform in size.

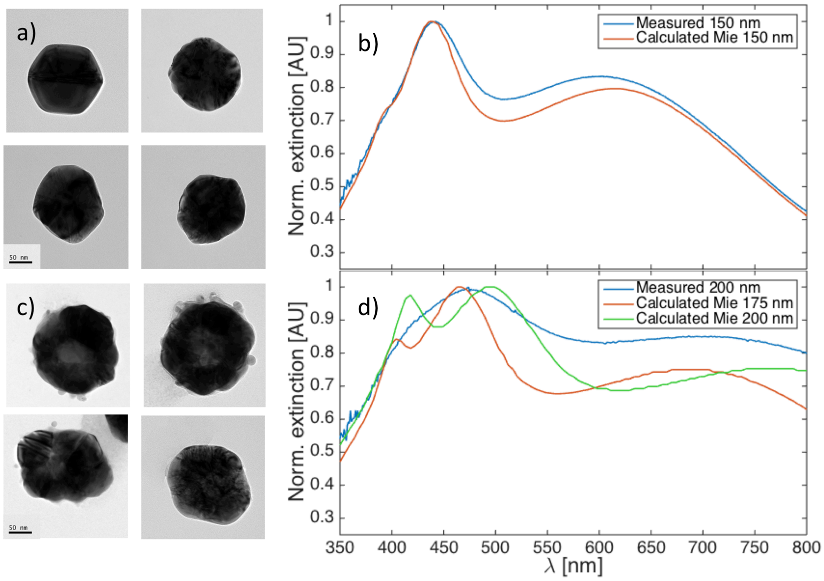

Figure S3: Transmission electron microscopy (TEM) and spectral analysis of Ag nanoparticles. (a) TEM images of 150 nm diameter Ag nanoparticles dispersed on a copper grid. Scale bar is 50 nm. (b) Normalized extinction spectrum of 150nm diameter Ag nanoparticle stock solution taken with a UV-Vis-IR spectrophotometer (blue curve). Peak maxima at 440 nm and 600 nm correspond to the dipole and quadrupole Mie scattering modes of a 150 nm diameter silver particle immersed in water (calculated values given as the red curve). (c) TEM images of 200 nm diameter Ag nanoparticles dispersed on a copper grid. Note the larger variance in size and shape. Scale bar is 50 nm. (d) Normalized extinction spectrum of 200nm diameter Ag nanoparticle stock solution taken with a UV-Vis-IR spectrophotometer (blue curve). Peak maxima are at 475 nm and 700 nm. Green and red curves respectively correspond to calculated Mie extinction spectra of a 175 nm and 200 nm diameter silver particle immersed in water. Note the broad width of measured peak compared to that of the the calculated values and the measured value from panel (b), implying a dispersion in particle diameters (and shapes) in the stock solution.

We also measured the ensemble extinction of the two stock solutions using a Cary 5000 UV/Vis/IR spectrophotometer (see Fig S3(b,d)). For the 150 nm diameter Ag nanoparticle solution we observed peaks at 440 nm and at 600 nm (blue curve in Fig S3(b). As there is good agreement between the measured and calculated resonance locations, these extinction peaks are assigned as the dipole and quadrupole modes calculated from Mie extinction of a silver particle of the same diameter immersed in water (red curve). However, for the 200 nm diameter Ag nanoparticle stock solution, we observed much broader extinction peaks at 475 nm and 700 nm (blue curve in Figure S3(d)). These peaks are wider than expected for a monodisperse suspension of Ag nano particles with a diameter of 175 or 200 nm (compare to red and green curves in Figure S3(d)). This implies that the solution is not monodisperse and is an ensemble of many different particle diameters with a mean value of around 180 nm. The reason for this non-uniformity results from the well-established difficulty in synthesis of Ag nanoparticles larger than 150 nm[S2].

Despite their non-uniformity, the "200 nm" Ag particles are consistently larger than their 150 nm counterparts and this size difference manifests itself in the non-reciprocal dynamics shown in the main text.

Theoretical description of non-reciprocal forces

An expression for the net optical force on a dimer (of spherical isotropic particles A and B) in a plane transverse to the propagation of plane-wave illumination can be obtained in the point dipole approximation. The component of the electric field in the i direction at particles A and B (at only the first order of scattering)[S3] is

$$E_A^i = E_0^i + G_{ij}^{AB} E_0^j \alpha^B; \quad E_B^i = E_0^i + G_{ij}^{BA} E_0^j \alpha^A \tag{S1}$$

where E_0^i is the incident electric field, α^A or α^B is the polarizability of particle A or B, and G_{ij}^{AB} are the elements of the dyadic Green's function for the vector between particles A and

B. If we assume that the particles lie on the x axis, only the diagonal elements of G_{ij}^{AB} are non-zero. For a circularly polarized plane wave propagating in the z direction this leads to a net force in the x direction F_x^{net} on the dimer

$$F_x^{net} = \frac{E_0^2}{2}\mathrm{Re}\left[(\alpha^{A*}\alpha^B - \alpha^A\alpha^{B*})\frac{\partial}{\partial x}(G_{xx}+G_{yy}) + (\alpha^{A*}|\alpha^B|^2 - |\alpha^A|^2\alpha^{B*})\left(\frac{\partial G_{xx}}{\partial x}G_{xx}^* + \frac{\partial G_{yy}}{\partial x}G_{yy}^*\right)\right]. \tag{S2}$$

This equation extends the treatment derived in *Sukhov et. al.*[S4] from particles trapped in a linearly polarized plane wave to a plane wave with circular polarization.

The corresponding result for a pair of particles (point dipoles) interacting in a beam linearly polarized along the x-axis (inter-particle axis) is

$$F_x^{net} = \frac{E_0^2}{2}\mathrm{Re}\left[(\alpha^{A*}\alpha^B - \alpha^A\alpha^{B*})\frac{\partial G_{xx}}{\partial x} + (\alpha^{A*}|\alpha^B|^2 - |\alpha^A|^2\alpha^{B*})\left(\frac{\partial G_{xx}}{\partial x}G_{xx}^*\right)\right], \tag{S3}$$

which after rearrangement is identical to the result in *Sukhov et al*[S4] except for a factor accounting for infinite-order interactions between the two particles. The additional factors of $\frac{\partial G_{yy}}{\partial x}$ and $\frac{\partial G_{yy}}{\partial x}G_{yy}^*$ in equation S2 for the case of circular polarization affect the dependence of the derived forces on interparticle separation. However, equations S2 and S3 are qualitatively similar. Both equations equal zero when $\alpha^A = \alpha^B$, in accordance with the experimental and simulation results presented in the main text. In fact, both expressions vanish if the two polarizabilities are proportional by a factor of a real number (e.g. $\alpha^A = C\alpha^B$ where C is a real number). *Therefore, it is necessary that the α^A and α^B have different angles in the complex plane for the non-reciprocal forces to exist within this approximation.* In summary, our analytical results show that non-reciprocal forces arise in pairs of particles with dissimilar polarizabilities under both linear and circular polarization, although the exact spatial dependence of these forces is different for those two cases.

Analysis of combined particle trajectories

We performed 11 independent experiments, each of which was 7,000 frames in length. Of these experiments we limited our analysis to frames in which we observed two particles in the trap without another particle nearby. We then used the intensity information from the sCMOS detector to identify whether the particle pair was a homodimer (5 experimental videos, 8,500 total frames) or a heterodimer (12 experimental videos, 18,900 total frames).

From each video frame we localized the particle centroids using particle-tracking algorithms (*e.g.* Mosaic in ImageJ[S5])and used their positions to calculate the interparticle separation θ_c. The motion of their mean angular position (or "center of geometry") ω_c was calculated by how much their mean angle changed between consecutive frames, *i.e.* for frame n, we define $\omega_{c,n} = \frac{\Delta\theta_n}{\Delta t} = \frac{\theta_{c,n+1}-\theta_{c,n}}{\Delta t}$ where $\theta_{c,n}$ is the mean angular position of the two particles in frame n, and Δt is the time step. This data was binned by interparticle separation, d_{12}, and used to produce the plots of ω_c as a function of d_{12} in Fig 2(b,c). By plotting the motion of the central interparticle angle as a function of interparticle separation we found the mean rotational velocity of a homodimer (Fig 2b in the main text) and a heterodimer (Fig. 2c in the main text). Fig S4 shows the distribution of ω_c along with the Gaussian fit for the homodimers and the heterodimers. The FWHM of the Gaussian fits are due to the thermal Brownian fluctuations inherent in the experiment. It is important to note that the error bars shown in Figure 2(b,c) in the main text are the 3σ confidence interval for the center of the Gaussian fits, and thus, despite the width of the Gaussian distribution, its central ω_c value is statistically significant.

The MSD results and the fitted transport exponents, α, for the entire homodimer and heterodimer dataset (*i.e.* $MSD(\theta_c|\forall d_{12})$, where d_{12} is the interparticle separation) were calculated by aggregating the trajectories from the entirety of the experimental videos identified above (*i.e.* all 8,500 homodimer video frames or 18,900 heterodimer video frames). These MSD curves are shown in the main text as the black and orange curves in Fig. 2(d).

Calculation of the MSD for cases where the particles were optically bound (*i.e.* $MSD(\theta_c|d_{12} <$

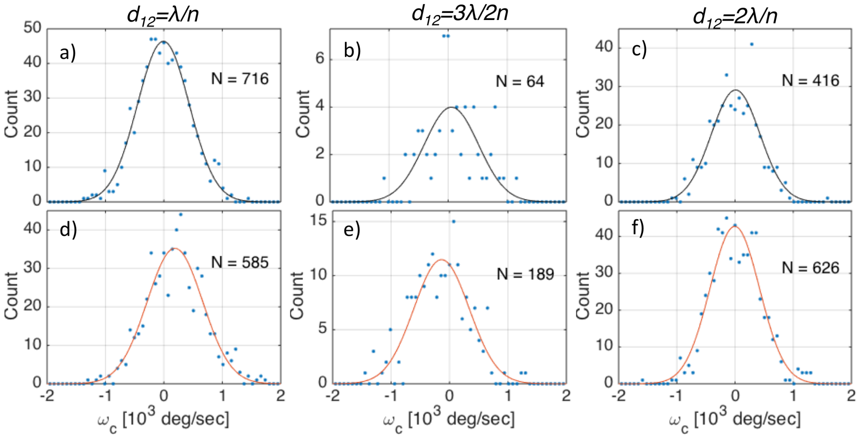

Figure S4: Distributions and Gaussian fits to the homodimer (a-c) and heterodimer (d-f) dimer velocity, ω_c, data shown in the main text in Figure 2(c,d). Different columns represent particles separated by one optical binding distance (a,d), 1.5 optical binding distance (b,e) and two optical binding distances (c,f). (a) Histogram of instantaneous angular velocity, ω_c, for homodimers where the particles are at one optical binding separation ($450 \leq d_{12} < 750$ nm). Center of the Gaussian curve is at -9 ± 26 deg s^{-1} (mean ± S.D). (b) Homodimer velocity data for the first unstable separation (($750 \leq d_{12} < 1050$ nm). Center of Gaussian fit is at 54 ± 130 deg s^{-1}. (c) Homodimer velocity data for the second optical binding separation (($1050 \leq d_{12} < 1350$ nm). Gaussian center is at 11 ± 52 deg s^{-1}. (d) Histogram of instantaneous angular velocity, ω_c, for heterodimers where the particles are at one optical binding separation ($450 \leq d_{12} < 750$ nm). Center of the Gaussian fit (orange curve) is at 190 ± 50 deg s^{-1}. (e) Heterodimers velocity data for the first unstable separation (($750 \leq d_{12} < 1050$ nm). Center of Gaussian fit is at -136 ± 70 deg s^{-1}. (f) Heterodimers velocity data for the second optical binding separation (($1050 \leq d_{12} < 1350$ nm). Center of Gaussian fit is at 5 ± 40 deg s^{-1}. The values of N in each panel indicate the total counts (events) in each histogram.

1.2 µm)) was done by selecting and analyzing the portions of the experimental trajectories where the interparticle separation was small enough for the particles to interact electrodynamically. Fig S5 shows the trajectories of 9 bound homodimers (a) and 12 bound heterodimers (b) from our experimental set. The start time of the trajectories was selected as when the interparticle separation was less than two optical binding separations (1.2 µm), and ended when the interparticle separation was greater than 1.5 µm for more than one time step. These values were chosen to allow analysis of cases in which the particles fluctuated away from optical binding separation for short periods of time. Fig S5(c,d) shows the calculated MSD values of the trajectories shown in Fig S5(a,b), as well as the mean MSD (connected grey diamonds) obtained by aggregating over the all the bound homodimer or heterodimer trajectories. The aggregated MSD curve for the bound heterodimer is identical to the orange curve shown in Figure 2(d) the main text. The Mean homodimer MSD shown in Fig S5(c) has a slightly different exponent than that of the entire homodimer population regardless of separation (black curve in Fig 2(d) in the main text). The reason for the slight difference between the exponent values ($\alpha = 0.96$ vs. $\alpha = 1.0$) is that the MSD shown in Fig S5(c) was fitted only to the trajectories in which the particles are at optical binding (*i.e.* $d_{12} \leq 1.2$ μm). Conversely, the exponent shown in Fig 2(d) in the main text was obtained by fitting the *entire* trajectory information. Trajectories that are shorter than 35 time steps (roughly 0.1s) are not shown in Figure S5. The value of α was unchanged whether or not the trajectories shorter than 35 time steps were used to calculate the MSD in addition to the longer trajectories.

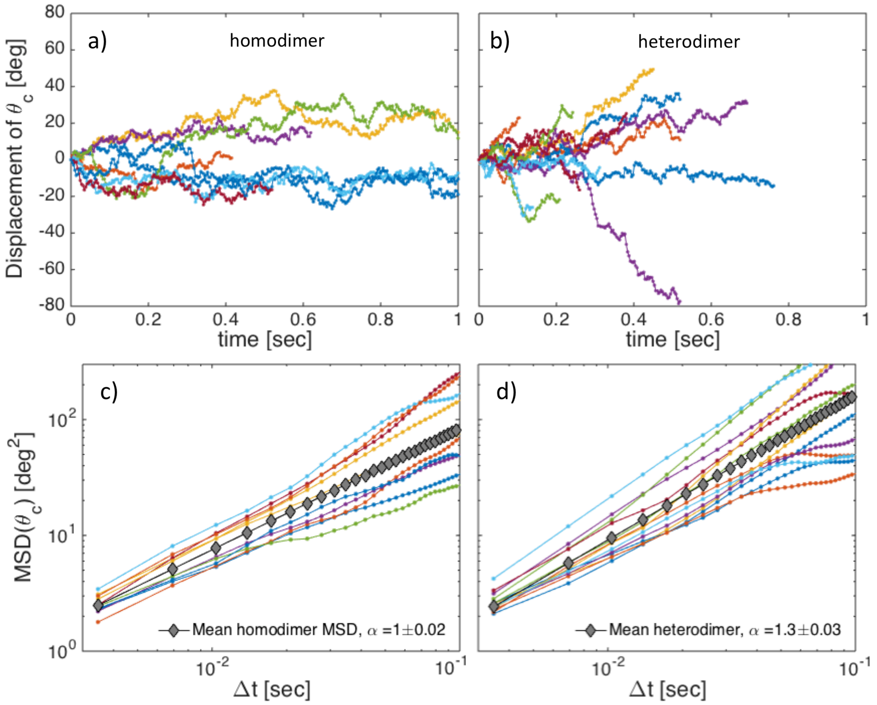

Figure S5: Experimental trajectories and MSD calculations for bound homodimers and heterodimers. (a-b) Time series of angular displacement for homodimers (a) and heterodimers (b). Trajectories were started when the particles were separated by less than 1.2 µm, and ended when the particles were separated by more than 1.5 µm for longer than one time step. This was done to include trajectories in which the particles fluctuate out of optical binding for short periods of time and to allow aggregation of long trajectories. Particle size was determined from the scattering intensity recorded by the sCMOS detector. (c-d) MSD values of trajectories for homodimer (c) and heterodimer (d). The different colors correspond to the trajectories shown in panels (a,b). The mean MSD value (marked as gray connected diamonds) is the mean MSD calculated from all the individual trajectories shown in (a,b). The mean heterodimer MSD is identical to that shown in the Figure 2(d) in the main text.

The MSD calculated from a single heterodimer trajectory demonstrates the driven nature of the heterodimer motion[S6]. Figure S6 shows an example of the MSD calculated from a single heterodimer trajectory (specifically the trajectory of the heterodimer driven in the CW direction motion shown in Fig 2(a) in the main text), along with a quadratic fit that signifies driven motion.

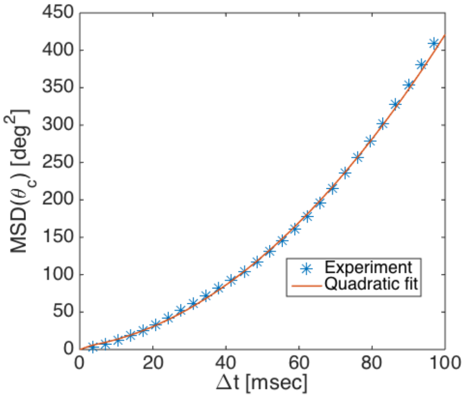

Figure S6: MSD calculated from a single heterodimer trajectory, specifically the CCW heterodimer trajectory shown in Fig 2(a) in the main text. The MSD was fitted with a quadratic function, demonstrating the driven nature of the motion.

Effect of nanoparticle heating

It is well established that micro- and nano-scale Janus particles exhibit driven motion through self-thermophoresis.[S7,S8] A Janus particle is usually designed so that half of its surface area is coated with a material such as Au which absorbs the laser light. When such a particle is illuminated it will heat the environment around the coated area and exhibit driven motion towards its cooler, uncoated side due to increased thermal fluctuations on the heated side. The driven motion we observe in this manuscript is significantly different from self-thermophoretic motion. In this section we will describe the observed differences between self thermophoresis and electrodynamically driven motion.

The first important point: if the cause of the motion of the heterodimer were solely due to self-thermophoresis, one would expect that increasing the interparticle separation would cause a monotonic decrease in the driven component of the pair. Essentially, as the inter-particle separation increases, they become less like a Janus particle and more like 2 independent particles so the driven component in their motion should decrease. However, as we show in Fig. 2c in the main text, when the particles are separated by $3\lambda/2$ we observe a statistically significant motion in the *opposite* direction (*i.e.* towards the smaller particle). This change in the direction of the directed motion cannot be explained by self-thermophoresis, and supports our observation that the motion is due to oscillatory electromagnetic interaction.

Another distinction from self-thermophoresis is the direction of the directed motion. We can calculate the heating of the particles in the trap using the methods described in the literature[S9]. The excess temperature of the environment, ΔT_{NP}, around a nanosphere trapped in water near the glass coverslip is defined as $\Delta T_{NP} = \sigma_{abs} I / 4\pi R \kappa_{glass}$, where σ_{abs} is the absorption cross section of the nanoparticles (1.96×10^3 nm^2 and 3.09×10^3 nm^2 for the 150 nm and 200 nm diameter nanoparticles respectively), I is the incident laser intensity ($1.5\,\mathrm{MW\,cm^{-2}}$), R is the particle radius and κ is the thermal permittivity of glass ($1.4\,\mathrm{W\,(m\cdot K)^{-1}}$), which is the dominant avenue for heat removal in our system. The result of this calculation is that the temperature difference between the particles is small ($\Delta T_{200nm} = 26.3^0$, $\Delta T_{150nm} = 22.3^0$). This slight temperature difference leads to a slight difference in dynamic viscosity of the water (0.52mPa for the 200nm nanoparticles, 0.56 mPa for the 150 nm diameter nanoparticles). If we consider only water as the sink for thermal energy from the nanoparticles ($\kappa = 0.6\,\mathrm{W}\,(\mathrm{m}\cdot\mathrm{K})^{-1}$), the particle temperature will be higher ($\Delta T_{200nm} = 61.3^0$, $\Delta T_{150nm} = 52.0^0$) and the viscosity will be lower (0.32mPa for the 200nm nanoparticles, 0.36mPa for the 150 nm diameter nanoparticles). Even in this regime, the temperature and viscosity difference between the two particles is not strikingly large.

Note that it is is not straightforward to consider our system as a Janus particle because the particles are not physically bound to each other and the separation between them changes. In addition, due to their separation ($\sim$ 600 nm), the temperature around each individual particle will be roughly uniform. The reason for this is that the gap between the particles is significantly larger than their individual size and thus the medium directly around them will be affected, to first approximation, by the heating of the individual particles (see treatment of particle pairs in G. Baffou et al[S9].

Nevertheless, even if we take the temperature difference between the particles as the cause of the driven motion, the observed motion direction is the *opposite* to what is expected for a Janus particle in water. The driven motion we have observed is towards the large particle, which is the slightly warmer particle and experiences a smaller local viscosity. In other words, based on the observed motion the Soret coefficient of our system (defined as $S_T = D_T/D$, where D is the diffusion coefficient and D_T is the thermodiffusion coefficient) is negative. By contrast, previous papers reported a positive Soret constant (*e.g.* motion of the Janus particle towards the cooler side) when the particle was placed in water[S8,S10,S11]. While it is possible to obtain a negative Soret coefficient by adding a surfactant to the water or by decreasing the water temperature, we performed our experiment in pure DI water and at room temperatures, and we do not anticipate a negative Soret coefficient.

Thus, the nature of the motion that we observe $-$ the direction of the dimer motion towards the larger, hotter particle, and the dependence of the driven motion direction on interparticle separation − suggest that the driving force is not thermophoretic in nature. We conclude that the reason for the driven motion is the electrodynamic interaction between the particles, in agreement with previous theoretical work and with our simulations.

Simulation methods

Force evaluation through Generalized Mie Theory

The electrodynamic interactions are computed using the Generalized Mie Theory (GMT) method.[S12,S13] In GMT, the incident and scattered fields are expanded into the vector spherical harmonic (VSH) functions for each particle. The incident field is expanded into the regular VSH's $\boldsymbol{N}_{nm}^{(1)}$ and $\boldsymbol{M}_{nm}^{(1)}$,

$$\boldsymbol{E}_{\text{inc}}^{j} = -\sum_{n=1}^{L_{\max}} \sum_{m=-n}^{n} \mathrm{i}E_{mn} \left[p_{mn}^{j} \boldsymbol{N}_{nm}^{(1)} + q_{mn}^{j} \boldsymbol{M}_{mn}^{(1)} \right] \tag{S4}$$

where $L_{\max}$ is the maximum number of multipole orders to expand in, E_{mn} is a normalization constant, and p_{mn} and q_{mn} are the expansion coefficients to be solved for. The scattered field is expanded into the scattering VSH's $\boldsymbol{N}_{nm}^{(3)}$ and $\boldsymbol{M}_{nm}^{(3)}$,

$$\boldsymbol{E}_{\text{scat}}^{j} = -\sum_{n=1}^{L_{\max}} \sum_{m=-n}^{n} \mathrm{i}E_{mn} \left[a_n^j p_{mn}^{j} \boldsymbol{N}_{nm}^{(3)} + b_n^j q_{mn}^{j} \boldsymbol{M}_{mn}^{(3)} \right] \tag{S5}$$

where a_n^j and b_n^j are the ordinary Mie coefficients[S14] of particle j.

The expansion coefficients are solved for a system of $2NL_{\max}(L_{\max}+2)$ equations,

$$\begin{aligned} p_{mn}^{j} &= p_{mn}^{(j\to j)} - \sum_{l\neq j}^{(1,N)} \sum_{v=1}^{L_{\max}} \sum_{u=-v}^{v} A_{mn}^{uv}(l\to j) a_v^l p_{uv}^l + B_{mn}^{uv}(l\to j) b_v^l q_{uv}^l \\ q_{mn}^{j} &= q_{mn}^{(j\to j)} - \sum_{l\neq j}^{(1,N)} \sum_{v=1}^{L_{\max}} \sum_{u=-v}^{v} B_{mn}^{uv}(l\to j) a_v^l p_{uv}^l + A_{mn}^{uv}(l\to j) b_v^l q_{uv}^l \end{aligned} \tag{S6}$$

where $p_{mn}^{(j\to j)}$ and $q_{mn}^{(j\to j)}$ are the expansion coefficients of the incident source and $A_{mn}^{uv}(l \to j)$ and $A_{mn}^{uv}(l \to j)$ are VSH translation coefficients from particle l to particle j. Solving this system includes induced dipole interactions as well as many-body interaction terms.

Once the expansion coefficients are solved for, the force on each particle can be determined by integrating the Maxwell stress tensor (MST) $\boldsymbol{T}$ over the surface of each sphere,

$$\boldsymbol{F} = \oint_{\Omega} \boldsymbol{T} \cdot d\boldsymbol{\Omega} \tag{S7}$$

Figure S7 shows the angular scattering from a heterodimer with the indicated separations. The small triangles represent the centroid of the angular field distributions showing that the centroid shifts to the $-x$ or $+x$ direction depending on the interparticle separation. That is, the light scattering is asymmetrical due to the asymmetry of the heterodimer and its separation.

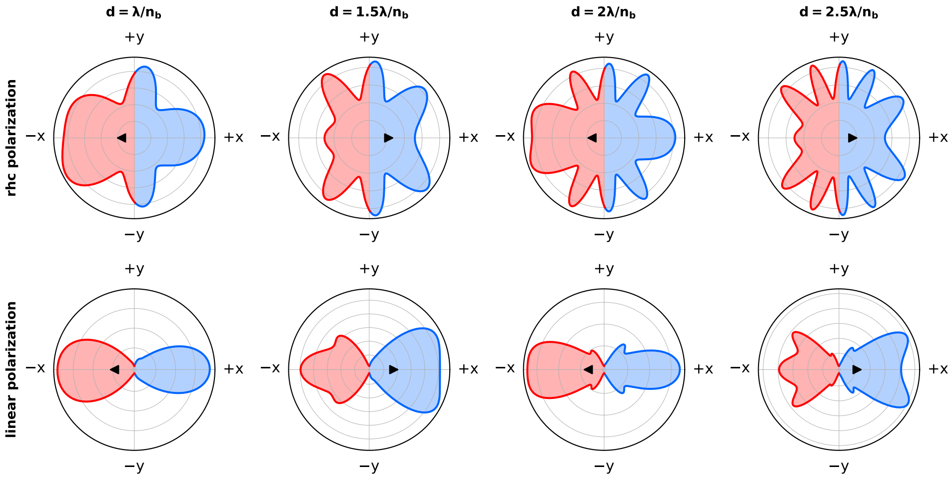

Figure S7: Angular scattering in the xy-plane for the hetero-dimer for different particle separations (integer and half integer multiples of the wavelength) and incident light polarization (right hand circularly polarized and linearly polarized along the y-axis). The black triangle is the centroid of the angular distribution and indicates the preferred direction of angular scattering. For separations equal to an integer multiple of the wavelength, more light is scattered in the $-x$ direction while for half integer multiples more light is scattered in the $+x$ direction.

Langevin equation of motion

The equation of motion for a 2-particle system undergoing dissipation and thermal noise is given by the Langevin equation

$$m_i \frac{d^2 \boldsymbol{r}_i}{dt^2} = \boldsymbol{F}_i(\boldsymbol{r}_i, t) - \lambda_i \frac{d\boldsymbol{r}_i}{dt} + \boldsymbol{\eta}_i \tag{S8}$$

where m_i is the mass of each nanoparticle, $\boldsymbol{F}_i$ is the electrodynamic force on each particle, $\lambda_i = 6\pi\nu R_i$ is the friction coefficient (ν is the dynamic viscosity of water), and $\boldsymbol{\eta}_i$ is a Gaussian noise term such that the fluctuation-dissipation theorem holds. Equation (S8) is integrated in time using a leap-frog Verlet integrator[S15] to give the trajectories of the nanoparticles.

Figure S8 shows the results of GMT-LD simulations of a 150-100nm diameter Ag dimer pair in a medium with the viscosity of water at T=300 K. The particles initially move to a separation of $\sim$ 600 nm (optical binding) and then the optically bound hetero-dimer moves as a "rigid body" towards the larger particle as in experiment. The slight wiggles in the trajectory reflect the Brownian (thermal) noise in the LD simulation.

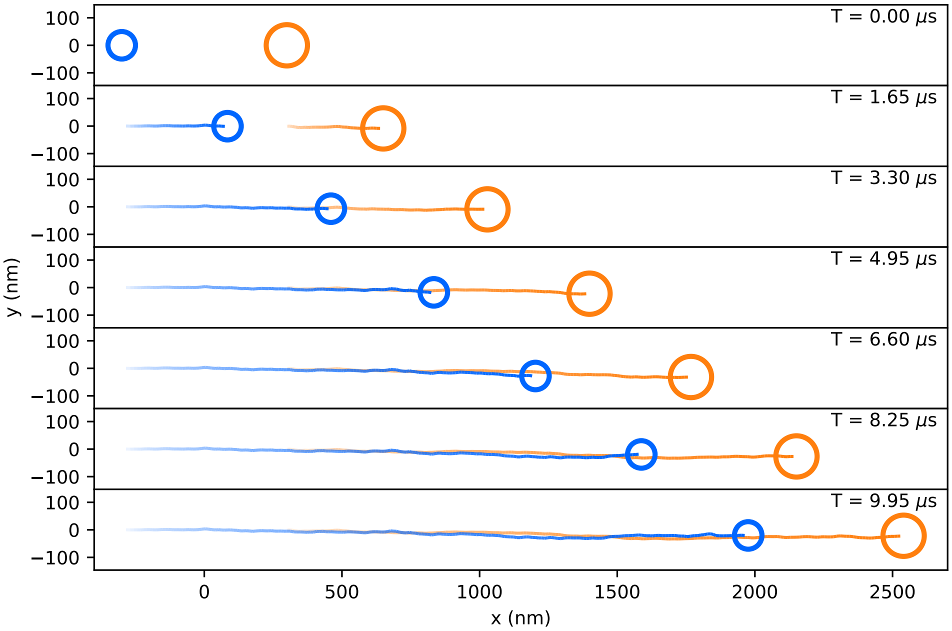

Figure S8: Trajectory snapshots of the simulated hetero-dimer using the GMT-LD method.[S16] The incident source is a y-polarized plane wave with no component of the Poynting vector in the xy-plane. The blue particle is 100 nm in diameter while the orange particle is 150 nm in diameter. A temperature of T = 300 K is used in a water medium (index of refraction n_b = 1.33). The motion of the hetero-dimer is a manifestation of the non-zero (non-reciprical) net electrodynamic force.

Characteristics of Au nanostars

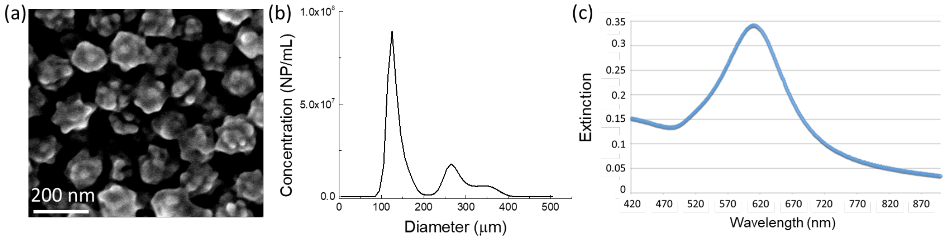

Figure S9: Characteristics of the gold nanostars. (a) Scanning electron microscopy image (SEM) images of Au nanostars. (b) Nanoparticle sizes were determined by tracking analysis (with Nanosight NS300-Malvern) reveal one major peak at 125nm diameter corresponding to the average diameter of single particles, and peaks at 265nm and 350nm. The latter reveals the significant presence of dimer and trimer aggregates in the solution. (c) Extinction spectra of the Au nanostar solution.

Characteristics of Au nanoparticle cluster

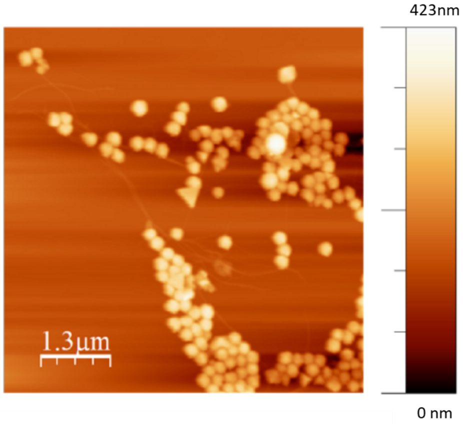

Figure S10: Characteristics of the Au nanospheres that form the large aggregate shown in Figure 4 of the main text. AFM image of the gold nanoparticles of 200nm diameter. Individual Au nanospheres as shown here are also present in the ring trap of Figure 4.

Driven motion of Au nano-star dimer and Au NP aggregate

While circularly polarized light provides isotropic excitation anywhere within the ring trap, we expect that the nanostar particles would spin (and a dimer would rotate) as has been demonstrated for an anisotropic nanoparticle such as a nanorod or nanowire, or nanosphere dimer in the near field interaction regime[S17,S18]. However, the confinement of the ring trap would hinder rigid-body type rotation. Therefore, since we want to focus on linear driven motion, it is desirable to prevent the emergence of a confounding effect such as spinning; even though understanding it will be an interesting separate study. Under linearly polarized light, the isotropic optical field-dimer interaction within the ring trap is broken. We expect the particles to align with the light polarization to minimize the induced torque, and to be driven due to asymmetric scattering. However, as mentioned above, the dimer cannot rotate as a rigid body, but thermal energy could cause internal rearrangements that essentially reverse the direction of the anisotropic polarizability causing a reversal in the direction of light scattering and of its motion. We observe that the dimer spends more time around $\Theta_c = 270^0$ (with an orientation parallel to the polarization). The nanostar dimer is able to rearrange because of the Brownian thermal noise.

We also studied the dynamics of an asymmetrical aggregate of spherical NPs. There is a noticeable difference in the dynamics of the Au NP aggregate vs. that of the nanostar dimer. We believe this to result from the intrinsic scattering properties of the aggregate and the electrodynamic interactions between the aggregate and the many Au NPs present in the ring trap. In the trajectory shown from A to B in Figure 4e in the main text, the mean speed is as high as $384^o s^{-1}$ then decreases to $68^o s^{-1}$ from B to C and increases, after flipping orientation, up to $267^o s^{-1}$ between C and D. Furthermore, as shown in Figure S11, the aggregate is oriented perpendicular (near 270^o) and parallel (near 180^o) to the polarization before it flips. Several frames from the video that demonstrate this change in orientation are shown in Figure S11 for a location of the aggregate near 180^o in the ring. The speed of the cluster is non-linear, it decreases near 245^o which corresponds to the region where it electrodynamically "contacts" the many single Au NPs also trapped in the ring. By contrast, these interactions are negligible in the case of the nanostar dimer because of the lower particle density in the ring.

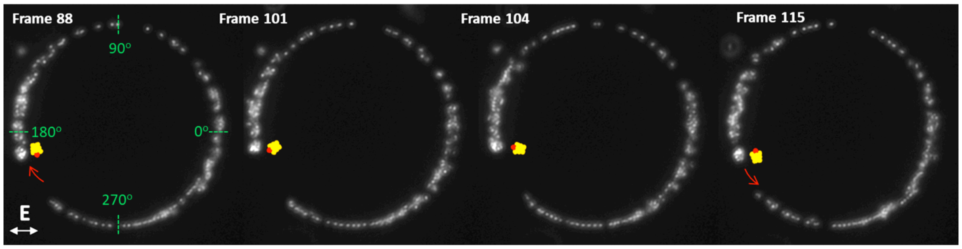

Figure S11: Dark field images of the Au NP aggregate and Au NPs optically trapped in the ring. Images are presented in chronological order showing the evolution of the cluster orientation around 200^o. Frame rate is 35fps. The dense groups of individual Au nanoparticles in the $< 180^0$ and $> 270^0$ regimes are due to a slight astigmatism.

The difference in the dynamics between the dimer and the aggregate is thus not only due the intrinsic scattering properties of the aggregates but also the result of the interaction of the aggregate with the optically bound Au NPs in the ring trap. The interactions reduce the net drift force even though the behavior of the aggregate is strongly super diffusive (see Figure 4f). Conversely, the interaction and driven motion of the Au NP aggregate affect the local NP density. As observed in the video, the Au cluster pushes the many single Au NPs inducing a compression of Au NPs in these two regions (around 180^o and 285^o). Notably, the aggregate does not proceed further presumably both because of the resistance of the Au NPs to further compression and also its interaction with the linearly polarized beam. We beleive the combination of factors cause the Au NP aggregate to rotate 180^o at these "turning points" and to then undergo the driven motion in the reverse direction until reaching the other turning piing.

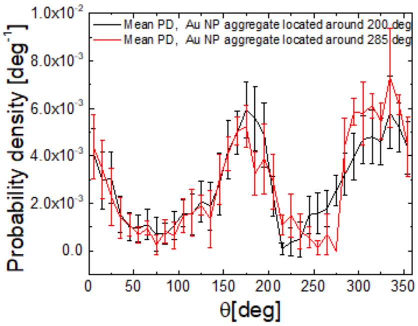

Figure S12: Evolution of the Au nanoparticle (NP) density in the ring. We show the average NP density depending on the two extreme positions of the aggregate in the ring trap. The local NP density is increased near the Au NP aggregate (i.e. near the 200^o and 270^o location). The error bars represent the standard deviation of the NP density.The Au NP density increases at angular values beyond where the Au NP aggregate goes due to its "sweeping" and forcing them into more compact angular regions of the ring.

As shown in Figure S12, our interpretation is supported by the average probability density calculated for the extreme position of the cluster. At 200^o (respectively 285^o), there is an increase (respectively a decrease) of the density of NPs around 180^o and a decrease (respectively an increase) of the density around 270^o when the Au NP aggregate is at 200^o (285^o) positions. Further investigation of the phenomenon is beyond the scope of the paper.

List of videos

Video S1 - video of homodimer in ring trap.

Video S2 - video of heterodimer in ring trap - motion in a CW direction

Video S3 - video of heterodimer in ring trap - motion in a CCW direction

Video S4 - video of the nanostar dimer in a ring trap.

Video S5 - video of Au nanoparticle cluster in the ring trap.

References

(S1) Horvath, H. Gustav Mie and the scattering and absorption of light by particles: Historic developments and basics. *Journal of Quantitative Spectroscopy and Radiative Transfer* **2009**, *110*, 787–799.

(S2) Bastus, N. G.; Merkoci, F.; Piella, J.; Puntes, V. Synthesis of highly monodisperse citrate-stabilized silver nanoparticles of up to 200 nm: kinetic control and catalytic properties. *Chemistry of Materials* **2014**, *26*, 2836–2846.

(S3) Dholakia, K.; Zemánek, P. Colloquium: Gripped by light: Optical binding. *Reviews of Modern Physics* **2010**, *82*, 1767–1791.

(S4) Sukhov, S.; Shalin, A.; Haefner, D.; Dogariu, A. Actio et reactio in optical binding. *Optics Express* **2015**, *23*, 247.

(S5) Sbalzarini, I. F.; Koumoutsakos, P. Feature point tracking and trajectory analysis for video imaging in cell biology. *Journal of structural biology* **2005**, *151*, 182–195.

(S6) Figliozzi, P.; Sule, N.; Yan, Z.; Bao, Y.; Burov, S.; Gray, S. K.; Rice, S. A.; Vaikuntanathan, S.; Scherer, N. F. Driven optical matter: Dynamics of electrodynamically coupled nanoparticles in an optical ring vortex. *Physical Review E* **2017**, *95*, 022604.

(S7) Golestanian, R.; Liverpool, T.; Ajdari, A. Designing phoretic micro-and nano-swimmers. *New Journal of Physics* **2007**, *9*, 126.

(S8) Jiang, H.-R.; Yoshinaga, N.; Sano, M. Active motion of a Janus particle by self-thermophoresis in a defocused laser beam. *Physical Review Letters* **2010**, *105*, 268302.

(S9) Baffou, G.; Quidant, R.; García de Abajo, F. J. Nanoscale control of optical heating in complex plasmonic systems. *ACS Nano* **2010**, *4*, 709–716.

(S10) Duhr, S.; Braun, D. Why molecules move along a temperature gradient. *Proceedings of the National Academy of Sciences* **2006**, *103*, 19678–19682.

(S11) Piazza, R.; Parola, A. Thermophoresis in colloidal suspensions. *Journal of Physics: Condensed Matter* **2008**, *20*, 153102.

(S12) Xu, Y.-l. Electromagnetic scattering by an aggregate of spheres. *Applied Optics* **1995**, *34*, 4573–4588.

(S13) Ng, J.; Lin, Z.; Chan, C.; Sheng, P. Photonic clusters formed by dielectric microspheres: Numerical simulations. *Physical Review B* **2005**, *72*, 085130.

(S14) Bohren, C. F.; Huffman, D. R. *Absorption and scattering of light by small particles*; John Wiley & Sons, 2008.

(S15) Birdsall, C. K.; Langdon, A. B. *Plasma physics via computer simulation*; CRC Press, 2004.

(S16) Sule, N.; Rice, S.; Gray, S.; Scherer, N. An electrodynamics-Langevin dynamics (ED-LD) approach to simulate metal nanoparticle interactions and motion. *Optics Express* **2015**, *23*, 29978–29992.

(S17) Sule, N.; Yifat, Y.; Gray, S. K.; Scherer, N. F. Rotation and Negative Torque in Electrodynamically Bound Nanoparticle Dimers. *Nano letters* **2017**, *17*, 6548–6556.

(S18) Shao, L.; Käll, M. Light-Driven Rotation of Plasmonic Nanomotors. *Advanced Functional Materials* **2018**, 1706272.

The following section is reproduced with permission from: Peterson, Curtis W., John Parker, Stuart A. Rice, and Norbert F. Scherer. Controlling the dynamics and optical binding of nanoparticle homodimers with transverse phase gradients. *Nano letters 19, no. 2 (2019): 897-903.* ©American Chemical Society

Supporting Information for Controlling the Dynamics and Optical Binding of Nanoparticle Homo-Dimers with Transverse Phase Gradients

Curtis W. Peterson,[†,‡] John Parker,[¶,‡] Stuart A. Rice,[†,‡] and Norbert F. Scherer*,[†,‡]

†*Department of Chemistry, The University of Chicago, Chicago, IL 60637*
‡*James Franck Institute, The University of Chicago, Chicago, IL 60637*
¶*Department of Physics, The University of Chicago, Chicago, IL 60637*

E-mail: nfschere@uchicago.edu

FORCE CALCULATIONS FOR SEVERAL PHASE GRADIENTS

We calculated the forces on each of two particles A (black) and B (red) as depicted in Figure 1a of the main text. The results are shown in Figure S1 for several regularly spaced phase gradients starting from $\xi = 0$ up to $\xi = 0.2$ in increments of $\xi = 0.025$, where $\xi = \frac{\partial \phi}{\partial R}$. Two general trends are apparent as ξ increases. The first is the force curves shift to larger force as ξ increases, corresponding to an overall larger driving force. The second is the increasing disparity in the separation dependence of the forces on each particle with increasing ξ. This progression shows the contrast between experiments with small ξ, where the optical binding locations are largely unchanged, and experiments with large ξ, where they are dramatically changed.

EXPERIMENTAL METHODS

A collimated laser beam from a Ti:Sapphire laser operating at 800nm (wavelength in vacuum) was reflected from a spatial light modulator (SLM; Meadowlark) adding a phase profile so that it formed a ring-shaped optical trap [1] when focused through a microscope objective (Olympus; APO 60x, water). A sample cell consisting of two glass cover-slips with a chamber formed by a spacer was filled with a dilute solution of 150nm dia. PVP-coated Ag nanoparticles (Ag NPs; Nanocomposix) in water. The sample was positioned so that the focus of the beam was close to the top cover slip. In this configuration the electrostatically charged PVP-coated Ag NPs become positioned close to the electrostatically charged upper glass cover slip at a distance

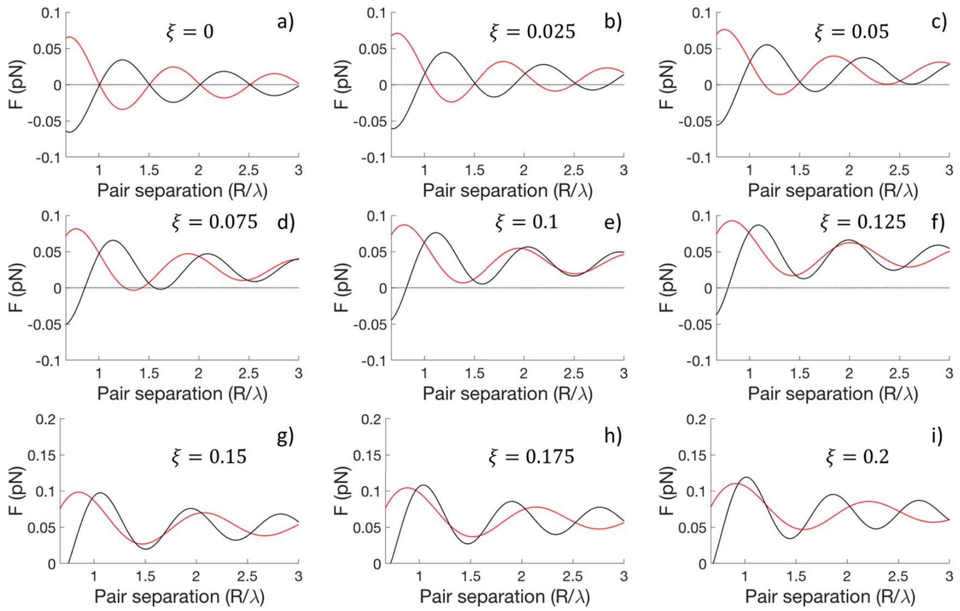

FIG. S1. (a)-(i) Calculated electrodynamic forces on two particles A (black) and B (red) for $\xi = 0$ - $\xi = 0.2$ in increments of $\xi = 0.025$.

where radiation pressure from the trapping laser is balanced by electrostatic repulsion from the cover slip [2]. The Ag NPs were, therefore, confined to a quasi-one-dimensional optical ring trap. The particles were imaged using dark-field video microscopy and tracked using the Mosaic particle-tracking suite in ImageJ. All of our experiments were carried out at low particle density (2-5 particles in the ring trap) so that our analysis could be carried out on particle pairs that were minimally disturbed by other nearby particles and our data was not conditioned on the location of a third particle. A representative example of the rad data is shown in Video S1.

An azimuthal phase gradient [2, 3] that depends on the topological charge, l, (the number of 2π phase wrappings around the ring) of the phase mask on the SLM can be added to the ring by encoding a suitable phase profile. The radius of the ring trap (r) and the phase gradient can be tuned independently, allowing a large range of experimentally accessible phase gradients to be applied.

For a sufficiently large ring, the curved path of the ring is approximately straight for distances relevant to our measurements and the direction of the phase gradient, which is tangent to the ring trap, is not much different. The periodic boundary condition of the ring trap also allows for very long trajectories to be collected under uniform intensity, polarization, and phase gradient using circularly polarized light because the relevant forces on a particle or particle pair do not depend on their angular position in the ring [4].

Phase gradient strength and parameter ξ

The explicit expression for the phase gradient parameter ξ can be derived in terms of the the magnitude of the wave vector k of the trapping light in the experimental medium (water), the topological charge l, and the ring radius r by noting that the total phase change once around the ring is

$$\Delta\phi = 2\pi l. \tag{S1}$$

Assuming that the phase varies uniformly around the circumference of the ring gives locally (over a small angular section of the ring)

$$\frac{\partial\phi}{\partial x} = \frac{2\pi l}{2\pi r} = \frac{l}{r} \tag{S2}$$

and thus

$$\xi = \frac{l}{kr}. \tag{S3}$$

In the small phase gradient regime we used a ring radius of $4.54\mu m$ with $l = 1$, $l = 3$, and $l = 5$ corresponding to $\xi = 0.021$, $\xi = 0.064$, and $\xi = 0.11$, respectively. In the large phase gradient regime we used a ring radius of $3.37\mu m$ with $l = 8$, $l = 10$, and $l = 12$ corresponding to $\xi = 0.23$, $\xi = 0.29$, and $\xi = 0.34$, respectively.

HYDRODYNAMIC INTERACTION

Our experimental and theoretical analysis is focused on electrodynamic interactions between driven nanoparticles. The hydrodynamic interactions between particles in our experiment are addressed here. The velocity of a single particle A of radius a in overdamped fluid conditions is $\mathbf{v}_A = B_A \mathbf{F}_A$, where $B_A = (6\pi\eta a)^{-1}$ is the Stokes self-mobility of the sphere in a medium with dynamic viscosity η and $\mathbf{F}_A$ is the force on sphere A [5]. The net force on a homo-dimer, $F_{net} = F_A + F_B$, determines the dynamics of the particle pair. The velocity of the center of mass of the homo-dimer follows from Stokes' law[5] given the overdamped conditions of the experiment:

$$\langle v_{cm} \rangle = \frac{1}{2}\langle v_1 + v_2 \rangle = \frac{1}{2}\frac{F_A + F_B}{6\pi\eta a} = \frac{F_{net}}{12\pi\eta a} \tag{S4}$$

where η is the dynamic (shear) viscosity of the medium, and a is the radius of the identical particles. For electrodynamically non-interacting particles in a linear phase gradient, $F_{net} = 2F_{driving}$ and Eq. S4 gives $\langle v_{cm} \rangle = \langle v_{iso,1} \rangle = \langle v_{iso,2} \rangle$, *i.e.* the average velocity of the center of mass is equal to the velocity of an isolated particle (measured experimentally for particles that are separated by more than $3\mu m$ from their nearest neighbor) in the same phase gradient.

A second identical particle nearby B will create a flow field at particle A given by $\overline{\overline{\overline{\mathbf{H}}}}(\mathbf{r}_{AB})\mathbf{F}_B$, where $\overline{\overline{\overline{\mathbf{H}}}}(\mathbf{r}_{AB})$ is the Oseen tensor [6]. Following from Sokolov *et al* [7] the modified tangential velocity of particle A due to hydrodynamic interaction separated by angle $\Delta\theta_{AB}$ in our annular experimental geometry is

$$v_A^\theta(\Delta\theta_{AB}) \approx \big[B_A + g(\Delta\theta_{AB})\big] F_B^\theta; \tag{S5}$$

where

$$g(\Delta\theta_{AB}) = \frac{1 + 3\ cos\Delta\theta_{AB}}{16\pi\eta r\sqrt{2(1 - cos\Delta\theta_{AB})}} \tag{S6}$$

and r is the radius of the ring. Similarly, the radial force on particle A due to hydrodynamic interaction from the flow field caused by particle B, F_A^r, is

$$F_A^r \approx B_A^{-1} h(\Delta\theta_{AB}) F_B^\theta, \tag{S7}$$

where

$$h(\Delta\theta_{AB}) = \frac{3\ sin\Delta\theta_{AB}}{16\pi\eta r\sqrt{2(1 - cos\Delta\theta_{AB})}}. \tag{S8}$$

Eqs. S5-S8 suggest that the effects of hydrodynamic interactions can be characterized by the ratios $\chi_\theta = \frac{g(\Delta\theta_{AB})}{B_A}$ and $\chi_r = \frac{h(\Delta\theta_{AB})}{B_A}$. Fig. S2a shows plots of χ_r and χ_θ over the range of interparticle separations measured in our experiments. Although χ_r is very small throughout this range, χ_θ has a value of roughly 0.2 near single wavelength separation (*i.e.* $600nm$ for nanoparticles of radius $a = 75nm$). However, this interaction cannot give rise to the results we presented in the main text. Stable inter-particle separations will not be affected by the tangential component of the hydrodynamic interaction since $g(\Delta\theta_{AB})$ is symmetric under exchange of labels A and B, and thus any hydrodynamic forces will cancel when considering $F_B - F_A$.

Figure S2b shows a comparison between our experimentally measured pair velocities and the expected pair velocity enhancement due to hydrodynamic interaction. As in the main text, experimentally measured values of $\langle v_{cm} \rangle$ are shown as solid curves and the measured velocity of isolated particles, $\langle v_{iso} \rangle$, is shown as dashed lines. The hydrodynamically enhanced pair velocity given by $(1 + \chi_\theta)$ is shown as dotted curves. Although hydrodynamic interactions will slightly alter the tangential velocity of a particle pair, the total magnitude of this change is smaller than the enhancement of the pair velocity that we measured at separations equal to the wavelength of the trapping laser. In contrast to the monotonically decaying enhancement predicted from

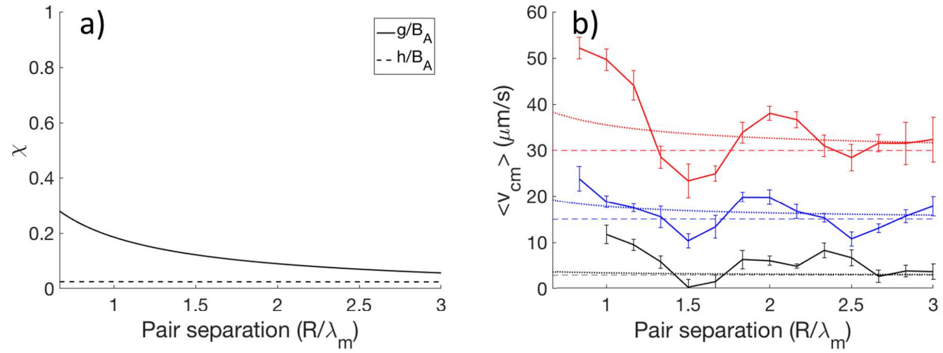

FIG. S2. Hydrodynamic interaction in particle pairs. (a) Magnitude of hydrodynamic interaction relative to the Stokes drag force as a function of pair separation in the tangential (solid) and radial (dashed) directions. (b) Comparison between our experimentally measured pair velocities and the expected pair velocity enhancement due to hydrodynamic interaction. Experimentally measured values of v_{cm} are shown as solid curves and the measured velocity of isolated particles v_{iso} is shown as horizontal dashed lines. The hydrodynamically enhanced pair velocity given by $(1 + \chi_\theta)$ is shown as monotonically decaying dotted curves.

hydrodynamics, we also measured diminished pair velocity compared to single-particle results at locations (*e.g.* $R = 1.5\lambda$) consistent with our theoretical predictions for electrodynamic interactions.

OPTICAL BINDING FOR SMALL PHASE GRADIENTS

Optical binding for small phase gradients has been covered in detail in Figliozzi *et al.*[2]. In Figure S3 we show experimentally measured particle separation PDFs (black) for $\xi = 0.021$ (a), $\xi = 0.064$ (b), and $\xi = 0.11$ (c). For comparison we have also plotted the energy (*i.e.* work) curves associated with optical binding (red). Vertical black dashed lines mark the significant minima in these energy curves, and correspond to peaks in probability. For Figure S3a-b, the first two minima are very close to $R = \lambda$ and $R = 2\lambda$, while for Figure S3c the phase gradient is strong enough to essentially eliminate the second optical binding energy minimum.

NET FORCE FOR A LARGE PHASE GRADIENT

Figure S4 shows the calculated net force in the point dipole approximation (solid) and our GMT simulations (dashed) on a homo-dimer for a large phase gradient ($\xi = 0.34$). The net force still depends on separation, but is no longer periodic and the modulations are proportionally weaker. Both of these effects can be understood from Equation 1 in the main text. Specifically, when the phase gradient is large, we expect the phase difference between the incident and scattered light at each particle to diverge from each other, *i.e.* $\Delta\phi_A \neq \Delta\phi_B$, and the interference effects that lead to the velocity enhancement for small phase gradients become much more

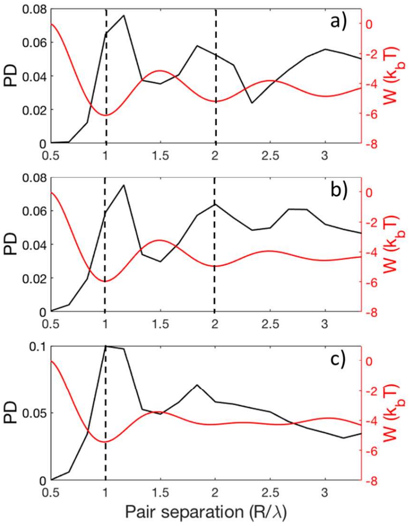

FIG. S3. (a)-(c) PDFs of measured inter-particle separations (black curves, left axis) for $\xi = 0.021$ (a), $\xi = 0.064$ (b), and $\xi = 0.11$ (c). The electrodynamic interaction potential is also plotted (red curves, right axis). The vertical dashed lines mark the significant minima in the electrodynamic interaction potential.

complicated.

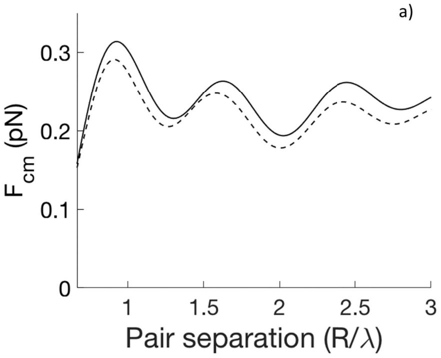

FIG. S4. Calculated net force in the point dipole approximation (solid) and our GMT simulations (dashed) on a homo-dimer for a large phase gradient ($\xi = 0.34$).

THEORETICAL POINT-DIPOLE CALCULATIONS

Describing the electromagnetic interactions in the point-dipole approximation allows employing analytical expressions for the total force on each particle. This approach provides fundamental insight into the origins of forces associated with phase differences compared to simulation methods that allow more exact calculation of the forces. We explain additional details of the theoretical model in this section.

Following the analysis of Dholakia *et al* [8], the total force on each isotropic particle along the R direction, in the point-dipole approximation, is

$$F_R^A = \frac{1}{2} Re\left[\left(\alpha_0^* \overline{\mathbf{E}}_0^{A*} + (\alpha_0^*)^2 \overline{\mathbf{E}}_0^{B*} \overline{\overline{\mathbf{G}}}^{AB*}\right)\frac{\partial \overline{\mathbf{E}}_0^{A}}{\partial R} + |\alpha_0|^2 \overline{\mathbf{E}}_0^{A*}\frac{\partial \overline{\overline{\mathbf{G}}}^{AB}}{\partial R}\overline{\mathbf{E}}_0^{B}\right], \tag{S9}$$

where α_0 is the polarizability of the identical particles, $*$ denotes complex conjugate, $\overline{\mathbf{E}}_0^{A}$ and $\overline{\mathbf{E}}_0^{B}$ are the incident electric field (vectors) at particles A and B, and $\overline{\overline{\mathbf{G}}}^{AB}$ is the dyadic Green's function that propagates the scattered field from particle B to particle A. The force on particle B can be obtained from Eq. S9 by exchanging the labels A and B. In this approximation we account for the phase gradient by explicitly plugging the phase and phase gradient derived from Eqs. S1-S2 into Eq. S9.

The polarizability of the spherical particles, α_0, is

$$\alpha_0 = \alpha_0^{'}\left(1 - \frac{2i}{3}\frac{k^3\alpha_0^{'}}{4\pi\epsilon_m}\right)^{-1} \tag{S10}$$

with

$$\alpha_0^{'} = \frac{4\pi a^3}{3}\frac{\epsilon_m(\epsilon_p - \epsilon_m)}{\epsilon_m + \frac{1}{3}(\epsilon_p - \epsilon_m)}, \tag{S11}$$

where k is the wavevector of the light interacting with the particle, ϵ_m is the permittivity of the medium surrounding the particle, and ϵ_p is the permittivity of the particle (silver; $\epsilon_p = -30.2 + 0.387i$) [9]. Equation S9 was evaluated using Matlab at various separations, R, for the parameters $a = 75nm$ (Ag NP radius), and an incident electric field strength of $E_0 = 10^6 V/m$.

The geometry used in our analytical treatment is one-dimensional; *i.e.*, only along the inter-particle axis. However, the field is incident from a perpendicular direction. The primary complication in our experimental ring-trap geometry is that the phase varies linearly with arc-length $r\theta$ in a ring trap, while R depends the chord-length between the two particles. In analyzing our experimental particle tracking data we only considered small angular sections of the ring (*i.e.* $\Delta\theta \ll 2\pi$), where these two distances are approximately equal (*i.e.* $sin(\theta) \approx \theta$).

To make predictions related to optical binding we evaluated the work required to separate two particles from some starting distance R_1 to another distance R_2

$$W(R_2) = -\int_{R_1}^{R_2} (F_R^B - F_R^A)\, dR'. \tag{S12}$$

Optical forces are generally non-conservative [10, 11], so it is not strictly correct to call W a potential energy. However, since our system is confined to one degree of freedom, the integration from R_1 to R_2 is guaranteed to lie on a single path, and therefore W will be a conserved quantity in the context of our experiment.

GENERALIZED MIE THEORY SIMULATIONS

Simulation Methods

The electrodynamic interactions are computed with the GMT method [12, 13] using the GMT software package MiePy that we developed. In this method, the incident and scattered fields are expanded into the vector spherical harmonic (VSH) wave functions for each particle. The incident field on particle j is expanded into the regular VSH's $\boldsymbol{N}_{nm}^{(1)}$ and $\boldsymbol{M}_{nm}^{(1)}$,

$$\boldsymbol{E}_{\text{inc}}^{j} = -\sum_{n=1}^{L_{\max}} \sum_{m=-n}^{n} iE_{mn} \left[p_{mn}^{(j\to j)} \boldsymbol{N}_{nm}^{(1)} + q_{mn}^{(j\to j)} \boldsymbol{M}_{mn}^{(1)}\right] \tag{S13}$$

where $L_{\max}$ is the maximum number of multipole orders to expand in, E_{mn} is a normalization constant, and $p_{mn}^{(j\to j)}$ and $q_{mn}^{(j\to j)}$ are the expansion coefficients of the incident source at particle j. The scattered field of particle j is similarly expanded into the scattering VSH's $\boldsymbol{N}_{nm}^{(3)}$ and $\boldsymbol{M}_{nm}^{(3)}$,

$$\boldsymbol{E}_{\text{scat}}^{j} = \sum_{n=1}^{L_{\max}} \sum_{m=-n}^{n} iE_{mn} \left[a_n^j p_{mn}^j \boldsymbol{N}_{nm}^{(3)} + b_n^j q_{mn}^j \boldsymbol{M}_{mn}^{(3)}\right] \tag{S14}$$

where a_n^j and b_n^j are the ordinary Mie coefficients [14] of particle j and p_{mn}^j and q_{mn}^j are the expansion coefficients of the light incident on particle j.

The expansion coefficients p_{mn}^j and q_{mn}^j are solved for in a system of $2NL_{\max}(L_{\max}+2)$ interaction equations

$$\begin{aligned} p_{mn}^j &= p_{mn}^{(j\to j)} - \sum_{l\neq j}^{(1,N)} \sum_{v=1}^{L_{\max}} \sum_{u=-v}^{v} A_{mn}^{uv}(l\to j) a_v^l p_{uv}^l + B_{mn}^{uv}(l\to j) b_v^l q_{uv}^l \\ q_{mn}^j &= q_{mn}^{(j\to j)} - \sum_{l\neq j}^{(1,N)} \sum_{v=1}^{L_{\max}} \sum_{u=-v}^{v} B_{mn}^{uv}(l\to j) a_v^l p_{uv}^l + A_{mn}^{uv}(l\to j) b_v^l q_{uv}^l \end{aligned} \tag{S15}$$

where $A_{mn}^{uv}(l\to j)$ and $B_{mn}^{uv}(l\to j)$ are the VSH translation coefficients from particle l to particle j.

Source decomposition in the GMT

To model the incident ring-shaped electric field, we use the following functional form of $\boldsymbol{E}$ in cylindrical coordinates,

$$\boldsymbol{E}(\rho,\theta,z) = \frac{E_0}{\rho_0^{u/2}\exp(-u/4)} \frac{\hat{\boldsymbol{x}} + i\hat{\boldsymbol{y}}}{\sqrt{2}} \rho^{u/2} \exp\left[-u\left(\frac{\rho}{2\rho_0}\right)^2\right] \exp\Big[i(l\theta + kz - \omega t)\Big], \tag{S16}$$

where ρ_0 is the radius of the ring, u determines the thickness of the ring, l dictates the strength of the phase gradient (equal to l/ρ_0), and $k = 2\pi n_b/\lambda$ is the wavenumber of light in the medium of index n_b. The normalization is chosen such that $|\boldsymbol{E}(\rho = \rho_0, \theta, z)| = E_0$. The following values were used for simulations in this work: $\lambda = 800\,\mathrm{nm}$, $n_b = 1.33$, $E_0 = 1 \times 10^6\,\mathrm{V/m}$, and $u = 40$. For the larger ring, $\rho_0 = 4.54\,\mu\mathrm{m}$ and $l = 1,\ 3, \text{or } 5$ and the for the smaller ring, $\rho_0 = 3.37\,\mu\mathrm{m}$ and $l = 0,\ 4, \text{or } 8$.

The incident electric field is decomposed into incident vector spherical harmonic wave functions using a near-field point matching method. [15] This provides the expansion coefficients $p_{mn}^{(j\to j)}$ and $q_{mn}^{(j\to j)}$ needed to solve the interaction equations, Eqn. S15. In this method, the coefficients are calculated so as to minimize, in a least squares sense, the difference between the expanded field, Eqn. S13, and the desired field, Eqn. S16.

Force evaluation in the GMT

Once the expansion coefficients are solved for, the time-averaged force on each particle can be determined by integrating the time-averaged Maxwell stress tensor (MST), $\langle \boldsymbol{T} \rangle$, over the surface of each sphere

$$\langle \boldsymbol{T} \rangle = \frac{1}{2}\mathrm{Re}\left[\varepsilon_b \boldsymbol{E} \otimes \boldsymbol{E}^* + \mu_b \boldsymbol{H} \otimes \boldsymbol{H}^* - \frac{1}{2}(\varepsilon_b E^2 + \mu_b H^2)\boldsymbol{I}\right] \tag{17a}$$

$$\langle \boldsymbol{F} \rangle = \oint_\Omega \langle \boldsymbol{T} \rangle \cdot d\boldsymbol{\Omega} \tag{17b}$$

where Ω is any surface enclosing the sphere. The electric field $\boldsymbol{E}$ is calculated using the field expansions in Eqs. S13-S14 and the magnetic field $\boldsymbol{H}$ is evaluated using similar field expansions. [12]

Comparison with Theoretical Point-Dipole Calculations

The GMT results presented in the main text are in very good agreement with our theoretical model, demonstrating that the approximations made (*e.g.* point dipoles, no higher order modes, finite sizes) do not result in significant inaccuracies. The magnitude of the net forces shown in Figure 2d in the main text differ slightly for the point-dipole theory and GMT method ($< 15\%$), with the largest difference at the peaks in net force. A combination of factors affects these forces, namely: (i) higher-order multipoles in the particles due to finite size, (ii) and the more realistic electric field distribution in the GMT simulations where the *peak intensity* was set equal to the uniform intensity in our theoretical calculations.

The energy curves in Fig. 3d further demonstrate the effect of the approximations made. The shapes of the curves differ most at small separations, where multipole effects and high-order scattering are most important. There is also a slight shift of the curves that grows with separation especially for the red curves ($\xi = 0.23$) shown in Fig. 3d in the main text. This is because in our theoretical point-dipole calculations phase varies linearly with separation R, while in our GMT simulations (and experiments), phase varies linearly with arc length. For short distances these two quantities are approximately equal, but when the particles are separated by a significant angle on a circle this approximation breaks down. The relatively small shifts seen in Figure 2d in the main text demonstrate that our experiments and theoretical results were in the regime where this approximations holds relatively well.

---

* nfschere@uchicago.edu

[1] Y. Roichman and D. G. Grier, in *Complex Light and Optical Forces*, Vol. 6483 (International Society for Optics and Photonics, 2007) p. 64830F.

[2] P. Figliozzi, N. Sule, Z. Yan, Y. Bao, S. Burov, S. K. Gray, S. A. Rice, S. Vaikuntanathan, and N. F. Scherer, Phys. Rev. E **95**, 22604 (2017).

[3] Y. Roichman, B. Sun, Y. Roichman, J. Amato-Grill, and D. G. Grier, Phys. Rev. Lett. **100**, 013602 (2008).

[4] Y. Yifat, D. Coursault, C. W. Peterson, J. Parker, Y. Bao, S. Gray, S. A. Rice, and N. F. Scherer, Light Sci. Appl. **7**, 105 (2018).

[5] R. S. Berry, S. A. Rice, and J. Ross, *Physical Chemistry* (Oxford University Press, 2000).

[6] J. Happel and H. Brenner, *Low Reynolds number hydrodynamics: with special applications to particulate media*, Vol. 1 (Springer Science & Business Media, 2012).

[7] Y. Sokolov, D. Frydel, D. G. Grier, H. Diamant, and Y. Roichman, Phys. Rev. Lett. **107**, 158302 (2011).

[8] K. Dholakia and P. Zemánek, Rev. Mod. Phys. **82**, 1767 (2010).

[9] P. B. Johnson and R.-W. Christy, Phys. Rev. B **6**, 4370 (1972).

[10] S. Sukhov and A. Dogariu, Rep. Prog. Phys **80**, 112001 (2017).

[11] M. V. Berry and P. Shukla, J. Phys. A **46**, 422001 (2013).

[12] Y.-l. Xu, Appl. Opt. **34**, 4573 (1995).

[13] J. Ng, Z. Lin, C. Chan, and P. Sheng, Physical Review B **72**, 085130 (2005).

[14] C. F. Bohren and D. R. Huffman, *Absorption and scattering of light by small particles* (John Wiley & Sons, 2008).

[15] T. Nieminen, H. Rubinsztein-Dunlop, and N. Heckenberg, J. Quant. Spectrosc. Radiat. Transf. **79–80**, 1005–1017 (2003).

Bibliography

[1] George M Whitesides and Bartosz Grzybowski. Self-assembly at all scales. *Science*, 295(5564):2418–2421, 2002.

[2] Marek Grzelczak, Jan Vermant, Eric M Furst, and Luis M Liz-Marzán. Directed self-assembly of nanoparticles. *ACS Nano*, 4(7):3591–3605, 2010.

[3] Yiyong Mai and Adi Eisenberg. Self-assembly of block copolymers. *Chemical Society Reviews*, 41(18):5969–5985, 2012.

[4] Peng Yin, Harry MT Choi, Colby R Calvert, and Niles A Pierce. Programming biomolecular self-assembly pathways. *Nature*, 451(7176):318–322, 2008.

[5] John D Joannopoulos, Pierre R Villeneuve, and Shanhui Fan. Photonic crystals. *Solid State Communications*, 102(2-3):165–173, 1997.

[6] Alexander Poddubny, Ivan Iorsh, Pavel Belov, and Yuri Kivshar. Hyperbolic metamaterials. *Nature Photonics*, 7(12):948–957, 2013.

[7] Xiaoyu Zheng, Howon Lee, Todd H Weisgraber, Maxim Shusteff, Joshua DeOtte, Eric B Duoss, Joshua D Kuntz, Monika M Biener, Qi Ge, Julie A Jackson, et al. Ultralight, ultrastiff mechanical metamaterials. *Science*, 344(6190):1373–1377, 2014.

[8] Steven A Cummer, Johan Christensen, and Andrea Alù. Controlling sound with acoustic metamaterials. *Nature Reviews Materials*, 1(3):1–13, 2016.

[9] Marcin Fialkowski, Kyle J. M. Bishop, Rafal Klajn, Stoyan K. Smoukov, Christopher J. Campbell, and Bartosz A. Grzybowski. Principles and implementations of dissipative (dynamic) self-assembly. *The Journal of Physical Chemistry B*, 110(6):2482–2496, 2006. PMID: 16471845.

[10] Bartosz A Grzybowski, Howard A Stone, and George M Whitesides. Dynamic self-assembly of magnetized, millimetre-sized objects rotating at a liquid-air interface. *Nature*, 405(6790):1033–1036, 2000.

[11] Eric Karsenti. Self-organization in cell biology: a brief history. *Nature Reviews Molecular Cell Biology*, 9(3):255–262, 2008.

[12] Mario Tagliazucchi, Emily A Weiss, and Igal Szleifer. Dissipative self-assembly of particles interacting through time-oscillatory potentials. *Proceedings of the National Academy of Sciences of the United States of America*, 111(27):9751–9756, 2014.

[13] Michael M. Burns, Jean Marc Fournier, and Jene A. Golovchenko. Optical Binding. *Physical Review Letters*, 63(12):1233–1236, 1989.

[14] Michael M Burns, Jean-Marc Fournier, and Jene A Golovchenko. Optical matter: Crystallization and binding in intense optical fields. *Science*, 249(4970):749–754, 1990.

[15] Kishan Dholakia and Pavel Zemánek. Colloquium: Gripped by Light: Optical Binding. *Review of Modern Physics*, 82(2):1767–1791, 2010.

[16] Vassili Demergis and Ernst-Ludwig Florin. Ultrastrong optical binding of metallic nanoparticles. *Nano Letters*, 12(11):5756–5760, 2012.

[17] Zijie Yan, Stephen K Gray, and F Scherer. Potential energy surfaces and reaction pathways for light-mediated self-organization of metal nanoparticle clusters. *Nature Communications*, 5:3751, 2014.

[18] Sergey Sukhov, Alexander Shalin, David Haefner, and Aristide Dogariu. Actio et reactio in optical binding. *Optics Express*, 23(1):247–252, 2015.

[19] Yuval Yifat, Delphine Coursault, Curtis W Peterson, John Parker, Ying Bao, Stephen Gray, Stuart A Rice, and Norbert F Scherer. Reactive optical matter: Light-induced motility in electrodynamically asymmetric nano-scale scatterers. *Light: Science & Applications*, 7(1):105, 2018.

[20] Nishant Sule, Yuval Yifat, Stephen K Gray, and Norbert F Scherer. Rotation and negative torque in electrodynamically bound nanoparticle dimers. *Nano Letters*, 17(11):6548–6556, 2017.

[21] Fei Han, John A Parker, Yuval Yifat, Curtis Peterson, Stephen K Gray, Norbert F Scherer, and Zijie Yan. Crossover from positive to negative optical torque in mesoscale optical matter. *Nature Communications*, 9(1):4897, 2018.

[22] Yuval Yifat, Nishant Sule, Yihan Lin, and Norbert F Scherer. Analysis and correction of errors in nanoscale particle tracking using the single-pixel interior filling function (spiff) algorithm. *Scientific Reports*, 7(1):1–10, 2017.

[23] John Parker, Curtis W Peterson, Yuval Yifat, Stuart A Rice, Zijie Yan, Stephen K Gray, and Norbert F Scherer. Optical matter machines: Angular momentum conversion by collective modes in optically bound nanoparticle arrays. *Optica*, 7(10):1341–1348, 2020.

[24] Jennifer E Curtis, Brian A Koss, and David G Grier. Dynamic holographic optical tweezers. *Optics Communications*, 207(1-6):169–175, 2002.

[25] Eric R Dufresne, Gabriel C Spalding, Matthew T Dearing, Steven A Sheets, and David G Grier. Computer-generated holographic optical tweezer arrays. *Review of Scientific Instruments*, 72(3):1810–1816, 2001.

[26] Fan Nan and Zijie Yan. Synergy of intensity, phase, and polarization enables versatile optical nanomanipulation. *Nano Letters*, 20(4):2778–2783, 2020.

[27] Yohai Roichman and David G Grier. Three-Dimensional Holographic Ring Traps. In David L. Andrews, Enrique J. Galvez, and Gerard Nienhuis, editors, *Proceedings of SPIE*, volume 6483, page 64830F, feb 2007.

[28] Curtis W. Peterson, John Parker, Stuart A. Rice, and Norbert F. Scherer. Controlling the dynamics and optical binding of nanoparticle homodimers with transverse phase gradients. *Nano Letters*, 19(2):897–903, 2019.

[29] J Y Wang and D E Silva. Wave-front Interpretation with Zernike Polynomials. *Appl. Opt.*, 19(9):1510–8, 1980.

[30] Caroline A Schneider, Wayne S Rasband, and Kevin W Eliceiri. Nih image to imagej: 25 years of image analysis. *Nature Methods*, 9(7):671–675, 2012.

[31] John C Crocker and David G Grier. Methods of digital video microscopy for colloidal studies. *Journal of Colloid and Interface Science*, 179(1):298–310, 1996.

[32] Shiqi Chen, Curtis Peterson, John Parker, Stuart A Rice, Andrew Ferguson, and Norbert Scherer. Data-driven reaction coordinate discovery in overdamped and non-conservative systems: Application to optical matter structural isomerization. 2020.

[33] Patrick C Chaumet and Manuel Nieto-Vesperinas. Time-averaged total force on a dipolar sphere in an electromagnetic field. *Optics Letters*, 25(15):1065–1067, 2000.

[34] Craig F Bohren and Donald R Huffman. *Absorption and Scattering of Light by Small Particles.* John Wiley & Sons, 2008.

[35] K Lance Kelly, Eduardo Coronado, Lin Lin Zhao, and George C Schatz. The optical properties of metal nanoparticles: The influence of size, shape, and dielectric environment. *The Journal of Physical Chemistry B*, 107:668–677, 2003.

[36] S A Tatarkova, A E Carruthers, and K Dholakia. One-dimensional optically bound arrays of microscopic particles. *Physical Review Letters*, 89(28):283901, 2002.

[37] Davit Hakobyan and Etienne Brasselet. Left-handed optical radiation torque. *Nature Photonics*, 8(8):610–614, 2014.

[38] Jun Chen, Jack Ng, Kun Ding, Kin Hung Fung, Zhifang Lin, and Che Ting Chan. Negative optical torque. *Scientific Reports*, 4:6386, 2014.

[39] Zijie Yan, Raman A. Shah, Garrett Chado, Stephen K. Gray, Matthew Pelton, and Norbert F. Scherer. Guiding Spatial Arrangements of Silver Nanoparticles by Optical Binding Interactions in Shaped Light Fields. *ACS Nano*, 7(2):1790–1802, feb 2013.

[40] Zijie Yan, Manas Sajjan, and Norbert F Scherer. Fabrication of a material assembly of silver nanoparticles using the phase gradients of optical tweezers. *Physical Review Letters*, 114(14):143901, 2015.

[41] Jana Damková, Lukáš Chvátal, Jan Ježek, Jindřich Oulehla, Oto Brzobohatỳ, and Pavel Zemánek. Enhancement of the 'tractor-beam' pulling force on an optically bound structure. *Light: Science & Applications*, 7(1):17135, 2018.

[42] Oto Brzobohatỳ, Lukáš Chvátal, Alexandr Jonáš, Martin Šiler, Jan Kanka, Jan Jezek, and Pavel Zemánek. Tunable soft-matter optofluidic waveguides assembled by light. *ACS Photonics*, 6(2):403–410, 2019.

[43] Fan Nan and Zijie Yan. Tuning nanoparticle electrodynamics by an optical-matter-based laser beam shaper. *Nano Letters*, 19(5):3353–3358, 2019.

[44] Bernhard Lamprecht, Gerburg Schider, RT Lechner, Harald Ditlbacher, Joachim R Krenn, Alfred Leitner, and Franz R Aussenegg. Metal nanoparticle gratings: Influence of dipolar particle interaction on the plasmon resonance. *Physical Review Letters*, 84(20):4721, 2000.

[45] Vira V Kravets, Oleg A Yeshchenko, Victor V Gozhenko, Leonidas E Ocola, David A Smith, James V Vedral, and Anatoliy O Pinchuk. Electrodynamic coupling in regular arrays of gold nanocylinders. *Journal of Physics D: Applied Physics*, 45(4):045102, 2012.

[46] Peter Nordlander, C Oubre, E Prodan, K Li, and MI Stockman. Plasmon hybridization in nanoparticle dimers. *Nano Letters*, 4(5):899–903, 2004.

[47] Prashant K Jain and Mostafa A El-Sayed. Plasmonic coupling in noble metal nanostructures. *Chemical Physics Letters*, 487(4-6):153–164, 2010.

[48] Shengli Zou and George C Schatz. Narrow plasmonic/photonic extinction and scattering line shapes for one and two dimensional silver nanoparticle arrays. *The Journal of Chemical Physics*, 121(24):12606–12612, 2004.

[49] Shengli Zou, Nicolas Janel, and George C Schatz. Silver nanoparticle array structures that produce remarkably narrow plasmon lineshapes. *The Journal of Chemical Physics*, 120(23):10871–10875, 2004.

[50] FJ Garcia De Abajo. Colloquium: Light scattering by particle and hole arrays. *Reviews of Modern Physics*, 79(4):1267, 2007.

[51] Weijia Wang, Mohammad Ramezani, Aaro I Väkeväinen, Päivi Törmä, Jaime Gómez Rivas, and Teri W Odom. The rich photonic world of plasmonic nanoparticle arrays. *Materials Today*, 21(3):303–314, 2018.

[52] Lukas Novotny and Bert Hecht. *Principles of Nano-Optics*. Cambridge university press, 2012.

[53] John Moore, Conrad Stanitski, and Peter Jurs. *Principles of Chemistry: the Molecular Science*. Cengage Learning, 2009.

[54] Barbara Wild, Lina Cao, Yugang Sun, Bishnu P Khanal, Eugene R Zubarev, Stephen K Gray, Norbert F Scherer, and Matthew Pelton. Propagation lengths and group velocities of plasmons in chemically synthesized gold and silver nanowires. *ACS Nano*, 6(1):472–482, 2012.

[55] Edward M Purcell, Henry Cutler Torrey, and Robert V Pound. Resonance absorption by nuclear magnetic moments in a solid. *Physical Review*, 69(1-2):37, 1946.

[56] Matthew Pelton. Modified spontaneous emission in nanophotonic structures. *Nature Photonics*, 9(7):427, 2015.

[57] Yuen-Ron Shen. The principles of nonlinear optics. *wi*, 1984.

[58] Rongchao Jin, Justin E Jureller, and Norbert F Scherer. Precise localization and correlation of single nanoparticle optical responses and morphology. *Applied Physics Letters*, 88(26):263111, 2006.

[59] Guangnan Meng, Natalie Arkus, Michael P Brenner, and Vinothan N Manoharan. The free-energy landscape of clusters of attractive hard spheres. *Science*, 327(5965):560–563, 2010.

[60] Rebecca W Perry, Miranda C Holmes-Cerfon, Michael P Brenner, and Vinothan N Manoharan. Two-dimensional clusters of colloidal spheres: Ground states, excited states, and structural rearrangements. *Physical Review Letters*, 114(22):228301, 2015.

[61] Melody X Lim, Anton Souslov, Vincenzo Vitelli, and Heinrich M Jaeger. Cluster formation by acoustic forces and active fluctuations in levitated granular matter. *Nature Physics*, 15(5):460–464, 2019.

[62] Andrew J Archer and Nigel B Wilding. Phase behavior of a fluid with competing attractive and repulsive interactions. *Physical Review E*, 76(3):031501, 2007.

[63] Juan Carlos Fernandez Toledano, Francesco Sciortino, and Emanuela Zaccarelli. Colloidal systems with competing interactions: From an arrested repulsive cluster phase to a gel. *Soft Matter*, 5(12):2390–2398, 2009.

[64] Alan Barros de Oliveira, Giancarlo Franzese, Paulo A Netz, and Marcia C Barbosa. Waterlike hierarchy of anomalies in a continuous spherical shouldered potential. *The Journal of Chemical Physics*, 128(6):064901, 2008.

[65] Sergey Sukhov and Aristide Dogariu. Non-conservative optical forces. *Reports on Progress in Physics*, 80(11):112001, 2017.

[66] R. S. Berry, S. A. Rice, and J. Ross. *Physical Chemistry*. Oxford University Press, 2000.

[67] Fei Han and Zijie Yan. Phase transition and self-stabilization of light-mediated metal nanoparticle assemblies. *ACS Nano*, 14(6):6616–6625, 2020. PMID: 32422042.

[68] A V Ivlev, J Bartnick, M Heinen, C R Du, V Nosenko, and H Löwen. Statistical mechanics where newton's third law is broken. *Phys. Rev. X*, 5(1):011035, 2015.

[69] Vítězslav Karásek, Martin Šiler, Oto Brzobohatý, and Pavel Zemánek. Dynamics of an optically bound structure made of particles of unequal sizes. *Optics Letters*, 42(7):1436–1439, 2017.

[70] Hongxu Chen, Qilong Zhao, and Xuemin Du. Light-powered micro/nanomotors. *Micromachines*, 9(2):41, 2018.

[71] Lei Shao and Mikael Käll. Light-driven rotation of plasmonic nanomotors. *Adv. Funct. Mater.*, page 1706272, 2018.

[72] Leilei Xu, Fangzhi Mou, Haotian Gong, Ming Luo, and Jianguo Guan. Light-driven micro/nanomotors: From fundamentals to applications. *Chemical Society Reviews*, 46(22):6905–6926, 2017.

[73] Patrick Figliozzi, Nishant Sule, Zijie Yan, Ying Bao, Stanislav Burov, Stephen K Gray, Stuart A. Rice, Suriyanarayanan Vaikuntanathan, and Norbert F Scherer. Driven Optical Matter: Dynamics of Electrodynamically Coupled Nanoparticles in an Optical Ring Vortex. *Phys. Rev. E*, 95(2):22604, feb 2017.

[74] Yael Roichman, David G Grier, and George Zaslavsky. Anomalous collective dynamics in optically driven colloidal rings. *Physical Review E*, 75(2):020401, 2007.

[75] Ivo F Sbalzarini and Petros Koumoutsakos. Feature point tracking and trajectory analysis for video imaging in cell biology. *Journal of Structural Biology*, 151(2):182–195, 2005.

[76] Stanislav Burov, Patrick Figliozzi, Binhua Lin, Stuart A Rice, Norbert F Scherer, and Aaron R Dinner. Single-pixel interior filling function approach for detecting and correcting errors in particle tracking. *Proceedings of the National Academy of Sciences of the United States of America*, page 201619104, 2016.

[77] Hong-Ren Jiang, Natsuhiko Yoshinaga, and Masaki Sano. Active motion of a janus particle by self-thermophoresis in a defocused zlaser beam. *Physical Review Letters*, 105(26):268302, 2010.

[78] Albert Einstein. Über die von der molekularkinetischen theorie der wärme geforderte bewegung von in ruhenden flüssigkeiten suspendierten teilchen. *Ann. Phys. (Berlin, Ger.)*, 322(8):549–560, 1905.

[79] Ralf Metzler and Joseph Klafter. The restaurant at the end of the random walk: Recent developments in the description of anomalous transport by fractional dynamics. *Journal of Physics A: Mathematical and General*, 37(31):R161, 2004.

[80] Sergey Sukhov, Veerachart Kajorndejnukul, Roxana Rezvani Naraghi, and Aristide Dogariu. Dynamic consequences of optical spin-orbit interaction. *Nature Photonics*, 9(12):809–812, 2015.

[81] Yu-lin Xu. Electromagnetic scattering by an aggregate of spheres. *Appl. Opt.*, 34(21):4573–4588, 1995.

[82] Jack Ng, ZF Lin, CT Chan, and Ping Sheng. Photonic clusters formed by dielectric microspheres: Numerical simulations. *Physical Review B*, 72(8):085130, 2005.

[83] Jingjing Li, Alessandro Salandrino, and Nader Engheta. Shaping light beams in the nanometer scale: A yagi-uda nanoantenna in the optical domain. *Physical Review B*, 76(24):245403, 2007.

[84] Terukazu Kosako, Yutaka Kadoya, and Holger F Hofmann. Directional control of light by a nano-optical yagi–uda antenna. *Nature Photonics*, 4(5):312–315, 2010.

[85] Emmy Noether. Invariant variation problems. *Transport Theory and Statistical Physics*, 1(3):186–207, 1971.

[86] Stephen J Ebbens and Jonathan R Howse. In pursuit of propulsion at the nanoscale. *Soft Matter*, 6(4):726–738, 2010.

[87] Jonathan R Howse, Richard AL Jones, Anthony J Ryan, Tim Gough, Reza Vafabakhsh, and Ramin Golestanian. Self-motile colloidal particles: From directed propulsion to random walk. *Physical Review Letters*, 99(4):048102, 2007.

[88] John M Abendroth, Oleksandr S Bushuyev, Paul S Weiss, and Christopher J Barrett. Controlling motion at the nanoscale: Rise of the molecular machines. *ACS Nano*, 9(8):7746–7768, 2015.

[89] Fan Nan and Zijie Yan. Sorting metal nanoparticles with dynamic and tunable optical driven forces. *Nano Letters*, 18(7):4500–4505, 2018.

[90] Fan Nan and Zijie Yan. Optical sorting at the single-particle level with single-nanometer precision using coordinated intensity and phase gradient forces. *ACS Nano*, 2020.

[91] Arthur Ashkin, James M Dziedzic, JE Bjorkholm, and Steven Chu. Observation of a single-beam gradient force optical trap for dielectric particles. *Optics Letters*, 11(5):288–290, 1986.

[92] Richard W Bowman and Miles J Padgett. Optical trapping and binding. *Reports on Progress in Physics*, 76(2):026401, 2013.

[93] Aristide Dogariu, Sergey Sukhov, and José Sáenz. Optically induced 'negative forces'. *Nature Photonics*, 7(1):24, 2013.

[94] Lukáš Chvátal, Oto Brzobohatý, and Pavel Zemánek. Binding of a pair of au nanoparticles in a wide gaussian standing wave. *Optical Review*, 22(1):157–161, 2015.

[95] Stephen H Simpson, Pavel Zemánek, Onofrio M Maragò, Philip H Jones, and Simon Hanna. Optical binding of nanowires. *Nano Letters*, 17(6):3485–3492, 2017.

[96] Fan Nan, Fei Han, Norbert F Scherer, and Zijie Yan. Dissipative self-assembly of anisotropic nanoparticle chains with combined electrodynamic and electrostatic interactions. *Advanced Materials*, page 1803238, 2018.

[97] JM Taylor and GD Love. Spontaneous symmetry breaking and circulation by optically bound microparticle chains in gaussian beam traps. *Physical Review A*, 80(5):053808, 2009.

[98] Silvia Albaladejo, Juan José Sáenz, and Manuel I Marqués. Plasmonic nanoparticle chain in a light field: A resonant optical sail. *Nano Letters*, 11(11):4597–4600, 2011.

[99] Markus Aspelmeyer, Tobias J Kippenberg, and Florian Marquardt. Cavity optomechanics. *Rev. Mod. Phys.*, 86(4):1391, 2014.

[100] René Reimann, Michael Doderer, Erik Hebestreit, Rozenn Diehl, Martin Frimmer, Dominik Windey, Felix Tebbenjohanns, and Lukas Novotny. Ghz rotation of an optically trapped nanoparticle in vacuum. *Phys. Rev. Lett.*, 121:033602, Jul 2018.

[101] Sang-Hyuk Lee and David G Grier. Giant colloidal diffusivity on corrugated optical vortices. *Phys. Rev. Lett.*, 96(19):190601, 2006.

[102] Yohai Roichman, Bo Sun, Yael Roichman, Jesse Amato-Grill, and David G Grier. Optical forces arising from phase gradients. *Phys. Rev. Lett.*, 100(1):013602, 2008.

[103] Oto Brzobohatỳ, Vıtezslav Karásek, T Čižmár, and Pavel Zemánek. Dynamic size tuning of multidimensional optically bound matter. *Applied Physics Letters*, 99(10):101105, 2011.

[104] Delphine Coursault, Nishant Sule, John Parker, Ying Bao, and Norbert F. Scherer. Dynamics of the optically directed assembly and disassembly of gold nanoplatelet arrays. *Nano Letters*, 18(6):3391–3399, 2018.

[105] Patrick Figliozzi, Curtis W Peterson, Stuart A Rice, and Norbert F Scherer. Direct visualization of barrier crossing dynamics in a driven optical matter system. *ACS Nano*, 12(6):5168–5175, 2018.

[106] Yulia Sokolov, Derek Frydel, David G Grier, Haim Diamant, and Yael Roichman. Hydrodynamic pair attractions between driven colloidal particles. *Phys. Rev. Lett.*, 107(15):158302, 2011.

[107] A Ambari, B Gauthier-Manuel, and E Guyon. Wall effects on a sphere translating at constant velocity. *J. Fluid Mech.*, 149:235–253, 1984.

[108] Michael V Berry and Pragya Shukla. Physical curl forces: Dipole dynamics near optical vortices. *J. Phys. A*, 46(42):422001, 2013.

[109] T Čižmár, LC Dávila Romero, K Dholakia, and DL Andrews. Multiple optical trapping and binding: New routes to self-assembly. *J. Phys. B*, 43(10):102001, 2010.

[110] Graham R Fleming and Peter G Wolynes. Chemical dynamics in solution. *Phys. Today*, 43(5):36–43, 1990.

[111] Robert Zwanzig. *Nonequilibrium Statistical Mechanics*. Oxford University Press, 2001.

[112] Matthias Rief, Mathias Gautel, Filipp Oesterhelt, Julio M Fernandez, and Hermann E Gaub. Reversible unfolding of individual titin immunoglobulin domains by afm. *Science*, 276(5315):1109–1112, 1997.

[113] H Peter Lu, Luying Xun, and X Sunney Xie. Single-molecule enzymatic dynamics. *Science*, 282(5395):1877–1882, 1998.

[114] EH Trepagnier, Christopher Jarzynski, Felix Ritort, Gavin E Crooks, CJ Bustamante, and J Liphardt. Experimental test of hatano and sasa's nonequilibrium steady-state equality. *Proceedings of the National Academy of Sciences of the United States of America*, 101(42):15038–15041, 2004.

[115] Keir C Neuman and Attila Nagy. Single-molecule force spectroscopy: Optical tweezers, magnetic tweezers and atomic force microscopy. *Nature Methods*, 5(6):491–505, 2008.

[116] Steve Pressé, Julian Lee, and Ken A Dill. Extracting conformational memory from single-molecule kinetic data. *The Journal of Physical Chemistry B*, 117(2):495–502, 2013.

[117] Hao Shen, Xiaochun Zhou, Ningmu Zou, and Peng Chen. Single-molecule kinetics reveals a hidden surface reaction intermediate in single-nanoparticle catalysis. *The Journal of Physical Chemistry C*, 118(46):26902–26911, 2014.

[118] Krishna Neupane, Daniel AN Foster, Derek R Dee, Hao Yu, Feng Wang, and Michael T Woodside. Direct observation of transition paths during the folding of proteins and nucleic acids. *Science*, 352(6282):239–242, 2016.

[119] SC Kou, Binny J Cherayil, Wei Min, Brian P English, and X Sunney Xie. Single-molecule michaelis-nenten equations. *The Journal of Physical Chemistry B*, 109(41):19068–19081, 2005.

[120] Daniel L Floyd, Stephen C Harrison, and Antoine M Van Oijen. Analysis of kinetic intermediates in single-particle dwell-time distributions. *Biophysical Journal*, 99(2):360–366, 2010.

[121] Karel Svoboda and Steven M Block. Biological applications of optical forces. *Annual Review of Biophysics and Biomolecular Structure*, 23(1):247–285, 1994.

[122] Jeffrey R Moffitt, Yann R Chemla, Steven B Smith, and Carlos Bustamante. Recent advances in optical tweezers. *Annual Review of Biochemistry*, 77, 2008.

[123] Hans-Jürgen Butt, Brunero Cappella, and Michael Kappl. Force measurements with the atomic force microscope: Technique, interpretation and applications. *Surface Science Reports*, 59(1-6):1–152, 2005.

[124] Loïc Rondin, Jan Gieseler, Francesco Ricci, Romain Quidant, Christoph Dellago, and Lukas Novotny. Direct measurement of kramers turnover with a levitated nanoparticle. *Nature Nanotechnology*, 12(12):1130, 2017.

[125] AA Ovchinnikov and Ya B Zeldovich. Role of density fluctuations in bimolecular reaction kinetics. *Chemical Physics*, 28(1-2):215–218, 1978.

[126] Ahmed H Zewail. Femtochemistry: Atomic-scale dynamics of the chemical bond. *The Journal of Physical Chemistry A*, 104(24):5660–5694, 2000.

[127] D Allan, T Caswell, and N Keim. van der wel, c. trackpy: Trackpy v0. 3.2. *URL https://doi. org/10.5281/zenodo*, 60550:v0, 2016.

[128] N Sule, S A Rice, S K Gray, and N F Scherer. An Electrodynamics-Langevin Dynamics (ED-LD) Approach to Simulate Metal Nanoparticle Interactions and Motion. *Optics Express*, 23(23):29978, 2015.

[129] Max Born and Emil Wolf. *Principles of Optics: Electromagnetic Theory of Propagation, Interference and Diffraction of Light*. Elsevier, 2013.

[130] George I Bell. Models for the specific adhesion of cells to cells. *Science*, 200(4342):618–627, 1978.

[131] Olga K Dudko, Gerhard Hummer, and Attila Szabo. Intrinsic rates and activation free energies from single-molecule pulling experiments. *Physical Review Letters*, 96(10):108101, 2006.

[132] Pilar Cossio, Gerhard Hummer, and Attila Szabo. On artifacts in single-molecule force spectroscopy. *Proceedings of the National Academy of Sciences of the United States of America*, 112(46):14248–14253, 2015.

[133] Casper van der Wel and Daniela J Kraft. Automated tracking of colloidal clusters with sub-pixel accuracy and precision. *Journal of Physics: Condensed Matter*, 29(4):044001, 2016.

[134] Christopher Battle, Chase P Broedersz, Nikta Fakhri, Veikko F Geyer, Jonathon Howard, Christoph F Schmidt, and Fred C MacKintosh. Broken detailed balance at mesoscopic scales in active biological systems. *Science*, 352(6285):604–607, 2016.